United States Department of Commerce
Technology Administration
National Institute of Standards and Technology

NIST Special Publication 930

Technical Digest
Symposium on Optical Fiber Measurements, 1998

Sponsored by the National Institute of Standards and Technology
in cooperation with the IEEE Lasers and Electro-Optics Society
and the Optical Society of America

NIST Special Publication 930

Technical Digest—Symposium on Optical Fiber Measurements, 1998

Digest of a symposium sponsored by the
National Institute of Standards and Technology
in cooperation with the
IEEE Lasers and Electro-Optics Society
and the Optical Society of America

Edited by

G.W. Day
D.L. Franzen
P.A. Williams

Electronics and Electrical Engineering Laboratory
National Institute of Standards and Technology
Boulder, Colorado 80303-3328

September 1998

U.S. DEPARTMENT OF COMMERCE, William M. Daley, Secretary
TECHNOLOGY ADMINISTRATION, Gary R. Bachula, Acting Under Secretary for Technology
NATIONAL INSTITUTE OF STANDARDS AND TECHNOLOGY, Raymond G. Kammer, Director

National Institute of Standards
and Technology
Special Publication 930
Natl. Inst. Stand. Technol.
Spec. Publ. 930
196 pages (September 1998)
CODEN:NSPUE2

U.S. Government Printing Office
Washington: 1998

For sale by the Superintendent of
Documents
U.S. Government Printing Office
Washington, DC 20402-9325

Preface

This year marks the 10th biennial Symposium on Optical Fiber Measurements, held September 15-17, 1998 at the laboratories of the National Institute of Standards and Technology in Boulder, Colorado.

Over these last 20 years, the SOFM has been a good indicator of the issues that concern the fiber optic measurement community. At first glance, the second day's multimode fiber measurement talks may seem like a trip back in time to an SOFM from the eighties. However, recent events have brought multimode fiber issues back into the measurement arena. Polarization-mode dispersion (PMD) continues to be a topic of much interest with two full sessions devoted to a variety of subtopics in the field. Fiber geometry has several contributions, as does the broad topic of fiber mapping with length (including such parameters as chromatic dispersion and polarization properties).

This year's Symposium consists of 44 papers (10 invited and 34 contributed), and continues to show a strong international participation, with two-thirds of the papers originating outside the United States.

G.W. Day
D.L. Franzen
P.A. Williams
Boulder, Colorado
September 1998

SYMPOSIUM COMMITTEE

D.L. Franzen, NIST, General Chair

G.W. Day, NIST, Program Co-Chair

P.A. Williams, NIST, Program Co-Chair

M. Artiglia, CSELT

A. Barlow, EG&G Fiber Optics

J. Benson, NPL

S.C. Fleming, University of Sydney

N. Gisin, University of Geneva

T.A. Hanson, Corning

B.L. Heffner, Hewlett-Packard

R.B. Kummer, Lucent Technologies

P.S. Lovely, PK Technology

H. Nagai, Anritsu

W.A. Reed, Lucent Technologies

L.A. Reith, Bellcore

D.K. Roland, SpecTran

G.W. Schinn, EXFO

K. Takada, NTT

CONTENTS

DWDM Component Characterization

Bruce Nyman
JDS Fitel

Introduction

Wavelength division multiplexing has enabled tremendous growth in fiber optic communication systems. Initial WDM systems used two channels at 1.3 and 1.5 μm while today's systems pack up to 96 channels into the 35 nm bandwidth provided by erbium doped fiber amplifiers. As the channel spacing has approached 50 GHz the component characterization requirements have increased. A typical system contains many devices such as isolators, taps, and wavelength division multiplexers. The key component in today's WDM systems is the demultiplexer. Its performance limits the overall system capacity and design margin. Therefore, we will examine the measurement requirements of this device. Other devices will have similar measurement needs.

The function of the demultiplexer is to separate the channels at the end of a transmission system. There are currently four different technologies used; dielectric filters, fiber Bragg gratings, Difraction Gratings and waveguide based devices. Devices for 100 GHz systems have been demonstrated in each of these technologies. The best technology for 50 GHz devices is still not clear. A key issue for 50 GHz systems will be the stability of the lasers.

The number of channels in the system will be determined by the channel spacing of the demultiplexer. As we will see later the allowable channel spacing is a combination of the passband width and the out of band isolation. For systems without amplifiers the insertion loss will limit the overall system power budget.

Insertion Loss Based Measurements

The key measurement for characterizing DWDM devices is insertion loss versus wavelength. Many of the device parameters are based on an interpretation of the insertion loss data. The requirements for the insertion loss measurement are very stringent for the demultiplexer.
As an example we consider the case of an 80 channel demultiplexer for a 50 GHz system.

The first requirement for this measurement is the wavelength range. For the 80 channel system the wavelength range is at least 35 nm. The accuracy of the wavelength should be better than 0.01 nm. The dynamic range required will be at least 50 dB. This is needed to measure the performance of the demultiplexer at adjacent channels. Finally, the most difficult requirement is slope accuracy. For 50 GHz (0.4 nm) spacing, the channel width measured at the 1 dB down points might be 0.2 nm. At the edge of the next channel, 0.2 nm away, the system needs the loss of this channel to be at least 30 dB. Assuming a linear slope, the slope accuracy must be better than 145 dB/nm. I real devices the slope will be even sharper.

Once the insertion loss versus wavelength data is available it can be analyzed to obtain the desired device parameters. Below, these parameters are discussed.

Center Wavelength: How should the nominal center wavelength be defined? Ideally, the center wavelength is the designated ITU wavelength. However, an alternative definition might be the

center of a nominal bandwidth. For example, the center of two points measured 1 dB down from the minimum insertion loss could be used. This approach is useful if the passband is not flat.
Bandwidth: The bandwidth is specified relative to the minimum insertion loss point. The exact bandwidth is then expressed as the number of dBs below the minimum insertion loss point. For example, a 1 dB bandwidth might specify the usable channel bandwidth, while a 30 dB bandwidth would lead to the limits on adjacent channel spacing.

Isolation: This isolation is typically defined as the amount of light from other channels that will be transmitted through the device. This is sometimes divided into two components, the power from the adjacent channel and the power from all the other channels. This is also sometimes referred to as crosstalk. One interesting aspect of this requirement is that the entire system wavelength band must be examined. Indeed what is really required is the sum of all the powers at all other channels. This is especially true for fiber Bragg gratings and waveguide devices.

Return Loss: The reflectivity of the device should be measured across the entire wavelength band. This is the integrated total return loss not a spatially resolved measurement.

In measuring these quantities one must consider the degree of polarization and the polarization state of the light source used. All the measurements discussed above are polarization dependent. Therefore it will be necessary to determine the variations that occur with polarization. This leads to some interesting questions about definitions. There are no standards that define the concepts of polarization dependent bandwidth and crosstalk.

For example, lets consider the bandwidth. One way to determine the worst case bandwidth would be to measure the polarization dependent loss at each wavelength and plot the maximum and minimum loss. The bandwidth would then be defined as the maximum or minimum loss envelope as required. The minimum loss envelope might be used for the 30 dB bandwidth while the maximum loss envelope might be used for the 1 dB channel passband. This approach makes no assumptions about how polarization dependent loss at each wavelength varies with the state of polarization at adjacent wavelengths. In real systems this may be required due to the effect of PMD on the state of polarization. So the question is, what is this the proper way to define the polarization dependent bandwidth?

Once techniques to measure these quantities over wavelength and polarization are available making measurements for reliability testing are possible. Typically these involve characterizing the device's performance over a temperature range and a humidity range. These tests are defined in documents such as Bellcore 1209 and 1221.

Other Measurement Needs

There are two other measurements that are needed for DWDM components, chromatic dispersion, and polarization mode dispersion (PMD). The chromatic dispersion must be measured both at the center of the passband and at the edges. The chromatic dispersion at the edges of the passband can effect adjacent channels in add/drop configurations. The chromatic dispersion has been examined for various filter types.[1] For devices with narrow passbands the traditional measurement methods[2] will not suffice. The measurement method must be modified for the narrow passbands.

PMD can be a problem for many DWDM components. Typically devices such as isolators, circulators and the erbium fiber itself can have significant PMD. Demultiplexers and other narrow

band devices must be characterized for PMD. This will require measurement techniques modified for the narrow bandwidths. In addition, there are higher order PMD effects that need to be measured.

Measurement Methods

In DWDM systems there is a large variation in the types of devices used. Some devices, such as isolators and taps have little spectral information, and thus need simple measurement methods. Devices for optical supervisory channel add and drop functions are more complex. Demultiplexers and channel add drop devices will require more complicated measurement methods. These devices need both high wavelength resolution and accuracy, on the order of 5 pm. At the same time, measurements must be made over the entire wavelength range.

The simplest measurement technique will use a broadband noise source and an optical spectrum analyzer (OSA). The broadband noise source is unpolarized with a short coherence length. This approach provides a fast way to measure insertion loss versus wavelength. This approach can be used to measure isolation and return loss. However, measurements of PDL will require additional equipment.

The more advanced measurements require a tunable laser source. This source has a narrow linewidth (< 10 MHz), and is polarized. The laser can be tuned in 1 pm steps over the entire wavelength range. The combination of a tunable laser with either a power meter or an OSA provides a high resolution measurement with the needed wavelength and power accuracy. The only drawback of this method is scan speed. Each measurement takes about a few seconds. Thus the time for covering the entire 35 nm span with 5 pm resolution could be a few hours. This is what would be needed to measure isolation in a demultiplexer. Adding polarization dependent measurements will increase the measurement time. Improving the measurement time has been the topic of recent developments. A system that reduces the measurement time to 3 seconds for the entire wavelength range with 3 pm resolution will be discussed.

The measurement methods for chromatic dispersion and PMD have similar issues with the wavelength characteristics of the devices. For the narrow bandwidth devices a tunable laser must be used. For chromatic dispersion a phase sensitive technique is typically used. Here the tunable laser is modulated and the phase delay to the device is measured. For PMD the tunable laser is used as the light source for a Jones matrix PMD measurement method.

Conclusions

The variety of devices used in DWDM systems lead to various measurement requirements and methods. Demultiplexers have the most difficult measurement requirements and test methods. Common definitions for the measurements should be developed. Given the need for high resolution measurements over the entire 35 nm bandwidth new testing methods will be required.

References

[1] "Optimal Dispersion of Optical Filters for WDM Systems," G. Lenz, B. J. Eggleton, C. K. Madsen, C. R. Giles, and G. Nykolak, IEEE Photon. Tech. Lett., 567(1998).
[2] "Fiber Optic Test and Measurement," Dennis Derickson, editor, Prentice Hall, chapter 12.

Accurate Polarization Dependent Loss Measurement and Calibration Standard Development

R. M. Craig, S. L. Gilbert, and P. D. Hale
National Institute of Standards and Technology, 325 Broadway, Boulder, CO 80303

Abstract - We have implemented an automated, nonmechanical approach to the measurement of polarization dependent loss. We use a deterministic fixed-states method to obtain Mueller matrix elements from intensity measurements at specific polarization states. Voltage-modulated liquid-crystal variable retarders set the input polarization states. Synchronous detection is employed to increase the signal-to-noise ratio of the system and thereby allow a measurement resolution of better than 0.001 dB. We present polarization-dependent loss measurements from 0.0016 to 0.56 dB at 1550 nm to verify performance. We also present results from potential artifact calibration standards of an all-fiber design.

Introduction

Polarization dependent loss (PDL) is defined as $10\log(T_{max}/T_{min})$ (dB) where T is transmittance taken over the entire polarization-state space. Polarization dependent loss is usually characterized as a localized component effect as opposed to the distributed nature of polarization mode dispersion. PDL measurement methods can be divided into three categories, all of which are represented by commercial instrumentation: deterministic fixed-states, deterministic all-states, and pseudorandom all-states [1]. We have implemented a deterministic fixed-states technique. Our goal is to establish the capability to measure PDL with a resolution finer than 0.001 dB and to determine the absolute accuracy of our method. In this paper we summarize an approach to polarization dependent loss measurement that employs a nonmechanical technique capable of synchronous detection. This system has been described more fully in [2]. We also present new results from an all-fiber PDL artifact reference that is potentially useful as a transfer standard. This may lead to a Standard Reference Material for the calibration of commercial instrumentation.

Because PDL is always greater than or equal to zero, noise in the PDL measurement system can degrade the sensitivity to very small PDL values (where the PDL is less than the system's single-measurement noise). Sensitivity to these small PDL values cannot be improved by increasing the number of measurements; the average of multiple PDL measurements will always yield a positive value that is proportional to the single-measurement noise. However, synchronously averaging measured intensities in a deterministic fixed-states method can improve sensitivity due to the increase in the signal-to-noise ratio.

We implemented our system using voltage-modulated liquid-crystal variable retarders (LCVR) and synchronous detection. A different LCVR approach has also been reported [3]. However, in our case, modulation of the polarization state allows differential measurement as well as an improvement in sensitivity due to synchronous time averaging.

Concept

Our method, which we call the Mueller-Stokes technique, is a variation on a matrix technique developed by Favin et al. [4], and relies solely on power measurements at specific polarization states. In this deterministic fixed-states method, four well-defined polarization states are necessary to determine the first-row Mueller matrix elements of a component. The global polarization dependence of transmittance can then be determined from these four elements.

Because the measurement depends only on the relative coordinates of the four states, the only requirements on the set are that they maintain relative angular separations of 90° about the origin of the polarization (Poincaré) sphere. This implies that constant intervening retardance, as represented by rotations of the sphere, will have no net effect. A representative sample of states is shown in Fig. 1a, while a rotation of those states is

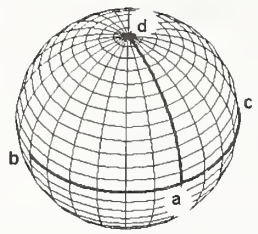

Figure 1a: Initial Poincaré trajectories of the LCVR pair over a measurement.

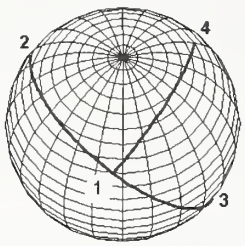

Figure 1b: LCVR trajectories following birefringent displacement

seen in Fig. 1b.

In our system, the polarization states are produced by two LCVR units in series. These modulate the polarization state of a low-coherence polarized beam. The effect of the pair is to produce final polarization states equivalent to those produced by a quarter-wave and half-wave retarder combination undergoing independent rotations. Following generation of the four polarization states (with average powers I_a, …, I_d), the light is transmitted by a single mode fiber with arbitrary but relatively stable birefringence through the device under test (DUT). It proceeds to a polarization-insensitive detector which measures the four time-averaged output powers (I_1, …, I_4). We measure the time-averaged input powers (I_a, …, I_d) in the same way with the DUT removed to establish a baseline system response. The four first-row Mueller matrix elements (m_{11},…, m_{14}) are combinations of ratios of these powers [2]. Information about the global transmittance extrema are contained in the first row matrix elements. The transmittance extrema, T_{min} and T_{max}, are

$$T_{max} = m_{11} + \sqrt{m_{12} + m_{13} + m_{14}} \ ,$$

$$T_{min} = m_{11} - \sqrt{m_{12} + m_{13} + m_{14}} \ . \qquad (1)$$

Polarization dependent loss then follows as defined above.

The essential advantage of this technique is nonmechanical retardance modulation, which allows rapid synchronous time averaging in a low noise environment at a frequency set by an external clock. Synchronous time averaging improves the signal-to-noise ratio and can be applied in different ways depending on the method of signal acquisition chosen.

Implementation

Figure 2 shows a schematic of the measurement system. Our system consists of five major sections: source, LCVR cavity, detector, boxcar averager and control computer. We connect the polarization-modulated light directly to the DUT without any intervening components other than single-mode fiber and fiber connectors. Measurements at each polarization state are

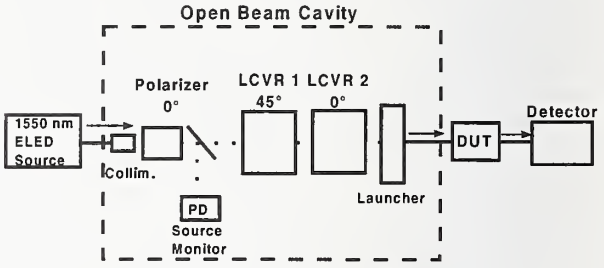

Figure 2: Simplified block diagram of the LCVR PDL measurement system.

limited to a fixed number N of modulation cycles at clock frequencies of 3.5 Hz to 10 Hz. Each of the three congruent line segments in Fig. 1 originating from the vertex represents the modulation path between two Mueller-Stokes states and therefore a signal to be sampled. This signal is routed to two averager channels, and each channel has a delay set to position the respective gates on alternate periods. To the extent that we can control birefringence drift during the sampling of each polarization state, resolution increases as $\sqrt{N}$. In addition, we use differential measurements to eliminate common-mode drift. To obtain the proper Stokes powers, each of the three difference measurements must be subtracted from the absolute power of the central polarization state. We measure the central state power by chopping the source at the clock frequency.

Uncertainties

A detailed analysis of the uncertainties in our PDL measurement system shows several dominant uncertainty sources. We list them in order of decreasing importance. Values listed correspond to one standard uncertainty (1σ) about the signal power I_{sig}.

Polarization state uncertainty. Polarization state accuracy depends on the accuracy of the calibrating polarimeter as given by the manufacturer. Value: ±0.83% of I_{sig}.

Retarder temperature dependence. We quantify temperature dependence primarily in terms of its effect on the LCVR elements. A worst-case temperature variation of 0.5 °C is used to derive the uncertainty in signal power due to variation in the polarization state of ±0.2%. Value: ±0.12% of I_{sig}

System internal PDL variation. The system retardance elements contribute their own PDL (0.02 dB) to that of the DUT. If this value is constant during both phases of the measurement, it is cancelled in the ratios. Our quoted PDL variation was derived from the maximum observed slope of the internal PDL over 15 minute intervals. Value: ±0.12% of I_{sig}.

Propagated measurement system uncertainty. We have propagated the uncertainties above inherent to the measurement system in a model of the nonideal system. The combined total PDL deviations are then calculated from the defining equations [2] to be ±2.1%. Value: ±2.1% of PDL.

PDL measurement repeatability. The repeatability given is one standard deviation (1σ) of repeated undisturbed measurements following the initial baseline measurement. By undisturbed, we mean that one sample follows another with no connector disconnection in between. This value is the effective system noise. Value: ±0.0008 dB.

Combined standard uncertainty. The effects are assumed uncorrelated, so we combine the above results using the root-sum-of-squares (RSS) method as (±0.0008 dB & 2.1% of PDL) RSS.

A significant source of uncertainty, which was not inherent to the LCVR system, was variations in measured PDL of DUT artifacts with connectorized pigtails following disconnection and reconnection. This could be explained by connector alignment errors. For those artifacts we add an additional ±0.0029 dB uncertainty. In our system, we took care to minimize fiber motion during connector handling. However, if this is not done, one could introduce errors from alterations in the relative orientations of system, DUT, and connector PDL axes due to shifts in pigtail birefringence

Stability in system birefringence is important both during and between each set of power measurements in any fixed-states scheme. Large intermediate instabilities or drifts could lead to significant uncertainty. While the effects can be modeled, it is best to simply minimize the instability. An advantage of our technique is that measurements can be performed quickly, so the stability criterion is easily satisfied.

We compared measurements between the fixed-states technique and the commonly used polarization-scanning (or all-states) method. The all-states technique relies on pseudorandom sampling of all polarization states with a total uncertainty that is proportionally reduced by increasing measurement time and/or scanning speed. For PDL ≤ 0.1 dB, uncertainties in the range of ± 3% to ±5% of PDL are claimed for a 30 second measurement [5].

Results

The primary artifact chosen to test the performance of the system provides a calculable PDL of moderate accuracy. It consists of an open beam launcher/collimator (a cleaved section of single-mode fiber and objective lens) followed by

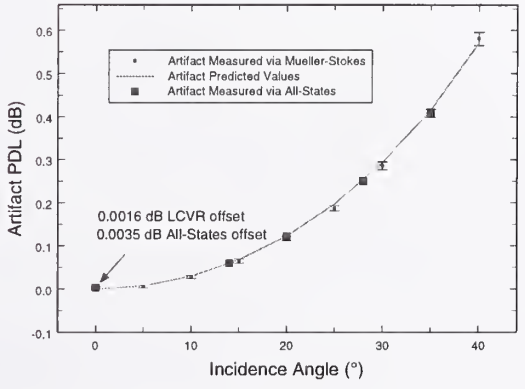

Figure 3: Open-beam artifact data from both the Mueller-Stokes and all-states systems. Error bars represent total uncertainty. The solid line is the calculated PDL value.

a polished BK7 glass cube. We mount the cube on a rotation stage with 5' resolution. The InGaAs detector (which includes a ceramic depolarizer) is translated to compensate for beam displacement following rotation. Calculated PDL (Fresnel) and measured (Mueller-Stokes) values as a function of input angle are presented in Fig. 3 and are in good

agreement. Our residual system PDL was measured and accounted for as a 0.0016 ± 0.0001 dB offset at normal incidence, where the uncertainty quoted is the statistical uncertainty of the mean with 95% confidence interval ($2\sigma/\sqrt{N}$). This nominally left only the dual glass/air interfaces to produce PDL.

To test the measurement resolution, a series of Mueller-Stokes measurements were performed by alternating between 15° and 15°5' and measuring the PDL difference. We found the average of those measurements, 0.0008 ±0.0003 dB, to be in good agreement with the predicted value.

All-Fiber PDL Artifact

We have constructed a series of all-fiber PDL artifacts based on fusion-spliced sections of single-mode, polarizing, and multimode fiber as shown in Fig. 4. These artifacts show promise for use as calibration transfer standards. We use hot-wire splicing to produce clean joints between dissimilar fibers. The input is a short

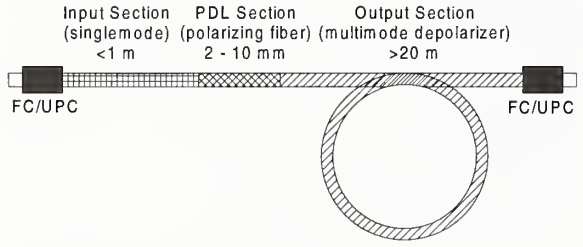

Figure 4: Schematic of the prototype all-fiber PDL artifact.

single-mode section for accurate coupling to system leads. The artifact section is a few millimeters of polarizing fiber (18 dB/m rejected mode extinction) that provides stable PDL. We have generated PDL in the range of 0.063 to 0.230 dB with lengths of 5 to 17 mm, where PDL increases with polarizing fiber length. Splices can modify artifact behavior, possibly by introducing additional PDL or changing the rejected-mode extinction. The output section is composed of several meters of multimode fiber to minimize losses due to aperture mismatch and depolarize the signal, thereby reducing uncertainty due to detector PDL. These artifacts provide good temperature stability over the range of 0 to 40 °C. We have measured a PDL temperature dependence of -0.00015 dB/°C for a 10 mm artifact with 0.085 dB of mean PDL and a dependence of -0.001 dB/°C for a 17 mm artifact with 0.230 dB of mean PDL. These artifacts are suitable both for fusion splicing as well as connectorizing the input lead.

Conclusions

We developed a nonmechanical technique of polarization dependent transmittance measurement for both single-mode and bulk-optic devices that offers advantages over more traditional methods. The technique is capable of synchronous time averaging, which allows resolution of better than 0.001 dB and agreement within 0.0016 dB ±2% of PDL values calculated for an open-beam artifact. The accuracy can be improved in the future by improving the accuracy of the polarization state calibration.

A new PDL artifact standard candidate is proposed. Measurements of the temperature dependence of prototypes show PDL slopes as low as 0.00015 dB/°C over the temperature range 0 to 40 °C.

References

[1] M. Gadonna and A. Mabrouki "Polarization Sensitivity Measurements Methods for Passive Optical Components," *Conference on European Fibre Optic Communications and Networks, EFOC&N '93,* The Hague, Netherlands, Technical Digest, pp. 65-67.

[2] R. M. Craig, S. L. Gilbert and P. D. Hale, "High Resolution, Nonmechanical Approach to Polarization Dependent Transmission Measurements," *IEEE J. Lightwave Technol.* (in press).

[3] M. A. Bhatti and A. S. Siddiqui, "A New Polarization Dependent Loss Measurement System," *Int. J. Optoelectronics*, vol. 11, no. 1, pp. 39-41, 1997.

[4] D. L. Favin, B. M. Nyman, and G. Wolter, "System and Method for Measuring Polarization Dependent Loss," *U. S. Patent 5371597*, Dec. 6 1994; B. M. Nyman, D. L. Favin, and G. Wolter, "Automated System for Measuring Polarization Dependent Loss," *Optical Fiber Communications Conference, OFC '94*, San Jose, California, U.S.A., Technical Digest, pp. 230-231.

[5] Derickson, D. ed., *Fiber Optic Test and Measurement.* Prentice Hall PTR, 1998, chap 9.5.

Measurement of Wide-Bandwidth Gain-Flat Fiber Amplifiers

Paul F. Wysocki

Lucent Technologies, Bell Labs
Specialty Fiber Devices
25 Schoolhouse Rd.
Somerset, NJ 08873

Abstract:

The impact of spectral hole burning, polarization hole burning and temperature dependent gain on the measurement and design of wide-bandwidth EDFAs is assessed.

Summary:

Wide-bandwidth erbium-doped fiber amplifiers (EDFA) are presently in widespread development for dense wavelength division multiplexed (DWDM) systems. To design and fully characterize such EDFAs it is necessary to choose measurement techniques which recognize the contributions of spectral hole-burning (SHB), polarization hole-burning (PHB) and fiber temperature change on the resultant gain spectrum and noise figure (NF). SHB is significant in EDFAs at room temperature, especially near 1530 nm, and it varies with signal wavelength and EDFA compression level[1,2] PHB is a substantially smaller effect which varies with signal wavelength, compression and the polarization states of signals and pumps.[3-4] The temperature dependence of EDFA gain has been discussed[5-6] These effects are increasingly important as gain flatness specifications tighten to 1.5, 1.0 or even 0.5 dB total variation across 30-80 nm.

EDFAs flattened using filters have recently appeared in profusion in the literature[7-9] Single-band designs with 1 dB flatness over 40 nm[8] and dual-band designs for about 80 nm[9] bandwidths have been demonstrated. Few flat EDFAs have been measured using a full complement of saturating signals. Until recently, acquisition of 40, 80 or 100 independently controlled signal sources has been expensive and time-consuming. However, as DWDM systems are installed, such sources are becoming readily available. Many EDFA gain spectra in the literature have been measured using a single or a few saturating tones to establish the erbium ion inversion and a small-signal (either tunable or broadband) probe to measure the gain. Whether such measurements adequately characterize the multi-wavelength gain is discussed below in light of SHB and PHB. Typically, NF has been measured by polarization nulling or time-domain extinction (TDE) of the saturating tone so that the ASE power can be measured. Such techniques do not lend themselves to DWDM measurements because nulling of a large number of signals is difficult. A computer model is used below to explore some of the design concepts and measurement issues which are unique to producing ultra-flat EDFAs for DWDM use.

Spectral Hole-Burning:

Computer models of EDFAs have generally treated erbium as a homogeneous medium. Such models are inadequate for designing filters to flatten highly-saturated EDFAs to within 1 dB. While SHB has been measured at certain wavelengths and in certain operating conditions,[1,2] no general model including SHB has been reported. The results presented here are based on a new model which uses the measured SHB data to incorporate the correct wavelength dependence of the SHB magnitude and hole spectral width. A portion of the EDFA saturation is assigned to each signal at each position in the fiber and SHB is added at each wavelength based upon its contribution. The model serves as a tool for observing saturation behavior in EDFAs to obtain precise gain and NF data. The results here are for a dual-stage EDFA made from 27.16 m of Lucent Technologies MP980 fiber divided into a 9 m first stage and a 18.16 m second stage and pumped with 100 mW copropagating at 980 nm in stage 1 and 150 mW at 1480 nm counterpropagating in stage 2. This high-power in line EDFA is flattened using an interstage filter and is assumed to include 8 dB of interstage loss to account for isolators, a variable attenuator and other components. The total input power into the EDF is -4 dBm and the output is +21 dBm (25 dB internal gain) for all simulations.

Using a homogeneous model, a filter for the EDFA was designed, as shown in Fig. 1. Being an ideal filter, this produced the perfectly flat spectrum shown in Fig. 2 when modeled assuming homogeneity. The model included 76 saturating tones spaced by 0.8 nm from 1520 to 1580 nm. When simulated with SHB, the filter was found to be improperly designed for flatness (as shown in Fig. 2) and the gain was tilted towards longer wavelengths. Some of the gain tilt could be removed by shortening the total fiber length (as shown in Fig.2 for 0.5 m and 1.0 m reduction) but flatness could not be achieved. In all cases, the total output power was independent of the presence of SHB in the model. However, the filter designed using a homogeneous model

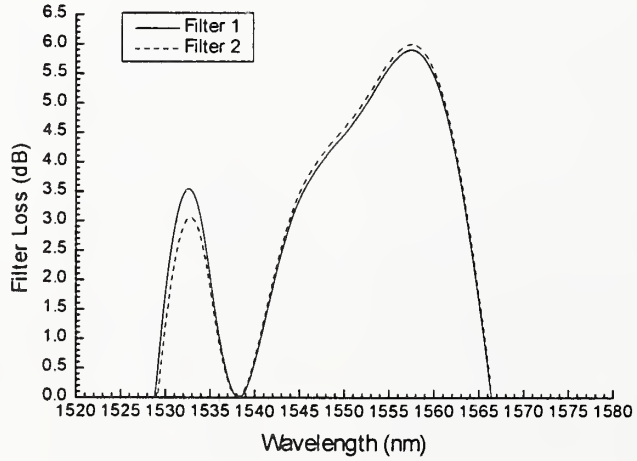

Fig. 1: Filters for flattening 25 dB EDFA. Filter 1 is for homogeneous gain. Filter 2 accounts for SHB.

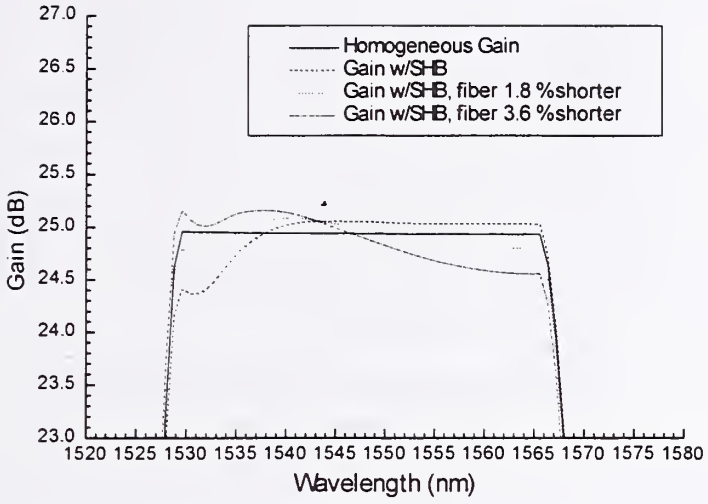

Fig. 2: Model result for filtered EDFA using Filter 1 for homogeneous EDFA and for EDFA with SHB. Last two plots show fiber length reduction to compensate for filter inaccuracy.

produced at least 0.5 dB gain ripple, even with fiber length adjustment. Measurement of gain using a small-signal or an out-of-band saturating tone would reveal the homogeneous spectrum, but misrepresent the flatness achieved by the filter. A correction to the filter can be generated by subtracting the plots with and without SHB in Fig. 2. An adjusted filter is shown in Fig. 1. The spectrum produced using this filter is shown in Fig. 3.

It is important to consider how many saturating signals are adequate for characterizing broad bandwidth EDFAs. The impact of SHB on EDFA measurements depends on the measurement

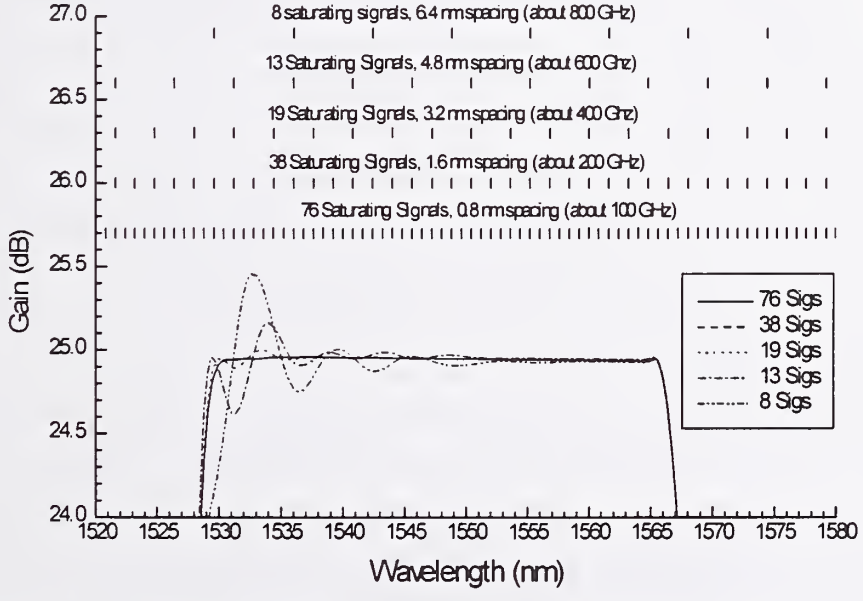

Fig. 3: Model gain result for filtered EDFA using Filter 2 for EDFA with SHB saturated by various numbers and spacing of channels as shown.

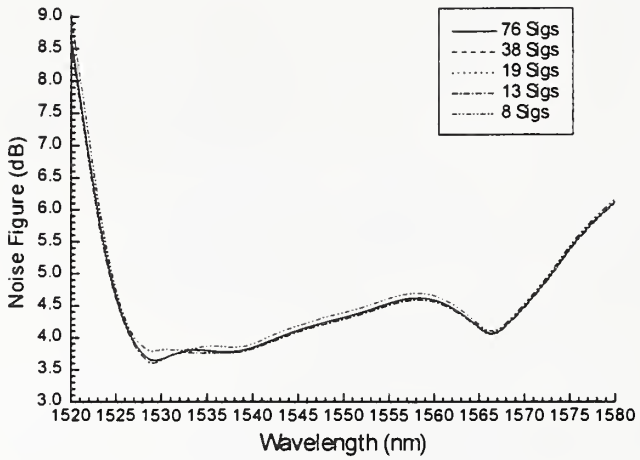

Fig. 4: Model NF result for filtered EDFA using Filter 2 for conditions of Fig. 3.

technique and the EDFA design. Any technique which fully loads the EDFA and accurately measures the gain and generated ASE versus wavelength is ideal. Techniques which substitute less channels must meet two conditions to be accurate. The first condition requires that the reduced number of channels saturate the EDFA to the same level produced when all channels are present. In fact, if the measurement is to characterize the NF properly, it must reasonably recreate not only the average ion inversion but also the distribution of ion inversion. The second condition is that, in any wavelength range, the saturating signals must not be spaced substantially as far apart as the SHB hole width, unless this is the full EDFA loading condition.

Fig. 3 shows the spectrum of an EDFA predicted by model for a variety of different channel spacings and wavelengths in which the total power was distributed equally amongst the saturating tones. It shows that a 100 GHz channel spacing can be replaced by a 200 GHz spacing without noticeable difference (condition 2 is not violated). A 400 GHz spacing is an adequate substitute for signal wavelengths above 1538 nm but not near 1530 nm where SHB is a strong effect (condition 2 violated near 1530 nm). The total output power was virtually independent of the choice of channels. This is expected to be the case only for highly-saturated, high-power EDFAs, but not for small-signal preamplifiers or low power in-line EDFAs. The NF of this EDFA is shown in Fig. 4. Interestingly, it was virtually independent of the choice of saturating tones, as long as the total input power was distributed uniformly across the band.

Condition 1 above is usually achieved by distributing the substitute channels to guarantee nearly the same distribution of saturating power with wavelength. Condition 2 is the tougher condition to meet and requires far more channels. Even if condition 2 is violated however, both power output and NF measurements may still be accurate for highly-saturated EDFAs as long as condition 1 is still met. Substitution of a single saturating tone has often been used. This was

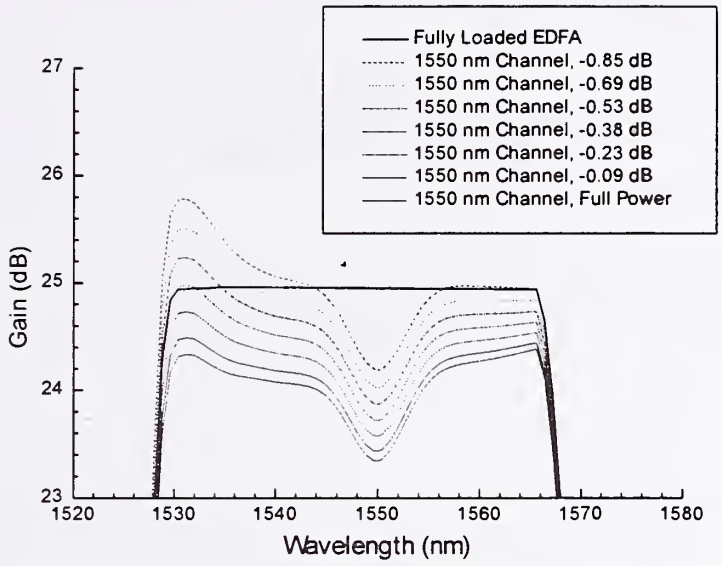

Fig. 5: Single 1550 nm channel saturation result for EDFA at various power levels.

simulated here using a 1550 nm saturating tone, very near the center of the band. This clearly violates condition 2 but may or may not violate condition 1. The spectrum for various signal levels is shown in Fig. 5. Because this saturating tone does not approximate the full EDFA load, the gain at full power is low. When the signal power is reduced, the average gain can approach the fully loaded case, but the spectrum is seriously distorted. In fact, far from 1550 nm, the error is just the difference between the two filters of Fig. 1. At these wavelengths, the homogeneous gain has been measured, not the fully loaded gain.

Polarization Hole-Burning and Polarization Dependent Loss:

Fortunately, polarization-dependent loss (PDL) is usually a small effect in a modern WDM test set because available components have low PDL. However, PDL of some EDFA components is still an issue. PHB has been extensively studied for single-channel EDFAs.[3-4] Signal-induced PHB increases the orthogonal ASE in a measurement, which tends to makes NF measurements high. However, since no single channel does much of the overall saturating in a DWDM EDFA, the effect is small. The likelihood of any substantial number of channels being in like polarization state for a substantial portion of the EDFA is small. The effect of PHB from all other channels on a given channel is on average 0. The main PHB effect in a DWDM EDFA is expected to be pump-induced PHB. This again averages to 0 but a coincidental alignment of a pump and a single channel can change its gain be several tenths of a dB.[3] Of course, a 980 nm pump is expected to wander in polarization state relative to a 1550 nm signal, so its PHB effect should be reduced. A 1480 nm pump may maintain polarization relative to a signal for longer. Scrambling of the pump polarization and averaging all measurements over several scrambling cycles can eliminate this effect.

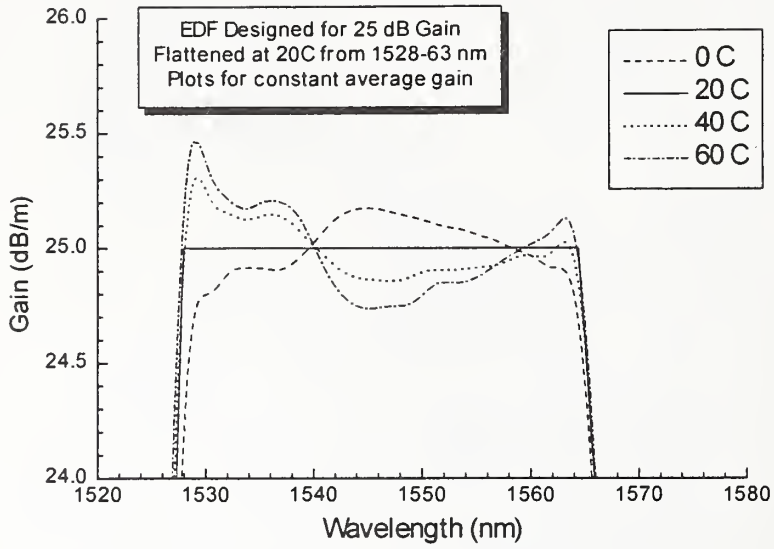

Fig. 6: Gain spectrum of typical EDFA as a function of temperature.

Temperature Dependent Gain:

Tight tolerances on gain flatness have forced EDFA designers to consider the temperature dependence of the EDF gain. To model the dependence, the absorption and gain coefficients of a typical high aluminum EDF have been measured as a function of temperature. These coefficients were used to predict the change of gain expected in an EDFA with temperature. For a 25 dB EDFA flattened at 20 C, the predicted change in gain spectrum with temperature is shown in Fig. 6. The gain ripple produced by a 20 C change is on the order of 0.5 dB. The implication is that a flat DWDM EDFA must be designed and measured at its nominal operating temperature and across all temperatures of use. To guarantee excellent flatness over all operating conditions, temperature control of the entire EDFA may be needed.

References

1. J. Sulhoff, A. Srivastava, C. Wolf, Y. Sun and J. Zyskind, *IEEE Photonics Technology Letters*, Vol. 9, p. 1578 (Dec. 1997).
2. A. Srivastava, J. Zyskind, J. Sulhoff, J. Evankow and M. Mills, *Proc. Optical Fiber Conf. OFC 96,* San Jose, CA, p. 33 (1996).
3. P. Wysocki and V. Mazurczyk, *IEEE Journal of Lightwave Technology*, Vol 14, p. 572 (Apr. 1996).
4. V. J. Mazurczyk and J. L. Zyskind, *IEEE Photon. Technol. Lett.*, Vol. 6, p. 616 (1994).
5. J. Kemtchou, M. Duhamel, F. Chatton, T. Georges and P. Lecoy, *Proc. Optical Amplifiers and their Applications '96*, Paper FD2, p. 126 (1996).
6. J. Lee and N. Park, *Proc. Optical Fiber Conf. OFC 98,* San Jose, CA, paper WG1 (1998).
7. P. Wysocki, *Proc. Optical Fiber Conf. OFC 98* San Jose, CA, paper (1998).
8. P. Wysocki, J. Judkins, R. Espindola, M. Andrejco, A. Vengsarkar, and K. Walker, *Tech. Dig. OFC'97,* paper PD2 (1997).
9. Y. Sun, J. Sulhoff, A. Srivastava, J. Zyskind, C. Wolf, T. Strasser, J. Pedrazzani, J. Judkins, R. Espindola and A. Vengsarkar, *Tech. Dig. Optical Amplifiers and Their Applications 97,* paper PD2.

Polarisation Mode Dispersion in Chirped Fibre Bragg Gratings

David Ives
National Physical Laboratory
Teddington, Middx, TW11 0LW, UK

Abstract

An explanation of the high level of polarisation mode dispersion, PMD, in chirped fibre Bragg gratings is reported. Initial measurements support the theory and suggest that PMD in such gratings could be a significant contribution to the total PMD in a fibre system.

Introduction

Chirped Bragg gratings written into optical fibres are now readily available for use as chromatic dispersion compensators[1][2]. Such devices are only beneficial if they accurately compensate chromatic dispersion without impairing other system parameters. PMD is an important parameter in long haul high bit rate systems. Initial measurements of PMD in chirped fibre Bragg gratings are reported here.

Theory

Consider an ideal linear chirped grating. Consecutive wavelengths are reflected at progressively further or nearer positions along the grating giving a time delay which varies linearly with wavelength (a constant chromatic dispersion). The wavelength, λ, is reflected at a point z along the grating given by

$$z = a\lambda + b$$

where a and b are constants. This leads to a time delay, τ,

$$\tau = \frac{2n_g}{c} z = \frac{2n_g}{c}(a\lambda + b)$$

where n_g is the group index and c the speed of light. The chromatic dispersion, D, is given by

$$D = \frac{\partial \tau}{\partial \lambda} = \frac{2n_g}{c} a$$

The grating is formed from periodic refractive index variations with a spacing, S, given by

$$S = \frac{\lambda}{2n} = \frac{z - b}{2na}$$

where n is the average refractive index.

For real fibre there will be some residual birefringence. The refractive index for light propagating parallel to the birefringent axis and perpendicular to the birefringent axis is then given by

$$n_{\parallel} = n - \frac{\beta}{2} \qquad \text{and} \qquad n_{\perp} = n + \frac{\beta}{2}$$

where, β, is the birefringence.

Thus, at a given wavelength, light propagating parallel to the birefringent axis is reflected at the point, $z_{\parallel}$, where $\lambda_{\parallel}$ is given by

$$\lambda_{\parallel} = 2\left(n-\frac{\beta}{2}\right)S = \left(n-\frac{\beta}{2}\right)\frac{(z_{\parallel}+b)}{na}$$

while light propagating perpendicular to the birefringent axis is reflected at the point, $z_{\perp}$, where $\lambda_{\perp}$ is given by

$$\lambda_{\perp} = 2\left(n+\frac{\beta}{2}\right)S = \left(n+\frac{\beta}{2}\right)\frac{(z_{\perp}+b)}{na}$$

This difference in reflected position leads to a corresponding difference in the propagation times for the parallel and perpendicular modes giving a differential group delay (DGD), $\Delta\tau$,

$$\Delta\tau = \frac{2n_g a\lambda}{c}\frac{\beta}{n} = D\lambda\frac{\beta}{n}$$

Assuming that the birefringence is independent of wavelength (such that the birefringence and group birefringence, β_g, are approximately equal) the DGD coefficient, Δ, for light propagating straight through the grating is given by

$$\Delta = \frac{\beta_g}{c} \sim \frac{\beta}{c}$$

Hence the DGD for the straight through and reflected signals can be related through

$$\Delta\tau = D\lambda\Delta\frac{c}{n}$$

It can be seen that the DGD for the reflected signal is a large multiple of the DGD for the straight through signal.

PMD Measurements

The set up used to measure PMD at NPL is shown in Figure 1. Radiation from the tuneable laser source passes through a polarisation rotator before being launched into the grating under test. The output polarisation state from the grating is measured using a polarisation state analyser.

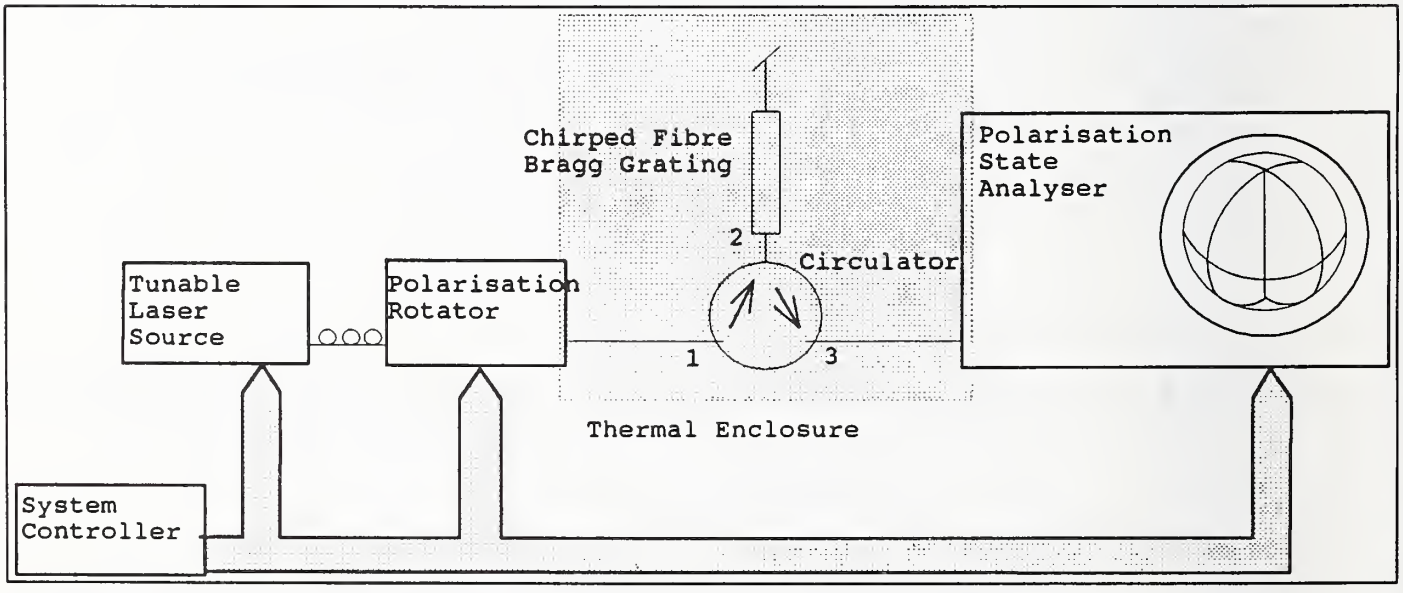

Figure 1 PMD Measurement System

The output polarisation state is measured for a number of different input states [typically having

normalised stokes vectors (1,0,0), (0,1,0) and (0,0,1)] at each wavelength step. Prior to making measurements the polarisation state controller settings are adjusted for each wavelength to launch the required state. The measured data is analysed by calculating the rotation of the stokes vector on the surface of the Poincaré sphere[3][4]. This gives values of the DGD and the principle states of polarisation (PSP)[5] for each wavelength step. Polarisation dependent loss and second order PMD can also be estimated.

Measurements

Test were performed on a dispersion compensating grating with a centre wavelength of 1549.2 nm and a bandwidth of 1 nm. The chromatic dispersion was measured to be approximately 700 $ps.nm^{-1}$. The grating was used with an optical circulator to provide a transmission dispersion compensation system.

The PMD of each element was measured. Measurements were made in the wavelength range 1484 nm to 1564 nm at 20 nm intervals. Six launched polarisation states were used with normalised stokes vector (1,0,0), (0,1,0), (0,0,1), (-1,0,0), (0,-1,0) and (0,0,-1). This gave a differential group delay sensitivity of approximately 1 fs.

The optical circulator had a DGD of 47 $\pm$ 5 fs from port 1 to 2 and 49 $\pm$ 5 fs from port 2 to 3. By applying a 4% reflection to port 2 the PMD of the combined route 1 to 2 and 2 to 3 could be measured. PMD values consistent with combinations of the single pass values were obtained.

The optical fibre grating was measured in transmission giving a DGD value of 22 $\pm$ 3 fs. All of these measurements were performed outside the reflective region of the grating.

Where the uncertainties quoted correspond to a 95% confidence interval.

The grating and circulator were combined to achieve dispersion compensation. Measurements of the output polarisation state were measured in the wavelength range 1548.6 nm to 1549.7 nm at 0.1 nm intervals. Three launched polarisation states were used with normalised stokes vectors (1,0,0), (0,1,0) and (0,0,1). In this geometry a DGD of 6940 $\pm$ 1250 fs was obtained. The principle state of polarisation was observed to have only a slight wavelength dependence across the measurement range.

Comparison with theory

The measured forward DGD of the fibre grating can be used to calculate the birefringence of the fibre in which the grating is fabricated. The total connectorised grating length of 3.1 m with its DGD of 22 fs results in an average DGD coefficient of 7.1 $fs.m^{-1}$. This in turn results in an expected PMD for the grating in reflection of 1540 fs. This compares well with the measured value.

While it is expected that there will be no mode coupling within the length of the grating there may be some mode coupling in the pigtail fibre at each end of the grating. This will increase the apparent DGD coefficient of a short piece within the pigtailed length. A PMD coefficient of Δ $fs.m^{-1}$ will result in a total PMD of

$$\Delta\tau = \Delta\sqrt{l\,h}$$

where l is the fibre length and h the coupling length[6]. For the grating measured, taking h = 0.15 m and so Δ = 32 $fs.m^{-1}$ and the PMD for the grating in reflection would be calculated at 6940 fs, as measured.

The PMD contributed by the optical circulator is not considered to be significant.

Fine Structure

The output polarisation state of the compensation system was monitored as a function of wavelength. It was observed that the rate of rotation of the stokes vector around the principle axis varied with wavelength. This suggests a variation of the DGD. This variation occurred over a wavelength period of approximately 0.05 nm and was observed through the whole wavelength scan. The magnitude of the periodicity of these changes compares well with those observed in the time delay curve. Accurate measurement of the DGD for small variations of wavelength proved difficult because of the noise induced in the DGD associated with the wavelength step accuracy.

Conclusion

A simple theory to explain the high values of DGD within chirped fibre Bragg gratings has been developed. Initial measurements support the theory but structure on a small wavelength scale needs further investigation. The grating tested had a chromatic dispersion of approximately 700 $ps.nm^{-1}$ and a PMD of 6940 fs. While the chromatic dispersion will compensate for perhaps 40 km of standard optical fibre the PMD will add to the system total giving an extra PMD which will appear as 1 $ps.km^{-½}$. This is larger than the typical fibre specification of 0.5 $ps.km^{-½}$.

Acknowledgement

This work was supported by the DTI National Measurement System Policy Unit.

References

1) HILL K.O., BILODEAU F., MALO B., KITAGAWA T., THÉRIAULT S., JOHNSON D.C., ALBERT J., TAKIGUCHI K., "Chirped in-Fiber Bragg Gratings for Compensation of Optical-Fiber Dispersion", *Optics Lett.*, 1994, **19**, pp1314-1316.

2) LOH W.H., LAMING R.I., ELLIS A.D., ATKINSON D., "10 Gb/s Transmission over 700 km of Standard Single-Mode Fiber with 10 cm Chirped Fiber Grating Compensator and Duobinary Transmitter", *IEEE Photonics Tech. Lett.*, 1996, **8**, pp1258-1260.

3) ANDRESCIANI D., CURTI F., MATERA F., DAINO B. "Measurement of the Group-Delay Difference between the Principle States of Polarization on a Low-Birefringence Terrestrial Fibre Cable", *Optics Lett.*, 1987, **12**, pp844-846.

4) POOLE C.D., BERGANO N.S., WAGNER R.E., SCHULTE H.J. "Polarization Dispersion and Principle States in a 147km Undersea Ligthwave Cable", *J. of Light Tech.*, 1988, **6**, pp1185-1190.

5) POOLE C.D., WAGNER R.E. "Phenomenological Approach to Polarisation Dispersion in Long Single-Mode Fibres", *Elect Lett.*, 1986, **22**, pp1029-1030.

6) GISIN N., VON DER WEID J.P., PELLAUX J.P. "Polarisation Mode Dispersion of Short and Long Single-Mode Fibres", *J. of Light Tech.*, 1991, **9**, pp821-827.

Measurement of Polarisation Mode Dispersion in Fibre Amplifiers

C. Geiser, B. Huttner, N. Gisin (1);

R. Caponi, M. Potenza, M. Schiano, M. Artiglia (2);

I. Joindot (3)

(1) GAP, Université de Genève, Genève, SWITZERLAND (bruno.huttner@physics.unige.ch)
(2) CSELT, Torino, ITALY (marcello.potenza@cselt.it)
(3) France Telecom/CNET, Lannion, FRANCE (irene.joindot@cnet.francetelecom.fr)

Abstract: The behaviour of the Polarisation Mode Dispersion (PMD) in various types of optical fibre amplifiers has been studied by the European consortium FAME (Fibre Amplifier Measurement Methods). We present some guidelines for precise measurement of PMD in amplifiers. Our main result is that the PMD of such devices is inherently deterministic and can be specified simply using a maximum tolerable value.

Introduction

The Standard, Measurement & Testing European project FAME (Fibre Amplifier Measurement MEthods) is involved in the characterisation of Optical Fibre Amplifiers for advanced applications such as multi-channel and analogue transmission systems. One of the major issues of FAME is to get a satisfactory operative definition of Polarisation Mode Dispersion (PMD) for such amplifiers. The problem, which could present some difficulty, originates from the fact that the usual way to measure the PMD on a fibre, consists in averaging the Differential Group Delay (DGD) over some wavelength interval and is based on the assumption that PMD in a fibre is statistical in character /1/. Amplifiers usually contain elements (filters, isolators, wavelength selective couplers...) which restrict DGD measurements to short wavelength intervals. Moreover, the gain spectrum of OFAs further limits this region to a typical operation interval of 1530-1570 nm for Erbium-Doped Fibre Amplifiers (EDFAs) or Erbium-Doped Fluoride Fibre Amplifiers (EDFFAs) and of 1270-1330 nm for Praseodymium-Doped Fluoride Fibre Amplifiers (PDFFAs). Furthermore, in three-level OFAs PMD must be measured under pumping conditions suited to assure a significant Degree Of Polarisation (DOP) level during the measurement.

This contribution reports on the experimental work carried out by the FAME Consortium. We give some guidelines for precise measurement of PMD, in particular with respect to pump and signal powers. We show that the DGD of the amplifier is very stable, even on a scale of weeks and in presence of large environment temperature fluctuations. This indicates that a proper definition for PMD in OFAs should be given a deterministic character. This result is of considerable relevance for standardisation and customer/contract specifications of OFAs.

Guidelines for PMD measurements

A set-up for PMD measurements is shown in Fig. 1. A tunable source launches the optical signal – the power of which is maintained in the –13 to-3 dBm range – into a State-Of-Polarisation (SOP) generator (polariser). The output of the SOP generator is injected in the Amplifier Under Test (AUT). The device output is sent to a polarimeter through an optical attenuator, to avoid detector saturation. The polarisation behaviour of the attenuator is checked preliminarily, to verify that it cannot affect results significantly.

The PMD calculation is performed with the Jones Matrix Eigen-analysis. Amplifiers under test were four conventional EDFAs, four EDFFAs and one PDFFA, including commercial line- and booster amplifiers, and laboratory prototypes.

Fig. 1 - Set-up for the measurement of PMD in OFAs

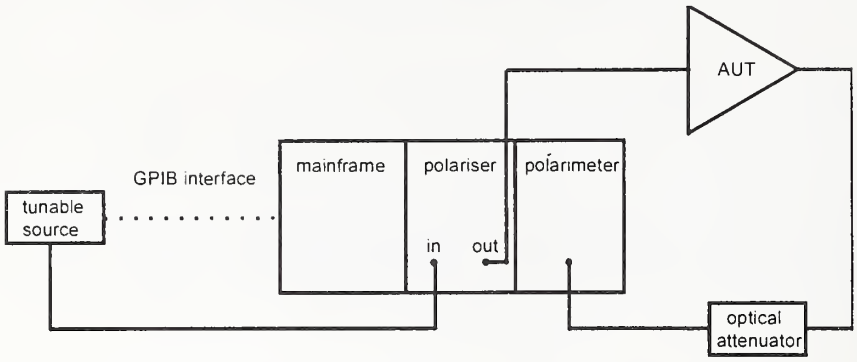

A first measurement on an EDFA was made with the pump off, and shown in Fig. 2. The DGD is drawn as a full curve, and presents an unexpected and somewhat irregular behaviour. In the region between 1510 and 1540 nm, we see that DGD is extremely low and is not representative of the real DGD of the amplifier. Our explanation is that in this wavelength region, the radiation at 1550 nm is absorbed and incoherently re-emitted by Er-atoms. Since the re-emitted light is not polarised, the DOP drops (as seen on the dashed curve of Fig. 2), which makes the measurement unreliable. This behaviour is observable only because the attenuation is so high (30 dB), that the intensity of incoherently re-emitted light is roughly the same as that of directly transmitted light. We can simply avoid this behaviour by turning the pump on, thus turning attenuation into gain.

In addition, when the pump is on, the unpolarized ASE may perturb the measurement. In order to obtain significant results, the probe power must also be large enough, so that the output signal is larger than the ASE. As above, this can be checked by measuring the DOP. We choose the input power so that the DOP remains between 60% and 100%.

The principle of the Jones Matrix Eigen-analysis used for the amplifier's PMD measurement imposes another condition, especially when the pump is turned on. The measurement consists in analysing successively three linear output states of polarisation (SOP). Imagine the worst case, when the SOP of the probe is orthogonal to one of the three polarizers. The probe power is then set to zero and we analyse only unpolarized ASE instead of the expected amplified signal. The solution to avoid this problem is simply to choose a circular SOP, so that the probe intensity after any of the three polarizers is the same.

Fig. 2 - DGD measurement on an EDFA: unpumped conditions

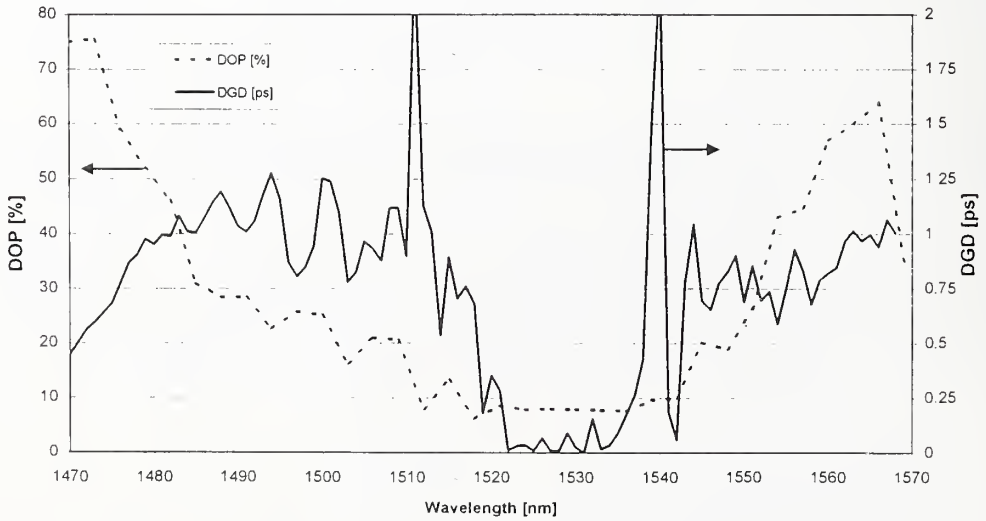

To conclude this section, we state again the three conditions necessary for a correct measurement of PMD with the standard polarimetric method:

- Pump on (gain)
- Probe intensity large enough, i.e. signal laser larger than ASE in order to get DOP > 60 %
- Circular input polarisation before the polarising stage

Results of PMD measurements

In Fig. 3, we present a set of measurements performed on a commercial EDFFA.

Fig. 3 PMD of a commercial EDFFA;
DGD curves measured at different power levels and different measurement settings

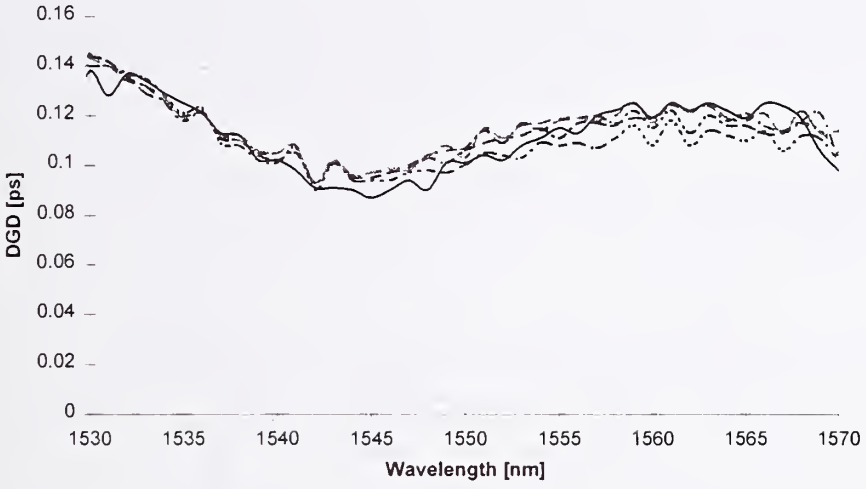

We see that, once the conditions discussed above are met, the DGD of the device as a function of wavelength remains largely independent of the measurement set-up.

The time dependence of DGD was also analysed, for one EDFA. Fig. 4 shows 89 measurements of the PMD, taken every 30 minutes during 2 days in stable conditions. It is manifest that each curve is quite the same as all others except for little details. The DGD seems to be stable in such conditions. We also made longer-term measurements, by comparing measurements made at an interval of one month. The result was that even after such a long time, the DGD at a fixed wavelength remained stable. Lastly, we measured the PMD of the amplifier at different temperatures. The result was again the same curve, but slightly shifted in frequency. This can simply be explained by the thermal variation of the Er-doped fibre length or of other EDFA components.

Our conclusion is that the PMD of the EDFAs we measured is a deterministic PMD, which is not affected by random coupling changing with time or with external conditions, but results from the intrinsic birefringence and stable polarisation mode couplings.

Fig. 4: Stability of DGD curves measured every half an hour along two days

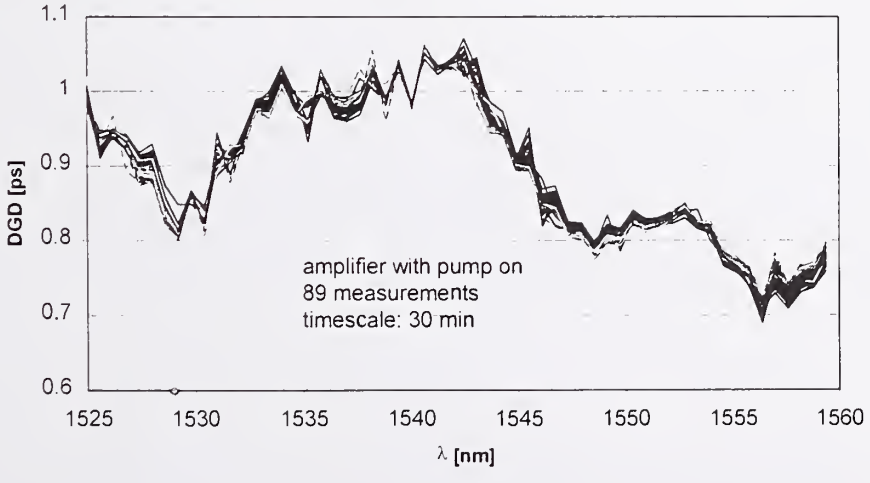

Conclusion

In this work, we have pointed out some difficulties encountered when measuring the PMD of an amplifier. First, the pump must be turned on, to avoid depolarisation effects. Second, for a given pump power, the probe power has to be larger than ASE. These two conditions can be checked by measuring the DOP of the output signal before any PMD measurement. We found that a minimum value of 60% was appropriate. Third, the input SOP has to be circular before passing through the linear polarizers in the polarimeter. This precaution allows us to obtain the same probe power for the three independent SOPs when measuring the Jones matrix of the AUT.

We have tested the stability of DGD with time and found that it was excellent. We have also analysed its temperature dependence, and found it consistent with a PMD created by intrinsic birefringence. Our conclusion is thus that the PMD of the Er-based amplifier is deterministic. Therefore, it is sufficient to measure the DGD in the window of interest. Such a deeper understanding of the PMD nature is a key feature for a standardisation of polarisation mode dispersion tailored to optical fibre amplifier characteristics (in contrast to the usual definition for transmission fibres). Besides, it is also important for device customer and contract specifications. Further work is under way to assess the PMD nature in different (still non-conventional) OFAs, such as PDFFAs for the second telecommunication window and others, in which possible imperfections of the fibre structure could play a role in adding a partially stochastic component to the device PMD.

Acknowledgements

This activity has been partially funded in the framework of the European SM&T Project FAME and by the Swiss Office Fédéral de l'Education et de la Science.

References

/1/ N. Gisin, B. Gisin, J. P. Von der Weid, R. Passy, "How accurately can one measure a statistical quantity like polarisation mode dispersion?", SOFM'96, Boulder (CO), Tech. Dig. p. 131 (1996), or in IEEE Photon. Technol. Lett., Vol. 8, No. 12, pp. 1661-ff., (1996).

/2/ N. M. O'Sullivan, T. A. Birks, C. D. Hussey, "Control of polarisation degradation in fibre amplifier WDMs", Electron. Lett. Vol. 28, No. 17, pp. 1616-1618, (1992).

/3/ Y. Namihira, T. Kawazawa, H. Taga, "Polarisation effects on BER degradation at 10 Gbit/s in an IM-DD, 1520 km optical amplifier system", Electron. Lett. Vol. 29, No. 18, pp. 1654-1655, (1993).

/4/ R. Leners, T. Georges, P.L. François, G. Stéphan, "Analytic model of polarisation dependent gain in erbium doped fibre amplifiers", Conf. on Optical Amplifiers and Their Applications, 1994, Yokohama (Japan); Tech. Dig. Post-deadline papers.

Narrowband measurements of polarization-mode dispersion using the modulation phase shift technique

P.A. Williams[1], A.J. Barlow[2], C. Mackechnie[2], and J.B. Schlager[1]

[1]*National Institute of Standards and Technology, Boulder CO, USA*
[2]*EG&G Fiber Optics, Wokingham, UK*

A common characteristic of the current methods for measuring polarization-mode dispersion (PMD) is the need for a broad optical bandwidth. With the increasing use of wavelength division multiplexing the need to make PMD measurements within a very narrow optical bandpass will also increase. One technique which is well suited to narrowband measurements of PMD is the modulation phase shift technique (MPS). While the concept is not new [1-4], we believe the work here to be the first published demonstration of the accuracy of the technique in measuring differential group delay (DGD) vs. wavelength.

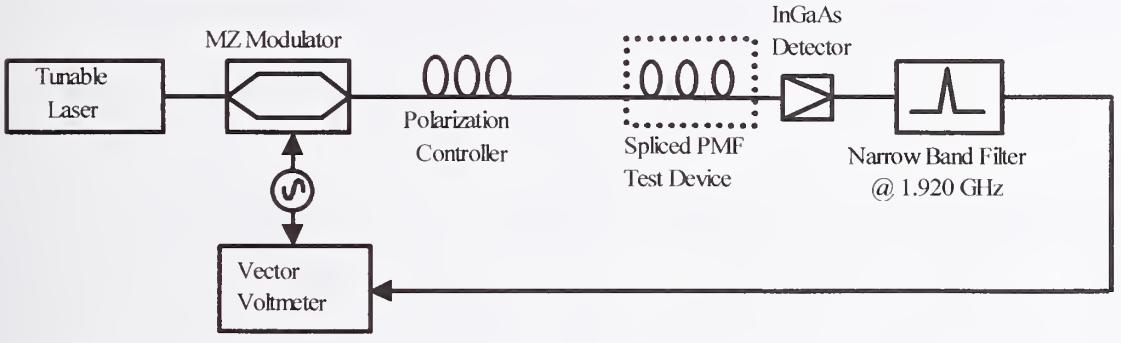

Figure 1 Schematic diagram of modulation phase shift system for DGD measurement.

The MPS technique is well known for its use in chromatic dispersion measurements [5]. The basic principle is to directly measure the group delay of light traveling through each of the two principal states of polarization of the device under test. The experimental setup is shown in Figure 1. The light from a tunable laser diode with an RF-broadened linewidth of 50-500 MHz undergoes an external 1.920 GHz intensity modulation from a $LiNbO_3$ Mach-Zender modulator. The modulated light passes through a polarization controller, passes through the device under test, and is detected with a high-speed InGaAs photodetector and filtered with a narrowband filter at 1.920 GHz. A vector voltmeter is used to measure the phase between the RF electrical modulation signal and the optical signal out of the device under test. The phase is a measurement of the group delay through the optical system, so adjusting the polarization controller to maximize the optical phase delay means that the light is being launched down the slow principal axis of the device under test. Likewise, the polarization orientation for minimum phase delay corresponds to a launch down the fast principal axis. The difference in phase between these two launch conditions is a measure of the DGD at the wavelength under test. That

is, DGD ($\Delta\tau$) is given by

$$\Delta\tau = \frac{\varphi_+ - \varphi_-}{360° \cdot f}, \qquad (1)$$

where $\Delta\tau$ is in seconds, φ_+ and φ_- are the measured phases (in degrees) for the transmission along the slow and fast axes respectively, and $f = 1.920\times10^9$ Hz.

In order to demonstrate the accuracy of this technique, we made a measurement on three concatenated segments of bow-tie polarization-maintaining fiber (PMF) oriented at roughly 45° angles so as to mix polarization modes, providing a DGD with a strong wavelength dependence. The maximum DGD of the PMF concatenation is about 8 ps. The vector voltmeter used in this measurement has a phase resolution of 0.1° which at 1.920 GHz corresponds to a time resolution of 0.145 ps. A 360° phase change would represent a 520 ps delay. Therefore, given the PMD of the device being measured, there is no danger of a 2π phase ambiguity. Using the MPS technique, we measured the DGD of the PMF device over about a 20 nm range and compare the results with DGD-vs.-wavelength measured by the more conventional Jones matrix eigenanalysis (JME) method [6]. Measurement results for the two techniques are compared in Figure 2.

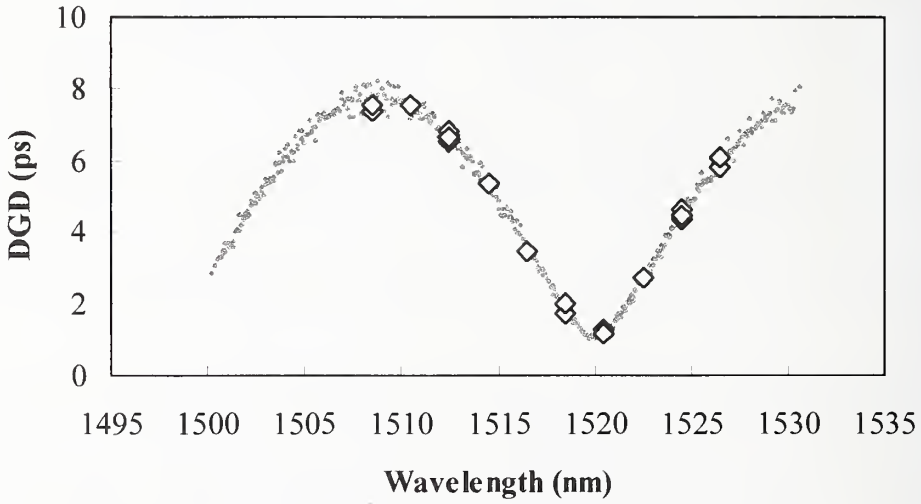

Figure 2 DGD vs Wavelength for JME technique (dots) and MPS technique (diamonds) on a three-section PM fiber.

It should be noted that the JME measurements were made at a temperature ~3 °C lower than the MPS measurements. The temperature dependence of the birefringence (Δn) of PMF $d(\Delta n)/dT$ is on the order of -4×10^{-7}/°C [7]. This means that for a single section of PMF, a few degrees of temperature change will affect the DGD by only a few tenths of one percent. However, a change in the birefringence of the fiber sections also changes the mode-coupling conditions. This effect depends on the retardance of the sections, which is proportional to $\Delta nL/\lambda$ (where L is the length of the PMF section and λ is the optical wavelength). From this relationship, we see that a change in ΔnL will be equivalent to a change in λ (wavelength shift). Multiple measurements of the PMF test device using the

JME system showed an effective wavelength shift with temperature of –0.8 nm/°C. We therefore anticipate that the data taken at the lower temperature (JME) would be offset by about 2-3 nm. The agreement between the JME and MPS data is good when we shift the JME data down by 2.5 nm. This value gives the best fit and corresponds well to a 3 °C temperature shift. Consequently, the JME data shown in Figure 2 have been shifted by 2.5 nm.

The uncertainty in the MPS measurement comes primarily from two sources: phase uncertainty due to the resolution of our vector voltmeter and the degree to which we were able to launch exactly on the principal axes. Fabry-Perot effects in the measurement system are significantly reduced by RF-broadening the source, and the residual random phase uncertainty is completely explained by the 0.1° phase uncertainty of the vector voltmeter. The uncertainty due to launching nonprincipal states is a source of systematic error. The measured phase difference between two orthogonal launch states is a function of the alignment of the launch states with respect to the principal axes. Figure 3 shows the fractional DGD error encountered for a given alignment error. Alignment error is the angle (on the Poincare sphere) between the launch polarization state and the slow principal axis of the device under test. Any misalignment error therefore causes a reduction in the measured DGD. Fortunately, the error is a weak function of misalignment for small angular errors. For example, a 5° misalignment angle will yield a measured DGD which is only 0.4% below the true value.

We found the principal state by merely manipulating the polarization controller by hand and watching for the maximum and minimum phase delays. Repeated measurements showed that the measured phase differences for repeated runs differed by no more than 0.2° (consistent with the phase resolution of the system). Figure 2 shows that the JME and MPS techniques agree within the measurement noise. Therefore, our technique of finding fast and slow axes by hand appears to be accurate (but tedious).

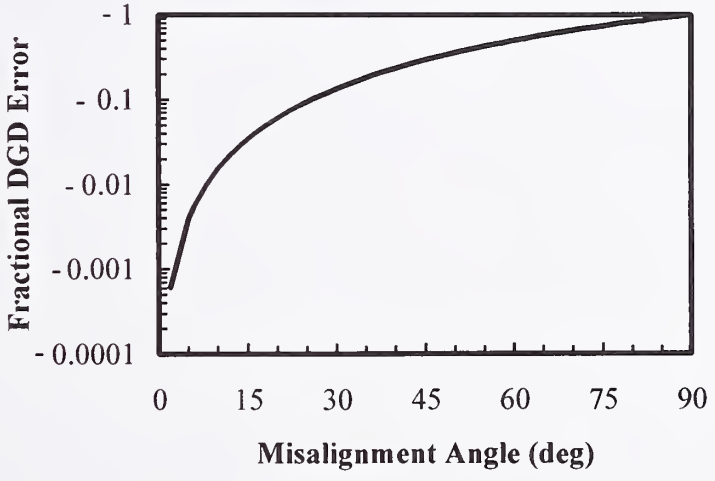

Figure 3 Fractional DGD measurement error as a function of launch state orientation (0° is ideal launch along principal states, 90° is worst-case misalignment).

In order to reduce measurement noise and add some degree of automation, we are experimenting with a differential phase (DP) measurement technique [1]. For the DP measurement, we use a commercial chromatic dispersion test system and an electronically controlled three-stage polarization controller. The first stage (a half-wave

plate) is used to toggle between orthogonal states of polarization at a rate of tens of Hertz. The other two stages are used to search for the principal states of the device under test. Preliminary results predict an improved DGD resolution with a much narrower 200 MHz bandwidth requirement.

References

[1] Roger S. Jones, "Fiber optic dispersion method and apparatus" United States Patent 4,740,833 (1985).
[2] M. Monerie, P. Lamouler, L. Jeunhomme, "Polarisation mode dispersion measurements in long single mode fibers", *Electronics Letters* **16**, 907-908 (1980).
[3] S.E. Mechels, *Measurements of the zero-dispersion wavelength in single-mode optical fibers*, Ph.D. thesis, University of Colorado (1996).
[4] Dennis Derickson, Ed., *Fiber optic test and measurement*, p. 512, Prentice Hall, New Jersey (1998).
[5] Anonymous, "Chromatic dispersion measurement of single-mode optical fibers by the phase-shift method", Fiber Optic Test Procedure (FOTP) 169, Telecommunications Industry Association.
[6] B.L. Heffner, "Automated measurement of polarization mode dispersion using Jones matrix eigenanalysis", *Photonics Technology Letters* **4**, 1066-1069 (1992).
[7] A. Ourmazd, Malcolm P. Varnham, R.D. Birch, and David N. Payne, "Thermal properties of highly birefringent optical fibers and preforms", *Applied Optics* **22**, 2374-2379 (1983).

Impact of signal wavelength and input state-of-polarization on PMD induced pulse distortion in ≥10 Gbit/s transmission systems

Ralph Leppla[1], *Arnold Mattheus*[2]

[1]*University of Kaiserslautern, Erwin Schrödinger Straße, D-67633 Kaiserslautern*
[2]*Deutsche Telekom AG, Technologiezentrum, Am Kavalleriesand 3, D-64295 Darmstadt*

Abstract: We present experimental results and numerical calculations which show the dependence of pulse distortion caused by polarization mode dispersion (PMD) on both the differential group delay (DGD) at the signal wavelength and the state-of-polarization (SOP) of the light launched into the fiber. The maximum pulse broadening versus to the input SOP is related to the DGD at the signal wavelength. The results demonstrate the possibility to achieve nearly undistored transmission at any wavelength by proper adjustment of the input SOP. Conclusions are drawn for ≥10 Gbit/s data transmission in single channel and in WDM systems.

1. Introduction

In the last few years PMD has attracted considerable attention due to its potential limitation on optical transparent high speed transmission systems. PMD can cause system penalties [1] or even detrimental signal distortions and thus unacceptable bit error rates [2, 4] when installing the next generation systems (STM-64 / OC-192) on already embedded cables. It is often argued that the impact of PMD on pulse propagation along a fiber piece cannot be predicted in a deterministic way because of the stochastic nature of PMD. This is not entirely true. In previous long-term PMD measurements on installed standard monomode fibers (SMF) [2, 4] it was observed that the DGD and the output SOP usually remain stable for at least several minutes for any input SOP and signal wavelength. In this case it seems to be justified to approximate the transmission fiber by a concatenation of birefringent elements (CBE) with well-defined angles for the fast and slow axis of each birefringent element.

In this article we present a simple experimental setup of a CBE which was used to compare theoretical and experimental results for both, firstly the DGD versus wavelength and input SOP, and secondly the impact of PMD on pulse distortion. Recent ≥10 Gbit/s field trials are mentioned confirming the applicability of this simple model of a CBE for optically transparent systems on installed fibers.

2. Experimental setup

The experimental setup is shown in Fig. 1. A wavelength-tunable mode-locked fiber-ring laser generated Fourier-limited nearly $sech^2$-shaped pulses (FWHM) of about Δt_{in}=6 ps and 70 GHz temporal and spectral width (FWHM) at around 1550nm central wavelength, respectively. The pulseform is adapted to a 40 Gbit/s transmission system using return to zero

format. These pulses passed a polarization control unit (PCU) - enabling to manipulate the input SOP - before being launched into a CBE, namely a chain of ten identical pieces of polarization maintaining single-mode fiber (PMF). Each PMF segment had a geometrical length of 1 m and offered a wavelength-independent DGD of $\tau = 1.51$ps. The input SOP behind the PCU and the spectral and temporal output pulse shapes were measured by a polarization analyzer based on the Jones-Matrix-Eigenanalysis (JME) method, an optical spectrum analyzer and a streak camera, respectively.

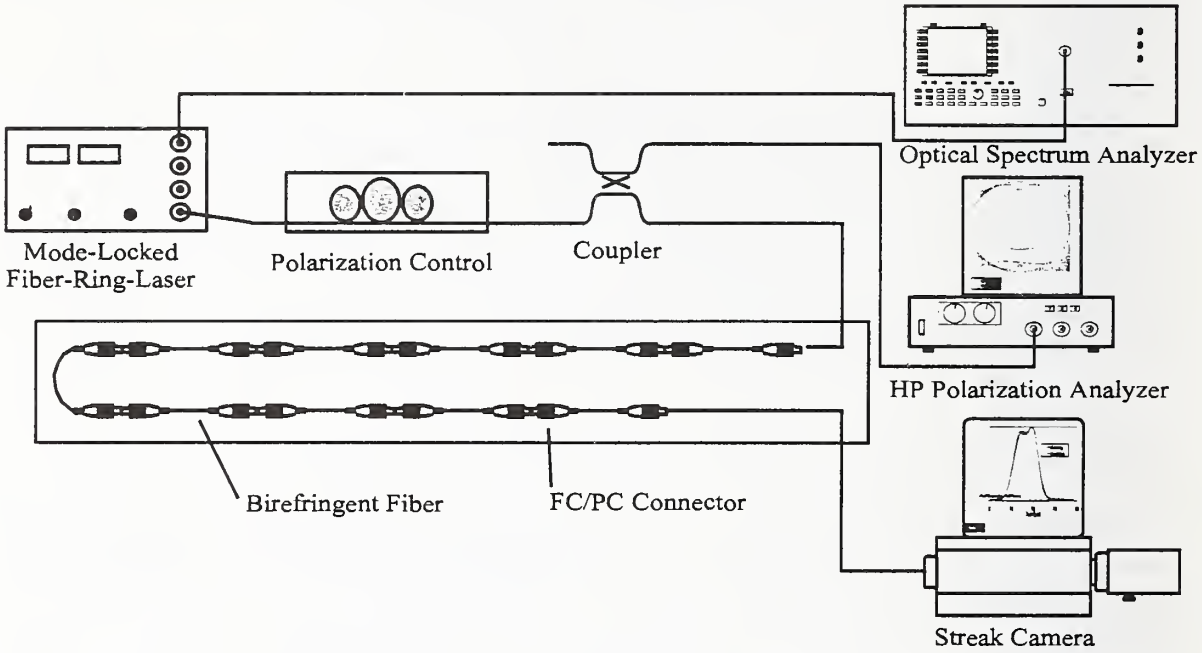

Fig. 1: Experimental setup for measurement of PMD induced pulse-distortion versus wavelength and input-SOP

3. Theory

In our numerical calculations each PMF piece was described by a delay matrix D while the interface between two subsequent PMD pieces was represented by a rotation matrix R according to well-established previous approaches (see e.g. [5]). Thus the Jones-Matrix $J(\lambda)$ of the CBE was defined for each wavelength λ. The DGD and PSOP were found using the Polarization-Dispersion-Matrix $J(\lambda_1)\cdot J^{-1}(\lambda_2)$ [3]. The output pulse was calculated by multiplying each Fourier component of the pulse with its corresponding Jones-Matrix.

4. Results

Firstly, all coupling angles between the slow and fast axis of subsequent PMF pieces were calibrated by measuring the DGD versus wavelength λ and minimizing the standard deviation

between the experimental and simulated DGD(λ). A global minimum and thus a well-defined set of angles was found.

Next the output pulse shape was measured versus the input SOP by rotating the polarization analyzer's half-wave plate. Thus the output pulse shape was tuned from the undistorted pulse (which was identical to the input pulse) up to maximum distorted pulse (showing two separated peaks). An example is illustrated in Fig. 2 for λ=1547.8 nm central wavelength. As can be seen the output pulse width Δt_{out} covered the range of 6 ps ≤ Δt_{out} ≤ 12.5 ps. In Fig. 3 the maximum distorted pulse of Fig. 2 was depicted along with the corresponding numerical simulation. Similar good agreement between measured and simulated output pulse shapes was also observed for other signal wavelengths.

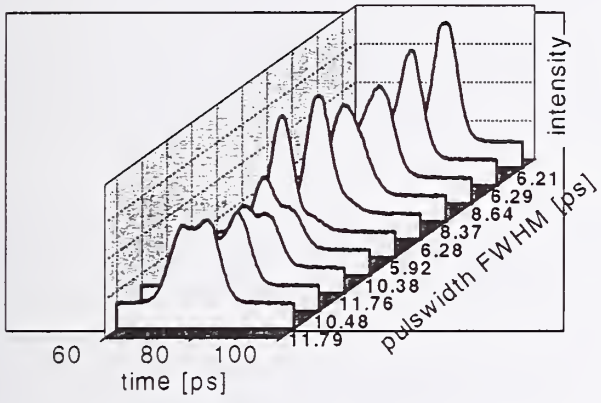

Fig. 2 Pulse-distortion for different input SOP at a fixed signal wavelength (λ_{signal}=1547.8 nm)

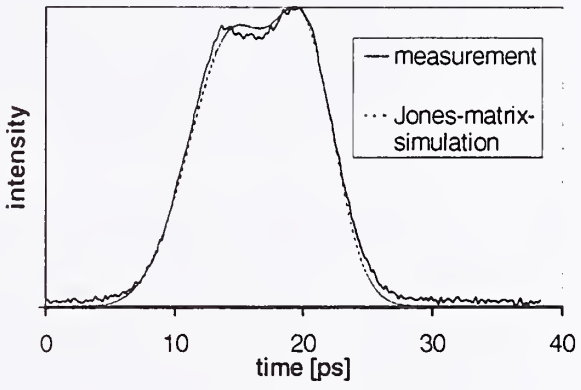

Fig. 3 Comparison of numerical calculation and measurement for the maximum distorted output pulse.

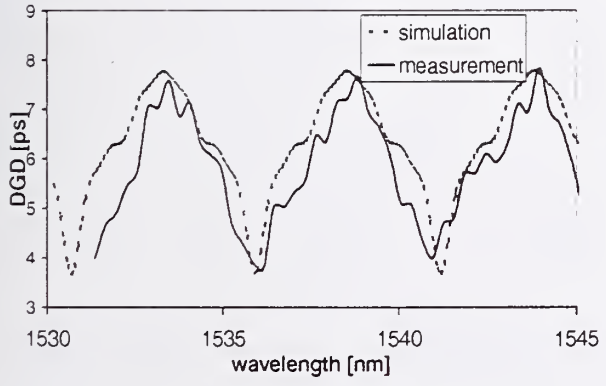

Fig. 4 Measurement and calculation of DGD of CBE.

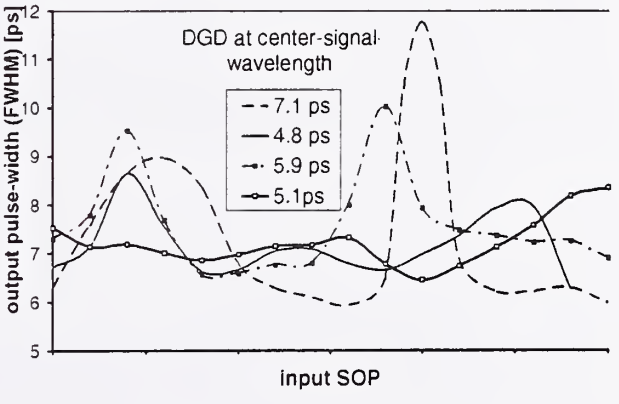

Fig. 5 Measured output pulse width (FWHM) for different input SOP at different signal wavelengths.

Both, measured and simulated data revealed that the DGD versus wavelength is a periodic function in sequences of $\Delta\lambda=\lambda^2/c/\tau = 5.3\,\text{nm}$ with $\tau = 1.51$ ps (Fig. 4) resulting from the periodic structure of the CBE. Next the impact of the input SOP on the output pulse width was analyzed for various signal wavelengths (Fig. 5). Similar to the particular example presented in Fig. 2 the input SOP was tuned along a circle of the Poincaré sphere. The maximum output pulse width was correlated to the wavelength (and the corresponding DGD). The minimum output pulse width was approximately the same (namely $\Delta t_{out} \approx \Delta t_{in} = 6\text{ps}$) for all wavelengths.

5. Summary and Conclusion

It was shown that PMD induced pulse distortion at each signal wavelength can be manipulated between a maximum and a minimum value by changing the SOP of the light launched into the fiber. Thus an almost undistorted pulse transmission can be realized even if the DGD exceeds the pulse width. The maximum achievable pulse distortion is correlated to the DGD at the signal wavelength. This wavelength dependence may yield different signal degradation for the various channels of a WDM system.

We observed that the polarization behaviour of installed single-mode fibers is pretty well reflected by the deterministic model of CBE discussed in this paper while commonly used stochastic models are too pessimistic. The DGD and the PSOP of optical transparent high speed systems in the field remain stable for at least several minutes, and the input SOP can always be optimized for almost undistorted signal transmission [1, 4]. In a recent 10-Gbit/s field trial [1] with more than 40 ps PMD the BER varied from $10^{-6} \leq \text{BER} \leq 10^{-12}$ without polarization control. It was possible to stabilize the system at the minimum BER just by controlling of the input SOP in sequences of minutes.

References

[1] Niall Robinson, Gary Davis, John Fee, 4 x SONET OC-192 Field Installed *Dispersion Managed Soliton System over 450 km of Standard Fiber in the 1550 nm Erbium Band*, OFC'98, Postdeadline Paper, San Jose, 1998.

[2] Ralph Leppla, A. Mattheus, J. Ruffler, F. Wittl, H. Haunstein, B. Teichmann, L.C. Garcia, *Polarization induced system penalties in 10 Gbit/s field trial at 1.3 µm using semiconductor optical amplifiers*, COST workshop on SOA-based Components for Optical Networks, Prague, October 27-28, 1997.

[3] Bernhard Scholl, *Faseroptischer Polarizationsanalysator*, Shaker Verlag ISBN 3-8265-1522-6, 1996.

[4] H.Bülow, G. Veith, *Temporal dynamics of error-rate degradation induced by polarisation mode dispersion fluctuation of a field fiber link*, Proc. ECOC'97, Vol. 1, pp. 115-118, Edingburgh, September 22-25, 1997.

[5] N. Gisin, R. Passy, J.P. Von der Weid, *Definitions and measurements of polarization mode dispersion: Interferometric versus fixed analyzer methods*, IEEE Photonics Technology Letters, vol. 6, pp. 730-732, 1990.

Repeated Measurement of Polarisation Mode Dispersion in Installed Cables

Ádám KAPOVITS
PKI Telecommunications Development Institute,
MATÁV – Hungarian Teleçommunications Company Ltd.

Abstract: *Nowadays the effect and importance of polarisation mode dispersion (PMD) is well known and measurement instruments are commercially available. Repeated measurement of PMD in installed cables is reported in this paper. The PMD of fibres in two different cables were measured on three different occasions. The measurements were performed with commercially available, but different measurement systems. PMD was found to vary significantly with time. Measurement results are discussed and some trends are identified. However, no explanation is found for the large changes.*

Introduction

In the last few years much attention has been paid to polarisation mode dispersion (PMD). This is due to the effect of PMD on transmission quality. Therefore in case of a telecommunications network operator it is essential to characterise its cable network in this respect. In this paper we report on repeated measurements taken on long installed cable sections with different commercially available measurement systems from two different manufacturers.

Discussion

PMD was repeatedly measured on the dark fibres of two relatively long cable sections, the 47 km long Budapest-Bicske section, and the 57 km long Budapest-Dabas section. Both cable sections comprised of underground cables, but of different construction and from different suppliers. The fibres in the two cable sections were also different. In case of the Budapest-Bicske section the fibres were manufactured with the OVD (Outer Vapour Deposition) method, while in case of the Budapest-Dabas section the fibres were manufactured with the MCVD (Modified Chemical Vapour Deposition) method. The cables were installed about 7 and 6 years ago, respectively.

PMD at 1550 nm was measured on three occasions, in May 1996, March 1997 and November 1997. PMD at 1310 nm was measured in May 1996 and November 1997, only. The measurement instruments were kindly lent by two different manufacturers. Both commercially available instruments are using the interferometric technique with broadband sources to measure the PMD. (In May 1996 and November 1997 the measurements were taken with different versions of the same instrument from the same manufacturer.) We have found that both equipment are well suited for field use and a number of measurements could be taken in a short time.

In some cases fibres were re-measured on the same day (after a few minutes or a few hours) or on the second day.

The PMD delay values of the Budapest-Dabas section measured at 1550 nm are presented in Figure 1, while PMD delays of the Budapest-Bicske section (also measured at 1550 nm) are presented in Figure 2. At 1550 nm the fibres of the Budapest-Dabas section have moderate PMD coefficients (<0,4 ps/$\sqrt{km}$), while the fibres in the cable of the Budapest-Bicske section have low PMD coefficient (<0,2 ps/$\sqrt{km}$), so they are excellent in this respect. Actually this might be the reason for the large fluctuation of the measured PMD.

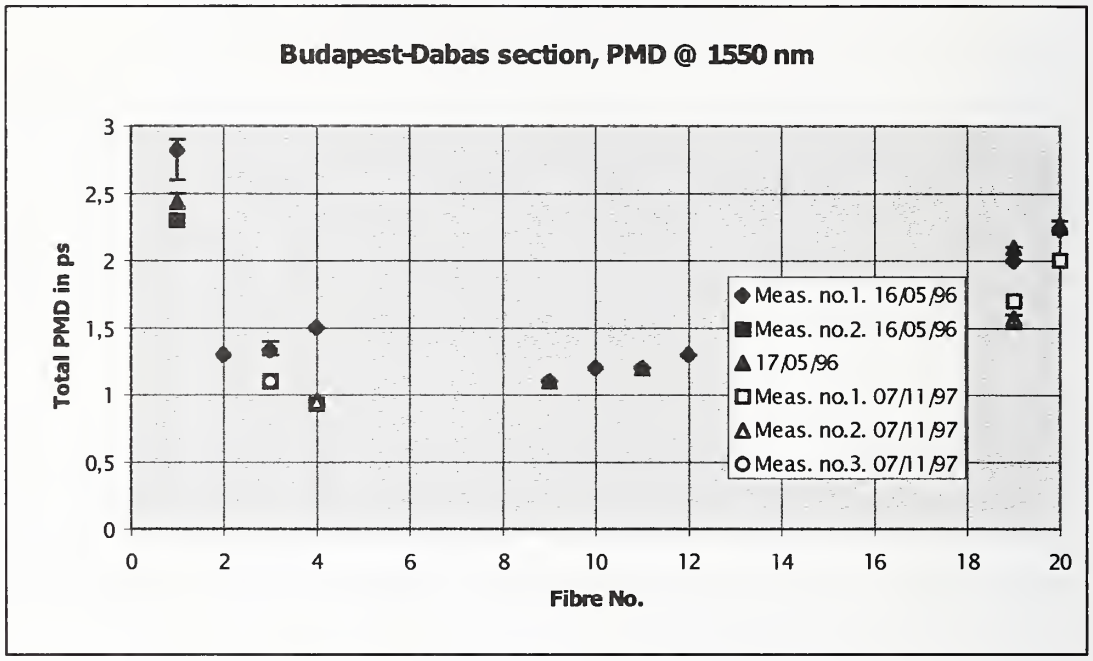

Figure 1.

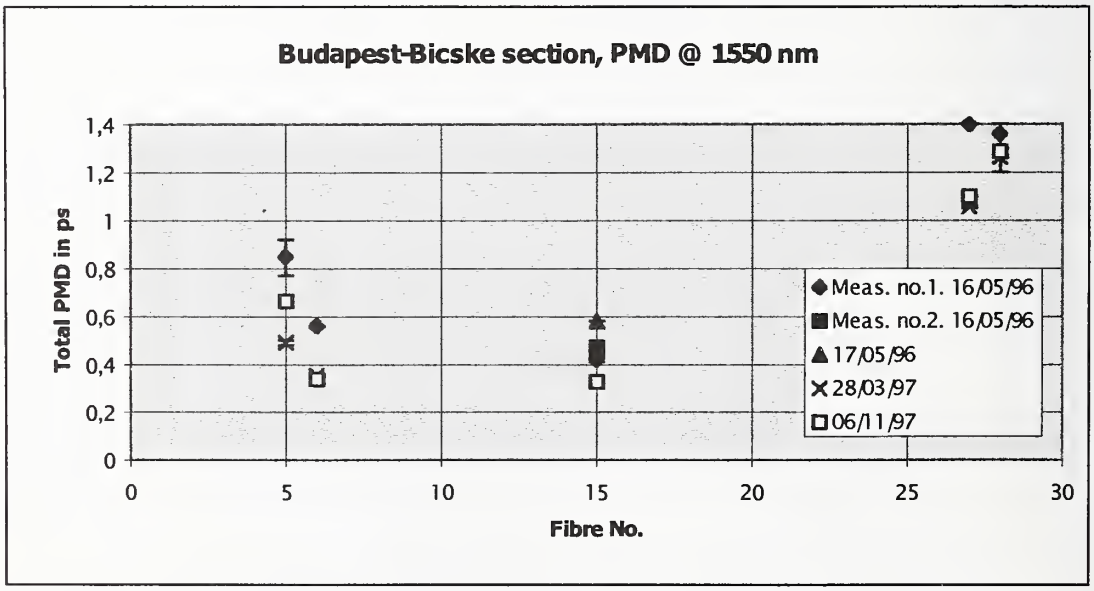

Figure 2.

In Figure 3 and 4 the PMD delays of the fibres of the Budapest-Dabas and Budapest-Bicske section (measured at 1310 nm) are presented, respectively.

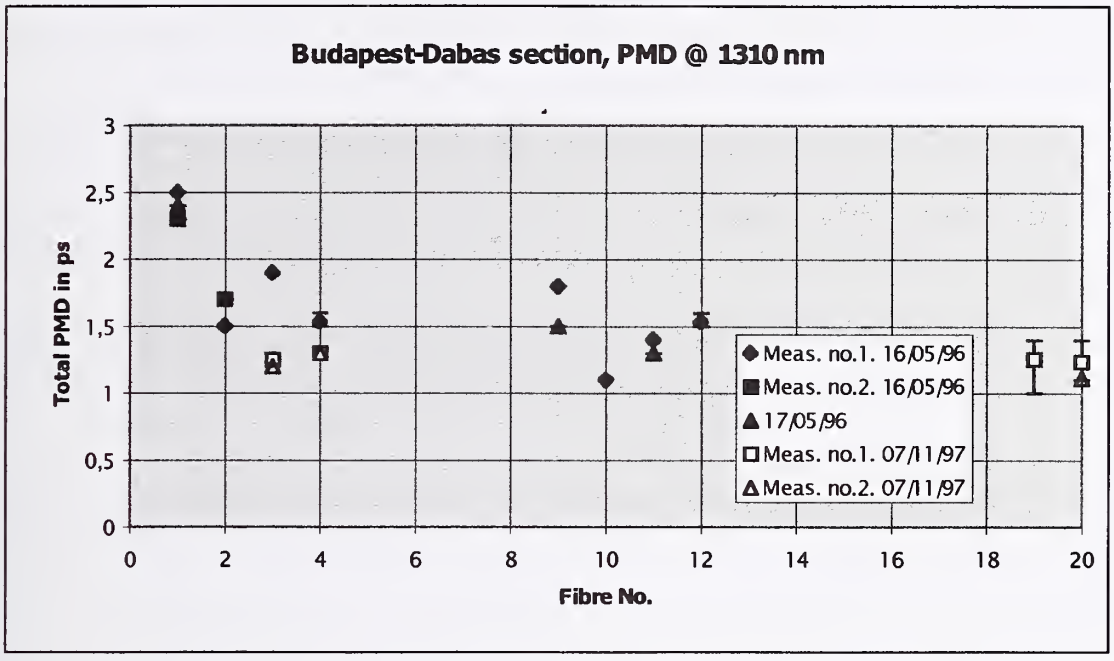

Figure 3.

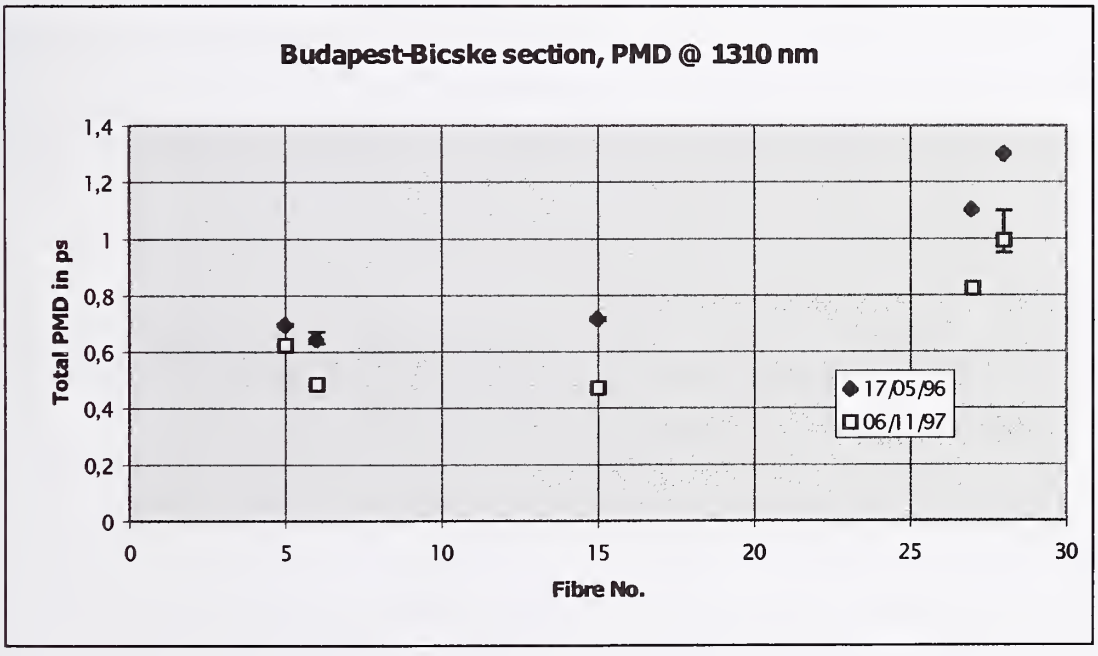

Figure 4.

Key Findings

- The measurements showed that the fibres have good, sometimes very good PMD performance. It was so, despite the fact that PMD was not covered by the specifications when the cables were procured. The tight specifications acted indirectly and ensured good PMD performance.
- The PMD values measured at 1310 and 1550 nm are in the same order, but there is no tendency of being smaller (larger) at one of the wavelengths.
- There are cases, when the PMD values can vary significantly from measurement to measurement, from one day to another, as it is in case of fibre 5, 15 and 28 of the Budapest-Bicske section at 1550 nm (see Figure 2) or fibre 19 and 20 of the Budapest-Dabas section at 1310 nm (see Figure 3). Probably the best example for such a behaviour is, however, fibre 1 of the Budapest-Dabas section at 1550 nm (see Figure 1).
- There are cases (e.g. fibre 19 and 20 of the Budapest-Dabas section) when large short term variation in the PMD at 1310 nm could be observed, while the PMD at 1550 nm is fairly stable.
- The two measurements taken in 1997 on the Budapest-Bicske section at 1550 nm were in a good agreement, except in case of fibre 5 (see Figure 2).
- There is a clear tendency, that PMD measurement results in 1997 are lower than those obtained in 1996. This holds for both cable sections and for both wavelengths. There are cases when the PMD values measured in 1997 are almost the same as those measured in 1996 (i.e. sometimes the difference is less significant), but the 1997 measurement results are always lower than the 1996 ones.

Conclusions

In some cases large variations could be observed from measurement to measurement. The repeatability of the PMD measurement was found relatively poor, especially from 1996 to 1997. This finding is especially difficult to explain, since the cables are in the ground, in stable conditions. Until now we do not know the reason for that, but the scatter of the measured PMD values was significantly larger than the theoretical limit [1].

References

[1] N. Gisin, B. Gisin, J. P. Von der Weid, R. Passy, "How Accurately Can One Measure a Statistical Quantity Like Polarization-Mode Dispersion?", IEEE Photonics Technology Letters, Vol. 8., No. 12., December 1996, pp.1671-1673

Twin-photon techniques for fiber measurements

N. Gisin J. Brendel and H. Zbinden
Group of Applied Physics, University of Geneva, 1211 Geneva 4, Switzerland
A. Sergienko and A. Muller
Dept. of Electrical and Computer Engineering, Boston University

July 7, 1998

1 Introduction

Characterization of single-mode optical fibers requires a basis for time, wavelength and polarization. Parametric downconversion in non-linear crystals naturally provide pairs of photons extremely highly correlated in time, energy (thus wavelength) and polarization. It is thus tempting to explore such photon pairs for fiber and fiber device characterization. Historically, entangled photon pairs where first used in delicate tests of quantum mechanics [1]. Indeed, their correlation is higher than classically possible! However, nowaday photon pair sources can be made cheap and compact enough to offer practical alternatives for many of the traditional measurement schemes. In addition photon pairs provide entirely new possibilities and open the door to new developments in metrology. The purpose of this contribution is first to present some concrete proposals and results along the above lines, and next to draw the attention of the audience to these rather revolutionary new combinations of quantum optics and communication.

2 A photon pair source

Figure 1 presents an example of a photon pair source. A non-linear crystal, like BBO, $KNbO_3$, $LiIO_3$, is pumped by a 15 mW laser diode, at 660 nm in the present example. The prism between the laser diode and the crystal removes all extra infra-red light. The crystals are well known for frequency doubling, as in doubled Nd-YAG lasers. Here we use the time reversed process: wavelength doubling, better known as downconversion (recall that all elementary quantum processes are time symmetric). Since initially the infrared modes are empty (ie are in their quantum vacuum state and the power of pump radiation is not very strong), this downconversion process is spontaneous: a photon from the pump spontaneously splits into two infrared photons. Energy and momentum conservation forces these two photons to be highly correlated: they are created exactly at the same time and the sum of their energy (optical frequency) equals the energy of the pump photon. Note that the latter is defined within the spectral width of the laser, typically expressed in MHz, hence the sum of the two downconverted photon is well defined. But the spectral width of each downconverted photon can be quite large, up to tens of nm, or even hundreds of nm. Following the optical path on Fig. 1, the photon pairs are then injected into a single mode fiber, with standard techniques (microscope objective in the shown example). Next, a directional coupler separates both photons and guides them to two optical connectors.

Figure 1 presents one possible implementation. Other examples are discussed in the next sections. For instance, it might be useful to replace the directional coupler by a wavelength demulti-

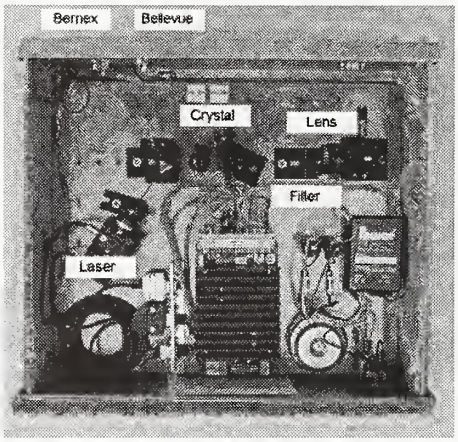

Figure 1: Example of a compact twin-photon source.

plexer: the two photon are still quantum correlated (ie extremely highly correlated) in time and energy, but the photon at one output is in the short wavelength end of the spectrum, while the companion photon is in the complementary long wavelength range. In fig. 1 a collinear configuration is present: the pump and both downconverted photons follow parallel trajectories. Another possibility exploits momentum conservation: if one photon emerges at an angle with respect to the pump beam, the companion photon emerges on the opposite angle (the detail depend on the exact phase matching conditions, wavelength filters, etc). This will be illustrated in the next section for various dispersion measurements.

So far we did not mention polarization, but since the crystals are anisotropic, polarization is important (actually birefringence is required for the phase matching condition). There are two kinds of downconversion processes. In type I both infrared photons have identical polarization, both orthogonal to the pump laser's polarization. In type II downconversion, on the contrary, the two infrared photons can be totally unpolarized, however their polarization states are quantum correlated: if one passes through a polarizer, the other one is immediately polarized in the orthogonal direction. This will be illustrated in subsection 4.3 for polarization mode dispersion measurement.

Other examples of interesting configurations for 2-photon sources are described in [2, 3].

3 Photon counters

Photomultipliers exist for years, but are not effective at telecom wavelengths (1.3 and 1.55 μ). Photon counting devices based on silicon Avalanche Photo-Diodes (APD) are commercially available, but also limited to wavelengths below 1 μ. However, a few groups around the world have demonstrated that germanium and InGaAs APD are suitable for photon counting at telecom wavelengths [4]. Admittedly, this is still the weak point of "quantum optics at telecom wavelengths", because most of the demonstrations used liquid nitrogen cooled APD. Actually, very recently we have demonstrated that InGaAs APDs Peltier cooled are suitable for metrology applications where noise requirement is not as severe as for quantum communication applications. Anyway, progress in this field is fast. The fact that until now not much efforts have been put into these developments, allows one to be optimistic about a possible breakthrough in the near future.

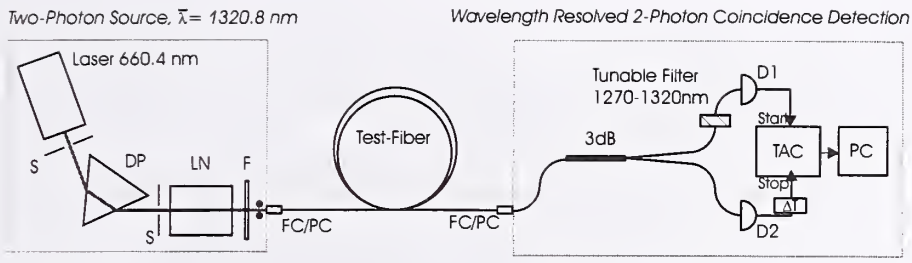

Figure 2: Setup for chromatic dispersion measurements.

4 Dispersion measurements

The intrinsic time-energy-polarization correlation of the downconverted photons make them natural candidates for dispersion measurements, as illustrated in the next 3 subsections.

4.1 Chromatic dispersion measurements on long fibers

This is possibly the simplest example. It exploits only the time and energy correlations of the photons: the difference in detection times provides the information on the time of flight and the measurement of the wavelength of one photon is enough to obtain the necessary information on the wavelength of the companion photon. Therefore we have direct access to the group delay between complementary wavelengths. Choosing moreover the central wavelength near the zero chromatic dispersion, these delays will be small, thus not necessitating any long electronic delay lines. In short, this technique makes use of the photon pairs as a broadband lightsource, comparable to a LED, with sub-picosecond pulsewidth.

A possible implementation is presented in Fig. 2. For technical details we refer the interested reader to [5]. In our first experiment we could determine the zero chromatic dispersion wavelength with a precision of ± 0.5 nm [5]. In a forthcoming experiment, we expect to achieve higher resolution, larger spectral width (up to 300 nm) and measurement times of minutes.

4.2 Chromatic dispersion measurements on short fibers

The spectra of the downconverted photons are large, like LEDs or even broader. However, the photon pairs, considered as a whole, still enjoy the high coherence of the pump laser. Hence, using 2-photon interferometry, the chromatic dispersion of meters long samples of fiber can be determined. This is similar to the well-known white light interferometric measurement technique [6], but with the advantage that the fiber sample length does not need to be adjusted with millimeters accuracy. Thanks to the meter long coherence of the pump laser, the sample length needs only to be adjusted within cm or meter precision. The proposed setup is presented in Fig. 3. Admittedly, this example is more complex than the previous one. Depending on the temperature of the crystal the wavelengths of the collinearly emitted photons vary between 1250 and 1350 nm for one photon and between 1450 and 1600 nm for the other, the central wavelength being at 1400 nm. The interferometer is unbalanced, having the test-fiber in the long arm and a wavelength division multiplexer (WDM) and a moveable mirror in the short arm. The two photon have four choices: The first one can either take the long arm and the other one the short one or vice versa, or both photons take either the short or the long arm. The first two cases are distinguishable due to the time difference between

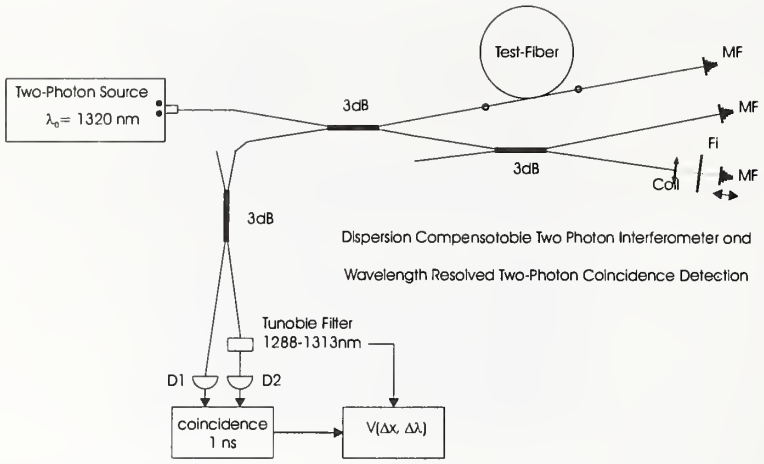

Figure 3: Setup 2-photon interferometric measurements.

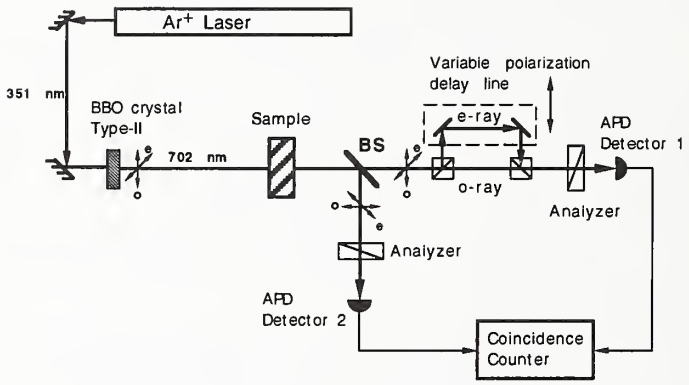

Figure 4: Setup for PMD mesurements.

the arrival times of the two photons. The latter two possibilities are indistinguishable, hence lead to two photon interference. The visibility of the interference pattern is reduced, if the dispersion is not identical in the two arms of the interferometer. We can compensate for the difference in the group velocities in test fiber between the photon around 1300 nm and the photon around 1500 by separating them with the WDM in the short arm and by introducing an adjustable delay for one of them by a moveable mirror. The position of this mirror for optimal interference visibility is a measure for the time delay between the two wavelengths introduced by the dispersion in the test fiber. We can now scan over the whole wavelength range by tuning the temperature of the nonlinear crystal and obtain the dispersion between 1250 and 1600 nm, thus obtain the group delay as function of wavelength.

4.3 Polarization mode dispersion measurements

In this example, the photon pairs are produced by type II parametric downconversion. Hence, in addition to their time and energy correlations, they are also entangled in polarization, thus suitable

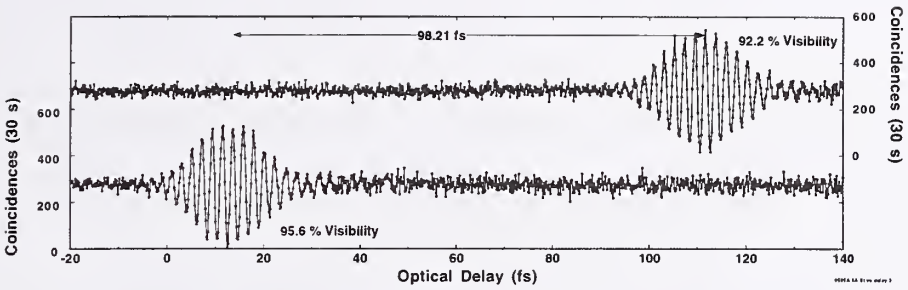

Figure 5: Result of the PMD measurement with sub-femtosecond resolution.

for Polarization Mode Dispersion (PMD) measurements. A possible implementation is presented in Fig. 4, for details see ref. [7]. In this experiment, birefringent plates where actually measured, not fibers, and the source was an Argon laser. However, the results clearly demonstrate the potential of the method, see Fig. 5. Essentially the method is similar to the white light interferometric technique, but thanks to the wide spectrum of the downconverted photons (about 300 nm is this experiment), a resolution of 0.01 fs was achieved. This should be contrasted with the 50 to 100 fs resolution of the standard interferometric technique based on LEDs [8].

5 Absolute calibration of sources and detectors without black-body radiation

As a last example, we present the use of photon pairs for the determination of the absolute efficiency of detectors. Let us emphasize that this technique, contrary to all other techniques we are aware of, is not based on a light source calibrated with black body radiation. Hence, this new technique allows to determine detector efficiencies independently of temperature. The basic idea is simple [9]. Since the downconverted photons are always produced by pairs, the number N_{AB} of coincidence detections with two detector A and B equals:

$$N_{AB} = N\eta_A\eta_B \tag{1}$$

where N is the total number of photon pairs, and η_A and η_B are the efficiencies of detectors A and B, respectively. Moreover the single counts at detector B equals $N_B = N\eta_B$. Consequently, the efficiency of detector A is given by the simply relation:

$$\eta_A = \frac{N_{AB}}{N_B} \tag{2}$$

This elegant idea has now been tested in several labs [9], in particular at the NIST-Washington, and the accuracy limitations due to the statistics of photon counting has been estimated [10]. A trial to extend this technique to analog detectors is presented in [11].

Analogoulsy, a calibrated source can be devised.

6 Conclusion

The potential of highly correlated photon pairs produced in parametric downconversion for optical fiber and devices has been emphasized. The huge technological progress in simple and efficient

photon pair sources and the ongoing progress in photon counting techniques at telecom wavelengths open new possibilities for the fiber optic community. The intrinsic correlations of the photon pairs offer advantages such as automatic determination of a common time basis, complementary wavelengths and polarization. Thus all the degrees of freedom of photons in single-mode fibers are entangled in these photon pairs. Each photon may be totally depolarized and cover a bandwidth of tens or even hundreds of nanometers. Now, at the same time the two photons form a single quantum object (a bi-photon) with large coherence lengths, up to meters. This offers the possibility to combine advantages of low and high coherence interferometry.

The examples presented in this contribution are but a few ones, more should be expected. Finally, let us briefly mention that quantum optics has also interesting potentials for communication. As examples we mention quantum cryptography [12] and noiseless amplifiers that beat the 3dB "quantum limit"[13].

Acknowledgments

This work profited from support by the Swiss Priority Program in Optics and by the European TMR network on "The physics of quantum information".

References

[1] see e.g. J. Freedman, and J. F. Clauser, Phys. Rev. Lett., **28**,938-941, (1972); A. Aspect, P. Grangier, and G. Roger, Phys. Rev. Lett., **47**, 460-463, (1981); Z. Y. Ou and L. Mandel, Phys. Rev. Lett., **61**, 50-53, (1988); Shih and Alley, Phys. Rev. Lett. **61**, 2921, (1988); P. R. Tapster, J. G. Rarity, and P. C. M. Owens, Phys. Rev. Lett., **73**, 1923-1926, (1994). W. Tittel et al., Phys. Rev. A **57**, 3229, 1998.

[2] P. G. Kwiat et al., Phys. Rev. Lett., **75**, 4337, (1995). ??? nb400

[3] P. Kwiat, CLEO/IQEC, pp, San-Fransisco, 1998.

[4] F. Zappa et al, Optics Lett. **19**,846-848,1994; P.C.M. Owens et al, Applied Optics **33**,6895-01,1994; G.L. Morgan et al, Los Alamos National Laboratoty report LA-UR-97-4375, 1997; G. Ribordy et al, Applied Optics, in press, 1998.

[5] J. Brendel, H. Zbinden and N. Gisin, Optics Commun., in press, 1998.

[6] L. Thvenaz et al, J. Lightwave Tech. **6**, 1-7, 1988.

[7] A.V. Sergienko et al., preprint, Boston University, 1998.

[8] N. Gisin et al, JEOS Pure & Applied Optics **4**, 511, 1995.

[9] see e.g. A.V.Sergienko and A. N. Penin, Applied Optics, **30**, 3582, 1991; A.L. Migdall et al., Metrologia **32**, 479-483, 1995; G. Brida et al, preprint, Istituto Electtrotecnico Nazionale G. Ferraris, Torino, Italy, 1998.

[10] P. Kwait et al, Applied Optics **33**, 1844, 1994; N. Gisin, J. Brendel and A. Stefanov, preprint, Geneva University, 1998.

[11] A. Sergienko and A.N. Penin, Sov. Tech. Phys. Lett. **12**, 328, 1986.

[12] W. Tittel, G. Ribordy and N. Gisin, Phys. World, March 1998.

[13] D.J. Lovering et al, Optics Lett. **21**, 1439, 1996.

COMPARISON BETWEEN INTERFEROMETRIC AND POLARIMETRIC PMD MEASUREMENT TECHNIQUES BASED ON FIBER IMPULSE RESPONSE

Marco Schiano

CSELT, via Reiss Romoli 274, 10148 Torino (Italy)

Abstract

Up to now, the assumption of a gaussian impulse response for fibers affected by Polarization Mode Dispersion has represented the theoretical background of the interferometric measurement technique. This paper introduces a new model, based on the theory of the Principal States of Polarization, which leads to an original interpretation of the interferometric results and establishes a clear relationship between the Interferometric and the Polarimetric PMD measurement methods. Experimental data supporting the new model are also presented.

1. Introduction

Comparison between Interferometric (IM) and Polarimetric (PM) PMD measurement methods has represented an important issue since the early development of the two techniques [1, 2, 3]. However, the time and wavelength random fluctuations of PMD and the deep difference between the theoretical approaches of the two measurement methods made this task quite difficult.

In particular, the fiber Impulse Response (IR) due to PMD is a fundamental element in the IM technique theory [4] that models the fiber as a concatenation of linearly birefringent waveplates with random orientations. On the contrary, to the author's knowledge, the IR has never been calculated on the basis of the Principal States of Polarization (PSPs) theory [5], where the PM techniques are established [6, 7]. In paragraph 2 it is demonstrated that, according to the PSPs theory, the IR has a two-lobe shape and, in general, is different from the gaussian hypothesis of [4]. The calculation of the IR starting from PM measurements allows a direct comparison with IM measurements, not only in terms of average Differential Group Delay (DGD) of the PSPs, but also in terms of full interferometric pattern. This is the subject of paragraph 3 that illustrates the new comparison technique by means of examples based on experimental data.

Although this comparison technique is somewhat complex and is still sensitive to PMD time fluctuations, it represents a well-established relationship between IM and PM methods and offers the opportunity of further investigations on the spectral behavior of the PSPs.

2. Impulse response evaluation

The impulse response of a fiber affected only by PMD is of course a theoretical abstraction: a broadband optical input pulse, indeed, can not be considered unaffected by chromatic dispersion. Nevertheless, it becomes an important tool when IM measurements are considered. In an IM set-up [4], the interferometer measures the autocorrelation function, *I(T)*, of the fiber output field component, linearly polarized along a given direction, when the input is a broadband, incoherent, CW light source:

$$I(T) = \int E(T) \cdot E(T+\tau) d\tau \,.$$

E(T) is the electric field component parallel to the interferometer polarizer (or to the polarization eigenaxis in case of a polarization maintaining fiber interferometer).

Although the modulus of the power spectrum of the light source is similar to that of a short pulse source, however its phase is a random function rather than zero and thus *E(T)* can not be regarded as the fiber IR. Nevertheless, when it passes through the interferometer, the random phase difference between *E(T)* and $E(T+\tau)$ is averaged by the photodetector and the resulting interferogram can be considered an approximation of the IR autocorrelation function.

Furthermore, interference occurs only between spectral components at the same wavelength traveling with the same group velocity. This makes chromatic dispersion negligible in IM measurements.
To conclude these preliminary considerations, it should be reminded that PMD produces a random modification on a signal travelling in a fiber and therefore IR must be determined on a statistical basis. In the following, the approach of [4] is adopted: IR is calculated as the Probability Density Function (PDF) of the Group Delay (GD) of the electric field, regardless of its input polarization state.
As already stated, a fiber affected by PMD only is considered and polarization dependent loss and chromatic dispersion in the whole bandwidth of interest are neglected.
According to the PSPs theory, the group delay of a signal traveling on the slow PSP is given by:

$$T_+ = \tau_m + \Delta\tau / 2 \ ,$$

and similarly for a signal traveling on the fast PSP:

$$T_- = \tau_m - \Delta\tau / 2 \ ,$$

where τ_m and $\Delta\tau$ are the mean group delay and the DGD of a given couple of PSPs respectively.
If a statistical ensemble of PSPs is considered, $\Delta\tau$ must be regarded as a random variable and hence T_+ and T_-, as linear functions of $\Delta\tau$, became random variables as well. τ_m has been implicitly assumed constant because, as far as it concerns PMD measurements, neither IM nor PM techniques are sensitive to the mean GD of PSPs, but only to their DGD.
It is now straightforward to derive the probability density functions of T_+ and T_- from that of $\Delta\tau$ [8]:

$$f_+(T_+) = 2g[2(T_+ - \tau_m)], \quad f_-(T_-) = 2g[-2(T_- - \tau_m)],$$

where $g(\cdot)$ is the PDF of $\Delta\tau$ and the factor 2 is a normalization factor.
If the input signal is unpolarized, then both slow and fast PSPs can be considered equally excited and the PDF of the group delay of such a signal is simply the normalized sum of $f_+(T_+)$ and $f_-(T_-)$:

$$f(T) = g[2(T - \tau_m)] + g[-2(T - \tau_m)], \qquad (1)$$

where T is the group delay regardless of the PSP.
The function $f(T)$ consists of two replicas of the PDF $g(\cdot)$, symmetric with respect to τ_m, with a time scale factor of 2. Some examples of measured $f(T)$ are shown in the next paragraph. It should be noted also that the effectiveness of relation (1) is not limited to the case of random DGD, but it also fits the case of polarization maintaining fibers, where the PDF of the DGD is a Dirac function.
Finally, it is important to remind that, in the IM set-up, the interferometer selects a linear polarization state aligned with a given direction. Applying the total probability theorem [8] it is easy to demonstrate that equation (1) modifies in:

$$f(T, X) = \sqrt{X}\, g[2(T - \tau_m)] + \sqrt{1 - X}\, g[-2(T - \tau_m)], \qquad (2)$$

where X is the fraction of optical power coupled from a slow PSP to the linear polarization state of the interferometer eigenaxis: $X = \frac{1}{2}(1 + \cos\vartheta)$, ϑ being the angle between the unit Stokes vectors representing the two polarization states [9].
This second random variable X, which is itself a function of time and wavelength, makes the impulse response (2), and hence its autocorrelation function, more complicated and susceptible to time fluctuations.

3. Comparison of interferometric and polarimetric techniques

Experimental evidence of the previous model has been searched by PMD measurements on an ITU-T G.652 fiber plant, 72 km long, installed in buried ducts. IM measurements have been carried out with an unpolarized LED source, whose 3 dB bandwidth ranged from 1480 nm to 1570 nm. PM measurements have been performed by the Jones Matrix Eigenanalysis (JME) method [6], in the same spectral range, with a wavelength step of 1 nm. JME measurements have been repeated several times in order to collect a number of samples large enough for PDF calculation. Then the PDF of the JME data set was determined, and by means of equation (1) the IR of the fiber was calculated as well. At the end, the autocorrelation function of the calculated IR was compared with the IM measurement. This procedure is illustrated in detail in figure 1, while other examples of the final comparison are reported in figure 2.

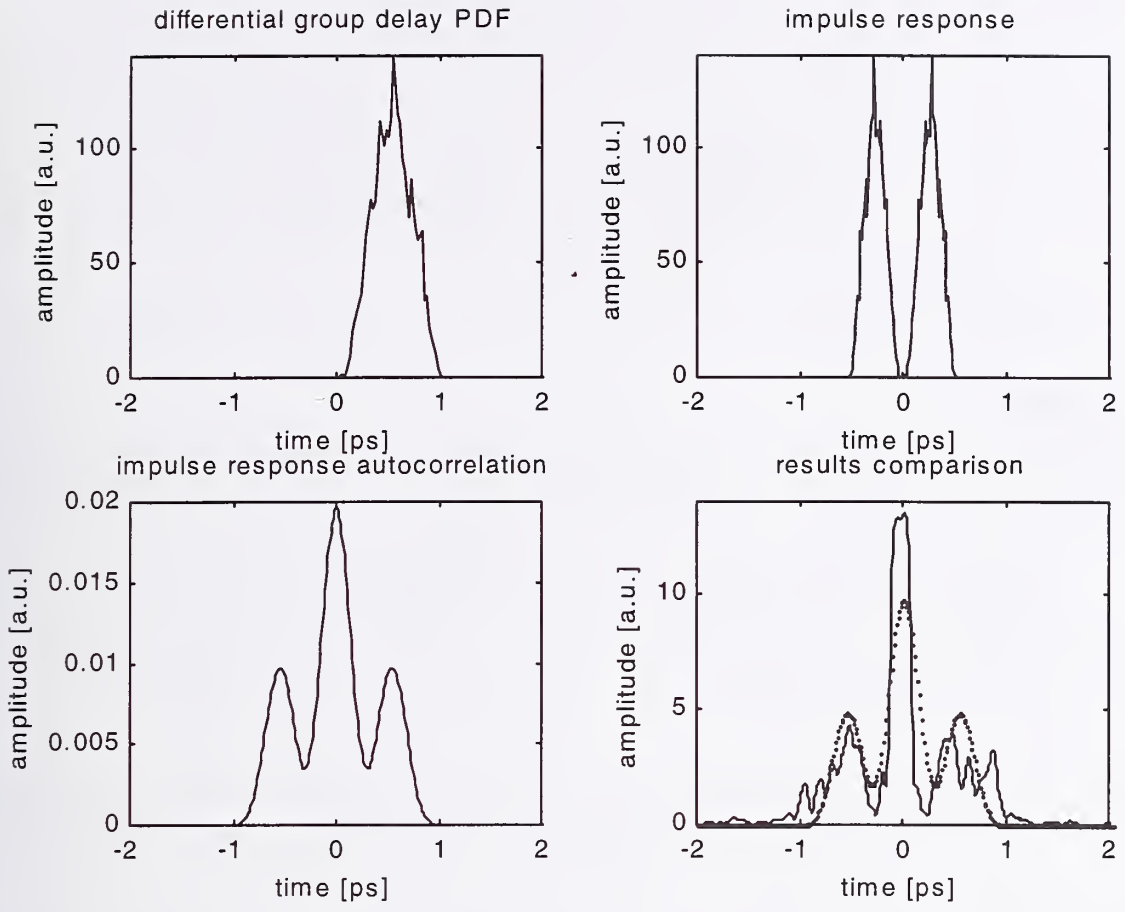

Figure 1-Comparison procedure for IM and PM methods: the picture labeled *results comparison* reports the autocorrelation function of the IR calculated from PM data (doted line), compared to the measured interferometric pattern (continuous line)

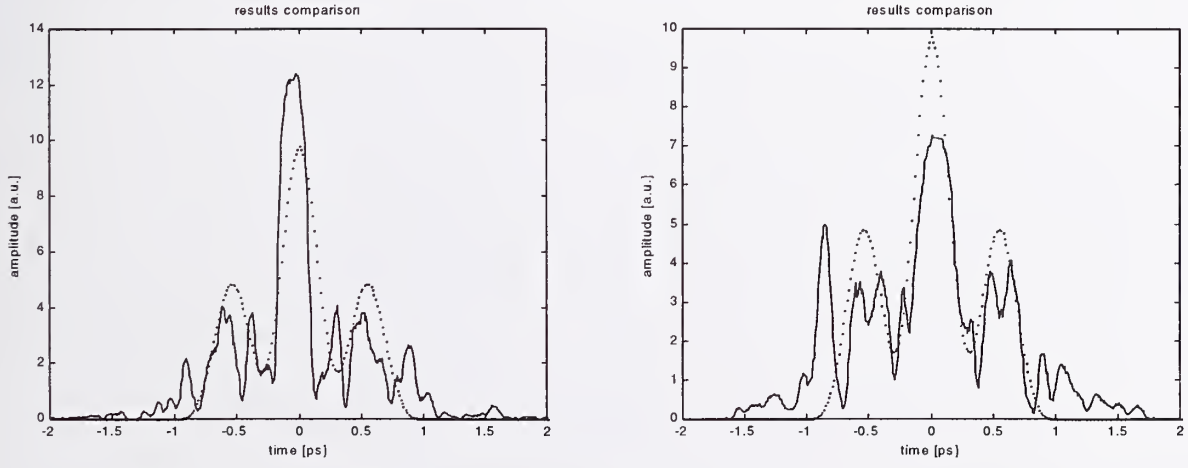

Figure 2-Further comparison of IM patterns measured at different times (continuous line) with the autocorrelation function of the calculated IR (doted line)

Some important observations can be derived from these experimental results.
First of all, it should be noted that the central peak of the interferogram is the autocorrelation function of the source spectrum and is not related to PMD [3], so the mismatch of the compared functions around zero is not significant. A second remark is that the autocorrelation function of the IR calculated from PM data, i. e. the autocorrelation of (1), does not take into account fluctuations of the PSP's Stokes vector direction. For this reason, measured interferometric patterns, which on the contrary depend on the random variable X, are more irregular than the calculated autocorrelation function of the IR, and present wide time fluctuations. Unfortunately, up to now, commercially available polarimeters can not measure this quantity which could improve the comparison accuracy. Furthermore, due to small misalignment of the interferometer, interferometric patterns are slightly asymmetric and this degrades the comparison quality as well.
Taking into account previous considerations, the results of the comparison technique can be considered satisfactory and well supporting the theoretical model.

3. Conclusions

A new comparison technique between interferometric and polarimetric PMD measurement methods has been presented. It is based on the calculation of the impulse response of a fiber affected by PMD according to the theory of the Principal States of Polarization, and allows a direct comparison of the interferometric pattern with the autocorrelation function of the impulse response calculated from Polarimetric measurements. Experimental results indicate that, despite time fluctuations of interferometric patterns, a quite satisfactory agreement between the two methods can be found. A further improvement of the technique could be achieved by the measurement of the wavelength fluctuations of the Stokes vectors representing the output PSPs, that is, at present, not allowed by commercial polarimeters. Finally, a revision in the data analysis algorithms of interferometric patterns seems to be advisable to fit the behavior of experimental data that are, at the same time, non gaussian-like and time fluctuating.

Acknowledgments

The author gratefully thanks Dr. T. Tambosso for continuous encouragement and Dr. P. Morra for preparing the plant.

References

[1] N. Gisin et al., *Experimental comparison between two different methods for measuring polarisation mode dispersion in singlemode fibres*, Electronics Letters, Vol. 27, No. 24, pp.2292-2293, November 1991.
[2] N. Gisin, B. Perny, F. Prieto, C. Zimmer, *Polarisation Mode Dispersion: large scale comparison of Jones Matrix Eigenanalysis against Interferometric measurement techniques,* Electronics Letters, Vol. 32, No. 7, pp.680-681, March 1996.
[3] B. L. Heffner, *Influence of optical source characteristics on the measurements of polarization-mode dispersion of highly mode-coupled fibers*, Optics Letters, Vol. 21, No. 2, pp.113-115, January 1996.
[4] N. Gisin, J. P. Von der Weid and J. P. Pellaux, *Polarization mode dispersion of short and long single-mode fibers*, Journal of Lightwave Technology, Vol. 9, No.7, pp. 821-827, July 1991.
[5] C. D. Poole, R. E. Wagner, *Phenomenological approach to polarization dispersion in long single-mode fibres*, Electronics Letters, Vol. 22, No. 19, pp.1029-1030, 11th September 1986.
[6] B. L. Heffner, *Automated measurement of polarization mode dispersion using Jones matrix eigenanalysis*, Photonics Technology Letters, Vol. 4, No. 9, pp. 1066-1069, September 1992.
[7] D. Andresciani et al., *Measurement of the group-delay difference between the principal states of polarization on a low-birefringence terrestrial fiber cable*, Optics Letters, Vol. 12, No. 10, pp. 844-846, October 1987.
[8] A. Papoulis, *Probability, Random Variables and Stochastic Processes,* McGraw-Hill, New York, 1991.
[9] C.D. Poole, D.L. Favin, *Polarization-mode dispersion measurements based on transmission spectra through a polarizer*, Journal of Lightwave Technology, Vol. 12, No. 6, pp. 917-929, June 1994.

Determination of Small PMD Values via the Poincaré Sphere Method Using Wavelength Scanning Data

N.Cyr
EXFO Electro-Optical Engineering, Inc.
465, av. Godin, Vanier, Québec, Canada, G1M 3G7

1. Introduction

Polarimetric PMD-measurement techniques, such as the Jones Matrix Eigenanalysis[1] (JME) and Poincaré Sphere[2] (PS) methods, permit the PMD to be fully characterized by determining the optical frequency dependence of the polarization dispersion vector Ω. The magnitude of this vector is the differential group delay (DGD), and its orientation yields the principal states of the device under test (DUT). The PMD is defined as the mean or rms value of the DGD averaged over all optical frequencies. In the case of the PS technique, the output state of polarization (SOP) describes a curve on the Poincaré sphere, whose local angular velocity yields the DGD. Both the JME and PS methods require the measurement of the three Stokes parameters describing the SOP as a function of optical frequency, a frequently tedious acquisition process which can take many minutes to carry out using a tunable laser and a polarimeter. Other commonly used approaches to PMD measurement, such as the interferometric[3] (INT) and wavelength-scanning fixed analyzer[4] (WSFA) methods, measure the projection of the output SOP along one axis characteristic of the measurement instrument, for a rapid determination of the PMD. However, the information lost in 'discarding' the other two components severely hampers measurement of extremely small (<50-fs) PMD values, particularly when the medium exhibits intermediate or strong mode coupling.

We describe here a method permitting a PS-determination of the PMD using 'incomplete' polarimetric data. The measurement of small values of PMD using this PS variant requires only two 'polarimetric' parameters, which can be deduced from WS measurements with different linear axes of analysis. This time-saving technique is based on the fact that it is the magnitude and not the sense of the local angular velocity on the Poincaré sphere which determines the DGD.

2. Measurement concept

Fig. 2 shows a schematic diagram of the measurement concept. The output from a broadband light source (BBS) is polarized by a linear polarizer (P1). The light exiting the DUT is analyzed with another linear polarizer (P2). An optical spectrum analyzer registers the optical-frequency-dependent transmission through P2. The setup is similar to that of broadband wavelength scanning[5], except that polarizer P1 and analyzer P2 can be rotated. A number of spectra are registered and used in combination to obtain trajectories of the output SOP on the Poincaré sphere.

In the simplest implementation, one needs to perform three spectral acquisitions: successive WS measurements with the analyzer P2 oriented at 0, 45, 90°, (and, optionally as a crosscheck, 135°), the sum of the powers $P_0 + P_{90}$ (or $P_{45} + P_{135}$) being equivalent to a measurement of the spectrum at the input of P2. On account of this normalization of the transmission, the spectral shape of the broadband source is not important. In reality, this implementation is overly simplified. In order to ensure that the input SOP is not by chance aligned with one of the principal states of polarization (PSP) of the DUT, the above-mentioned

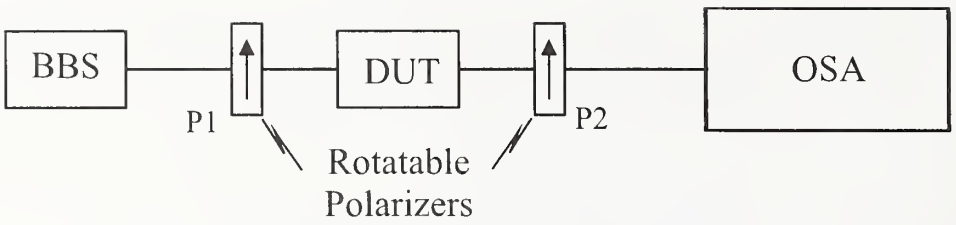

***Figure 2:**. Schematic diagram of the measurement concept. The polarizer P1 is oriented at 0 or 45°, and the analyzing polarizer P2 at 0, 45, 90 or 135°.*

procedure must, in general, be repeated with the first polarizer P1 rotated by 45° from its inital position. From these measurements, two of the three normalized Stokes parameters, i.e. s_1 and s_2 , can be calculated in terms of P_0 , P_{45} and P_{90} (all as a function of optical frequency ν). Moreover, since the light at a given optical frequency is fully polarized, we can also deduce s_3 to within a sign factor:

$$s_1(\nu) = \frac{2P_0(\nu)}{P_0(\nu) + P_{90}(\nu)} - 1 \qquad s_2(\nu) = \frac{2P_{45}(\nu)}{P_0(\nu) + P_{90}(\nu)} - 1 \qquad \left|s_3(\nu)\right| = \sqrt{1 - \left[s_1^2(\nu) + s_2^2(\nu)\right]} \qquad (1)$$

Given the trajectories of the output SOP on the Poincaré sphere, PMD can be deduced in different ways. Two main categories of situations lead to different analysis of the raw data.

In the weak mode-coupling regime, the trajectory on the sphere is an arc of a circle, its projection in the equatorial plane ($s_3 = 0$) is an ellipse, and the $s_i(\nu)$ are cosine functions with a period 1/DGD. We can make use of this property to obtain the DGD by fitting data points with cosines. Residual mode coupling or non-zero differential chromatic dispersion induce a slight change in both orientation and magnitude of the polarization dispersion vector with optical frequency (second-order PMD). An accurate value of the mean DGD is obtained by fitting cosines with varying periods, amplitudes and offsets.

In the strong mode-coupling regime, a piecewise analysis of the trajectories must be undertaken. Using the two trajectories in combination, the Poincaré sphere method[2] can be applied to obtain the DGD for each small interval of optical frequency. Although a mathematical ambiguity appears where the trajectory crosses the equatorial plane ($s_3 = 0$) (since we know only the magnitude of s_3 and not its sign) this is normally resolved by considering the trajectories corresponding to each of the two signs and verifying which of the two represents a smooth continuation of the curve before the zero crossing.

On the other hand, a simpler procedure consists in fitting cosines piecewise to obtain the mean DGD for each interval of optical frequency. The procedure do not require a knowledge of s_3; only the projection of the trajectories onto the equatorial plane is needed. In order to remain practical, this analysis should be restricted to small PMD values (< 0.3 ps). For large PMD values (> 1 ps), the trajectory would need to be divided into an excessively large number of intervals.

Of course, the small PMD technique described here could include an explicit measurement of s_3 by means of a supplemental spectral acquisition whereby a quarter waveplate was placed in front of P2 in Fig.2, at the expense of the overall measurement time and complexity.

3. Experiment

The technique is first illustrated by the measurement of a very small PMD in weak mode coupling. The DUT is a segment (7.5 cm) of intermediate-birefringence fiber (200 fs/m), pigtailed with short lengths of standard single-mode fibers. The broadband source is the superposition of two LEDs (1310 and 1550 nm), with a small but usable power in between. Figure 3 shows spectra registered by an OSA for one orientation

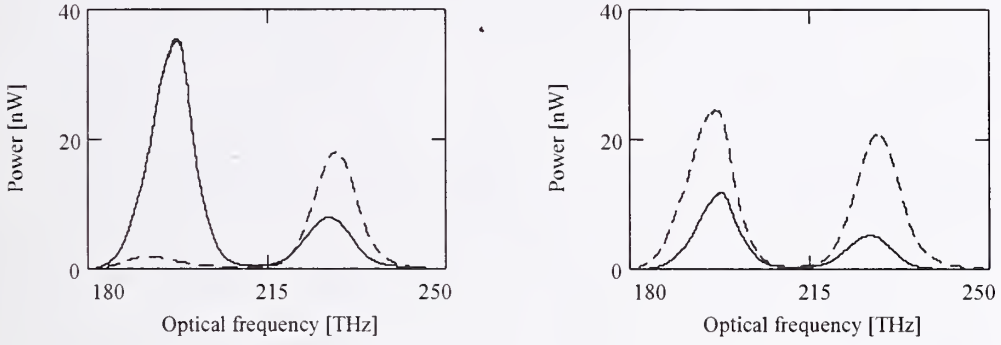

Figure 3: Observed spectra. (a) Analyzer P2 at 0° (—) and 90° (----). (b) at 45° (—) and 135° (----).

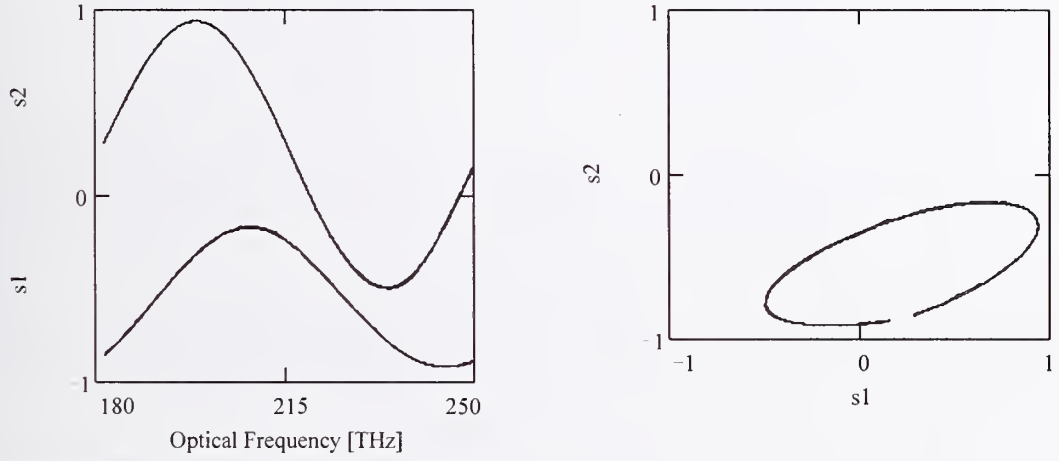

Figure 4: Measured trajectory and cosine fit, mean DGD = 14.3 fs. (a) Stokes parameters s_1 and s_2 as a function of optical frequency. (b) Projection of the trajectory onto the equatorial plane.

of P1, with four settings (0, 45, 90, 135°) of the analyzer orientation. Stokes parameters $s_1(\nu)$ and $s_2(\nu)$, obtained from the spectra according to Eq. (1), are plotted in Fig. 4(a) as a function of optical frequency, along with cosine fits as described in section 2. The two curves are superimposed. The mean DGD is 14.3 fs. Preliminary results indicate the repeatability of such measurements to be within 0.1 fs.

The second example is a 3 km long spool of SMF fiber. The observed spectra are shown in Fig. 5. The Stokes parameters $s_1(\nu)$ and $s_2(\nu)$ deduced from these spectra are plotted in Fig. 6(a) as a function of optical frequency. The projection of the trajectory in the equatorial plane, shown in Fig 6(b), is no longer an ellipse. In such a case, a single cosine function no longer suffices to fit each of $s_1(\nu)$ and $s_2(\nu)$ across the full frequency range. Instead, the projections are fitted piecewise with cosine functions to obtain the mean DGD in each interval of optical frequency (see section 2.). The average over the whole frequency range obtained this way is 68 fs.

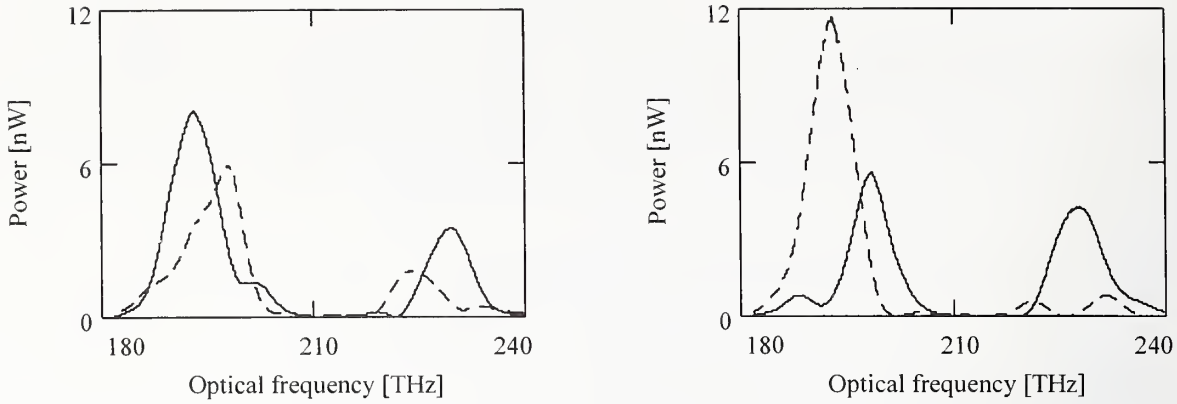

***Figure 5**: 3 km of spooled fiber: observed spectra. (a) Analyzer P2 at 0° (—) and 90° (----). (b) at 45° (—) and 135° (----).*

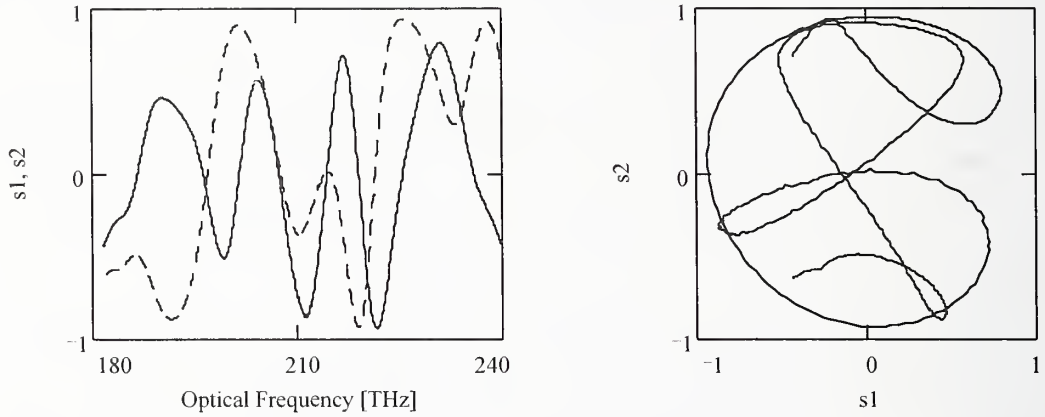

***Figure 6**: Measured trajectory with the 3 km spooled fiber. (a) Stokes parameters s_1 and s_2 as a function of optical frequency. (b) Projection of the trajectory onto the equatorial plane. Mean DGD = 68 fs.*

4. Conclusions

We have shown that a frequency-domain polarimetric analysis can be made, for an accurate determination of subpicosecond PMDs, from a limited number of WS measurements. The technique described here can be carried out in a much shorter time than standard polarimetric PMD methods. Moreover, it can be rendered even more rapid if used in conjunction with an 'adaptive' algorithm to limit the measurement to only two standard WS acquisitions if, as may often be the case, the DUT exhibits weak mode coupling.

References

1. B.L. Heffner, IEEE Photonics Technology Letters, **4**, 1066 (1992).
2. C.D.Poole, N.S.Bergano, R.E.Wagner, H.J.Schulte, IEEE J. Lightwave Technol., **6**, 1185 (1988).
3. N. Gisin, J.P. Von der Weid, J.P. Pellaux, IEEE J. Lightwave Technol., **9**, 821 (1991); Y. Namihira H. Wakabayashi, J. Opt. Commun., **12**, 2 (1991)
4. C.D. Poole, D.L. Favin, IEEE J. Lightwave Technol., **12**, 917 (1994)
5. F.Ravet, B.Heens, X.Wang, J.C.Froidure, M.Blondel, Conference Digest, OFMC'97, National Physical Laboratory, Teddington, UK, October 1997, pp. 86-89.

POLARISATION-INDUCED PULSE SPREADING IN BIREFRINGENT OPTICAL FIBRES WITH ZERO DIFFERENTIAL GROUP DELAY

B. Huttner, B. Gisin and N. Gisin

Group of Applied Physics
University of Geneva
20 Rue de L'Ecole de Medecine,
CH1211, Genève 4, Switzerland

Abstract: It was recently pointed out that the addition of polarisation dependent losses to birefringent optical fibre systems leads to non-intuitive results. In this work, we present computer simulations of concatenations of trunks of birefringent fibres and elements with polarisation dependent losses. We show that the concatenation may have zero differential group delay over a whole range of wavelengths, but that a pulse propagating down the concatenation may still experience significant pulse spreading. In this example, the two main methods used for characterising polarisation mode dispersion in optical fibre systems, i.e. Jones matrices eigenanalysis versus interferometric method give different results. This exemplifies the need for a careful assessment of the basic concepts related to polarisation effects in the presence of polarisation dependent losses.

Introduction

The birefringence properties of optical fibre systems are becoming increasingly important in telecommunication as a limiting factor of the bit rate. The concept of Principal States of Polarisation (PSP) [1] is central to the study of these birefringence properties. For a given optical fibre trunk, the PSP's are defined as the polarisation states for which the output polarisation is independent of the frequency to first order. For a fibre with no Polarisation Dependent Losses (PDL) the two PSP's are orthogonal. A light pulse polarised along a PSP propagates along the fibre without distortion or broadening (if we neglect the other factors such as chromatic dispersion or non-linear effects). Moreover, the two PSP's represent the slowest and fastest propagating pulses. Any other pulse will broaden during the propagation. The maximum broadening is given by the Differential Group Delay (DGD), which is the differential delay between the two PSP's [2]. However, for a real trunk of fibre, the PSP's are very unstable. Therefore, the parameter relevant to characterise the quality of the fibre trunk is the mean DGD or the RMS DGD. It was shown that this time-ensemble is equivalent to a frequency ensemble of the DGD [3]. This frequency average is known as the Polarisation Mode Dispersion (PMD) of the fibre [4]. It is the basic parameter required to estimate birefringence-induced distortions in optical fibre systems. An alternative procedure for measuring the PMD is the interferometric method [5]. This method, based on low coherence interferometry, gives directly the pulse spreading in a trunk of fibre, from which one can infer the PMD. This method is not related to the PSP concept. It is now well known that these two methods give equivalent results [6].

The basic concepts of PSP's and DGD still hold for the case of optical fibre links with both PMD and PDL. However, we recently showed that the interaction of PMD and PDL produces rather surprising results [7]. For example, we showed that the DGD of a concatenation of birefringent fibres and elements with PDL may produce a global DGD, which is larger than the sum of the DGD's of all the trunks. Moreover, in this case, the two PSP's are not necessarily orthogonal. Neither do they characterise the fastest and slowest pulse. Another important conclusion of this previous work is that, like the PMD, the PDL is a statistical quantity, varying with the wavelength [8]. For real fibre trunks, where the polarisation couplings vary with time, PDL also becomes a time dependent quantity. The relevant parameter is therefore its average, either in time, or in frequency.

In this work, we show another surprising result. We present a simulation of a concatenation of highly birefringent fibres (denoted HiBi fibres) and elements with PDL (denoted PDL elements), which is such that the total DGD of the concatenation is actually zero over a whole range of frequency. This seems to imply that pulses should propagate down the concatenation without distortion [4] (if we neglect all other causes such as chromatic dispersion). However, if we simulate the propagation of pulses, we see that they may still experience

significant broadening. This is confirmed by the interferometric method, which predicts non-zero PMD, in agreement with the broadening. This result shows that the properties of the DGD alone are not enough to fully characterise the birefringence properties of an optical fibre system, at least when PDL is present.

Formalism

We recently generalised the formalism of PSP's to include cases with PDL [7]. Here we shall briefly recall some results. The two PSP's are defined as the two output states, which do not depend on the frequency, to first order. In the Jones vector formalism, this gives:

$$\partial_\omega \Psi_{out}(\omega) = \partial_\omega T \cdot T^{-1} \Psi_{out}(\omega) = -i\frac{\chi}{2}\Psi_{out}(\omega) \; ; \tag{1}$$

where ∂_ω denotes the partial derivative with respect to ω, T is the transmission matrix of the fibre link, and χ is a complex number. Therefore, the PSP's are the two eigenvectors of $\partial_\omega T \cdot T^{-1}$. The two eigenvalues are: $\chi_\pm = \pm(\delta\tau + i\eta)$, $\delta\tau$ being the group delay and η being the derivative (in frequency) of the attenuation of the PSP. This shows that, when there is no PDL, the two eigenvalues are real (no attenuation), their difference being equal to the DGD. In this case, a zero DGD really means no birefringence. However, when the fibre link has PDL, the eigenvalues becomes complex. In this case, the DGD will be zero whenever the eigenvalues are purely imaginary. As we shall see, polarisation effects may still create pulse spreading.

A simple example

As a first test, we analyse a concatenation of three elements, composed of one element with only PDL (element 2) sandwiched between two HiBi fibres (elements 1 and 3). We make the usual assumptions that the attenuation of the PDL element and the birefringence of the HiBi fibres are both independent of the wavelength. Therefore, phase and group birefringences are equal. The domain of validity of these assumptions shall set the wavelength range in which the DGD remains zero. We obtain the analytic expression for the square of the eigenvalues:

$$\chi^2 = \beta_1^2 + \beta_3^2 + 2\beta_1\beta_3\left[\cosh\alpha(\hat{e}_1\cdot\hat{e}_3) + (1-\cosh\alpha)(\hat{e}_1\cdot\hat{e}_2)(\hat{e}_2\cdot\hat{e}_3) - i\sinh\alpha\;\hat{e}_1\cdot(\hat{e}_2\times\hat{e}_3)\right], \tag{2}$$

where $\hat{e}_i$ is the axis of birefringence or PDL of element number i on the Poincaré sphere, β_1, β_3 (in ps) is the modal birefringence of elements 1 and 3, and α gives the PDL of element 2: $e^\alpha = t_{max}/t_{min}$, t_{min} and t_{max} being the transmission coefficients for the amplitude. We thus see that whenever $\hat{e}_1, \hat{e}_2, \hat{e}_3$ are in the same plane χ^2 is real, but that it can be positive (usual case), or negative, which corresponds to zero DGD. For example, if $\hat{e}_1\cdot\hat{e}_3 = -1$, $\hat{e}_1\cdot\hat{e}_2 = \hat{e}_2\cdot\hat{e}_3 = 0$, and $\beta_1 = \beta_3 \equiv \beta$, we get:

$$\chi^2 = -2\beta^2(\cosh\alpha - 1) < 0 . \tag{3}$$

This corresponds to zero DGD over the full wavelength range where our approximations (i.e. wavelength-independent birefringence and PDL) are valid. It is easy to see that the precise directions of the axes $\hat{e}_1$, $\hat{e}_2$ and $\hat{e}_3$ are not important. Negative χ^2 can be obtained for a variety of setups. However, even though the DGD is zero, the device will still cause pulse spreading. Consider a short pulse (short with respect to β_1 and β_3), propagating down the fibre. The first HiBi fibre separates the pulse into two components along $\hat{e}_1$ and $-\hat{e}_1$. When no PDL is present, the second HiBi fibre recombines the two pulses exactly. This device therefore has zero global birefringence. The effect of a PDL element can be understood as follows: a pulse polarised along direction, say $\hat{e}_1$, is decomposed along the two axes $\hat{e}_2$ (axis with attenuation) and $-\hat{e}_2$ (axis with no attenuation). The effect of the differential attenuation is to reduce the amplitude along $\hat{e}_2$, thus creating a rotation of the input polarisation. Since the two components along $\hat{e}_1$ and $-\hat{e}_1$ experience a different rotation, the second HiBi fibre cannot recombine the pulses fully. For the case under consideration, the output state is therefore composed of 3 pulses separated by β. This time-domain analysis clearly explains the pulse spreading, and the fact that it is predicted by the interferometric method.

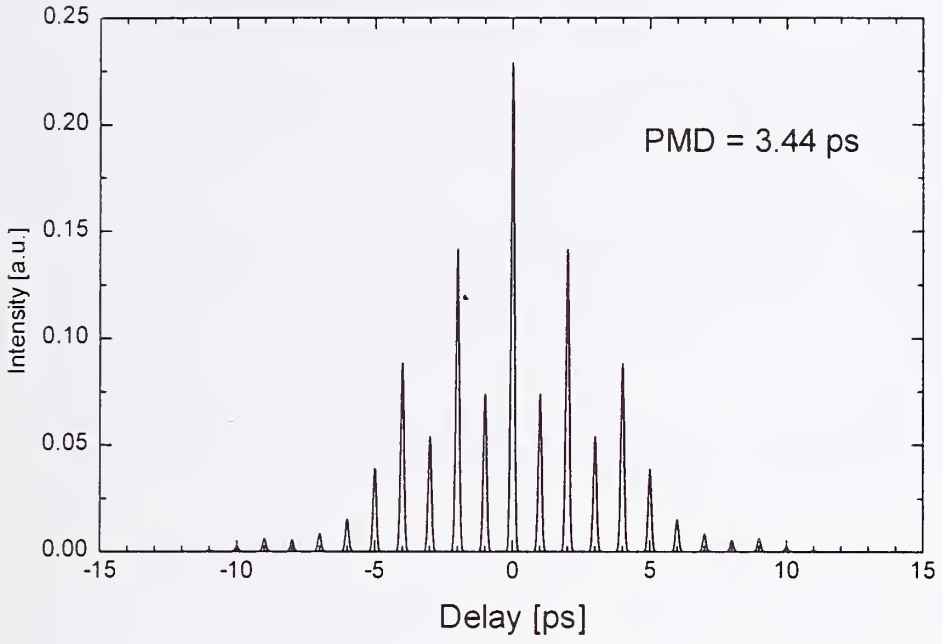

Fig.1 : Computer simulation of the interferogram.

The concatenation is made with 27 elements: 14 HiBi fibres with 1 ps DGD, and 13 PDL elements with PDL varying from 1 to 7 dB. The LED used has FWHM of 50 nm. The DGD is zero over the full frequency range of the LED (see text for details).

Computer simulations

The most interesting point is that a zero DGD can still be obtained with a much more complicated setup. In this case, we cannot continue with analytic expressions, but resort to computer simulations. We analyse a concatenation of several HiBi and PDL elements, such that the global DGD is still zero. In order to achieve this, the main requirement is that the concatenation is symmetric with respect to the central PDL element, the birefringence axis of two opposite HiBi fibres being crossed (i.e. fast to slow and vice versa). Each PDL element is sandwiched between HiBi fibres. The result of a simulation with a concatenation of 27 fibres is presented in Fig. 1 and Fig. 2. Each of the 14 HiBi fibre has 1 ps DGD, and the 13 PDL elements have PDL varying from 1 to 7 dB. These are rather high values, which were chosen to obtain a very clear effect. In Fig.1 we present the interferogram, with a 50 nm FWHM LED. We see the series of peaks separated by 1 ps each, corresponding to the 1 ps delay of each HiBi fibre. The PMD calculated from the interferogram is 3.44 ps. In Fig.2, we show the actual pulse spreading, for an input pulse with 7 ps FWHM. The output pulse has a FWHM of 7.8 ps. This is in excellent agreement with the value calculated from the interferometric PMD: $\sigma_{out} = \sqrt{\sigma_{in}^{\ 2} + (PMD)^2}$ This shows that the non-zero PMD predicted by the interferometric method is indeed translated into real pulse spreading.

Conclusion

We have shown that the two main methods for measuring PMD in birefringent fibres may give different results when applied to elements with both PMD and PDL. A concatenation may have zero DGD but may still create pulse spreading, in agreement with the interferometric method. Since this concatenation is purpose-built to generate this effect, we cannot say at present whether or not this result will have consequences for real fibres. However, the mere fact that one particular setup creates this discrepancy between the two measurement methods calls for a careful assessment of PMD characterisation when PDL is present. We are now working on making a real concatenation of fibres with zero DGD and pulse spreading, and measuring its PMD by the two methods.

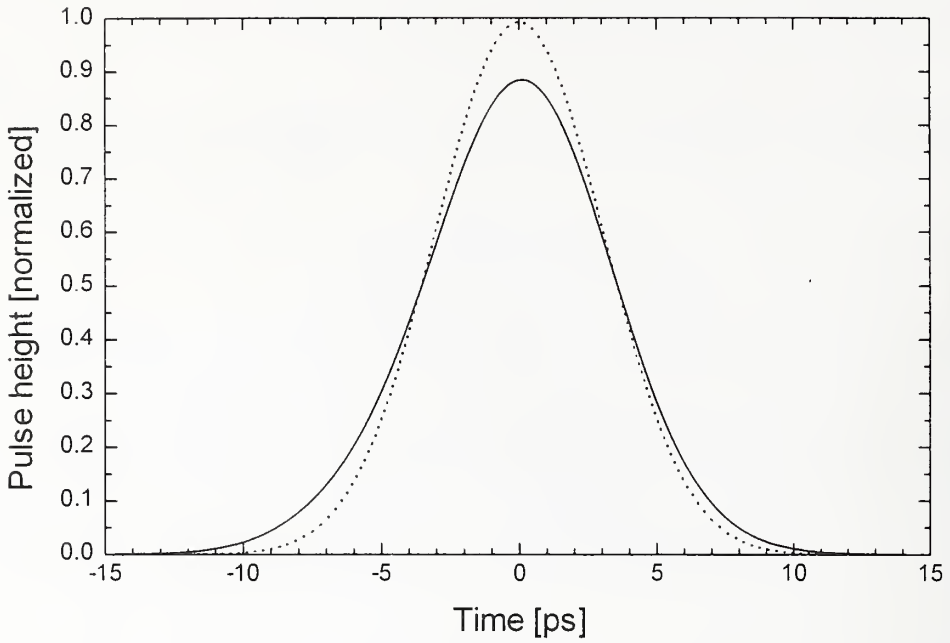

Fig.2: Computer simulation of pulse spreading

The input pulse has 7 ps FWHM, and is represented by the dotted curve. The full curve is the output pulse, which has been broadened by the concatenation. Its FWHM is 7.8 ps, in excellent agreement with the value calculated from the PMD measured with the interferometric method (see text). Again the DGD is zero over the whole frequency range of the pulse.

Acknowledgements

This work was supported by the Swiss Office Féderal de l'Education et de la Science within the COST 241 Europeen project.

References

[1] C.D. Poole and R.E. Wagner, Electron. Letts. 22, 1029 (1986).

[2] C.D. Poole and C.R. Giles, Opt. Letts. 13, 155 (1988).

[3] N. Gisin, Opt. Comm. 86, 371 (1991).

[4] B.L. Heffner, IEEE Photonics Techno. Letts. 4, 1066 (1992).

[5] N. Gisin, J.P. von der Weid and J.P. Pellaux, J. of Lightwave Techno. 9, 821 (1991).

[6] N. Gisin and J.P. Pellaux, Opt. Comm. 89, 316 (1992); B. Perny et al., Electron. Letts. 32, 680 (1996).

[7] B. Huttner and N. Gisin, Opt. Letts. 22, 504 (1997); N. Gisin and B. Huttner, Opt. Comm. 142, 119 (1997).

[8] A. Elamari et al., J. of Lightwave Techno. 16, 332 (1998).

Temperature Dependence of PMD Measurements

S. Corbeil and M. O'Sullivan
NORTEL (Northern Telecom) - Broadband Networks

Abstract - PMD correlation temperature is defined. A measurement of correlation temperature is described and values of correlation temperature are reported for various optical fibre communications components. A relationship between the correlation temperature and fibre length is empirically discovered.

I. INTRODUCTION

Polarization mode dispersion (PMD) can impair high capacity optical communication system performance. In a non-return to zero (NRZ) system, the PMD penalty is mainly due to intersymbol interference caused by a differential group delay (DGD) between the two principal states of polarization (or PSPs) associated with a single mode fibre link. The DGD of a fibre has a random value which varies over wavelength (or frequency) as well as time. The DGD distribution is usually known to be stationary at fixed temperature with a Maxwell probability density function.

The time dependence of DGD at a particular wavelength stems from environmental conditions which in turn vary with time. In particular, temperature can contribute to DGD change. To study the temperature dependence of DGD, we develop a method of measuring change in the DGD distribution.

II. THEORY

It is important to determine how temperature affects the variation of DGD. This change can be measured by slowly varying the temperature of a device and, at regular temperature intervals, measuring the DGD for a given wavelength. The correlation function of DGD over temperature can be evaluated as in (1):

$$C_{T,\lambda_0}(\Delta T) = \frac{\int_0^\infty (\Delta\tau(\lambda_0, T) - \overline{\Delta\tau})(\Delta\tau(\lambda_0, T + \Delta T) - \overline{\Delta\tau})dT}{\int_0^\infty (\Delta\tau(\lambda_0, T) - \overline{\Delta\tau})^2 dT} \quad (1)$$

Of course, an infinite temperature range cannot practically be achieved. In addition, multiple DGD values over a given wavelength range are usually obtained at each value of ΔT. The fact that the DGD process is stationary enables the DGD-temperature correlations to be averaged over an entire range of wavelengths to compensate for the loss of accuracy due to the limited temperature integral range in (1). Equations (1) and (2) are expected to have the same result:

$$C_T(\Delta T) = \frac{\int_0^\infty \int_0^\infty (\Delta\tau(\lambda, T) - \overline{\Delta\tau})(\Delta\tau(\lambda, T + \Delta T) - \overline{\Delta\tau})d\lambda dT}{\int_0^\infty \int_0^\infty (\Delta\tau(\lambda, T) - \overline{\Delta\tau})^2 d\lambda dT} \quad (2)$$

In practice, the integral ranges in (2) are replaced by the finite range of T and λ over which DGD measurements are taken.

The correlation temperature T_c separating independent instances of PMD is defined to be the full-width at half-maximum (FWHM) of the temperature correlation function $C_T(\Delta T)$. Figure 1 denotes an example temperature correlation function. (Figure 1 here).

III. EXPERIMENTAL SETUP

Using the Jones-Matrix Eigenanalysis (JME) measurement technique, an HP-8509 polarization analyzer was used to obtain DGD samples of various optical fibre devices, as described in Figure 2. Dispersion compensating modules (DCMs), an erbium doped fibre amplifier (EDFA), and several spans of single mode fibre (SMF) were measured. (Figure 2 here).

The samples were placed in an environmental chamber. For each device, the temperature in the oven was set to a value above the ambient temperature in the lab, and the device was allowed to soak until the temperature was approximately constant throughout. For this purpose, a control sample was used consisting of a tightly wound spool of SMF, with a thermocouple taped to the outside circumference. Another thermocouple was taped to the inside of the spool, where no air was permitted to circulate. The control sample was placed at an equal distance from the heat source as any other device, as shown in Figure 3. The average temperature of any device was taken to be the average of the two thermocouple readings. (Figure 3 here).

Allowing the temperature to relax towards ambient temperature in a controlled and incremental fashion, JME measurements over constant wavelength ranges were performed, recording the inner and outer temperatures at the start and end of each measurement (each JME measurement lasts in the order of several minutes). The scans of DGD over wavelength were then correlated two-by-two, and plotted against the

difference in average temperature between the two scans. The plot was then averaged over finite temperature ranges, and values of FWHM were obtained for each device. The stationarity at a given temperature was measured and ascertained for each device, with the knowledge of the expected variance on the mean given in [3].

IV. RESULTS and DISCUSSION

The correlation temperatures are tabulated in Table 1, along with the length of fibre in each device.

Table 1. Device Correlation Temperatures

Component	Fibre Length	Temperature Correlation (FWHM)
EDFA	10m	96°C
DCF	1000m	12°C
DCM	7000m	3.4°C
SMF	20,000m	2.2°C
SMF	80,000m	1.0°C

A logarithmic plot of T_c vs. l is shown in Figure 4 and appears to support a relation between the two: (Figure 4 here).

$$T_c \approx \frac{334}{\sqrt{l}} \quad (3)$$

Although the PMD instance changes when ΔT exceeds the correlation temperature, the stationarity of the random process may be at risk. Two different behaviours were noted in the samples measured above. In the DCMs, the mean DGDs of all measurements within the temperature range (-5 - 65°C) did not significantly differ: the DGD was stationary over the entire temperature range. On the other hand, the mean DGDs of the SMF spans showed a deterministic temperature dependence. If the primary objective is to determine with some accuracy the mean DGD of a particular device, all DGD measurements must be conducted in a regime where the DGD process is stationary. The generation of an independent instance of PMD can then be done through the use of temperature excursions returning to the constant measurement temperature, rather than simply increasing or decreasing the temperature by the correlation temperature.

V. CONCLUSION

The PMD correlation temperature was defined and measured for DCMs, lengths of SMF and an EDFA. The correlation temperature is empirically proportional to the square root of the length of the optical fibre device.

ACKNOWLEDGEMENTS

The work and use of equipment and facilities would not have been possible without T. Taraschuk, K. Visvanatha, and D. Atkinson. Acknowledgement also goes to P. Galko for helpful input.

REFERENCES

[1] C.D. Poole, R.W. Tkach, A.R. Chraplyvy, and D.A. Fishman, "Fading in Lightwave Systems Due to Polarization-Mode Dispersion," IEEE Photonics Technology Letters, vol. 3-1, pp. 68-70, Jan. 1991.

[2] F. Bruyere, "Impact of First- and Second-Order PMD in Optical Digital Transmission Systems," Optical Fiber Technology, vol 2, pp. 269-280, 1996.

[3] N. Gisin, B. Gisin, J.P. Von der Weid, and R. Passy, "How Accurately Can One Measure a Statistical Quantity Like Polarization-Mode Dispersion?," IEEE Photonics Technology Letters, vol. 8-12, pp. 1671-1673, Dec. 1996.

[4] C.D. Poole, J.H. Winters, and J.A. Nagel, "Dynamical equation for polarization dispersion," Optics Letters, vol. 16-6, pp. 372-374, Mar. 1991.

[5] B.W. Hakki, "Polarization Mode Dispersion in a Single Mode Fiber," Journal of Lightwave Technology, vol. 14-10, pp. 2202-2208, Oct. 1996.

[6] H. Bulow and G. Veith, "Temporal Dynamics of Error-Rate Degradation Induced by Polarisation Mode Dispersion Fluctuations of a Field Fiber Link," presented at 11th International Optics and Optical fibre Communication - 23rd European Conf. on Optical Communications, IOOC-ECOC 1997, Conf. Publ. No. 448, 1997, pp 115-18.

Figure 1.Temperature Correlation Function of a Dispersion Compensating Module

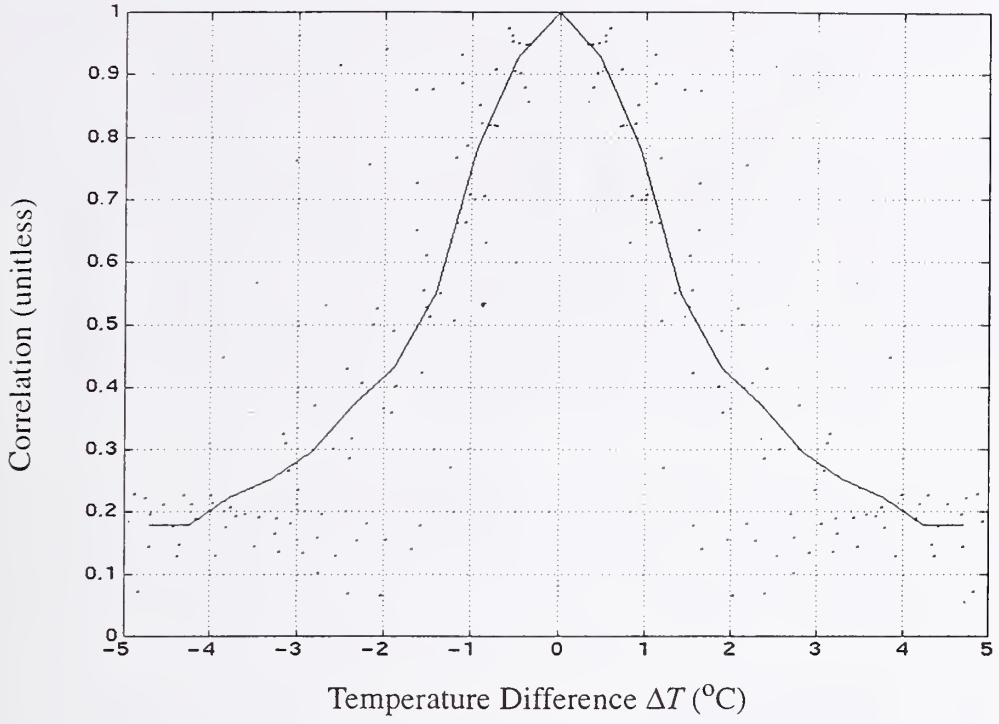

Figure 2. Experimental Setup

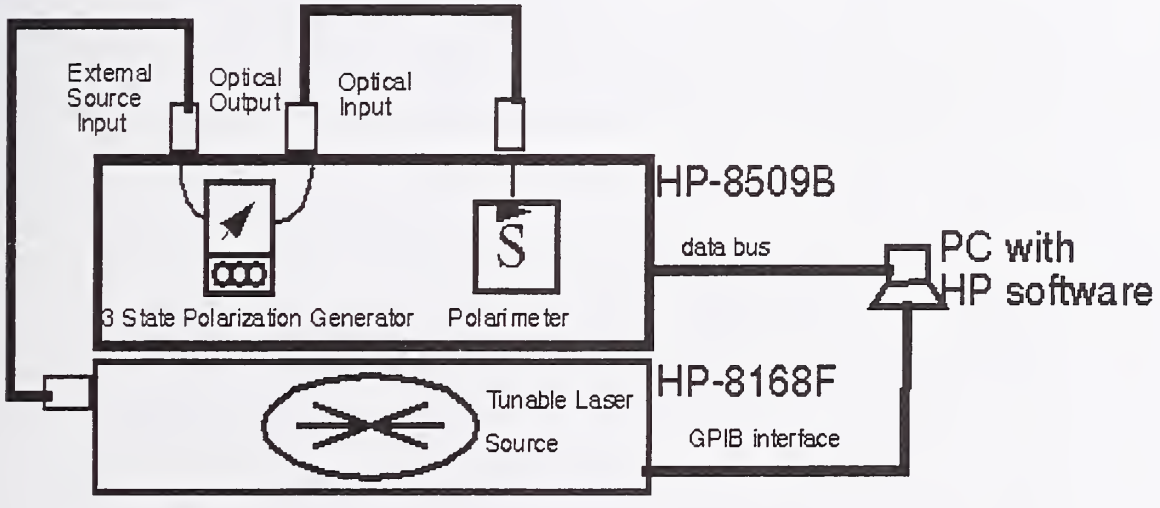

Figure 3. Oven Chamber Layout

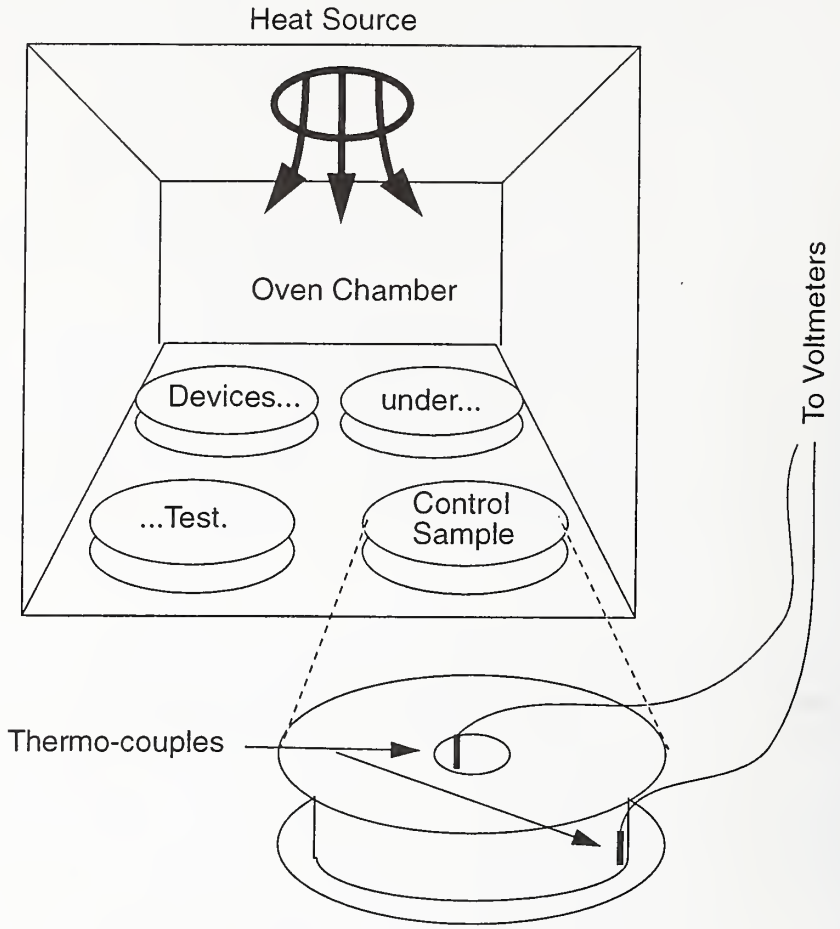

Figure 4.Correlation Temperature vs. Device Length

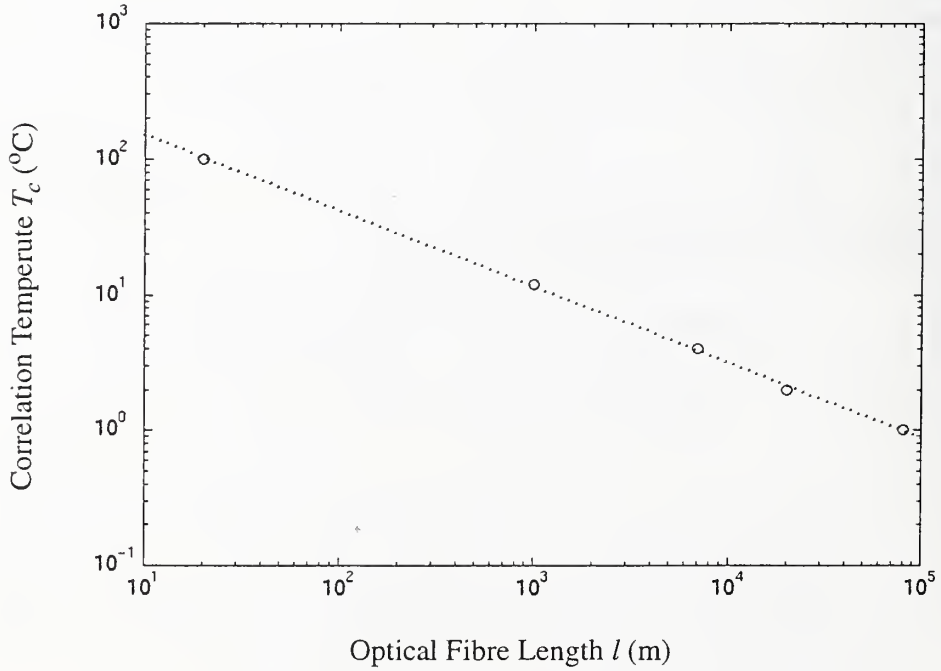

Measurement of Two Dimensional Axial Stress Profiles of Optical Fibres with High Spatial Resolution

K W Raine* and A J Parker**

* K&V Optics. UK. ** National Physical Laboratory. UK.

Introduction

At the 1997 OFMC conference[1], Raine described an instrument developed to measure birefringent retardation profiles, and hence axial stress profiles, in optical fibres with high spatial resolution and low noise. This instrument has now been modified to measure 2D and 3D profiles without the assumption of circular symmetry. The technique enables each full width retardation profile to be obtained in a few seconds. At present the spatial resolution has been limited to 0.8 μm but will be improved when a CCD camera with more pixels has been added. In this paper we present the axial stress profile of a polarization maintaining fibre in order to demonstrate the performance of the instrument and describe the practical and numerical challenges that had to be overcome.

Instrumentation

The instrument was described in detail at the 1997 OFM conference[1], and consists of a reversed strain viewer attached to a transmission microscope. Use of the half shadow[2,3], or half shade, principle leads to a linear birefringent phase profile free of the square terms of intensity and many of the background birefringent phase differences due to component imperfections[1]. The half shade device was originally formed by using a mica half-wave plate on axis, covering half of the beam only, and a polarizer rotated by the required half shade angle (H) as described by Laraunt[2] in 1880. The edge of the wave plate was focused into the plane of the fibre using the microscope condenser. The intensity profiles on each side were measured by an electronic system designed to sample two vertical lines from the TV image. For 3D work it is not possible to set up the same part of the image on the two sampling lines. Even in 2D work some care has to be taken to ensure correct image registration. To overcome this the half shade boundary was replaced by a time-modulation of the direction of the input polarization. This was conveniently achieved by use of a Faraday modulator consisting of a coil, of about two hundred turns, surrounding a cylindrical SF57 glass core about 10 cm long. Anti-reflection coatings were applied to both ends of the core. Multiple reflections need to be suppressed because the Faraday effect is additive and changes in the length of core due to temperature changes, lead to unwanted modulations. The modulator was able to produce up to a few degrees of modulation using a 50 Watt power amplifier. A one degree modulation was chosen for this work. The angle of polarization rotation produced by the Faraday modulator was controlled by the same computer used to acquire and analyse the video image. These modulators have very low noise making it possible to measure polarization angles as small as 0.1 arc sec[4], for precise measurement they are usually preferable to other modulators[4].

The two signals ($I_{\pm}$) obtained with each direction of Faraday cell modulation are shown for small angles, in the equation below:

$$I_{\pm} \propto [\pm H + 0.5u\delta + \theta + 0.5\beta]^2$$

Here H is the half shade angle, δ is the birefringent phase difference, θ is the angular rotation of the quarter-wave plate, u is $\pm$ 1 depending on the orientation of the quarter-wave plate axes. Similarly β is the rotation of a second half-wave plate. The difference between the two signals (ΔI) is proportional to the retardation profile and is free of squared terms present in each signal. It is given approximately by:

$$\Delta I \propto uH\delta + 2H\theta + H\beta.$$

Calibration of the retardation profile can therefore be achieved by measured rotations, θ or β, of the quarter-wave plate or half-wave plate respectively. The calibration profile contains cross-products between the rotations θ and β and background phases, which are nearly identical to those formed with the sample birefringence[1]; for simplicity these are not shown in equation above. The calibration therefore corrects some phase errors. Similarly a change in the sign of u reverses the sign of the signal but not signals arising from background phase imperfections and the effective birefringence of the aluminised mirror. This too, can therefore be used to remove instrumental phase

errors[1]. Alternatively, if the half-wave plate is used for calibration, a measured background phase profile must be subtracted to remove background phase errors. The advantage in using the half-wave plate is that only one measurement of the sample is needed, which is desirable when many views of the sample are required. The disadvantage is that the calibration uncertainty is increased. Thus the method and measurement procedures allow phases as small as 0.005° to be detected in the presence of background phases many times greater[1]. A more complete description of the instrument will be published later.

As can be seen in figure 1 the Faraday effect modulator was placed after the polarizer in the weakly focused beam. At the point of entry the beam diameter was smaller than the core diameter, so all of the light was guided by the core. The core was supported on two narrow rings, about 1 mm wide, near to the ends, to minimise losses due to frustrated internal reflection.

Prior to sampling the polarized images an additional polarizer, not shown in figure 1, is temporarily placed between the instrument polarizer and the Faraday modulator then aligned nearly parallel to the transmission axis of the analyser. This removes the polarization sensitivity and the resultant intensity profile can then be used to normalise the phase profiles for the intensity distribution of the illumination. It is also possible to remove the polarization sensitivity from the image by making measurements with zero modulation angle. However, this produces low signal values making the normalisation process too noisy.

The numerical aperture of the objective was 0.5 and the condenser was set to have an effective numerical aperture of 0.3. The analyser was high quality polarizing sheet that had a negligible effect on the wavefront.

It was necessary to rotate the fibre to generate different projections to form the 2D axial stress profile from the 2D phase profile. This leads to some practical problems. As a rough guide the axis of rotation should not move by more than about one tenth of the spatial resolution if artefacts from the transform are to be avoided[5]. This amounts to approximately 0.1μm for the instrument described here. The fibre must also rotate uniformly with no stiction. Alternatively if measurements are made through 360° instead of 180°, the apparent sampling redundancy can be used to remove the artefacts though this produces a profile with an apparent poor focus[5].

The coated part of the fibre was fixed into a thin steel tube that was connected to a computer-controlled rotation stage. The bare fibre was passed through two ceramic ST fibre connector ferrules whose coned ends were approximately 11 mm apart. These were located in two aligned 'V' grooves. The steel tube rotated in a plain bearing. The free part of the fibre passed over a small section of microscope slide. A glass cover slip was positioned above the fibre but not touching it. The fibre was surrounded in a silica index matching fluid. Movement of the fibre axis can be observed directly if there is stress at the outer edge of the cladding. Sticking and twisting of the fibre can also be monitored by watching the movement of small particles of dirt on the fibre surface.

Results

As a trial run, a bow-tie polarization maintaining fibre was measured by taking 144 projections around the full 360° rotation, each having a spatial sampling interval of 0.5 μm. Each projection was made by averaging 30 camera frames and over 12 pixels (6 μm) along the axis of the fibre, i.e. perpendicular to the sampling direction; each projection thus took a few seconds to measure.

The retardation data was analysed in two 180° sections using a least squares iterative technique[6]. The individual retardation profiles were numerically centred using the edges of the fibre, assuming that the fibre was elliptical. The second 180° data set was used to average out any remaining errors[5]. The optimum number of iterations was gauged by comparing the retardation profile, calculated from the transformed stress profile, with the measured retardation profile. Allowing the iterative process to go on too long can lead to the enhancing of noise due to rounding errors. The results are shown in figures 2, 3 and 4. The axial stress profiles show less than 2 MPa noise for the cladding, increasing to 5 MPa at the core centre. The core of the fibre is resolved. A value of 3.5×10^{-6} MPa^{-1} was used for the photo-elastic constant.

In this case the fibre centre only moved by about 1.5 μm, but movements of 10 μm have been observed during other measurements. Cleanliness of the fibre and ferrules as well as the correct selection of fibre ferrule internal diameter

are important to enable smooth rotation of the fibre and prevent fibre twist. As can be seen in figure 5 the effect of using uncentred data is to increase the noise, especially in the centre of the profile and introduce artefacts in the calculated stress profile. The exaggerated extension of the compression at the edge of the bow tie is probably due to decentring.

Care must be taken in quoting a spatial resolution as it will depend on the numerical aperture of the objective and condenser in a complicated way. The off-axis rays within the numerical aperture of the objective are effectively making different projections, with different retardations, which will be averaged out in the image. For example, this will have the effect of smoothing out sharp features. We intend to model this effect so that the effective spatial resolution can be estimated for given numerical apertures assuming optimum sampling intervals.

The use of alternative techniques for analysing the data, specifically the Back Projection Fourier Transform method[6] will also be investigated.

Conclusion

An instrument for measuring the 2 dimensional stress profiles of optical fibres has been presented. It offers increased spatial resolution, reduced noise and efficient data collection compared with other published methods. At this early stage we cannot estimate the overall uncertainty of the measurements and transformations as sources of systematic errors have yet to be fully investigated.

1 K W Raine. 'A microscope for measuring axial stress profiles with high spatial resolution and low noise'. Proc. 4th Optical Fibre Measurement Conference (NPL Teddington UK), 269, (1997)

2 R S Longhurst, 'Geometrical and Physical Optics', Longmans, 1964, p485

3 C J Koerster, "Optimum half shade angle in polarizing instruments.", J. Opt. Soc. Am, 49 (6), 556 (1959)

4 R J King and K W Raine, 'Polarimetry applied to alignment and angle measurement' Optical Engineering, 20, p39, 1980

5 The Image Processing Handbook Chap. 12, Second Ed. John C. Russ. CRC Press 1995.

6 Three-dimensional Reconstruction in Nuclear Medicine Emission Imaging. T.F. Budinger and G.T. Gullberg, IEEE Transactions on Nuclear Science Vol. NS-21, June 1974. pp2-20.

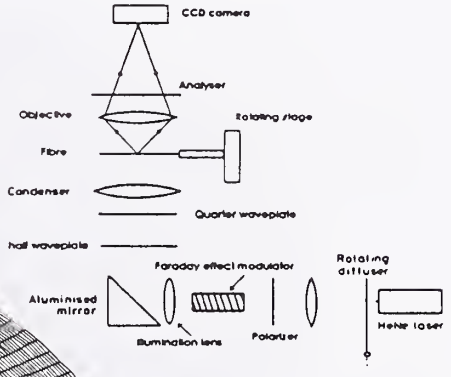

Figure 1. Schematic diagram of the instrument

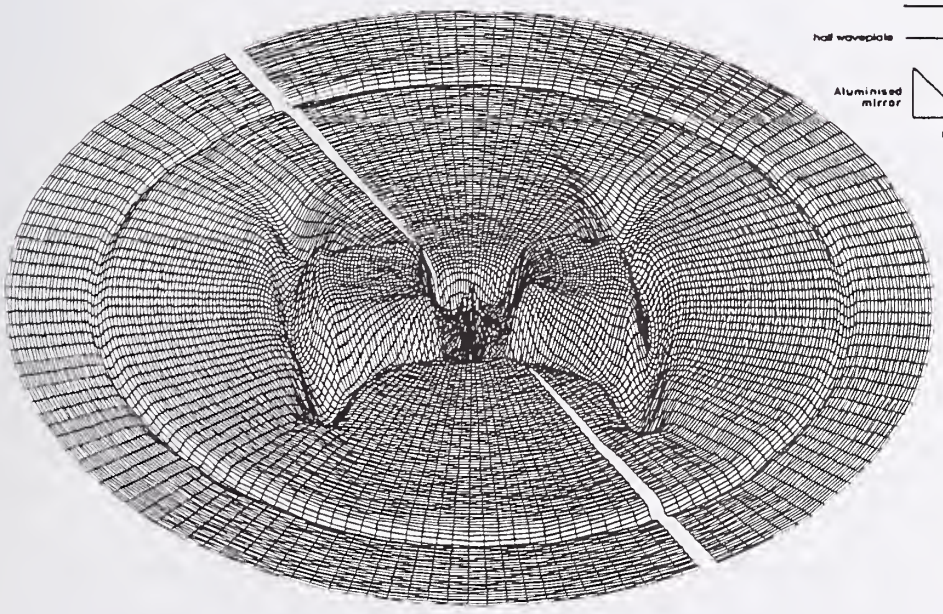

Figure 2 Axial stress profile obtained from measurements over 360°. Maximum stress value about 80 MPa.

Figure 3. As figure 2 but viewed from other side showing compressive axial stresses. Maximum values about -100 MPa.

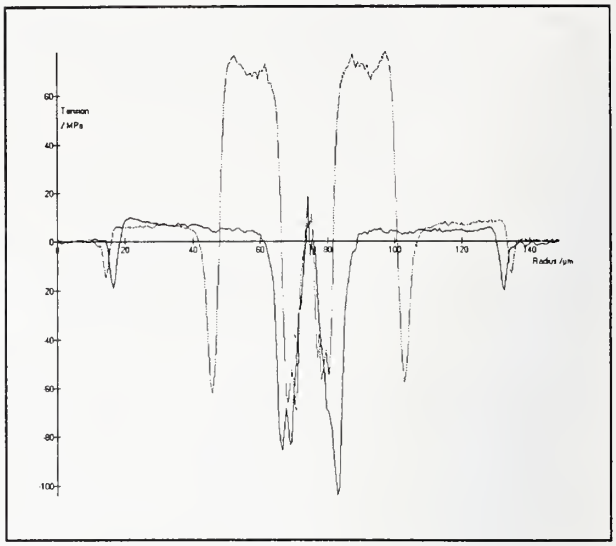

Figure 4. Two orthogonal axial stress profiles taken from figure 2.

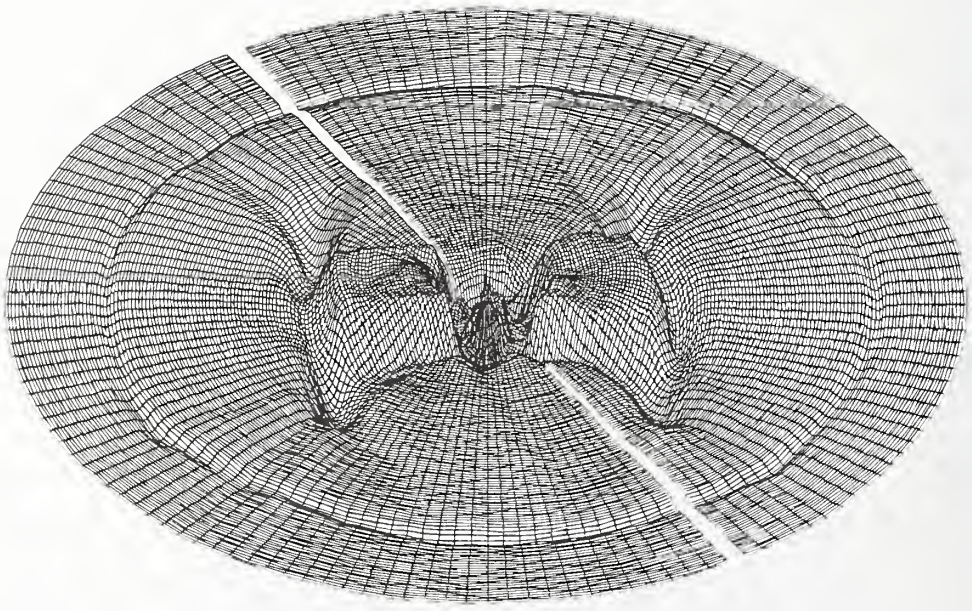

Figure 5. Axial stress profile calculated from uncentred data taken from projections over 180 degrees.

Biased perturbation method for index profiling single-mode fibers from near-field and far-field data

N. H. Fontaine and M. Young
Optoelectronics Division 815.02, National Institute of Standards and Technology, 325 Broadway, Boulder, CO 80303

We have developed a biased perturbation method for calculating the index profiles of single-mode fibers from either near-field or far-field data. Unlike other perturbation and direct inversion methods, which require smoothing of the near-field data, our method works by smoothing the perturbation. This biased perturbation method minimizes the loss of resolution and distortion at large radii and forces the index profile to converge to the cladding index. We have compared index profiles with those measured by the refracted near-field method, showing agreement within $\Delta n \approx 0.0005$ from the fiber axis to a radius of 20 μm.

THEORY

Under weakly guiding conditions the mode-field of a single-mode waveguide is closely described by the scalar wave equation [1]. The square of the refractive index profile $n_i^2 \equiv [n(\vec{r_i})]^2$ of the guide may be determined from a discrete set of near-field data $u_i \equiv u(\vec{r_i})$ by direct inversion of the discrete wave equation [2]

$$\nabla_i^2 u_i + (k^2 n_i^2 - \beta^2) u_i = 0 \qquad \longrightarrow \qquad n_i^2 = \frac{\beta^2}{k^2} - \frac{1}{k^2 u_i} \nabla_i^2 u_i. \tag{1}$$

The mode-field u_i is the square root of the measured intensity $\pm\sqrt{I(r_i)}$, β is the propagation constant, and ∇_i^2 is the discrete form of the Laplacian ∇^2 at the point $\vec{r_i}$. The discrete Laplacian $\nabla_i^2 u_i$ is very sensitive to noise and spatial measurement errors of the field u_i, which are amplified in the term $\nabla_i^2 u_i / u_i$ wherever u_i nears 0. The amplification of errors results in large fluctuations of the index profile [2-4]. Frequently, the near-field data u_i are smoothed to reduce the effects of errors on the $\nabla_i^2 u_i$ term [3-5]. However, smoothing the near-field data u_i can diminish the spatial resolution and distort and bias the index profile. The direct inversion method also requires a separate determination of the propagation constant β. While β shifts n_i^2 [4,6], it both shifts and scales the index n_i as [3]

$$n_i = \sqrt{\frac{\beta^2}{k^2} - \frac{1}{k^2 u_i} \nabla_i^2 u_i} \approx \frac{\beta}{k} - \frac{1}{2\beta k u_i} \nabla_i^2 u_i. \tag{2}$$

In principle, β may be determined by making the index profile equal to that of the cladding index at large radii. However the index fluctuations make this determination very difficult.

The perturbation mode-field [4,6] is formed by writing u_i as a trial function $E_{0,i}$ plus a sum of increasing mth-order perturbed fields $E_{m,i}$: $u_i = \gamma^0 E_{0,i} + \gamma^1 E_{1,i} + \gamma^2 E_{2,i} + \ldots$ The material parameter n_i^2 and propagation constant β are expanded as $n_i^2 = \gamma^0 n_{0,i}^2 + \gamma^1 n_{1,i}^2 + \gamma^2 n_{2,i}^2 + \ldots$ and $\beta^2 = \gamma^0 \beta_0^2 + \gamma^1 \beta_1^2 + \gamma^2 \beta_2^2 + \ldots$, repectively. Substitution of the expansions into the wave equation of Eq. (1) and separating powers of γ gives to first order

$$\gamma^0 : n_{0,i}^2 = \frac{\beta_0^2}{k^2} - \frac{1}{k^2 E_{0,i}} \nabla_i^2 E_{0,i} \quad \text{and} \quad \gamma^1 : n_{1,i}^2 = \frac{\beta_1^2}{k^2} + \frac{(E_{1,i} \nabla_i^2 E_{0,i} - E_{0,i} \nabla_i^2 E_{1,i})}{k^2 E_{0,i}^2}. \tag{3}$$

The trial function $E_{0,i}$ is determined by solving a simplified wave equation using *a priori* knowledge of the approximate form of the trial index profile $n_{0,i}$. The constant β_0 is determined by analytical methods, such as solving a characteristic equation for the mode-field.

The first-order field is the difference $E_{1,i} = u_i - E_{0,i}$ between the data and the trial function, which makes the perturbation term

$$\gamma^1 : n_{1,i}^2 = \frac{\beta_1^2}{k^2} + \frac{1}{k^2 E_{0,i}^2}\left(u_i \nabla_i^2 E_{0,i} - E_{0,i}\nabla_i^2 u_i\right). \tag{4}$$

Choosing the measured data as the trial mode-field ($E_{0,i} = u_i$) reduces the perturbation method to the direct inversion method. Therefore, if it were possible to obtain noise and error free data and to determine β, a perturbation method with $E_{0,i} \neq u_i$ could never lead to an index profile with greater accuracy than that obtained by direct inversion.

APPLICATION TO SINGLE-MODE FIBERS

We sought to compare the 1-dimensional direct inversion and perturbation methods to the index profile obtained by the refracted near-field method on a single-mode fiber [7]. We measured the far-field diffraction pattern of a single mode-fiber at a wavelength of 1.310 μm and Hankel-transformed these data to the near-field u_i [8]. We measured the index profile of a similar fiber by the refracted near-field method at 0.635 μm. The *concentration*-dependent dispersion was determined by Sellmeier's equation to be 0.00025 greater at 0.635 μm than at 1.310 μm when the dopant concentrations changed from 0 to 13.5 mole% GeO_2 in SiO_2 [9]. We ignored this small correction to the index and simply shifted the entire index profile measured with the refracted near-field method at 0.635 μm to match the SiO_2 cladding index of $n_B = 1.4468$ at 1.310 μm.

We constructed a simple trial field $E_{0,i}$ by matching the step-index solutions $AJ_0(\kappa_A r)$ for $r \leq a$ and $BK_0(\kappa_B r)$ for $r \geq a$ and their slopes at the core/cladding boundary $r = a$. The constants κ are $\kappa_{A,B} = \sqrt{|k^2 n_{A,B}^2 - \beta_0^2|}$. The trial function was determined by: choosing trial parameters $\{n_A, r = a\}$ and finding the effective propagation constant β_0 that minimized the characteristic equation

$$C = \frac{K_0(\kappa_B r)\partial J_0(\kappa_A r)/\partial r - J_0(\kappa_A r)\partial K_0(\kappa_B r)/\partial r}{K_0(\kappa_B r)\partial I_0(\kappa_A r)/\partial r - I_0(\kappa_A r)\partial K_0(\kappa_B r)/\partial r} \qquad \text{at } r = a; \tag{5}$$

using the value of β_0 to match the solution at the boundary

$$B = A\frac{I_0(\kappa_B r)\partial J_0(\kappa_A r)/\partial r - J_0(\kappa_A r)\partial I_0(\kappa_B r)/\partial r}{K_0(\kappa_B r)\partial I_0(\kappa_A r)/\partial r - I_0(\kappa_A r)\partial K_0(\kappa_B r)/\partial r} \qquad \text{at } r = a; \tag{6}$$

repeating the process to diminish the error $\sigma = \sum_i |E_{1,i}|^2$ as much as possible (Fig. 1(a)). The zeroth-order perturbation, first-order perturbation, and direct inversion solutions for the index profile are shown in Figure 1(b). The Hankel transformation of the discrete far-field data set introduced oscillations in u_i, and these were transferred to the index profile. The error was amplified as $|u_i|$ (and $|E_{0,i}|$) decreased.

BIASED PERTURBATION METHOD

Since the trial function $E_{0,i}$ of the perturbation method was piecewise analytic and independent of fluctuations in the data, $n_{0,i}^2$ was piecewise analytic and independent of fluctuations as well. Therefore, the perturbation term $n_{1,i}^2$ contained all of the errors due to the measurement and the far-field transformation. We smoothed the perturbation term $n_{1,i}^2$ and forced it to converge to 0 for large r_i by adding a small positive bias δ_i to the denominator in Eq. (4): $E_{0,i}^2 \longrightarrow E_{0,i}^2 + \delta_i$. The bias term was $\delta_i = 0$ for $r_i < 4.5$ μm and

$\delta_i = 0.01$ for $r_i \geq 4.5$ μm. We compared the index profile computed from the biased direct inversion and biased perturbation solutions

$$\begin{aligned} \text{biased direct inversion:} \quad & n_i^2 = \frac{\beta^2}{k^2} - \frac{1}{k^2 u_i + \delta_i} \nabla_i^2 u_i, \\ \text{biased perturbation:} \quad & n_{0,i}^2 = \frac{\beta_0^2}{k^2} - \frac{1}{k^2 E_{0,i}} \nabla_i^2 E_{0,i}, \\ & n_{1,i}^2 = \frac{\beta_1^2}{k^2} + \frac{1}{k^2 E_{0,i}^2 + \delta_i} \left(u_i \nabla_i^2 E_{0,i} - E_{0,i} \nabla_i^2 u_i \right), \text{ with } \beta_1 = 0. \end{aligned} \tag{7}$$

The biased direct inversion method greatly distorted the index profile in the cladding and did not converge to the cladding index (Fig. 2(a)). The biased perturbation method, however, smoothed the Hankel-transformation error and forced the index to converge to that of the cladding (Fig. 2(b)). The biased perturbation result agrees with the refracted near-field measurement within $\Delta n_i \lesssim 0.0005$ for $0 \leq r_i \leq 20$ μm. The remaining fluctuations can be reduced in the biased perturbation method by increasing δ_i at the expense of distorting the perturbation contribution to the index profile.

CONCLUSIONS

The perturbation method can be superior to the direct inversion method when smoothing is applied to the perturbation term $n_{1,i}^2$. The biased perturbation method is superior to both the direct inversion and unbiased perturbation methods because the index profile n_i can be forced to converge to the cladding index. Far-field diffraction data may be used to obtain very accurate index profiles of single-mode fibers. In addition to the work presented here, we have also shown through simulations that the biased perturbation method will substantially reduce the effects of noise in the mode-field measurement on the calculated index profiles. We plan to extend these analytical methods to two dimensions to enable calculation of the transverse index profiles of rectangular waveguides from two-dimensional far-field data.

REFERENCES

[1] C. Yeh, L. Casperson, and W. P. Brown, "Scalar-wave approach for single-mode inhomogeneous fiber problems," Appl. Phys. Lett., 34(7) 460–462, 1979.

[2] Leon McCaughan and Ernest E. Bergmann, "Index Distribution of Optical Waveguides from Their Mode Profile," J. Lightwave Technol., LT-1(1) 241–244, 1983.

[3] Jochen Helms, Joachim Schmidtchen, Bernd Schüppert, and Klaus Petermann, "Error Analysis for Refractive-Index Profile Determination from Near-Field Measurements," J. Lightwave Technol., 8(5) 625–633, 1990.

[4] Katsumi Morishita, "Refractive-Index-Profile Determination of Single-mode Optical Fibers by a Propagation Mode Near-field Scanning Technique," J. Lightwave Technol., LT-1(3) 445–449, 1983.

[5] I. Mansour and F. Caccavale, "An Improved Procedure to Calculate the Refractive Index Profile from the Measured Near-Field Intensity," J. Lightwave Technol., 14(3) 423–428, 1996.

[6] G. L. Yip, P. C. Noutsios, and L. Chen, "Improved propagation-mode near-field method for refractive-index profiling of optical waveguides," Appl. Opt., 35(1) 2060–2068, 1996.

[7] M. Young, "Optical fiber index profiles by the refracted-ray method," Appl. Opt., 20(19) 3415–3422, 1981.

[8] M. Young, "Mode-Field Diameter of Single-Mode Optical Fiber by Far-Field Scanning," Appl. Opt., (in press).

[9] J. W. Fleming, "Material and Mode Dispersion in GeO_2·B_2O_3·SiO_2 Glasses," J. Amer. Ceram. Soc., 59(11–12) 503–507, 1976.

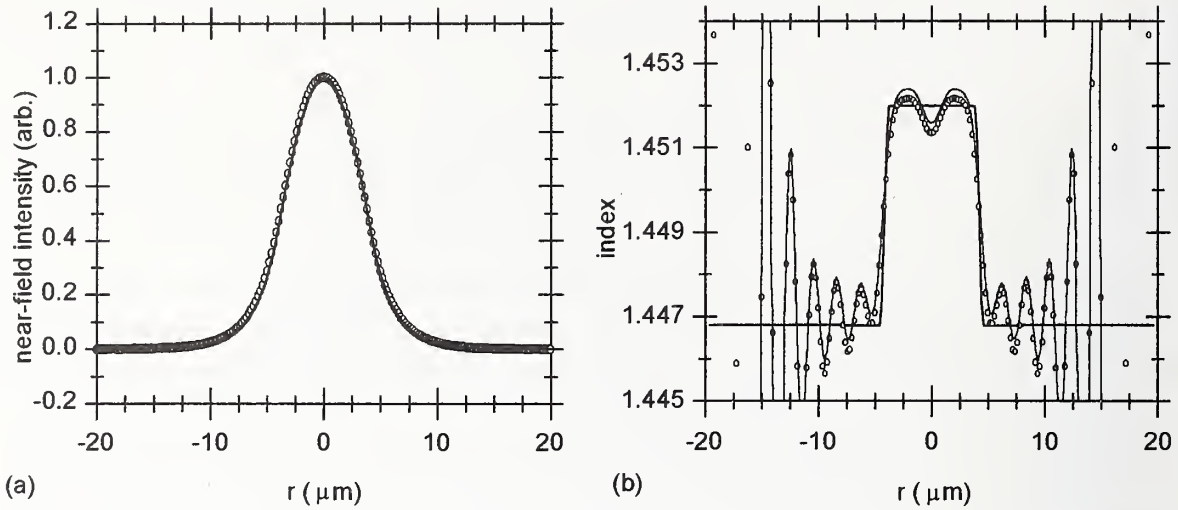

Figure 1(a). Far-field data Hankel-transformed to the near-field u_i (circles) and the trial function $E_{0,i}$ determined by iterative fitting on the parameters $\{n_A, a\}$ (solid line). We used the fused silica index $n_B = 1.4468$ at 1.310 μm. We determined the effective propagation constant $\beta_0 = 6.953\ \mu m^{-1}$, the effective core index $n_A = 1.4520$, and the effective core-cladding boundary $a = 4.177\ \mu$m when fitting the trial function to the mode-field. (b) Zeroth-order step-index profile $n_{0,i}$ (straight lines) calculated from the trial mode field $E_{0,i}$. The perturbation method (circles) gives a similar index profile to that of the direct inversion method (solid curve). The direct inversion method does not determine β, leading to an unknown shift of β/k and scaling of $1/(2\beta k)$. Here we have chosen a value of $\beta = 6.954\ \mu m^{-1}$.

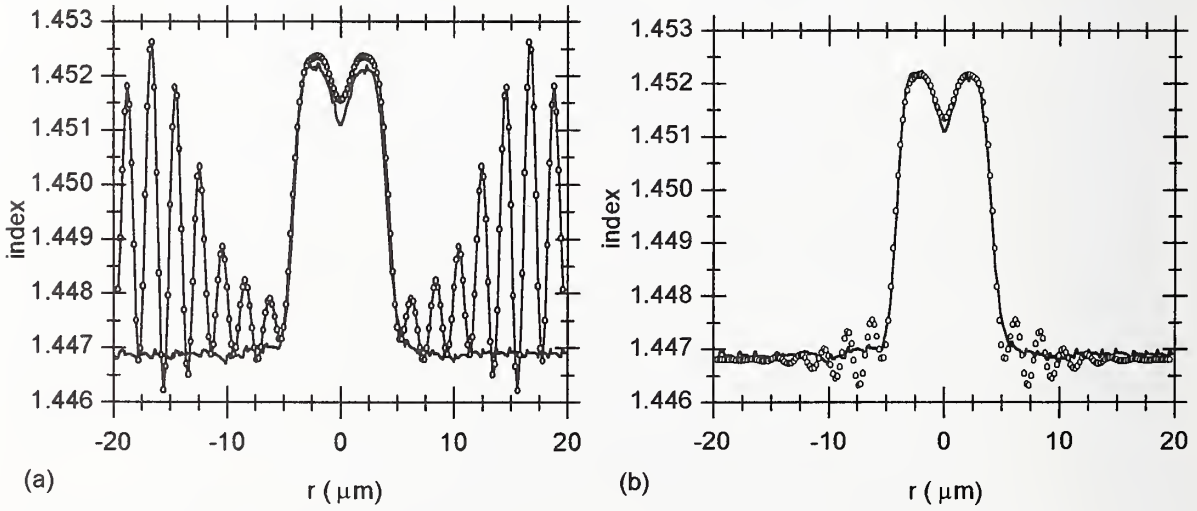

Figure 2 (a). Biased direct inversion method (connected circles) and the refracted near-field data (solid curve). Biasing fails to force convergence and distorts the index profile in the cladding. (b) Biased perturbation method (circles) and the refracted near-field data (solid curve). The index profile is smoothed and converges to that of the cladding index.

High precision fiber group refractive index measurement using an interferometric method

Gisella Marradi, Pier Giuseppe Peretta, Susanna Cattelan
SIRTI S.p.A. Cables and Optical Technologies
Via E. Fermi, 2-20060 Cassina de' Pecchi (MI)- ITALY

Abstract: Using high spatial resolution and large dynamic range Optical Low Coherence Reflectometry (OLCR), group refractive index can be determined by precisely measuring light optical path difference between a test fibre sample and a reference one.

1. Introduction

Using high spatial resolution and large dynamic range Optical Low Coherence Reflectometry (OLCR), group refractive index n_g can be determined for the fibers which n_g unknown is. Group refractive index is an interesting parameter who allows us to measure the light optical path in a fiber and therefore its geometrical lenght.
In the following pages our relative measurement procedure is described: group refractive index n_g is obtained comparing the light optical path between a test fiber sample and a reference one.

2. Theory

In this section the theory on which the technique we used to measure n_g is based and the error analysis are described.
Our aim was to measure the group refractive index n_g of an l_1 lenght fiber using a knwon refractive index n_2 of l_2 lenght standard SMR fiber as a reference.
Using an OLCR device is possible to measure the light optical path x in a fiber.
Refering to the reference fiber we obtain :

$$x_2 = l_2 \cdot n_2 \qquad (1)$$

Refering to a test fiber:

$$x_1 = l_1 n_g \qquad (2)$$

Combining equations (1) and (2) we obtain:

$$n_g = n_2 \cdot \frac{x_1}{x_2} \cdot \frac{l_2}{l_1} \qquad (3)$$

Supposing l_1=l_2 and knowing n_2 of the reference fiber, n_g can be easily calculated by means of the experimental measurement of the two optical paths.
At this point we have to define how much the length difference between the two fibers affects the ng value.
Let's modify equation (3) as follows:

$$n_g = \frac{l_1}{l_2} \cdot n_2 \cdot \frac{x_1}{x_2} = \bar{l} \cdot n_2 \cdot \frac{x_1}{x_2} \qquad (4)$$

The errors related the parameters in equation (5) are the followings:

- $\bar{l} = \frac{l_1}{l_2} = 1 \pm \delta\bar{l}$ where $\delta\bar{l}$ is the cutting error;
- $x_1 + \delta x_1$ e $x_2 + \delta x_2$; x_1 and x_2 can be considered equal as they depend on the OLCR precision which is $\geq 5\mu m$;

- $n_2 \pm \delta n_2 = 1.468 \pm 2 \cdot 10^{-3}$, according to the typical values for the third window supplied by SMR fibre manufacturers (see Table 1).

Computing the known error propagation equation and assuming $l_1 = l_2 \cong 1m$ we would obtain:

Case a) $\delta \bar{l} = 10^{-3}$ that is $l_2 - l_1 = 1mm$, $\delta n_g = 2.8 \cdot 10^{-3}$

Case b) $\delta \bar{l} = 10^{-4}$ that is $l_2 - l_1 = 0.1mm$, $\delta n_g = 2 \cdot 10^{-3}$

We conclude that by assuring a cutting error smaller than 0.1mm/m, we reach the reference fiber precision ($n_g \cong 2 \cdot 10^{-3}$, see Table 1).

Fiber type	1300 nm	ng	1550 nm
SM-R	1.467		**1.468**
SM-DS	1.471		**1.470**

Table 1- Nominal values (error of ±2 on third figure) for the refractive index of SMR and DS fibers

3. Experimental setup

All the group refractive index measurements have been performed with a OLCR implemented in the Sirti R&D labs [1,2]. Figure 1 shows the automated experimental test-bed, which uses low coherence sources (LEDs, ASE) to obtain a high resolution Michelson interferometer. The 3 dB coupler splits the light launched into the SMR fiber into two branches: the measurement and the reference one. Light is reflected by a mobile mirror placed at the end of the reference branch and in the measurement branch by the fiber under test connected at its end. We can calculate the optical path in the fiber under test by means of the interference peaks generated from both the fiber ends and the mirror at the detector interface.The dashed line in figure 1 shows that reference branch length can be varied, through special patch cords, in order to match different fiber lengths.

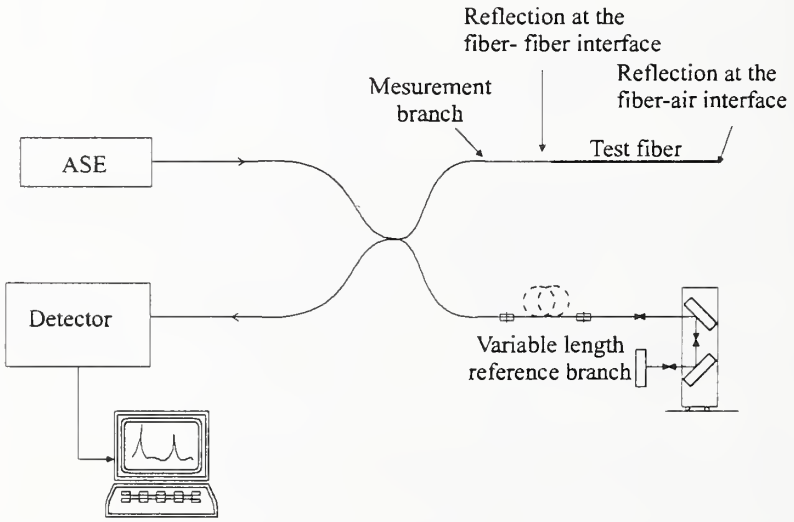

Figure1: experimental setup of OLCR developed by SIRTI

4. Measurements

4.1 Cutting error evaluation

By using two SMR fibers with known n_g one can easily find out the lenght difference from the distance between the interference peaks due to reflections generated at the fiber ends. In the ideal case of a perfect cut, the peaks overlap.

We have developed (Sirti R&D laboratories) a "double cleaver" device; it is based on two standard fiber cleavers and enables to cut the two fibers at the same time. OLCR measurements on several cutting trials showed that our double cleaver always keeps the length difference between the two fibers inferior to 0.1 mm/m .

In this way the theorical precision expected on n_g ($2x10^{-3}$) can be reached.

4.2 n_g measurements

After having verified the feasibility of the experimental method (& 4.1), we carried out a number of n_g measurements on different fibers: Single Mode fiber (SM), Single Mode- Dispersion Shifted fiber (DS), Multi Mode fiber (MM), Doped fiber, DISCO fiber.

The measurement procedure is the same as in § 4.1, except that the two fibers are different. The first is a SMR fiber with a known n_g value; the second is the fiber under test with a n_g value which must be measured. OLCR measures the optical path within each fiber: comparing these two values we can calculate the test fiber group refractive index (equation 4).

The mean values of the results are reported in Table 2. They are in agreement with the ones obtained in [3,4] using a numerical method.

Disco1	Disco 2	SM-DS 1	SM-DS 2	Multi Mode	Doped	SM
1.480	1.479	1.471	1.471	1.478	1.477	1.468

Table 2: mean values of n_g for seven fibers

As an example we report in figures 2, 3 some graphics showing the two interference peaks related to the fiber-air interface of the reference SMR fiber and the test DS (SM,..) one. In fact the fiber-fiber interface interference peaks are not shown because they overlap.

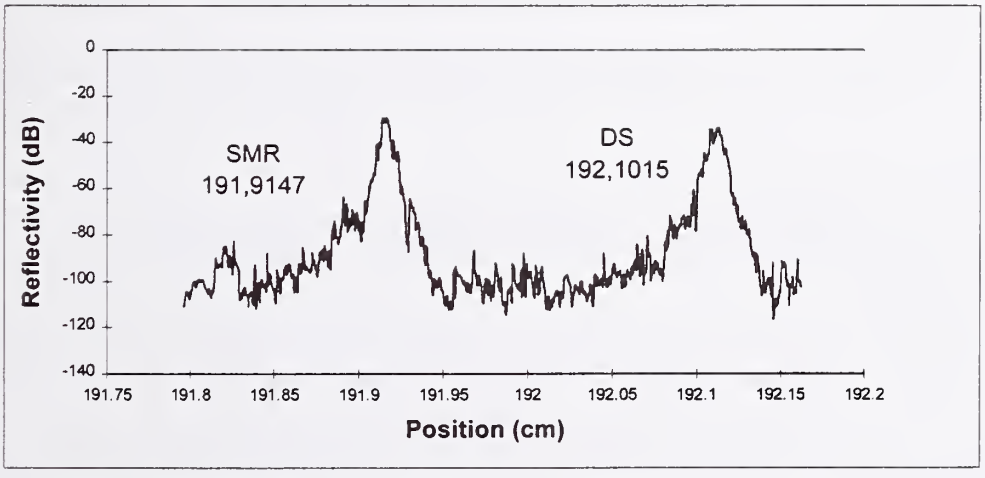

Figure 2: position difference between the reflection at the test DS fiber-air interface and the reflection at the reference SMR fiber-air interface

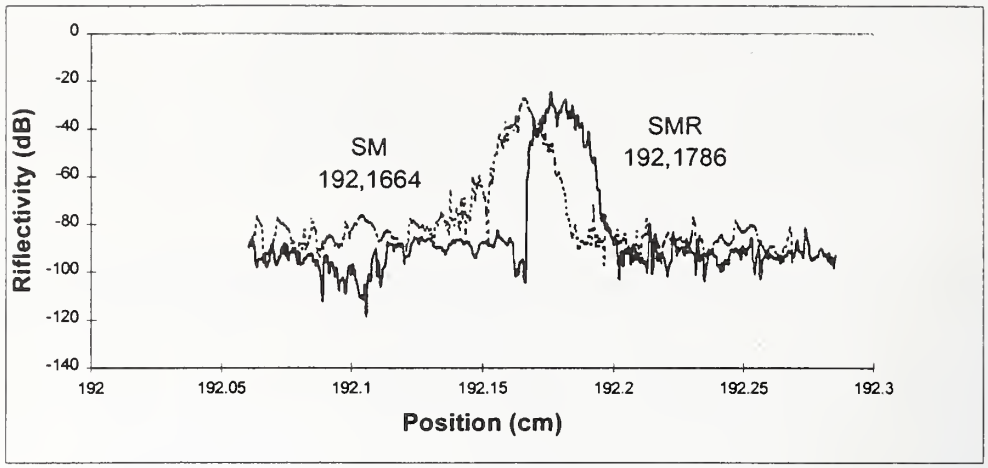

Figure 3: position difference between the reflection at the test SM fiber-air interface and the reflection at the reference SMR fiber-air interface

5. Conclusions

This article demonstrates that we can use the Optical Low Coherence Reflectometry technique to measure the fiber group refractive index n_g with an error of $2x10^{-3}$. n_g is evaluated by measuring the optical path difference between the test and the reference fiber having a lenght difference inferior to 0.1 mm/m.

The n_g experimental measurements satisfy the theoretical previsions and are in agreement with literature results obtained through a different method.

The n_g precision cannot be better than $2x10^{-3}$, that is the known ng precision of the reference SMR fiber.

REFERENCES

[1] Bottanelli & all
"A new wide scan range high resolution Optical Low Coherence Reflectometer", Symposium on Optical Fiber Measurements- Boulder (USA)

[2] Bottanelli & all
"Wide range Optical Low Coherence Reflectometer for high resolution fault detection and component characterization", 45th International Wire and Cable Symposium -IWCS 96 (USA)

[3] W.V. Sorin, D. F. Gray
"Simultaneous thickness and group index measurement using Optical Low-Coherence Reflectometry", IEE Photonics technology letters, Vol. 4, No 1, January 1992

[4] S. Morasca & all
"Measurement of group effective index in integrated semiconductor optical waveguides", IEE Photonics technology letters, Vol. 5, No 1, pag. 40-42, 1993

Are the Formulas for Mode-Field Diameter Correct?

Ronald C. Wittmann, Electromagnetic Fields Division

Matt Young, Optoelectronics Division

National Institute of Standards and Technology
325 Broadway, Boulder, Colorado 80303

We have found conceptual problems with the far-field formula[1] for mode-field diameter. First, the formulation is incomplete in that it ignores the obliquity factor; second, it assumes that the field at the end of a truncated fiber is identical to the mode field of the fiber. When both these factors are taken into account, the resulting integrals fail to converge. We suggest that the original far-field formula be taken as the *definition* of mode-field diameter and derive an alternate near-field formula.

It is important not only to avoid the paraxial approximation, but especially to avoid using a hybrid of paraxial and nonparaxial. Thus, we write for the far-field diffraction integral,

$$U(\rho) = 2\pi O(\theta)\int_0^\infty u_a(r) J_0(2\pi\rho r) r dr, \tag{1}$$

where $u_a(r)$ is the amplitude of the scalar field on the plane $z = 0$ (the *aperture plane*), $U(\rho)$ is the scalar far-field pattern, and $\rho = \sin\theta / \lambda$. See Figure 1. The notation is that of Gaskill.[2] We assume here that $u_a(r)$ is independent of azimuthal angle and that scalar theory is adequate; these assumptions are only approximately correct,[3] and both depend on the assumption of weak guidance. We discuss the factor $O(\theta)$ below. Note that $\rho = \sin\theta / \lambda$, not θ / λ.

Let us write (1) in the shorthand form

$$U(\rho) = O(\theta)\,\mathrm{HT}[u_a(r)], \tag{2}$$

where HT means Hankel transform. The inverse Hankel transform is

$$u_a(r) = 2\pi\int_0^\infty [U(\rho) / O(\theta)] J_0(2\pi r\rho)\rho\, d\rho, \tag{3}$$

or

$$u_a(r) = \mathrm{HT}^{-1}[U(\rho) / O(\theta)], \tag{4}$$

so the Hankel transform pair consists of $u_a(r)$ and $U(\theta)/O(\theta)$, not $u_a(r)$ and $U(\theta)$. In what follows, we will ignore evanescent waves; that is, we will ignore values of $\rho > 1/\lambda$ on the grounds that they are insignificant as $R \to \infty$. This limits the resolution in the aperture plane to approximately one wavelength.

The factor $O(\theta)$ is called the *obliquity factor* or the inclination factor, and it is equal to 1 in the paraxial approximation. It is often overlooked, even when the calculation is thought to be nonparaxial. This is so in part because the optics literature has sometimes been confused as to the functional form of $O(\theta)$. The correct form, however, was derived by Sommerfeld[4] and is well known to electromagnetic theorists, though their notation and terminology are different.[5] Specifically, when the aperture field is known, the obliquity factor is[6]

$$O(\theta) = \cos\theta, \tag{5}$$

not[7] $$O(\theta) = (1+\cos\theta)/2. \tag{6}$$

Petermann has derived a useful expression for the mode-field radius of a fiber:[8]

$$w_0^{(\mathrm{P})} = [2\int_0^\infty |u_\mathrm{m}(r)|^2 r dr / \int_0^\infty |\partial u_\mathrm{m}(r)/\partial r|^2 r\,\mathrm{d}\,r]^{1/2}, \tag{7}$$

where $u_\mathrm{m}(r)$ is the mode field of the fiber and differs from the aperture field $u_\mathrm{a}(r)$. Artiglia and coworkers used (2) and (7) with $O(\theta) = 1$ to derive the relation[9]

$$w_0 = (\lambda/2\pi)[2\int_0^{\pi/2} I(\theta)\sin\theta\cos\theta\,\mathrm{d}\,\theta / \int_0^{\pi/2} I(\theta)\sin^3\theta\cos\theta\,\mathrm{d}\,\theta]^{1/2}, \tag{8}$$

where $I(\theta) = U^2(\theta)$ is the intensity measured in the far field of a truncated single-mode fiber. Equation (8) is used in the TIA standard for measuring mode-field diameter by far-field scanning.[10]

Equation (8) is not quite correct: first, because it sets the obliquity factor equal to 1 and, second, because it assumes that the aperture field is the same as the mode field of the fiber.

We can easily correct the first defect by applying (5) and replacing $I(\theta)$ with $I(\theta)/\cos^2\theta$:

$$w_0^{(\mathrm{P}')} = (\lambda/2\pi)[2\int_0^{\pi/2} I(\theta)\tan\theta\,\mathrm{d}\,\theta / \int_0^{\pi/2} I(\theta)\sin^2\theta\tan\theta\,\mathrm{d}\,\theta]^{1/2}. \tag{9}$$

This is (7) transformed to the far field, except that the aperture field $u_\mathrm{a}(r)$ has to be used in place of $u_\mathrm{m}(r)$; hence, the superscript (P) is replaced by (P′). Equation (9) follows rigorously from applying (3) to the aperture field and could therefore be considered the "correct" result for scalar theory.

The integrals in (9) diverge unless the limit of integration is less than $\pi/2$ (see below). The calculated result therefore depends on the upper limit of integration, and it may be difficult to decide where to set that limit if the fiber has a particularly broad far-field pattern. Nevertheless, to assess using (9) in place of (8), we calculated the mode-field diameters of a step-index fiber and a dispersion-compensating fiber using both equations, that is, both with and without the obliquity factor.[11] Including the obliquity factor decreases the calculated mode-field diameter, because dividing $I(\theta)$ by $\cos^2\theta$ effectively broadens the far-field pattern and narrows the near-field pattern accordingly. With the step-index fiber, the decrease was 20-25 nm and did not change much with angle of scan, because the far-field intensity is small when angles are large. See Figure 2. If we could extend the integration to $\pi/2$, however, the integrals would diverge.

With the dispersion-compensating fiber, the decrease grew from 80 to100 nm as the angle of scan increased from 26 to 40°. That is, including the obliquity factor in the calculation may change the result by perhaps –25 nm with a common step-index fiber but possibly by –100 nm or more with a particularly small-cored fiber.

The difference between the two calculations, including or not including the obliquity factor, is not a component of uncertainty. To the contrary, if the calculation that includes the

obliquity factor is correct – or more nearly correct than the simpler theory – then the simpler calculation gives rise to a systematic error.

The discontinuity at the end of the fiber excites waves that are radiative in the hemisphere $z > 0$ and whose amplitudes fall off as $1/R$ in the limit $R \to \infty$. In the aperture plane, $R = r$; if we apply (7) to the aperture field with $u_a(r)$ in place of $u_m(r)$, we find, for example, that

$$\int |u_a(r)|^2 r\,\mathrm{d}r \to \int \frac{1}{r^2} r\,\mathrm{d}r \to \ln(r), \quad . \tag{10}$$

which diverges as $r \to \infty$. The denominator similarly diverges, so (7), when applied to the aperture field, is indeterminate.

The integrals in (9) likewise do not converge, because of the tangent terms. The integrals in (8), by contrast, converge but do not correctly follow from (7) when (7) is applied to the aperture field. We therefore suggest that (8), though arguably incorrect, be adopted as the *definition* of mode-field diameter in place of (7). This has advantage in that is consistent with present practice and gives at least a basis for comparing different fibers.

How can we correctly transform (8) to the near field? Let the field a distance $z > 0$ beyond the aperture plane be $u(r, z)$, where $z = 0$ is the aperture plane and $u_a(r) = u(r, 0)$. See Figure 1. In terms of the field in the plane defined by z, the far-field pattern may be expressed as

$$U(\theta) \exp(\mathrm{i}\, k_z z) = O(\theta)\, \mathrm{HT}[u(r,z)], \tag{11}$$

where $k_z = k \cos\theta$ is the z component of the propagation vector. Inverting (11) we find

$$u(r,z) = \mathrm{HT}^{-1}[U(\theta) / O(\theta) \exp(\mathrm{i}\, k_z z)]. \tag{12}$$

Taking the derivative of both sides of (12) with respect to z brings out a factor of $k_z = k \cos\theta$ on the right side; the factor $\cos\theta$ cancels the divisor $O(\theta)$. Apart from a constant factor, $\partial u(r, z)/\partial z$ and $U(\theta)$ are a Hankel transform pair, whereas $u(r, z)$ and $U(\theta)$ are not. This consideration leads us to the expression

$$w_0 = [2\int_0^\infty |u_a'(r)|^2 r dr / \int_0^\infty |\partial u_a'(r) / \partial r|^2 r\,\mathrm{d}r]^{1/2}, \tag{13}$$

where $u_a'(r) = [\partial u(r, z)/\partial z]_{z=0}$ is the normal derivative of the aperture field. In the region near the core, the aperture field is very nearly a TEM wave (and is probably very nearly equal to the mode field), so (13) reduces to Petermann's original definition (7). Equation (13) converges, however, whereas (7) will generally not converge if the mode field $u_m(r)$ is replaced by the aperture field $u_a(r)$. The vector equivalents of (7) and (13) may be obtained by carrying out the replacements $u \to |\mathbf{E}|$, $\partial u/\partial r \to |\partial \mathbf{E}/\partial r|$, $\partial u/\partial z \to |\partial \mathbf{E}/\partial z|$, and so on, where $\mathbf{E}$ is electric field.

Whether w_0 is useful for characterizing a fiber is not clear. Applying (13) experimentally to near-field scans may be difficult when the aperture field is not very nearly a TEM wave, since the near-field scan measures intensity as a function of position, whereas we need the axial derivative of the field to use (13). Thus, we should expect discrepancies between near- and far-field measurements of w_0.

We are indebted to Andy Hallam of PK Technology for pointing out the problem and to Dave Hill and John Schlager of NIST for their careful reading of the manuscript. Not subject to copyright.

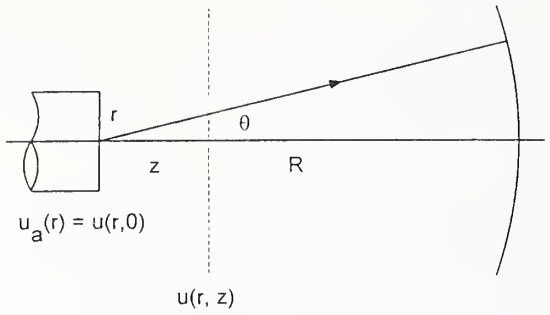

Figure 1. The vicinity of the aperture plane (the exit face of the fiber).

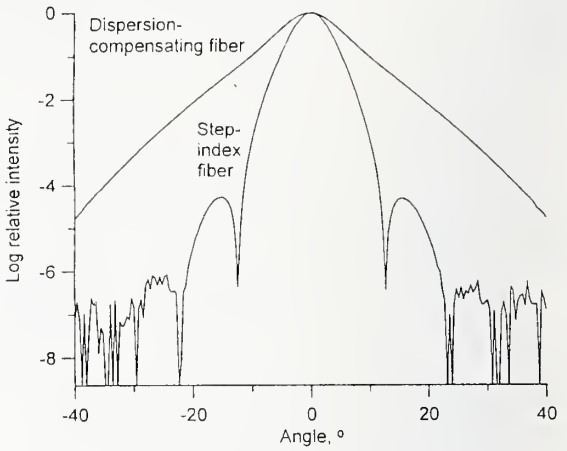

Figure 2. Far-field intensity of a dispersion-compensating fiber and a step-index fiber.

References.

1. M. Artiglia, G. Coppa, P. Di Vita, M. Potenza, and A. Sharma, "Mode field diameter measurements in single-mode optical fibers," IEEE J. Lightwave Technol. 7, 1139-1152 (1989).

2. Jack D. Gaskill, *Linear Systems, Fourier Transforms, and Optics*, Wiley, New York, 1978.

3. Matt Young, "Mode-field diameter of single-mode optical fiber by far-field scanning," *Appl. Opt.*, in press.

4. Arnold Sommerfeld, *Optics, Lectures on Theoretical Physics, Vol. IV*, Academic, New York, 1964, Sect. 34.

5. D. M. Kerns, *Plane-Wave Scattering Matrix Theory of Antennas and Antenna-Antenna Interactions*, Nat. Bur. Stands. (U. S.) Monogr. 162 (1981).

6. Matt Young and Ronald C. Wittmann, "Vector theory of diffraction by a single-mode fiber: Application to mode-field diameter measurements," Opt. Lett. **18**, 1715-1717 (1993).

7. M. Born and E. Wolf, *Principles of Optics*, Macmillan, New York (1964), Sect. 3.8.2.

8. K. Petermann, "Constraints for fundamental-mode spot size for broadband dispersion-compensated single-mode fibres," Electron. Lett. **19**, 712-714 (1983). C. Pask, "Physical interpretation of Petermann's strange spot size for single-mode fibers," Electron. Lett. **20**, 144-145 (1984).

9. Artiglia, Ref. 1.

10. Anonymous, "Measurement of mode field diameter of single-mode optical fiber." Fiberoptic Test Procedure FOTP-XX, Telecommunications Industry Association, 2500 Wilson Boulevard, Suite 300, Arlington, Va. 22201-3834, in preparation.

11. Young, Ref. 2.

Simultaneous measurement of relative outer diameter along fiber axis: nm resolution in diameter and mm coverage in length

Andrew W. Poon and Richard K. Chang
Department of Applied Physics and Center for Laser Diagnostics
Yale University
New Haven CT 06520-8284

I. Introduction

Uniformity of cladding diameter along the fiber axis is one of the critical parameters for successful splicing of optical fibers. Conventional techniques for measuring outer diameter involve counting the number of fringes in the far-field forward scattering pattern of a fixed wavelength laser beam.[1] Other precise methods based on resonant light scattering from fiber have also been reported.[2,3] However, these outer diameter measuring techniques only sample discrete positions along the fiber axis, and multiple measurements are required to characterize the diameter along the fiber. A simultaneous measurement of relative outer diameter along the fiber axis may therefore provide a more rapid and accurate in-line characterization of the fiber diameter uniformity. In this Symposium, we report a new technique that allows nm resolution in diameter and mm coverage in length, that is based on analyzing, at a fixed scattering angle, the morphology-dependent resonances (MDR's) in the elastic-scattering spectrum as a function of both wavelength and positions along the fiber axis.

Light that is incident perpendicularly to the fiber axis couples into the fiber and travels around the circumference via successive total internal reflections at the cladding-air surface. The circulating internal wave is on resonance when the internal wave after each round-trip is in-phase with the incident wave. The resonant wavelengths are therefore highly dependent on the fiber diameter, while the linewidth of the resonances are sensitive to the fiber surface roughness. MDR's in the light elastic-scattering from an optical fiber have been demonstrated in previous experimental studies.[2,3] The spectrum revealed sharp discrete resonance peaks. The positions of the resonances are insensitive to the scattering angle, but the intensity of the resonances is scattering angle dependent. The MDR's may ride on broad linewidth peaks associated with Fabry-Perot resonances between fiber surfaces at a high order rainbow scattering. The two polarization modes, TM and TE, have different sets of resonances.

II. Experiment and Results

We employed a new high-resolution technique to study MDR's along the fiber axis in commercially available optical fiber (Corning Inc.) with 125 μm nominal diameter. The plastic coating on the fiber is chemically removed by applying methylene chloride and rinsed with spectro-grade acetone to avoid introducing scratches that result from mechanical stripping. The fiber was illuminated perpendicularly to its axis with monochromatic light from a continuously tunable external-cavity diode laser (New Focus model 6202) with wavelength from 664 to 683 nm and linewidth ~ 10^{-5} nm. The wavelength was linearly scanned and our data-taking routine allowed a wavelength resolution ~ 0.01 nm. The incident and scattered polarization were set horizontally to the fiber axis (TE mode). Light was focused weakly by a ~ 14 cm cylindrical lens into a ~ 5 mm long sheet that was collimated along the fiber axis. Elastic-scattering at 90° scattering angle was detected by an intensified silicon photodiode array detector (EG&G model 1420) mounted with the array axis parallel to the fiber axis. This detector orientation allows simultaneous measurement of the resonant spectra along the fiber axis.

Figure 1(a) shows a series of elastic-scattering spectra in wavelength along an estimated 2 mm length of fiber. The scattered light intensity profile only spanned ~ 100 channels of the 1000 channels available in the ~ 2 cm array detector. Figure 1(b) shows the same set of data but plotted with the "head-on" view in order that the resonant wavelengths at different positions along the fiber axis can be visually compared. A series of five MDR's was observed with linewidth ~ 0.07 nm to < 0.03 nm. The sharper but weaker MDR's appeared to be resolution limited by our scanning technique.

Relative fiber diameter measurements are determined by relative shifts in the resonant wavelength. For both MDR's and Fabry-Perot resonances, the relative fiber diameter ΔD and the shift in resonance wavelength $\Delta\lambda$ are related by simple ratio as follows:

$$\Delta D = \frac{D}{\lambda} \Delta\lambda \qquad (1)$$

where D is the 125 μm nominal diameter, and λ is the resonant wavelength. The resolution in relative fiber diameter measurement is limited only by the linewidth of the MDR's. For an MDR with linewidth 0.03 nm, a shift in $\Delta\lambda$ as small as 0.03 nm can be readily discerned. For the resonant wavelength $\lambda \sim 670$ nm, $\Delta D < 6$ nm in diameter resolution can be achieved. Figure 1(b) reveals no shift in MDR's positions along the ~ 2 mm fiber length. This suggests that the fiber is highly uniform over the estimated 2 mm fiber axis.

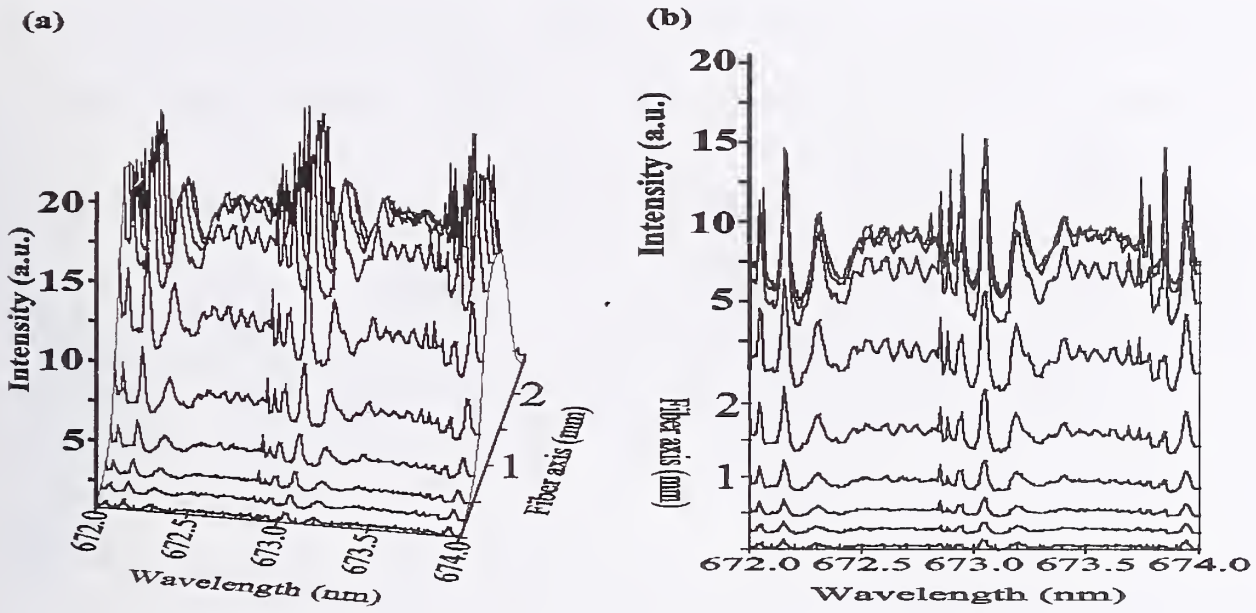

Figure 1 Elastic-scattering spectra along the fiber axis measured by detector at the shadow side of the edge-illuminated fiber (a) side-view (b) front view.

The quasi-periodic spacing between MDR's of similar linewidth also allow absolute measurements of average fiber diameter by matching the measured MDR's spacing and resonant wavelength with the numerical spectra from Mie calculations.

The ripples between the series of sharp peaks might be due to unavoidable interference from optical components in the optical path of the illumination and detection system. Fabry-Perot resonances were not pronounced because the fiber was transversely displaced from the focused beam by ~ 60 μm such that the illumination at the fiber edge allows preferential light coupling to the MDR's. For the data shown in Figs. 1(a) and (b), the detector and the focused beam were on opposite sides of the displaced fiber.

For the spectra shown in Figs. 2(a) and (b), the detector and the focused beam were on the same side of the transversely displaced fiber. The measured scattered light intensity is weaker than the scattering intensity observed with the detector on the shadow side of the edge-illuminated fiber. Similar series of five MDR's were observed with no shift among the MDR's along the estimated 2 mm fiber length. The broad resonances (with ~ 0.5 nm linewidth) are apparently Fabry-Perot resonances, which allows ~ 0.1 μm resolution in relative fiber diameter determination. The broad Fabry-Perot like resonances have a wavelength shift along the fiber-axis. We hypothesize that this wavelength shift might be related to slight fiber tilting in the plane perpendicular to the incident beam. Further experimental investigations are required. In fact, effects of fiber tilt in the incident-beam-fiber plane was recently studied using a similar MDR's related experimental setup.[4]

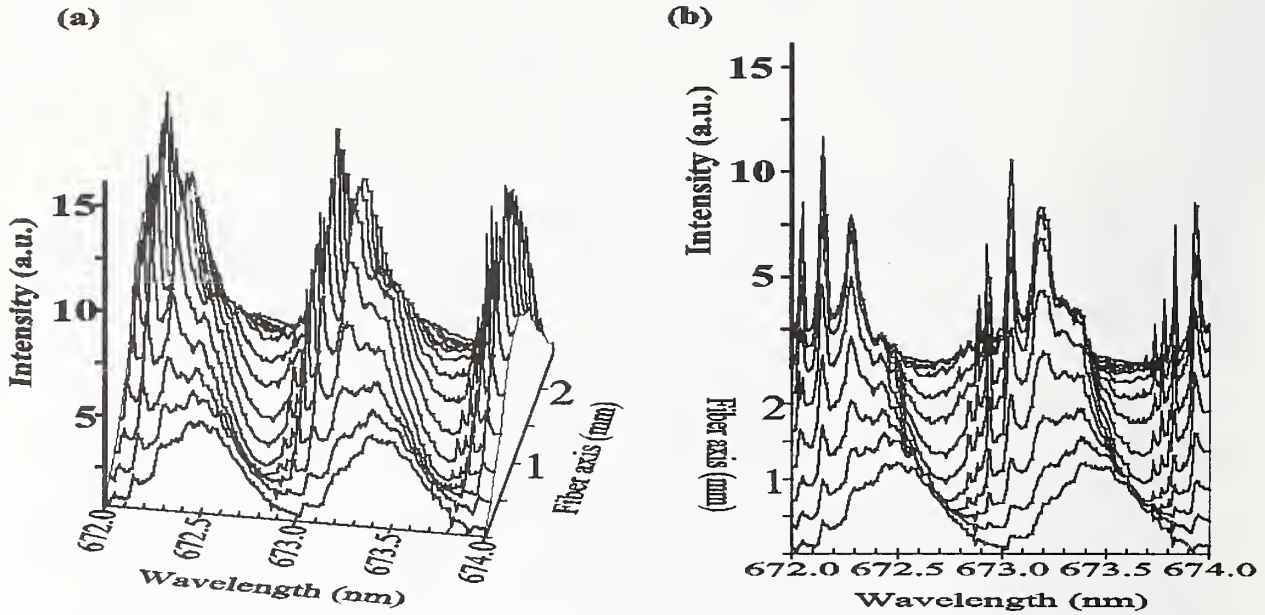

Figure 2 Elastic-scattering spectra along the fiber axis measured by detector at the illuminated side of the edge-illuminated fiber (a) side-view (b) front-view.

In summary, we have a technique that can detect nm fluctuation of the cladding diameter along mm length of the fiber axis. The absence of wavelength shift of narrow linewidth MDR's suggests a uniform fiber diameter (less than 6 nm) along the fiber length of several mm (~ 2 mm).

We gratefully acknowledge the financial support from the National Science Foundation under contract PHY-9612200 and the helpful discussions with Dr. Daniel Nolan of Corning.

References

[1.] D. H. Smithgall, L. S. Watkins, and R. E. Frazee, Jr., Appl. Opt. **16**, 2395 (1977).

[2.] J. F. Owen, P. W. Barber, B. J. Messinger, and R. K. Chang, Opt. Lett. **6**, 272 (1981).

[3.] A. Ashkin, J. M. Dziedzic, and R. H. Stolen, Appl. Opt. **20**, 2299 (1981).

[4.] A. W. Poon, R. K. Chang, and J. A. Lock, Opt. Lett. (to be published).

Measurement of the impact of fiber nonlinearities on high data rate, dispersion-managed WDM systems

(invited paper)

Sébastien Bigo and Michel W. Chbat

Alcatel Corporate Research Center, Route de Nozay, 91460 Marcoussis, France
Phone: +33 1 69 63 14 78 / Fax: +33 1 69 63 18 65
E-mail: bigo@aar.alcatel-alsthom.fr

Abstract:

To upgrade high data-rate WDM transmissian systems, fiber nonlineorities must be caped with. This requires the knowledge af their strength, via, in particular, the nonlineor index coefficient n_2. We shaw same measurement results af n_2 thraugh four-wave mixing aver severol fiber types. Then, we measure the system impoct ot 10 Gbit/s af various physicol effects resulting fram fiber nonlinearities : self-phase madulatian (SPM), cross-phase modulotion (XPM) ond stimulated Raman scattering (SRS). However, evaluating the impact af the combinotion af those effects is not straightforword, but it is essentiol for system design, especiolly dispersion management, far which we show experimentally that residual dispersion can no langer be used os performance criterian.

Introduction:

Two approaches are considered to upgrade WDM amplified transmission systems and thereby meet the ever growing demand for higher capacities on a single fiber. The first approach is to increase the bit-rate per channel. Simple optical noise considerations show that the signal-to-noise ratio (SNR), and thus the power per channel, must be increased in the same proportion. In a typical 500-km-long link consisting of five spans of realistic 28 dB power budget, the power requirement is such that, even at minimal recommended SNR (no margin), the transmission can no longer be viewed as linear. The second approach is to increase the number of channels, either by reducing the spectral spacing between channels or by occupying a larger amplifier bandwidth. In both cases, the optical interactions between channels stemming from fiber cross-nonlinearities increase significantly.

Therefore, to assess the performance of most high data-rate transmission systems, nonlinear effects must be considered [1]. A list of them is given in the first part of this paper. Considering the variety of fiber infrastructures, it is of primary importance to measure the strength of nonlinearities over each fiber type, and in particular the nonlinear index coefficient n_2. We review the measurement methods that have been proposed for measuring n_2, and we discuss the limits of the four-wave mixing method [2] with all fiber types. Then, we investigate experimentally the system impact of the physical effects resulting from fiber nonlinearities at 10 Gbit/s : self-phase modulation (SPM), cross-phase modulation (XPM) and stimulated Raman scattering (SRS). Unfortunately, their individual contributions to the system penalty cannot be added. Thus, to improve the design of a system, a simulation tool is highly recommended, especially for dispersion management. Indeed, we demonstrate that the analytical rules yielding the acceptable residual dispersion at receiver end can no longer be applied at 10 Gbit/s.

Nonlinear effects in fibers:

Kerr nonlinearity refers to the linear dependence of the fiber's refractive index on the injected channel power. Silica, the major constituent of fibers, has one of the lowest nonlinearity coefficients (n_2) of any optical material. Nevertheless, Kerr-induced signal distortions can occur at reasonable powers (a few dBm) in the

fiber because of the large distances traveled and the energy confinement. This confinement is characterized by the effective area of the fiber A_{eff}. The smaller A_{eff}, the higher the nonlinearities. ($A_{eff} \approx 80\ \mu m^2$ for standard single mode G.652 fiber (SMF), $A_{eff} \approx 50\ \mu m^2$ for dispersion-shifted G.653 fiber (DSF)).

Various, generally detrimental, effects result from Kerr nonlinearities. In the first effect, referred to SPM, the optical phase of a channel is modulated proportionally to its own instantaneous power. SPM appears as a broadening of the channel spectrum, as new optical frequencies are generated. However, since this effect primarily affects the signal phase, it does not affect the detection of intensity at the receiver end, unless the group-velocity dispersion (GVD) is non-zero. Indeed, the interplay of SPM results in a complicated phase-to-intensity conversion process during propagation. Depending on GVD, SPM can be either beneficial – leading to pulse compression – or detrimental – possibly leading to irretrievable breakup of the optical pulses.

The second effect stemming from Kerr nonlinearities is the nonlinear interaction of a signal with the amplified spontaneous emission (ASE) noise of the optical amplifiers, altering the SNR at fiber output. The effect is less detrimental in the normal dispersion regime than in the anomalous dispersion regime, where it is referred to as modulation instability (MI).

In WDM systems specifically, Kerr nonlinearities induce additional limitations such as the generation of intermodulation products between the carriers of a multiplex, a phenomenon called Four Wave Mixing (FWM). In a nonlinear fiber carrying two or more WDM channels, FWM can create additional frequencies, provided that a certain phase-matching condition is met, essentially if the relative velocity between the channels is low enough. Assuming the WDM channels are equally spaced, the wavelengths of the intermodulation products coincide with the other channel wavelengths, thereby creating undesirable in-band crosstalk.

Another nonlinear effect to be considered is XPM. Like SPM, this phenomenon manifests itself as an alteration of the optical phase of a channel, which translates into intensity distortions through GVD. However, in contrast to SPM, it is a multi-channel effect, whereby the phase modulation of a channel is induced by the intensity of the signal on neighboring channel(s). Thus it depends on the relative speeds of the interacting channels, that is, on GVD. The lower the GVD (and thus the difference in channel speeds), the higher the interaction between channels. However, at zero GVD, no phase-to-intensity conversion occurs. Consequently, it is not a simple matter to predict the impact of XPM and the other Kerr-related phenomena and a simulation tool is often useful, as illustrated further on.

Finally, two additional nonlinear limiting effects can be encountered in transmission systems, stimulated Brillouin scattering (SBS) and SRS. They do not originate from Kerr effect, but from a resonant parametric interaction with acoustical and optical phonons, respectively, within the fiber medium. SBS has been observed for a long time and well-known techniques can be implemented to reduce its impact. Conversely, SRS is inherently WDM-related and its impact is expected to grow as the amplifier bandwidth increases, in order to accomodate new channels. When two channels located a few tens of nanometers apart propagate along with each other, the lower-wavelength channel experiences power depletion through SRS, while serving as a pumping signal to amplify the higher-wavelength channel.

All of these nonlinear phenomena can result in severe transmission impairments especially at 10 Gbit/s base rate and above. It is therefore essential to be able to predict their impact over all existing fiber types, i.e. SMF, DSF, non-zero DSF (NZDSF) and dispersion-compensating fiber (DCF).

Measurement of nonlinear index n_2 through four-wave mixing:

The nonlinear index coefficient n_2 is one key parameter that is needed to characterize the strength of the Kerr nonlinearity. All of the techniques that have been proposed for measuring n_2 provide indirect estimation of n_2 through one of the aforementioned Kerr-related phenomena. A large number of them resort to the measurement of the nonlinear phase, be it the result of SPM [3-6] or XPM [6-8]. These techniques use interferometric devices, which are subject to environmental instability, a potential cause for large

uncertainties. In the other approaches, the distortions caused by SPM are analyzed through spectral measurements [9-11], which requires a good knowledge of the initial waveform. The simplest time-dependent waveform is probably a wave of sinusoidal envelope. Such a wave can be generated through the beating of two continuous-wave (cw) lasers, as in [11]. However, in this case, measuring the relative power of the harmonic components induced by SPM amounts to measuring the relative power of the intermodulation products induced by FWM as two cw tones propagate, a method described earlier in ref. [2]. The nonlinear index n_2 can be derived from these power measurements through an analytical formula in [11]. In ref. [2], a better accuracy is obtained through numerical simulations. Only DSF was tested this way, but one key advantage of the approach is that it can be extended to any fiber type with the same apparatus. We apply next this last technique to three fiber samples and discuss its limitations.

In our setup, we use a DFB laser (1554.0 nm) and an external cavity laser to generate two continuous waves of wavelengths separated by $\Delta\lambda$. The two waves, of equal power P_{in}, are sent to two booster amplifiers of 20 dBm saturation power, combined and sent to the fiber under test. The polarizations of the waves are ajusted until linear and parallel to each other using polarization controllers and a polarizer. After propagation, the signal is fed to an optical spectrum analyzer of 0.05 nm resolution. Typical input and output spectra are shown in Figure 1. The index coefficient n_2 is recovered when the experimental power ratio I_1/I_0 between the carriers and the harmonics matches that obtained after several numerical integrations of the nonlinear Schrödinger equation with a variable n_2. To assert a good accuracy, the fiber length and the spectral spacing $\Delta\lambda$ must be carefully chosen. Indeed, as shown in Fig. 1, when $\Delta\lambda$ increases, the efficiency of FWM and thus the ratio I_1/I_0 decrease, then rapid pseudo-oscillations occur as a result of the break-up of the phase-matching condition. These rapid variations must be avoided because a small error during the measurement of $\Delta\lambda$ would cause a potentially large error in the computed ratio I_1/I_0, leading to a wrong estimation of n_2. As illustrated in Fig. 1, this effect is all the more detrimental as the absolute value of the dispersion is high (up to approximately 80 ps/nm.km for the DCF). To circumvent it, small spacings $\Delta\lambda$ or small fiber lengths must be used. However, $\Delta\lambda$ cannot be made lower than 0.35 nm with our spectrum analyzer. Moreover, reducing the fiber length not only eases the constraints on $\Delta\lambda$ but also reduces the FWM efficiency and the ratio I_1/I_0, which must remain significantly higher than the amplifier noise level for a good accuracy. With the most troublesome fiber (DCF), we estimate the error on n_2/A_{eff} to be ±10%.

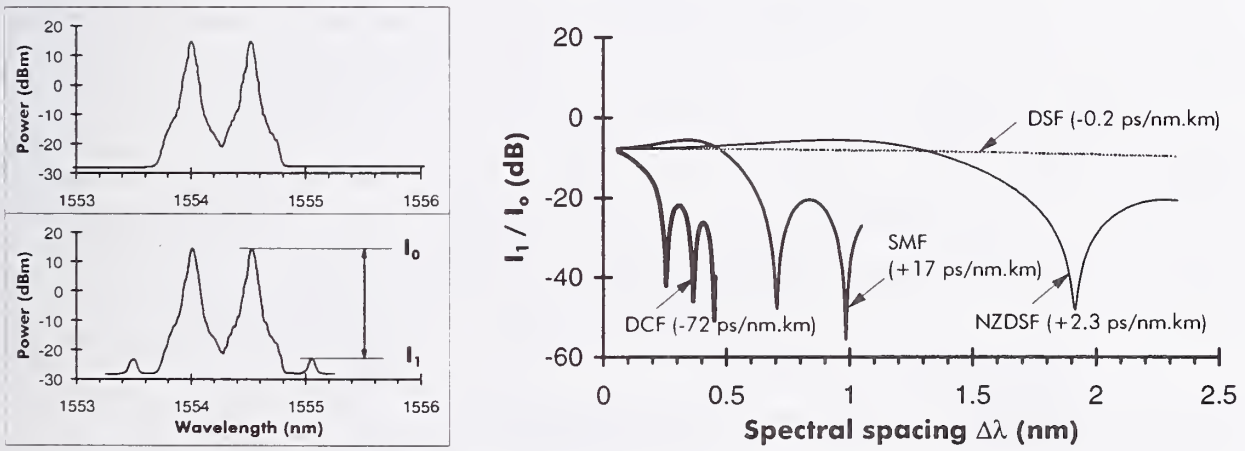

Figure 1 : Principle of n_2 measurement using FWM (left) and simulated effect of spectral spacing an harmanic-ta-carrier ratia I_1/I_0 far variaus types af 1-km lang typical commercially available fibers fed by twa cw tanes at17 dBm.

The results are summarized below (all parameters measured at 1550 nm).

	Dispersion (ps/nm.km)	Length (km)	loss (dB/km)	n_2/A_{eff} (10^{-20} /W)	A_{eff} (μm^2)	n_2 (10^{-20} m^2/W)
DCF	-81.3	0.50	0.54	7.20	35	2.5
SMF	17.7	1.00	0.20	3.20	78	2.5
NZDSF	-2.09	2.00	0.22	5.62	48	2.7

The knowledge of the nonlinear strength, through n_2 measurement in particular, is one unavoidable step towards the assessment of the impact of fiber nonlinearities in transmission systems. Another step is the characterization of all the phenomena that result from them.

Measurement of system impact of nonlinearities:
We now report an investigation of the limitations induced by **SPM** at 10 Gb/s over four types of fiber infrastructures [12]: DSF, (-0.1 ps/nm.km **[b]** and +0.1 ps/nm.km **[c]**), NZ-DSF with negative (-2.3 ps/nm.km **[a]**) or positive (+3 ps/nm.km **[d]**) GVD, and SMF (17 ps/nm.km **[e]**) followed by 10km of dispersion-compensated fiber (DCF, -80 ps/nm.km) to reduce the impact of GVD. The 2x100 km-long link (2x90 km in **[e]**), is fed by a transmitter incorporating a 10 Gb/s chirp-free intensity modulator. The transmission performance is characterized by the power penalty at 10^{-10} bit-error rate (BER). Insight on the origin of this penalty is given by the geometrical eye-diagram, computed from time-averaged waveforms, free of the noise contribution. The power P at fiber input is varied within [2 dBm, 20 dBm].

The experimental results are represented in Fig.2(a). In all configurations, a BER floor is measured within the investigated power range: a 3 dB penalty being reached at 8, 16, 16, 12, 17dBm in cases **[a]** to **[e]**, respectively. At high GVD ($|D| > 2$ps/nm.km), the geometrical eye-diagram shows that the predominant detrimental effect is waveform distortion. For negative GVD **[a]**, the interplay between GVD and SPM broadens isolated pulses, but does not improve the transmission. For positive GVD **[c, e]**, higher-order soliton-like effects increase the extinction ratio and hence reduces the penalty.

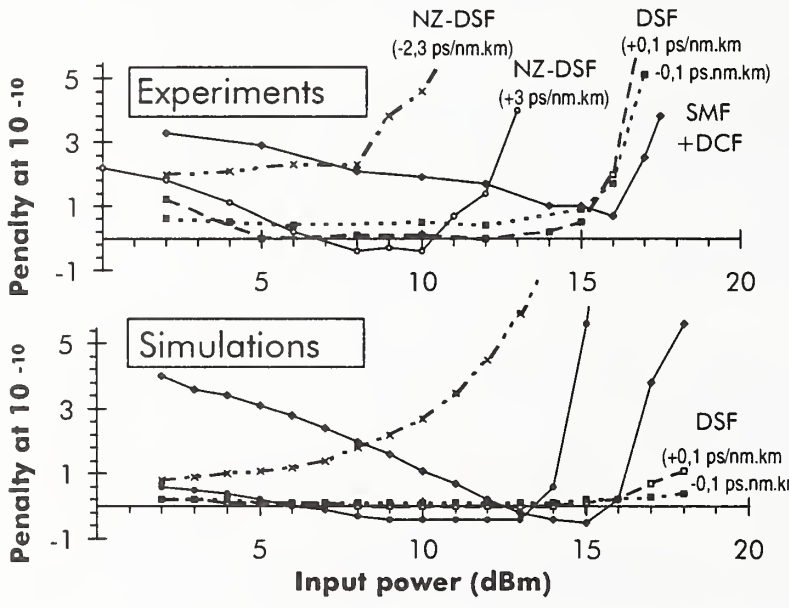

Figure 2: Effect of SPM : power penalty at 10^{-10} BER as a function of input power

However, above a certain threshold (P=10 and 17 dBm for **[b]** and **[e]**, respectively), the penalty sharply increases as an irretrievable break-up of pulses occurs. With DSF **[b, c]**, the power penalty is almost zero until P reaches 16 dBm. Above that threshold, signal-ASE nonlinear interactions cause a dramatic reduction of SNR.

Simulation results (Fig.2(b)) with the above parameters are in good agreement with the experiments, except for the DSF **[b, c]** at high power levels: the contribution of noise is computed analytically and added at the receiver end, which overlooks noise-signal interactions during propagation.

Consider now nonlinearities involving several channels. In the following, we investigate the impact of **XPM** using a very similar apparatus as that used for SPM. Two independently-modulated cw lasers, referred to as the probe and the pump, are combined, boosted and sent to two 100-km-long spans of NZDSF (+3 ps/nm.km) or DSF (+0.1 ps/nm.km). The power of the probe (+2dBm) is maintained 6 dB lower than that of the pump so that SPM effects to the probe can be neglected. SPM effects to the pump are assumed second-order effects. The polarization and the rf delay between the two waves are adjusted manually for best and worst BER.

The transmission performance is characterized through the power penalty at 10^{-10} BER. The results are displayed in fig. 3. When the channel decreases down to 100 GHz, the worst case penalty increases dramatically by 1 dB over DSF and by 2.2 dB over NZDSF. Conversely, the best case penalty is almost unchanged and corresponds to the penalty obtained in the linear regime. This result shows that, at 8 dBm and with only two channels, XPM can almost be suppressed by proper polarization arrangement at transmitter output. Should this arrangement not be carried out, the pump power or the number of channels be higher, the impact of XPM alone was found highly detrimental.

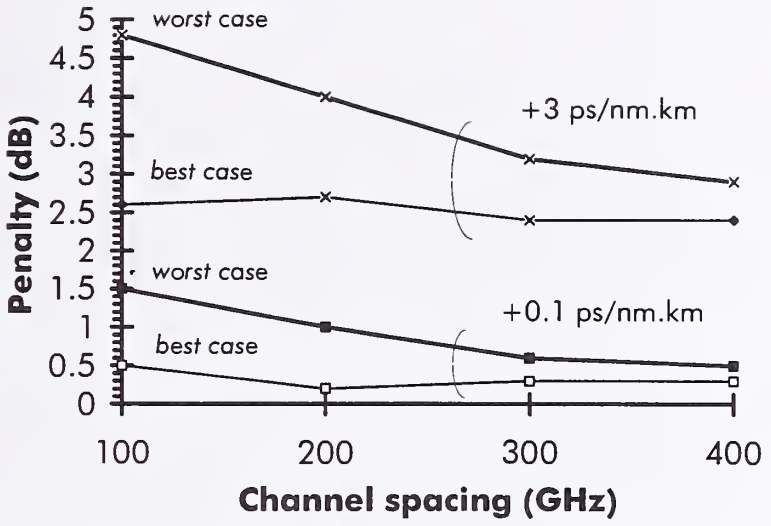

Figure 3: Effect of XPM : power penalty at 10^{-10} BER of os o function of power at fiber input.

Another WDM nonlinear effect is **SRS**. We characterize its impact in an unrepeatered 100-km long transmission based successively on two types of NZDSF (+2 ps/nm.km, and -2.3 ps/nm.km in average) employing 32 channels at 10 Gbit/s. At transmitter output, the power per channel is 5 dBm with a very low power excursion between channels (<1 dB). After propagation, a spectral analysis shows that the lower-wavelength channels have lower power levels than the higher-wavelength channels. Channel #1 to channel #32 relative loss difference is 2.6 dB, whereas the linear loss dependence of the fiber on wavelength leads to less than 1.5 dB only. The additional loss on lower-wavelength channels can be attributed to SRS. Our simple analytical model of SRS yields results in very good accordance with the experiments.

Impact of nonlinearities on dispersion management:

The experimental results described above show how severe nonlinear impairments can be at 10 Gbit/s. These impairments depend strongly on the fiber dispersion, as a result of the interplay with GVD. This explains why compensating for too much cumulated dispersion along the link, i.e. managing the dispersion, should be done carefully. Indeed, as a result of nonlinearities, the range of acceptable residual dispersions at receiver end is significantly reduced with respect to the commonly-used [-1000, +1000 ps/nm] range in the linear regime. This explains why, contrary to what was originally thought, dispersion management is compulsory not only in terrestrial links using SMF, but also in those using low dispersion NZDSF [13].

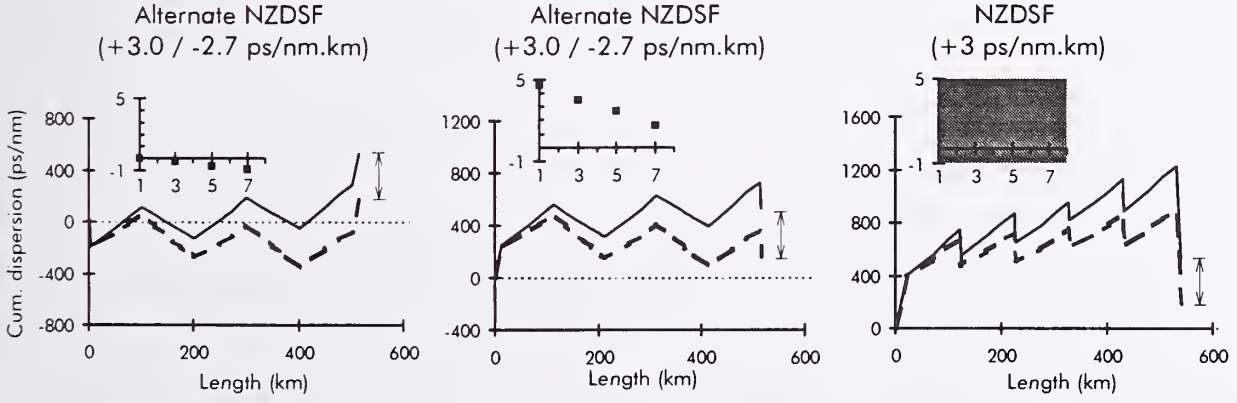

Figure 4 : Experimentol penolties (inset) ò 10^{-10} BER of every other chonnel in 8x10 Gbit/s tronsmission over three 500 km-long dispersion mops chorocterized by the some residuol dispersions. The groy oreo corresponds to error floors.

Another consequence is that, at 10 Gbit/s, residual dispersion cannot serve as a performance criterion. To illustrate this point, eight 200 GHz-spaced channels at 10 Gbit/s have been transmitted over five 100 km long spans with a realistic 28 dB loss per span. Five flat-gain, dual stage silica/fluoride amplifiers provide 5 dBm power per channel, yielding 23 dB SNR (in 0.1 nm bandwidth) at the end of the link. The transmission fiber consisted either of NZDSF with 3 ps/nm.km dispersion or alternate sections of NZDSF with 3 ps/nm.km and with -2.7 ps/nm.km dispersions. GVD compensation was achieved through DCF or SMF in the terminals and in-line when needed, but in the three investigated configurations, the residual dispersion is the same (350 ps/nm) for the multiplex central wavelength. The dispersion maps and the measured power penalties of every other channels are represented in Figure 4. It can be seen that the performance depends a lot on the transmission fiber, and, with the same transmission fiber, on the arrangement the dispersion compensating units in the terminals. Clearly, residual dispersion is not sufficient to assess the performance of a system.

Discussion and conclusion:

We have carried out experimental investigations of the limits induced by SPM, XPM and SRS individually in order to estimate their relative impact over several types of infrastructures. However, when all these phenomena are mixed altogether, as in an actual WDM transmission, a major difficulty is that the system power penalty is not just the sum of the individual penalties. Therefore, simulation tools are strongly recommended not only for performance evaluation but also for system design. In particular, we have conducted a comprehensive numerical investigation of dispersion management over several types of fiber infrastructures which coincide very well with the experimental results presented in this paper [14]. However, simulation tools require the characteristics of the fiber be accurately known, in particular the nonlinear index coefficient n_2, for which some measurement techniques have been shown.

Acknowledgement: The authors are grateful to Alain Bertaina and Gaëlle Le Meur for their contributions to this work.

References:

[1] A. Chraplyvy, "Limitations on lightwave communications imposed by optical fiber nonlinearities ", IEEE J. Lightwave Technol., vol. 8, pp. 1548-1557 (1990)

[2] L. Prigent et J.-P. Hamaide, "Measurement of fiber nonlinear Kerr coefficient by four-wave mixing", IEEE Photon. Technol. Lett., vol. 5, pp. 1092-1095 (1993)

[3] A. J. Taylor and G. Rodriguez, "Determination of n_2 by direct measurement of the optical phase", Optics Lett., vol. 21, n°22, pp. 1812-1814 (1996)

[4] L. P. Barry, J. M. Dudley, P. G. Bollond, J. D. Harvey and R. Leonhardt, "Simultaneous measurement of nonlinearity and dispersion using frequency resolved optical gating", Electron. Lett., vol. 33, pp. 707-708 (1997)

[5] M. Artiglia, R. Caponi, F. Cisternino, C. Naddeo, and D. Roccato, "A new method for the measurement of the nonlinear refractive index in optical fiber", Optical Fiber Technol., vol 2, pp. 75-79

[6] A. Fellegara, M. Artiglia, S. B. Andreasen, A. Melloni, F. P. Espunes, and S. Wabnitz, "COST 241 intercomparison of nonlinear refractive index measurements in dispersion shifted optical fibers at λ=1550 nm", Electron. Lett., vol. 33, n°13, pp. 1168-1169 (1997).

[7] T. Kato, Y. Suetsugu, M. Takagi, E. Sasaoka, and M. Nishimura, "Measurement of the nonlinear refractive index in optical fiber by the cross-phase modulation method with depolarized pump light", Optics Lett., vol. 20, n°9, pp. 988-990 (1995)

[8] L. Amato, A. Fellagara, P. Sacchatto, P. Boffi, A. Melloni, and M. Martinelli, "Polarization-independent Kerr coefficient measurement in optical fibers", Optics Lett., vol. 21, n°8, pp. 612-614 (1996)

[9] K. S. Kim, R. H. Stolen, W. A. Reed and K. W. Quoi, "Measurement of the nonlinear index of silica-core and dispersion-shifted fibres", Optics Lett., vol. 5, pp. 257-259 (1994)

[10] Y. Namihira, A. Miyata and N. Tanahashi, "Nonlinear coefficient measurements for dispersion shifted fibres using self-phase modulation at 1.55 μm", Electron. Lett., vol. 30, pp. 1171-1172 (1994)

[11] A. Boskovic, S. V. Chernikov, J. R. Taylor, L. Gruner-Nielsen and O. Levring, "Direct continuous-wave measurement of n_2 in various types of telecommunication fiber at 1.55 μm", Optics Lett., vol. 21, pp. 1966-1968 (1996)

[12] S. Bigo, S. Penninckx, M. W. Chbat , "Investigation of self-phase modulation limitation on 10 Gbit/s transmission over different types of fiber", Optical Fiber Communications Conference, paper FC2, San Jose, 22-27 Feb 1998.

[13] A. Bertaina, S. Bigo and M. W. Chbat, "Investigation of the limitations of WDM typical terrestrial transmissions over NZDSF and SMF", European Conference on Optical Communications, TuC11, Madrid, 20-24 Sep. 1998.

[14] A. Bertaina et al., to be submitted

Highly Accurate Nonlinear Coefficient Measurements by SPM Method for DSFs and Large Effective Area Fibers at 1.55μm

Yoshinori NAMIHIRA

KDD R&D Laboratories Inc.
2-1-15 Ohara, Kamifukuoka, Saitama 356-8502, Japan
Phone: +81-492-78-7801, FAX: +81-492-63-9328, E-mail: namihira@lab.kdd.co.jp

Introduction: Optical nonlinearites limit the maximum transmitted power through optical fibers and have become a serious problem in ultra-long distance transmission systems using Er-doped fiber amplifiers (EDFAs) such as transoceanic optical fiber undersea cable systems. Therefore, accurate determination of the nonlinear coefficient (n_2/A_{eff} ; n_2 is the nonlinear refaractive index, A_{eff} is the effective area [1]) of optical fibers is required for the amplifiered optical transmission systems. To date, the nonlinear coefficient of the optical fibers have been measured by using the self-phase modulation (SPM) method [2-5], the cross-phase modulation (XPM) method [6] and the four-wave mixing (FWM) method [7,8] at 1.55μm region.

This paper presents effect of chromatic dispersion in fiber length (DL) on the measurement accuracy of the nonlinaer coefficient and nonlinear refractive index measurements by the SPM method for the dispersion shifted fibers (DSFs) and the large effective area fibers (LEFs) for the first time.

Experiment: The experimental set-up of the nonlinear coefficient (n_2/A_{eff}) measurements for the various DSFs and the LEFs by the SPM method is shown in Fig.1 [5]. Wavelength tunable transform limitted (TL)-optical short pulse with variable repitition rates was generated by using a tunable CW laser source, a sinusoidally modulated InGaAsP electroabsorption (EA) modulator (JAE, FOEA-100B-023) [9], and a $LiNbO_3$ (LN) modulator. At first, ~650 MHz optical pulse train with pulse duration of 200 ps was generated by using the LN modulator driven by a pulse-pattern generator. To reduce the pulse width, the optical signal was modulated again by the EA modulator driven by 5 GHz sinusoidal wave [5]. The wavelength range was 1545-1565nm which was limited by the EDFA Gain bandwidth. The optical pulse width (FWHM, $\Delta\tau$) of around 21.7 ps was meausred by the autocorrelator (Oyokoden LAB, FEMTOWAVE Model 775) and the oscilloscope (HP 54120A). The autocorrelator trace of the obtained input optical short pulse is shown in Fig.2 [5]. From Fig.2, it was found that the optical pulse shape was almost Gaussian. The typical peak power P_0 of the optical pulse was around 1 W [5]. The spectral bandwidth $\Delta\nu$ was around 20.7 GHz. Accordingly, the time-bandwidth product of $\Delta\tau$ and $\Delta\nu$ was arround $\Delta\tau \cdot \Delta\nu \cong 0.45$, which means the optical pulse shape was very close to TL-Gaussian pulse. The output optical pulse was measured by the optical spectrum analyzer. As the input optical power increases, the maximum phase shift ϕ_{max} increases in proportion to the input peak power P_0, eventually wavelength spectra broadenes as shown in Fig.3. Fig.3 shows the output frequency spectra of the LEF of 6km long at $\phi_{max}=3.5\pi$. The (n_2/A_{eff}) was obtained from the relationship between the ϕ_{max} and P_0. The n_2 can be estimated from the (n_2/A_{eff}) multiplied by the A_{eff}. The mode field diameter (MFD) was measured by the variable aperture in the far field MFD measuring equipment (PK Technol. S25) [1]. From the far field pattern (FFP) of the output optical power $E(r)^2$, it is then possible to calculate the near field pattern (NFP) using Hankel transformation [1]. Accordingly, the A_{eff} can be derived from the NFP, $E(r)^2$ converted from the FFP. Here, A_{eff} was measured by the MFD measuring equipment with the software of NFP converted from FFP [1].

Results and Discussion: In the experiments, various DSFs and LEFs were measured, but the refractive index profiles (RIPs) were quite different. Here, DSFs 1, 2, and 4 are dual-shape core (DSC) RIP type as shown in Fig.4. Meanwhile, LEFs-2, 3 and

4 are segmented core (SGC) RIP type, and LEF1 is depressed segmented core (D-SGC) RIP type, respectively. In addition, LEF5 is special one, and it has Germanium (Ge) doped center core, and Fluorine (F) doped side (second) core and depressed cladding (F-DC) RIP.

Figs.5 (a) and (b) show (n_2/A_{eff}) and n_2 vs. chrmatic dispersion in fiber length (DL) of various DSFs and LEFs. Here, DL is given by eq.(1).

$$DL = - S_0 (\lambda_0 - \lambda) L \qquad (1)$$

where, λ_0 is zero-dispersion wavelength, S_0 is the dispersion slope at λ_0, λ is the measurment wavelength, and L is the fiber length.

From Figs.5 (a) and (b), it was found that the DL becomes larger, the values of (n_2/A_{eff}) and n_2 become smaller. It can be seen from Figs.5 (a) and (b), the experimental results of (n_2/A_{eff}) and n_2 are under estimated when the chromatic dispersion is large . Accordingly, it was confirmed that the DL limits of (n_2/A_{eff}) and n_2 measurement s for optical fibers were found to be less than -2.0 [ps/nm] at Region A for DSFs, and -8.0 [ps/nm] at region B for LEFs.

Figs.6 (a) and (b) show the SPM spectra of LEF2(SGC) at Point C (DL≅ -7.9 [ps/nm]) and Point D (DL≅ -28.4 [ps/nm]) as shown in Figs.5(a) and (b). It can be seen from Figs.6 (a) and (b) that there are great discrepancy of two SPM frequency spectra at $\phi_{max}=2.5\pi$ of the same LEF2(SGC) because of dispersion (DL) effects.

By considering DL limits, the nonlinear coefficient measurement results for various DSFs and LEFs at 1545-1565nm regions are summarized in Table 1 and Table 2, respectively. From Table 1, the averaged values of (n_2/A_{eff}) and n_2 for various DSFs were found to be around 4.86 x 10^{-10} [1/W] and 2.25 x 10^{-20} [m^2/W] , respectively. Also, from Table 2, it was found that the averaged values of (n_2/A_{eff}) and n_2 for various LEFs are around 2.49 (2.61) x 10^{-10} [1/W] and 2.00 (2.07) x 10^{-20} [m^2/W] , respectively. Here, ( ) means the averaged value obtained from without using LEF5(F-DC) data. The values of 2.25 x 10^{-20} [m^2/W] of DSFs and 2.00 (2.07) x 10^{-20} [m^2/W] of n_2 for various LEFs for random polarization states are in agreement with that of 2.1 - 2.3 x 10^{-20} [m^2/W] range of recently published results of the SPM [3-5], XPM [6] and FWM [7,8] methods, respectively.

Conclusion: By considering chromatic dispersion effect, a highly accurate nonlinear coefficient (n_2/A_{eff}) and nonlinear refractive index n_2 measurements in SPM at 1.55 μm was performed for the first time. It was clarified that the chromatic dispersion limits of (n_2/A_{eff}) and n_2 measurements were found to be less than -2.0 [ps/nm] for dispersion shifted fibers, and -8.0 [ps/nm] for large effective area fibers.

Acknowledgment: The author would like to thank M. Mure, Y. Tanaka of Oyokoden LAB. Co. Ltd., and M. Suzuki, I. Morita, H. Taga and Y. Matsushima of KDD R&D Labs. for their experimental supports, and also thank T. Muratani, K. Suzuki, Y. Mimura, and S. Akiba of KDD R&D Labs., for thier encouragement.

References:

[1] Y. Namihira, Electron. Lett., 30, 3, pp.262-263, 1994.
[2] K. S. Kim.et al., Optics Letters, vol.19, no.14, pp.257-259, 1994.
[3] Y. Namihira et al.,Electron. Lett., 30, 14, pp.1171-1172, 1994.
[4] R. H. Storen et al., OFC'95., FD 1, pp.312-313, 1995.
[5] Y. Namihira, OFMC'97, NPL,UK, pp.50- 53, 1997.
[6] T. Kato, et al., Optics Lett., 20, 9, pp.988-990, 1995.
[7] L. Prigent, et al., IEEE, Photonics. Technol. Lett., 5, 9, pp.1092-1095, 1993.
[8] A. Boskovic, et al., Optics Lett., 21, 24, pp.988-990, 1996.
[9] M. Suzuki et al., IEEE, JLT, vol.11, no.3,pp.468-473, 1993.

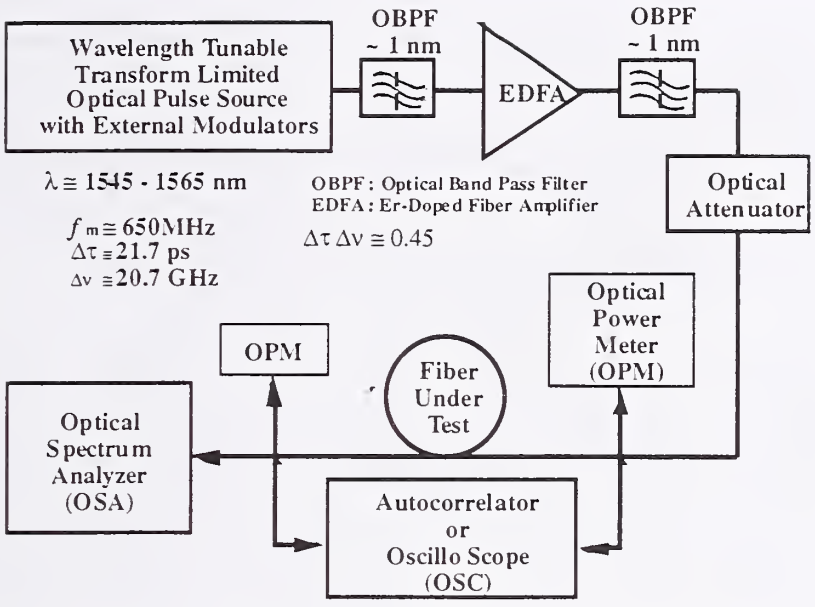

Fig.1 Experimental setup for nonlinear coefficient measurements of optical fibers using tunable transform-limited optical short pulse source with external modulators

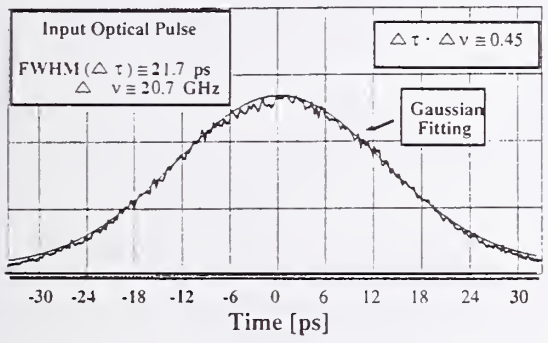

Fig.2 Input optical Transform-limited Gaussian pulse shape (measured by Autocorrelator)

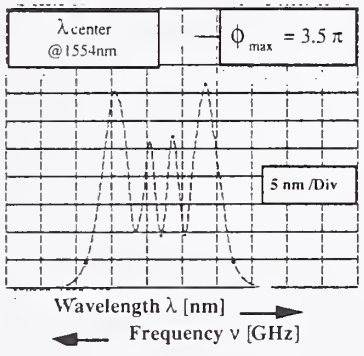

Fig.3 Output SPM frequency spectra of the LEF (L≅6km) [@ϕmax=3.5π]

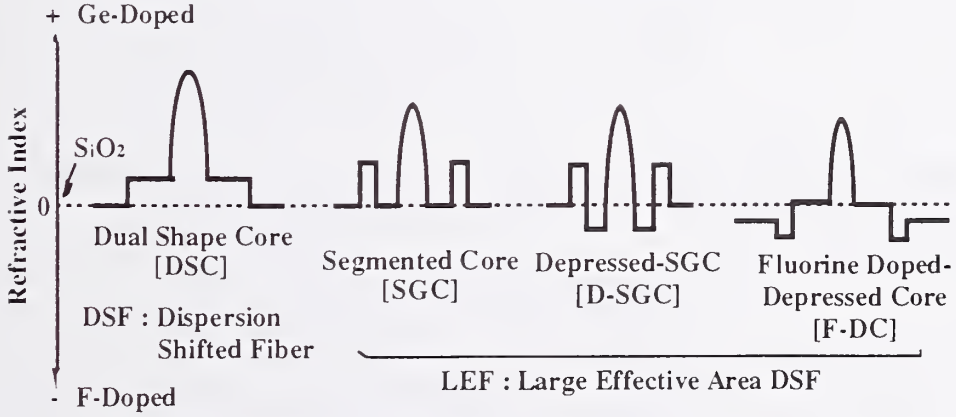

Fig.4 Various refractive index profiles (RIPs) of Dual-Shape Core (DSC), SegmentedCore (SGC), Depressed-Segmented Core(D-SGC), and Fluorine doped-DepressedCladding (F-DC)

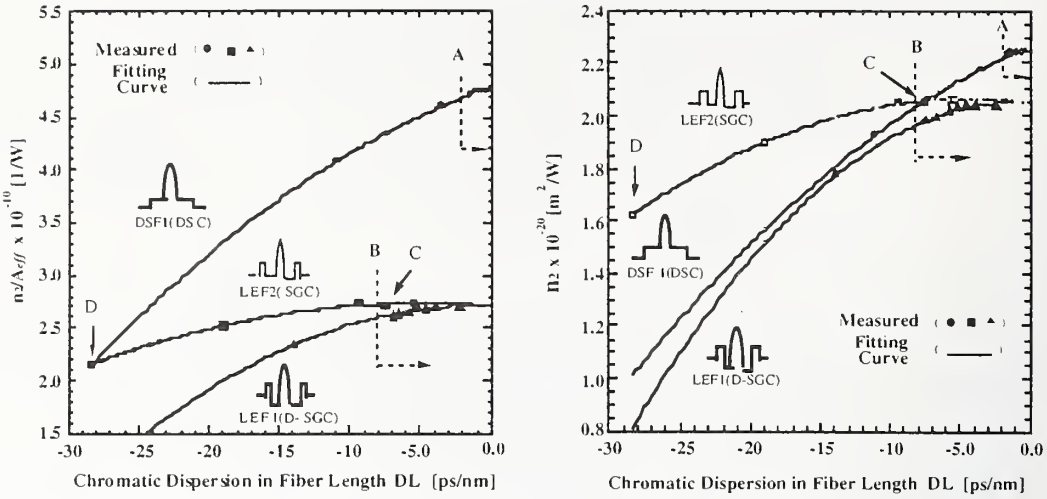

(a) n2/A*eff* vs. DL= - S0 (λ0 - λ) L (b) n2 vs. DL=- S0 (λ0 - λ) L

Fig.5 n2/A*eff* (a) and n2 (b) mesurements vs. chromatic dispersion in fiber length (DL)

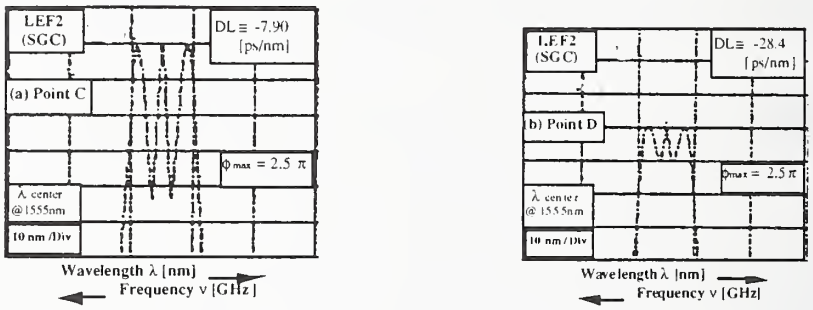

Fig.6 SPM frequency spectra of LEF2 at Point C (DL≅-7.9[ps/nm])
(a) and Point D (DL≅ -28.4[ps/nm]) (b)

Table 1 Nonlinear coefficient measurements results for various DSFs at 1545-1565 nm

DSFs	DL (*) [ps/nm]	A*eff* [μm²] @λ	n2/A*eff* [10^{-10}/W] @λ	n2 [10^{-20} m²/W] @λ
DSF1 (DSC)	- 1.29	47.3	4.90	2.32
DSF2 (DSC)	- 0.99	43.7	5.11	2.23
DSF3 (DSC)	- 1.66	46.6	4.99	2.21
(*) DL= - S0(λ0 - λ)L		Average	4.86	2.25

Table 2 Nonlinear coefficient measurements results for various LEFs at 1545-1565 nm

LEFs	DL (*) [ps/nm]	A*eff* [μm²] @λ	n2/A*eff* [10^{-10}/W] @λ	n2 [10^{-20} m²/W] @λ
LEF1 (D-SGC)	-6.87	75.6	2.71	2.05
LEF2 (SGC)	-5.54	75.3	2.77	2.09
LEF3 (SGC)	-7.90	76.7	2.69	2.06
LEF4 (SGC)	-3.34	92.0	2.26	2.08
LEF5 (#) (F-DC)	- 7.77	85.0	2.00 (#)	1.70 (#)
(*) DL= - S0(λ0 - λ)L		Average (wit hout #)	2.49 (2.61)	2.00 (2.07)
(#) Fluorine Doped Core				

Monitoring of optical signal quality using sum-frequency-generation optical sampling

Ippei Shake, Hidehiko Takara, Satoki Kawanishi and Yoshiaki Yamabayashi
NTT Optical Network Systems Laboratories
1-1 Hikari-no-oka, Yokosuka, Kanagawa, 239-0847 Japan

Introduction

One urgent problem to solve in realizing optical networks is monitoring the signal quality in the transmission fiber. A comprehensive and precise monitoring method is needed to determine failure location. Conventional digital networks commonly perform parity checking of the total bit sequence at each regenerator repeater for this purpose. One benefit of optical networks is their bit-rate or signal coding transparency [1], so the last measure we want to adopt is equipping line repeaters with bit-error monitoring or parity checking circuits at every monitoring point. The transparency would be lost because digital monitoring is workable only with predetermined bit-rates and frame formats. The new optical method proposed herein makes it possible to monitor the signal quality or signal-to-noise ratio (SNR) of a digital signal regardless of its bit-rate, frame format or even modulation format.

This method utilizes the sum-frequency-generation (SFG) optical sampling technique with the temporal resolution of 1 ps [2], and measures amplitude histograms of optical signals all-optically. Therefore, it can monitor the averaged quality (Q-factor) of optical signals in the optical networks with any bit-rate or coding. We also demonstrate averaged Q-factor monitoring of RZ or NRZ 10 Gbit/s optical signals using the SFG optical sampling method.

Principle

Figure 1 shows the fundamental configuration of the averaged Q-factor monitoring technique. The optical signal is split from the transmission line and fed to the Q-factor monitor system. Optical signal and optical sampling pulses are combined and injected into an SFG crystal in order to generate the cross-correlation signals (the SF lights). These signals are detected and the sampled values are processed to obtain an amplitude histogram.

Figure 2 shows the eye-diagram and the amplitude histogram. The amplitude histogram exhibits amplitude distributions in both mark and space levels. The Q-factor ($Q(t_0)$) is estimated from the amplitude histogram which is generally made at a fixed timing phase (t_0) in the pattern as opposed to the data eye [3]. It is defined by

$$Q(t_0) = | \mu_1(t_0) - \mu_0(t_0) | / (\sigma_1(t_0) + \sigma_0(t_0)) \qquad (1)$$

where $\mu_i(t_0)$ and $\sigma_i(t_0)$ are the mean and standard deviation of the mark(1) and space(0) levels at t_0, respectively. Whereas in this report, we define the averaged Q-factor (Q_{ave}) by

$$Q_{ave} = | \mu_{1,ave} - \mu_{0,ave} | / (\sigma_{1,ave} + \sigma_{0,ave}) \quad (2)$$

where $\mu_{i,ave}$ and $\sigma_{i,ave}$ are the mean and standard deviation of the mark(1) and space(0) levels of all sampled data, respectively. However, the sampled data obtained by optical sampling includes unwanted cross point data in the eye-diagram, which decrease the measured value of the averaged Q-factor. Thus, it is necessary to remove the cross point data. In this report, we set two threshold levels at $\mu_0+\alpha\mu$ and $\mu_1-\alpha\mu$. The coefficient α is defined to lie between 0 and 0.5. We regard histograms whose amplitudes are larger (smaller) than $\mu_1-\alpha\mu$ ($\mu_0+\alpha\mu$) as mark (space) level distributions. For both distributions, the means and standard deviations are determined. From these values, we can estimate the averaged Q-factor. Since this method measures the averaged Q-factor, it fundamentally doesn't need a clock recovery circuit and we can monitor the signal quality regardless of the bit-rate, frame format or even modulation format.

Experimental Setup

The Q-factor monitoring system is based on the optical sampling system that was reported previously [2]. We used either an NRZ optical signal or a RZ optical signal. The NRZ optical signal was generated by DFB laser and $LiNbO_3$ intensity modulator. The RZ optical signal was generated by a mode-locked Er-doped fiber laser and the same modulator. The wavelength λ_{Sig} of both lasers was 1553 nm. The bit-rate f_0 of the optical signal was 10 Gbit/s. The pulse width of RZ optical signal was 4.0 ps. The repetition rate of the sampling pulses was set to 9.7 MHz (f_0 /1024 GHz) minus the frequency offset Δf of 10 kHz. The pulse width and wavelength of the sampling pulse λ_{sam} were 0.41 ps and 1546 nm, respectively. The sampling pulses and signal were combined by an optical coupler and injected into a SFG crystal. The cross-correlation signals (the SF light) were detected with an APD and the sampled data was processed by the signal processing circuit. We measured the averaged Q-factor while changing the SNR using the optical attenuator placed before the Er-doped fiber amplifier in the transmission line. We also measured the bit-error-rate (BER) of the signal in the transmission line, and $Q(t_0)$ is estimated by equation (3) when the amplitude distributions are fit to a gaussian characteristic [3]

$$\mathrm{BER} = \mathrm{erfc}(Q(t_0)) \quad (3)$$

where erfc(x) is a complimentary error function.

Results and discussion

Figure 3 shows the measured amplitude histograms of the NRZ optical signal. At high SNR (Fig.3(a)), both peaks of mark and space are found clearly. Whereas for low SNR (Fig.3(b)), the mark peak level becomes lower and σ_1 becomes larger due to ASE noise from an Er-doped fiber amplifier in the transmission line. Figure 4 shows the relationship between the averaged Q-factor and $Q(t_0)$ calculated from measured BER for NRZ optical signal, when

signal SNR and coefficient α were changed. We can see that the averaged Q-factor changes with $Q(t_0)$. The maximum value of $Q(t_0)$ in this experiment is 16.5 dB which corresponds to the BER of 10^{-11}, so we expect this method can be used when the BER is less than 10^{-11}. According to Fig. 4, the optimum value of α is 0.3. In the cases of $\alpha < 0.2$ and $\alpha > 0.4$, the values of measured Q-factor fluctuate. The numbers of sampled points are not enough to decide the values of the mean and standard deviation in the case of $\alpha < 0.2$. In case of $\alpha > 0.4$, the sampled cross points of eye-diagram are included into either mark or space level and the mean and the standard deviation values are fluctuated. At $\alpha = 0.3$, the slope $\delta Q_{ave}/\delta Q(t_0)$ of linear fitting was 0.68, and a very high linear correlation coefficient of 0.99 was obtained. These results indicate that we can monitor signal quality by measuring the averaged Q-factor using this method. We can also know the BER by measuring the averaged Q-factor and referring to Figure 4 and equation (3).

Figure 5 plots the relationship between the averaged Q-factor and $Q(t_0)$ for the RZ optical signal. When α is 0.3, the slope of linear fitting is 0.68 and the linear correlation coefficient is 0.99, so we can also use this method for RZ optical signals. The pulse width of the RZ optical signal was 4.0 ps which is adequate for handling 100 Gbit/s optical signals, so this method can be applied to 100 Gbit/s TDM signals.

Conclusion

We have proposed a novel method of monitoring optical signal quality. This method utilizes a SFG optical sampling technique. We have confirmed that the NRZ or RZ optical signal quality at the BER of 10^{-11} can be estimated by this method, and that the averaged Q-factor measured by this method shows a strong correlation to $Q(t_0)$ calculated from the BER (the linear correlation coefficient is 0.99). It is expected that this method can monitor the signal quality of transmission systems at any bit-rate (up to 100 Gbit/s), any frame format, and even any modulation format.

Acknowledgment

The authors would like to thank Dr. Ikutaro Kobayashi for his encouragement.

References

[1] Paul. E. Green, Jr., "Optical Networking Update", *IEEE J. Select. Areas Commun.*, vol.14, No.5, pp. 764-779 (1996)

[2] H. Takara, S. Kawanishi, A. Yokoo, S. Tomaru, T. Kitoh and M. Saruwatari, "100 Gbit/s optical signal eye-diagram measurement with optical sampling using organic nonlinear optical crystal", *Electron. Lett.*, vol.32, No.24, pp. 2256-2258 (1996)

[3] Neal S. Bergano, F. W. Kerfoot, and C. R. Davidson, "Margin Measurements in Optical Amplifier Systems", *IEEE Photonics Tech. Lett.*, vol.5, No.3, pp. 304-306 (1993)

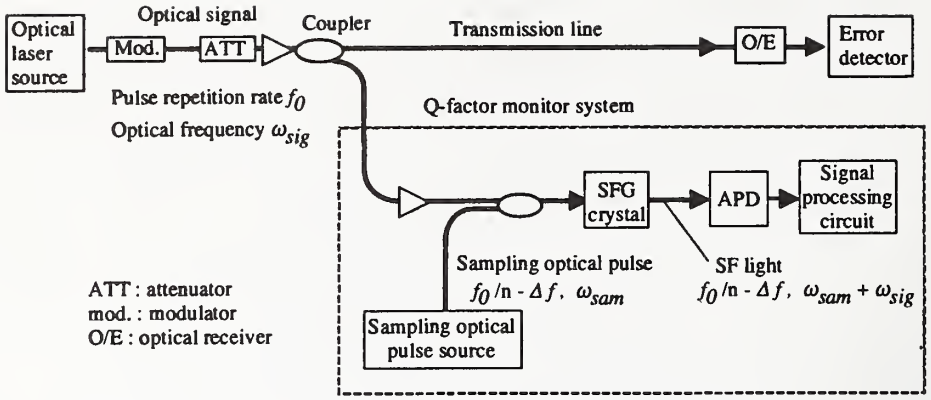

Fig. 1 Fundamental configuration for Q-factor monitoring

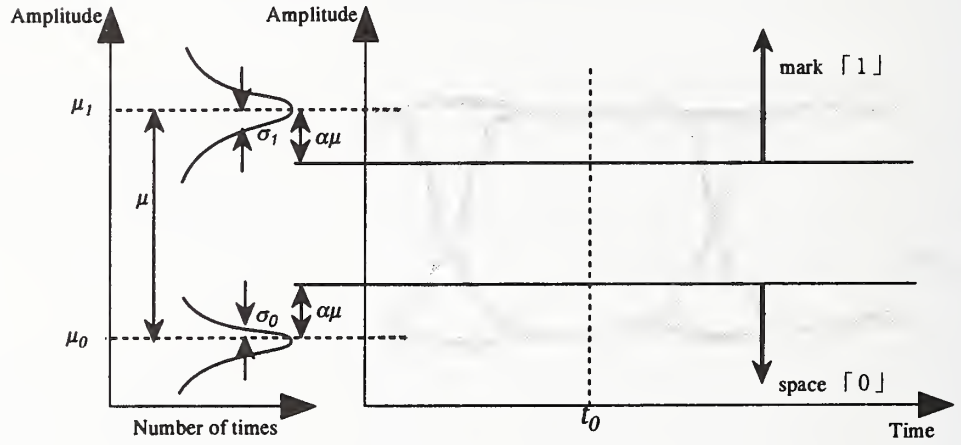

Fig. 2 Eye-diagram and amplitude histograms

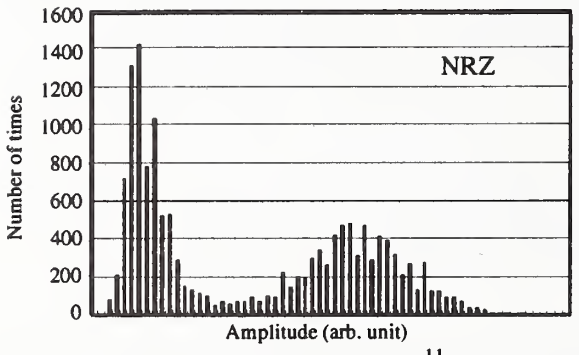

(a) high SNR (BER < 10^{-11})

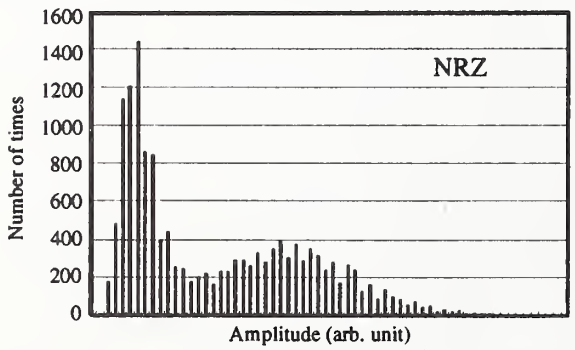

(b) low SNR (BER = 10^{-5})

Fig.3 Amplitude histograms of the NRZ optical signal

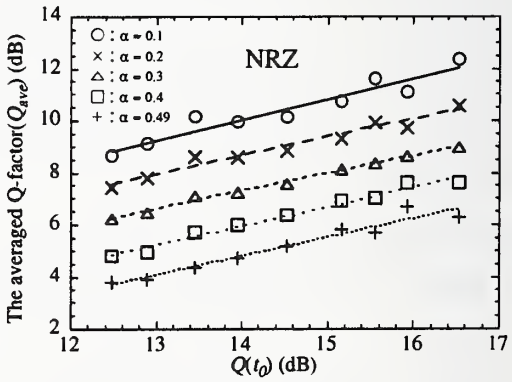

Fig. 4 Relationship between the averaged Q-factor and $Q(t_0)$ (NRZ optical signal)

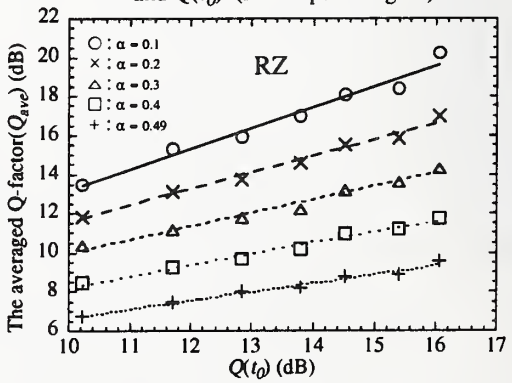

Fig. 5 Relationship between the averaged Q-factor and $Q(t_0)$ (RZ optical signal)

High Resolution Reflectometry for Diagnosis of Optical Devices by Synthesis of Optical Coherence Function

Kazuo Hotate and Takashi Saida

Department of Electronic Engineering, School of Engineering
The University of Tokyo
7-3-1 Hongo, Bunkyo-ku, Tokyo 113-8656, Japan

1. INTRODUCTION

The optical frequency of a laser diode (LD) can be controlled by directly modulating the injection current. In this way, many kinds of functional optical operations can be realized. For example, we can control the linewidth, i.e., the coherence length of the source by modulating the injection current with white noise. We have developed several optical sensing systems using this method, such as optical fiber interferometric sensors with linewidth control,[1, 2] and a quasi-heterodyne optical fiber sensor.[3]

Furthermore, We proposed and demonstrated that not only the coherence length but also the shape of the coherence function can be controlled and scanned by appropriately modulating the optical frequency of the laser source and the phase difference in an interferometer. We call the technique "the synthesis of optical coherence function."[4-8] It can be understood physically that a frequency modulation of the laser source produces a correspondent power spectrum in the view of time averaging. Thus a particular shape of coherence function, which is given as the Fourier transformation of the power spectrum,[9] is synthesized. The technique has found various applications in optical reflectometry, distributed and multiplexed fiber-optic sensing, and optical information processing with the advantages of neither post-calculations nor mechanical scanning.

In this presentation, the principle of the synthesis of optical coherence function is summarized, and a typical synthesized coherence function, delta-function-like coherence function, are given. The performance deterioration factors and correspondent countermeasures are shortly discussed. Then, the reflectometry systems for diagrosis of optical devices are shown.

2. SYNTHESIS OF OPTICAL COHERENCE FUNCTION

2.1 Principle of the synthesis of optical coherence function [6-13]

Consider a modified Mach-Zehnder interferometer with a phase modulator at one of the two arms as shown in Fig. 1. The visibility of the interference pattern observed at the screen is defined as [9]

$$V = \frac{I_{\max} - I_{\min}}{I_{\max} + I_{\min}} = \frac{2\sqrt{I_1 I_2}}{I_1 + I_2}|\gamma(\tau)|, \tag{1}$$

where $I_{\max}$ and $I_{\min}$ are the local maximum and minimum intensities, I_1 and I_2 the intensities from arm I and arm II, respectively, τ the differential time delay between the two arms, and $|\gamma(\tau)|$ the optical coherence function. In general, the optical coherence function is determined by the optical spectral characteristics of the light source.[9]

When we synchronously modulate the optical frequency of the laser source and the phase difference in stepwise waveforms of N steps, the optical coherence function can be expressed as

$$|\gamma(\tau)| = \frac{\left|\sum_{n=1}^{N} k_n \exp(j2\pi f_n \tau)\right|}{\sum_{n=1}^{N} |k_n|}, \tag{2}$$

$$k_n = t_n \exp(-j\phi_n), \tag{3}$$

where f_n, ϕ_n and t_n are the optical frequency shift, the differential phase shift and the time duration at the nth

step of the modulations. Because Eq. (2) is in the form of a Fourier series with a complex coefficient k_n, the coherence function $\gamma(\tau)$ can be synthesized into any arbitrary shapes theoretically by modifying the parameters f_n, ϕ_n and t_n appropriately, i.e., by appropriate waveforms of the frequency and phase modulations. For example, the modulations shown in Figs 1(a) and (b) will produce a coherence function of triangle shape as shown in Fig. 1(c). In practice, we have synthesized coherence functions, such as a notch-shaped function, a square-shaped function and a sharp notch-shaped function.[14,15]

The coherence function can be scanned by the phase modulation. When the phase ϕ_n is modulated in proportion to the optical frequency shift as $\phi_n = 2\pi f_n \kappa$, Eq. (2) becomes

$$|\gamma(\tau)| = \frac{\left|\sum_{n=1}^{N} t_n \exp\left[j2\pi f_n(\tau-\kappa)\right]\right|}{\sum_{n=1}^{N} t_n}. \tag{4}$$

It can be seen that the coherence function is scanned by the delay of κ.

One of the most useful synthesized coherence function may be that of the delta-function-like shape, which has been applied for various distributed information detection systems. When the stepwise optical frequency modulation is equally spaced as shown in Fig. 2(a), delta-function-like peaks are synthesized, which is shown in Fig.2(c). Additionally we can see that the peaks can be scanned by adjusting the κ, the phase modulation parameter. Even when $\kappa = 0$, i.e., the phase modulator is not used, the peaks are still movable by adjusting the frequency modulation parameter Δf except for that at $z = 0$. The full width at half maximum (FWHM) of the peak in terms of distance, which determines the spatial resolution of the system, and the period of the peaks, which determines the detection range of the system, are given, respectively, as

$$z_{reso} = \frac{c}{2Nf_s}, \tag{5}$$

$$z_{range} = \frac{c}{2f_s}. \tag{6}$$

2.2 Performance deterioration factors and countermeasures [16-19]

As a technique using discrete modulation, the method suffers the problem of subpeaks in the synthesized coherence function, which limits the dynamic range of the system. By the phase modulation with properly designed ϕ_n and t_n, the Hanning or Hamming window function can be introduced to suppress the subpeaks.[19] Those window functions can also be realized by the frequency modulation with properly designed f_n and t_n.

When modulating the optical frequency directly by the injection current of the LD, the major difficulties come from the nonlinearity between the optical frequency and the injection current amplitude, and the frequency modulation (FM) response of the LD. Both deteriorate the shape of the synthesized coherence function. In the case of delta-function-like coherence function, the width of the peaks are broaden, i.e., the system resolution is deteriorated.

The nonlinearity between the injection current and the optical frequency can be compensated by pre-distortion in the frequency modulation waveform. To do so, an accurate knowledge of the transfer function between the current and the frequency is needed. We have developed an interferometric method to measure the dynamic relationship between them. To cope with the FM response of the LD, a countermeasure employing an inverse filter and an optical gate is developed. The inverse filter compensates the FM response roughly, while the optical gate suppresses the residual deterioration by masking the transient parts in the modulation steps.

3. HIGH RESOLUTION REFLECTOMTRY BY SYNTHESIS OF COHERENCE FUNCTION[4, 5, 10,11,17,19]

A high resolution optical reflectometry is of increasing interest as a powerful tool to evaluate fiber-optic and waveguide devices. Though various methods, such as the optical low coherence reflectometry (OLCR) [20] and the frequency modulated continuous wave (FMCW) reflectometry,[21,22] have been developed for the

purpose, there are still some difficulties, such as the need of a high speed modulation/detection technique, mechanical moving parts and large amount calculations. Those difficulties will introduce further limitations in detection ability and stability.

On the contrary, we have proposed an optical coherence domain reflectometry (OCDR) [4, 5, 17] and a phase modulated optical coherence domain reflectometry (p-OCDR) [7, 8, 16] by synthesis of the coherence function. They synthesize the coherence function into the delta-function like peak as discussed in 2.1. When the modulation parameters are chosen so that only one coherence peak exits in the device under test, the reflected light intensity at the peak position can be selectively detected. The OCDR does not utilize the phase modulation, and scans the coherence peak by adjusting the frequency modulation parameters, while the p-OCDR scans the coherence peak by the phase modulation. Generally speaking, the compensation of the non-linearity in the optical frequency modulation in the p-OCDR is much simpler than that in the OCDR. Besides, the p-OCDR is more tolerant of the non-ideal factors in the optical frequency modulation, because it detects the 0th-order coherence peak of small time delay difference, while the OCDR uses the 1th-order peak for detection.

Fig. 3 shows the experimental setup of the p-OCDR. It is a heterodyne interferometer with a three electrode distributed feedback laser diode (DFB-LD) as the light source. The optical frequency is directly modulated via the injection current into the center electrode. A phase modulation is adopted to scan the coherence peak. The interference signal is detected with the balanced detector and demodulated by the narrow band pass filter (BPF) and the square-law detector. Fig. 4 shows an example of the reflectivity distribution measured by the p-OCDR. The spatial resolution of about 1.2 mm is achieved.

4. LONG RANGE REFLECTOMTRY BY SYNTHESIS OF COHERENCE FUNCTION [23, 24]

In recent years, for installing and maintaining the optical subscriber networks, measurements of reflectivity distribution at a distance of several kilometers with centimeter spatial resolution are required. Among present methods of reflectometry, it is difficult to realize the cm-resolution for time domain methods. The FMCW method may be a candidate with its high spatial resolution and wide dynamic range [31], but its measurement time should get much shorter than its present status for avoiding the optical phase noise due to environmental fluctuation over a long fiber.

On the other hand, we have developed a solution by the synthesis of optical coherence function as shown in Fig. 5. It is basically the same as the p-OCDR, except for an acousto-optic (AO) switch after the DFB-LD source. The AO switch generates a series of optical pulse. The optical pulse forms a window to determine a test region along the tested fiber, because a pulse from the reference path can meet a pulse from the path of the tested fiber only when the two paths have nearly the same lengths. While, the coherence function is synthesized so that there is only one coherence peak inside the region under test, and other periodical coherence peaks are masked by the window. Therefore, the width of the window is set shorter than the spacing of the coherence peaks. Consequently, the reflectivity distribution inside the window can be measured by scanning the coherence peak. For measurement outside the window, the reference delay need to be changed to determine another region. An example of reflectivity distribution obtained by this system is shown in Fig. 6. Two reflections of around -30 dB from optical connectors can be seen clearly, while the reflection at the end of the fiber is completely suppressed by the pulse window. The spatial resolution is 6 cm inside a region of 8 m after 5 km optical fiber.

The system can test the reflectivity at one location in one period of the optical frequency modulation waveform, which is about 80 μsec in the experiment It corresponds to a frequency sweep-rate of higher than 23 THz/sec in the FMCW method. It is very difficult to realized a continuous linear optical frequency sweep at that rate with presently available laser devices.

We have also demonstrated another configuration using an optical fiber loop with frequency shifter as the light source, which is shown in Fig. 7[26]. The system can select the test region by simply tuning the center frequency of the BPF, instead of changing the delay lines. Figure 8 shows the reflectivity distribution measured by the system with 13cm resolution..

5. CONCLUSION

In this presentation, the principle of the technique "synthesis of optical coherence function" is summarized. It has been demonstrated that, by the optical frequency modulation and the phase modulation, actually arbitrary coherence function can be synthesized for different applications. One of the most useful synthesized coherence function is that of the delta-function-like shape, which has found many applications in distributed

information detection. In this preseatation, the high resolution and the long range reflectometry have especially been discussed. Additionally, we have already proposed, with this technique, the 2-D and 3-D information processing such as optical tomography of scattering medium[27-32], and distributed and multiplexed fiber-optic sensing[33-35]. In these applications, the technique is featured as a full optical processing with neither mechanical scanning nor digital processing, compared with the OLCR and FMCW methods. The spatial resolution of the technique is inversely proportional to the tunable range of the laser source. It is expected to be improved to several tens of micrometers by using a widely tunable LD, such as the super-structure grating distributed Bragg reflector (SSG-DBR) LD.[36]

ACKNOWLEDGMENTS

The authors would like to thank Zuyuan He for his support in the prparation of this manuscript.

REFERENCES

1. D. T. Jong and K. Hotate, *Proc. OFS-6*, pp. 94-100, Paris, 1989.
2. K. Hotate, N. Okumura, M. Higashiguchi and N. Niwa, *Opt. Lett.*, vol. 7, no. 7, pp. 331-333, 1982.
3. K. Hotate and D. T. Jong, *Appl. Opt.*, vol. 28, no. 7, pp. 1289-1297, 1989.
4. K. Hotate and O. Kamatani, *Electron. Lett.*, vol. 25, pp. 1530-1505, 1989.
5. K. Hotate and O. Kamatani, *J. Lightwave Technol.*, vol. 11, no. 10, pp. 1707-1709, 1993.
6. K. Hotate, Optical Fiber Technology, vol. 3, no.4, pp.356-402, 1997. [Invited]
7. K. Hotate, T. Saida and Z. He, *Proc. Intl. Conf. on Applied Optical Metrology*, Balatonfuered, 1997. [Invited]
8. K. Hotate, Z. He and T. Saida, *Proc. SPIE's 43rd Annual Meeting*, San Diego, 1998. [Invited]
9. M. Born and E. Wolf, *Principle of Optics*, 5th edition, New York: Pergamon Press, 1975, Chapter X.
10. K. Hotate and T. Saida, *Proc. OFS-10*, pp. 534-537, Glasgow, 1994.
11. K. Hotate and T. Saida, *Electron. Lett.*, vol. 31, pp. 475-476, 1995.
12. K. Hotate, T. Okugawa and T. Saida, *Proc. SPIE*, vol. 2507-8, pp. 66-77, Munich, 1995. [invited]
13. K. Hotate and T. Saida, *Proc. CLEO Pacific Rim'95*, p. 53, Chiba, 1995. [invited]
14. T. Okugawa and K. Hotate, *Proc. CLEO Pacific Rim'95*, p. 156, 1995.
15. T. Okugawa and K. Hotate, *Photon. Technol. Lett.*, vol. 8, pp. 1710-1712, 1996.
16. K. Hotate and T. Okugawa, *J. Lightwave Technol.*, vol. 12, no. 7, pp. 1247-1255, 1994.
17. O. Kamatani and K. Hotate, *J. Lightwave Technol.*, vol. 11, no. 11, pp. 1854-1862, 1993.
18. K. Hotate and T. Saida, *Proc. SPIE*, vol. 2294, pp. 22-31, San Diego, 1994.
19. T. Saida and K. Hotate, *Proc. OFS-11*, pp. 398-401, Sapporo, 1996.
20. K. Takada, *J. Lightwave Technol.*, vol. 14, pp. 1677-1689, 1996.
21. U. Glombitza and E. Brinkmeyer, *J. Lightwave Technol.*, vol. 11, pp. 1377-1384, 1993.
22. R. Passy, N. Gisin, J. P. von der Weid and H. H. Gilgen, *J. Lightwave Technol.*, vol. 12, pp. 1622-1630, 1994.
23. T. Saida and K. Hotate, *Proc. CLEO'97*, pp. 419-420, Baltimore, 1997.
24. T. Saida and K. Hotate, *Photon. Technol. Lett.*, vol. 10, no. 4, pp.419-420, 1997.
25. K. Tsuji, K. Shimizu, T. Horiguchi and Y. Koyamada, *Electron. Lett.*, vol. 33. pp. 408-410, 1997.
26. T. Saida and K. Hotate, *Proc. IOOC/ECOC'97*, pp. 283-286, Edinburgh, 1997.
27. K. Hotate and T. Okugawa, *Opt. Lett.*, vol. 17, no. 21, pp. 1529-1531, 1992.
28. T. Okugawa and K. Hotate, *Photon. Technol. Lett.*, vol. 8, pp. 257-259, 1996.
29. T. Okugawa and K. Hotate, *Optical Review*, vol. 1, no. 1, pp. 8-11, 1994.
30. Z. He, T. Okugawa, N. Mukohzaka and K. Hotate, *Proc. CLEO'96*, CPD4, Anaheim, 1996.
31. Z. He, T. Okugawa, N. Mukohzaka and K. Hotate, *Proc. SPIE*, vol. 2899, pp. 222-229, Beijing, 1996.
32. Z. He, N. Mukohzaka and K. Hotate, *Photon. Technol. Lett.*, vol. 9, no. 4, pp. 514-516, 1997.
33. T. Saida and K. Hotate, *Photon. Technol. Lett.*, vol. 9, no. 4, pp. 484-486, 1996.
34. B. Zhu and K. Hotate, *Proc. CLEO Pacific Rim'97*, pp. 257-258, Chiba, 1997.
35. B. Zhu and K. Hotate, *Proc. OECC'98*, Chiba, 1998.
36. H. Ishii, H. Tanobe, F. Kano, Y. Tohmori, Y. Kondo and Y. Yoshikuni, *J. Quantum Electron.*, vol. 32, no. 3, pp. 433-441, 1996.

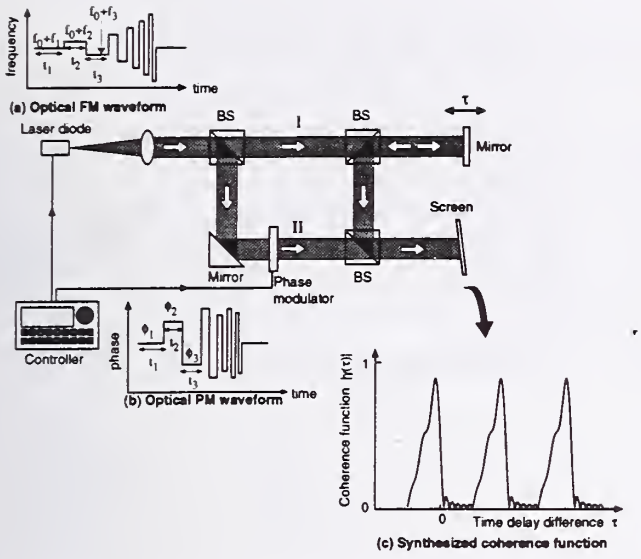

Fig. 1 Basic configuration of synthesis of optical coherence function. (a) Frequency modulation waveform, (b) phase modulation waveform, and (c) synthesized coherence function.

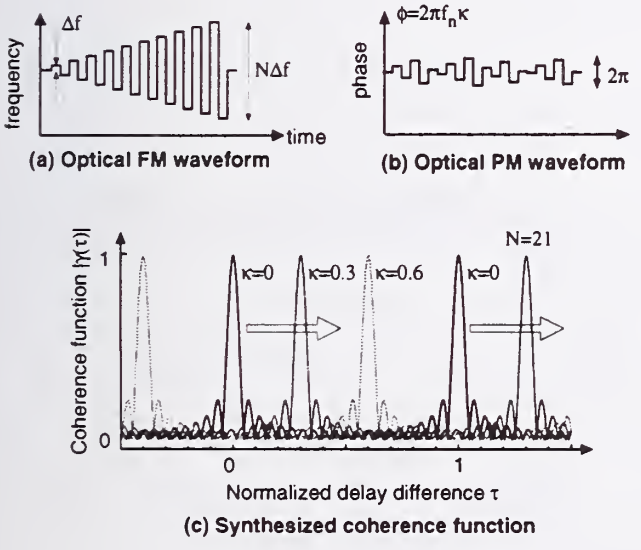

Fig. 2 Synthesis and scanning of the coherence peak by synchronous frequency modulation and phase modulation.

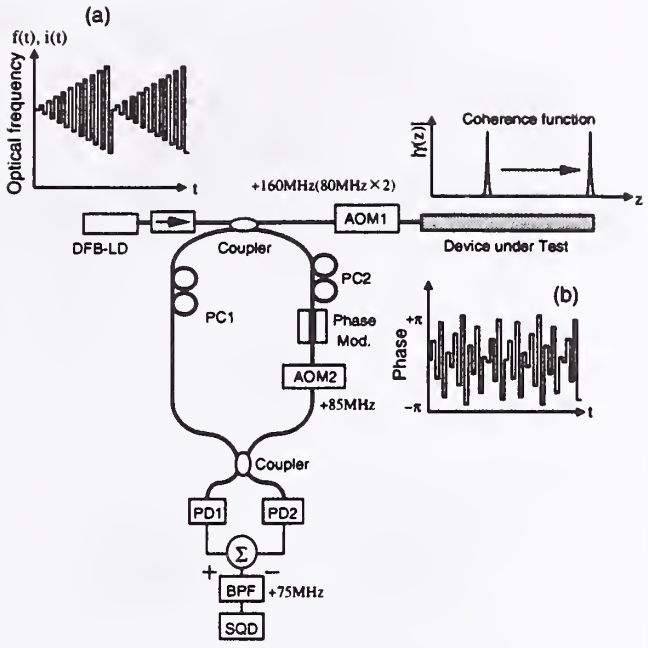

Fig. 3 Experimental setup of phase-modulated optical coherence domain reflectometry by synthesis of the optical coherence function.

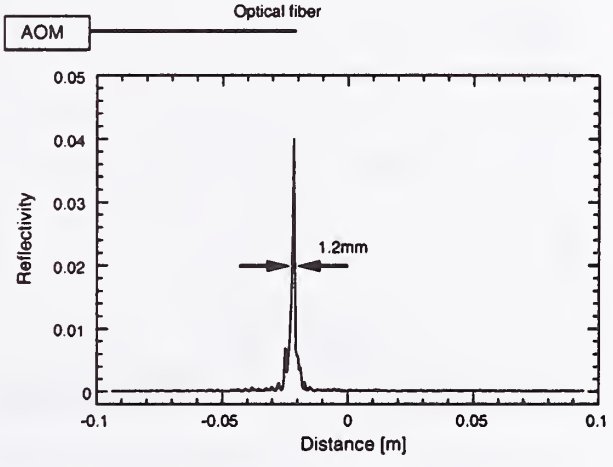

Fig. 4 Reflectivity distribution measured by the phase-modulated optical coherence domain reflectometry.

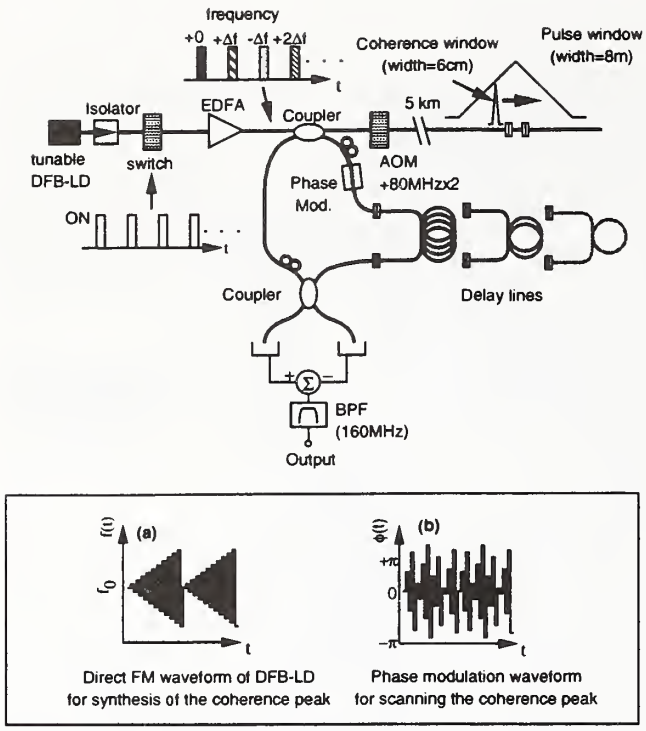

Fig. 5 Experimental setup of long-range reflectometry by synthesis of the optical coherence function.

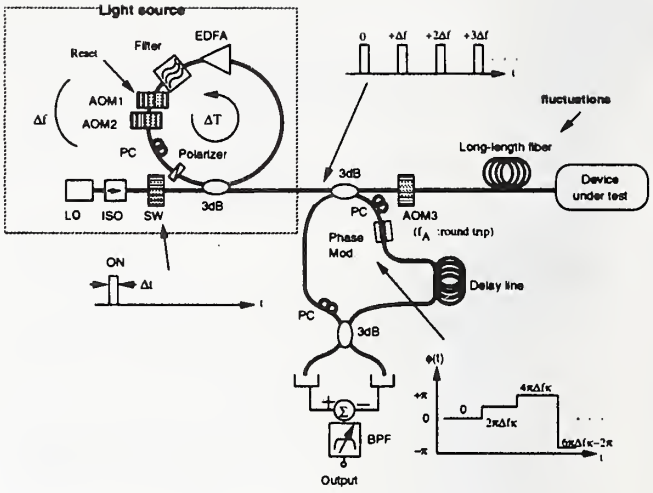

Fig. 7 Experimental setup of long-range reflectometry by synthesis of the optical coherence function using the optical delay loop with a frequency shifter.

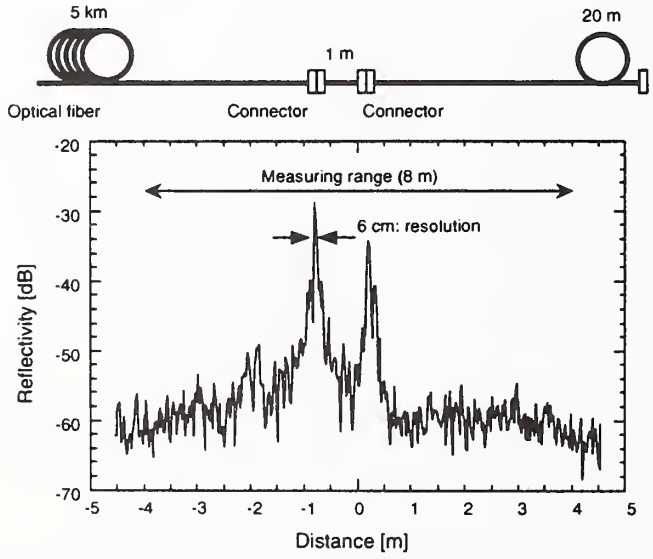

Fig. 6 Reflections at two connectors located at 5 km distance measured by the long-range reflectometry.

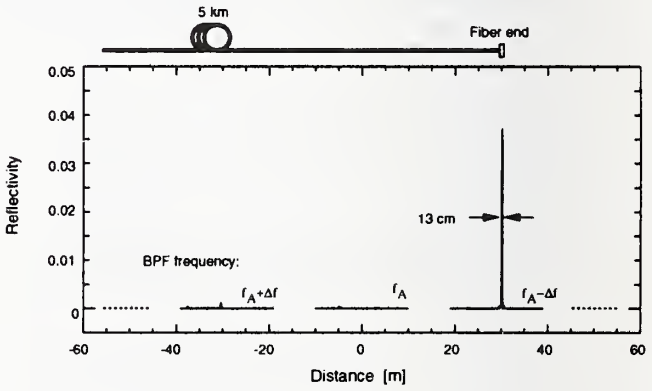

Fig. 8 Reflectivity distribution measured at 5 km distance with changing the measurement ranges.

Distributed-Gain Measurements of Erbium-Doped Fibers

J. F. von der Weid, A. O. Dal Forno, J. A. Pereira da Silva and R. Passy
Center for Telecommunications Studies - Catholic University of Rio de Janeiro (Brazil)
Rua Marques de São Vicente 225 - Gávea - Rio de Janeiro, RJ 22453-900
M. R. Xavier de Barros
CpqD -Telebrás (Brazil)
B. Huttner and N. Gisin
Group of Applied Physics - University of Geneva (Switzerland)

Abstract

A non-desctructive optimum gain calibration of erbium-doped fiber amplifiers was achieved by using the Coherent Optical frequency Domain reflectometry. The Coherent OFDR detection technique intrinsically filters ASE, allowing precise measurements of Rayleigh Backscattering levels.

Introduction

Optical amplifiers based on erbium-doped fiber have enabled tremendous increases in the capacity and functionality of optical networks. One of the key parameter in an EDFA fabrication is the ideal length of the doped fiber, which is normally calculated theoretically [1]-[2]. However, the practical determination of the optimum length for maximum gain is done with a cutback method, which is a destructive technique and very inconvenient due to the high cost of the Erbium doped fiber. The distributed gain in non-isolated long EDFA's could be measured with OTDR by employing optical filters to eliminate ASE but only long, of the order of some kilometers, and low doped fibers could be measured due to the limited resolution of the technique [3]. Coherent Optical Frequency Domain Reflectometry (C-OFDR) is a very powerful technique for the characterization of return loss of optical components with high dynamic range and sensitivity [4]. Because of the coherent detection technique, ASE is naturally filtered so that C-OFDR is specially indicated for the characterization of optical circuits with gain and ASE features. Return loss and gain measurements were indeed performed with this technique [5]. Here we present C-OFDR measurements of the distributed gain of Erbium doped fibers for optimum length determination for different amplifier applications.

Experiment

C-OFDR is based on the detection of the beat signal generated in a Michelson interferometer when the optical frequency of a laser source is swept linearly. One of the arms gives a reference

reflection, whereas the other is connected to the fiber under test. The sensitivity of the technique is determined by the laser intensity and its intensity noise, whereas the maximum detectable range is given by the laser linewidth. In our experimental setup we used a three electrodes semiconductor laser coupled to an external cavity in order to increase its coherence length [6]. When coupled to the external cavity the laser linewidth decreased from ~2 MHz to ~5 kHz, so that Rayleigh backscattering levels could be measured in the kilometre range. The OFDR probe power was -14 dBm, and the coherence loss due to the finite linewidth of the laser is $\eta = 0.013$ dB/m, so that the maximum coherence correction within our full 100 m measurement range will be 1.3 dB. The spatial resolution depends on the range of the measurement, being ~ 20 cm in the particular 100 m range presented here. Figure 1 presents the experimental set-up, in which the detailed configuration of the OFDR reflectometer is the same as described before [6]. The optical isolator was used when small signal gain measurements were performed. The isolator reduced the probe intensity to -40 dBm without any further reduction of the Rayleigh backscattering signal detected by the OFDR. Also 20 m of a standard single mode fibre were spliced to the WDM pigtail in order to provide a reference Rayleigh backscatter signal. The Fiber under test was a 120 m long, 120 ppm Er^{3+} doped fibre fabricated at CpqD-Telebrás.

Results

Figure 2 shows the small signal gain curves of a 80 m long fiber obtained from the OFDR measurement of the Rayleigh backscattering signal. Here the probe power was -40 dBm, and the curves clearly shows that the optimum length is strongly dependent of the pump power, the optimum length being 40 m for 19.8 dBm pump power, and the corresponding gain is 25.7 dB. The fiber was cut at 40 m in order to measure the gain, which was 24.5 dB, slightly less than the OFDR result. This difference can be explained by the fact that the cutback measurement includes splices and connections other than the OFDR, which measures the fiber gain only. Also, the coherence loss of 40 m contributes with a ~0.6 dB additional decrease in the OFDR measurement, so that the agreement between the two methods is remarkable.

A numerical simulation based on the Er^{3+} doped fiber parameters was performed in order to evaluate the gain along the fiber, figure 3. The optimum length obtained by the numerical analysis shown to be longer than the values found experimentally with average difference around 7 meters. In the worst case, this optimum length difference produced a gain difference of 2 dB, figure 4. Practically, the use of numerical simulation for the optimum length determination implies an accurate knowledge of the injected pump power in the Er^{3+} doped fibre which can be dificult to determine without a spatially resolved reflectometry technique due to splice losses and insertion losses on the WMD coupler, filters and isolators.

Large signal gain curves are presented in figure 5, and were measured with a modified set-up in which a second laser was connected to the amplifier via an optical 3 dB coupler, launching - 3 dBm into the amplifier. This second laser wavelength was only ~50 GHz away from the probe wavelength (1557.6 nm) so that the depleted gain curve corresponds to the same probe wavelength. As it can be seen in figure 5, the optimum length in this condition decreased to ~20 m with ~12 dB gain for the maximum pump power.

Conclusions

The distributed-gain of Erbium-doped fibres was measured with coherent Optical Frequency-Domain reflectometry. Because of its coherent detection technique, OFDR naturally filters the ASE within the 100 kHz detection bandwidth. Although filtered, the ASE white beat noise limits the detector amplifier gain, increasing the noise floor of the measurement. Our experiments place the OFDR technique as a powerful technique for fibre Lasers and Amplifier manufacturers for WDM system applications.

Acknowledgements

This work was partially supported by CPqD Telebrás under the contract JPqD 779/97, Brazilian National Research Council CNPq, Swiss CTI Project 3160, and the European ACTS Bliss AC065 project.

References

[1] F. F. Rühl, "Calculation of Optimum Fiber Lengths for EDFAs at arbitrary pump wavelengths", *Electron. Lett.*, (1991), Vol. 27, No. 16, pp. 1443-1445.

[2] M. Lin and S. Chi, "The Gain and Optimal Length in the Erbium-Doped Fiber Amplifiers with 1480 nm Pumping", *IEEE Photonics Technol. Lett.* (1992) Vol. 4, No. 2, pp. 354-356.

[3] M. Nakazawa, Y. Kimura and K. Suzuki, "Gain-Distribution Measurement along an Ultralong Erbium Doped Fiber Amplifier using Optical Time Domain Reflectometry", *Optics Lett.* (1990), Vol. 15, No. 1, pp. 1200-1202.

[4] J. P. von der Weid, R. Passy, G. Mussi and N. Gisin, "On the Characterization of Optical Fiber Network Components with Optical Frequency Domain Reflectometry", *IEEE J. Lightwave Technol.* (1997), Vol. 15, No 7, pp. 1131-1141.

[5] J. P. von der Weid, R. Passy and N. Gisin, "Coherent Reflectometry of Optical Fiber Amplifiers" *IEEE Photonics Technol. Lett.* (1997) Vol. 9, No. 9, pp 1253-1255.

[6] J. P. von der Weid, R. Passy and N. Gisin, "Mid range coherent optical frequency domain reflectometry with a DFB laser diode coupled to an external cavity", *IEEE J. Lightwave Technology* (1995), Vol. 13, 5, 954-960.

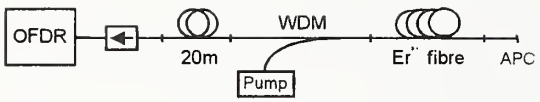

Figure 1 - Experimental setup for small gain measurements

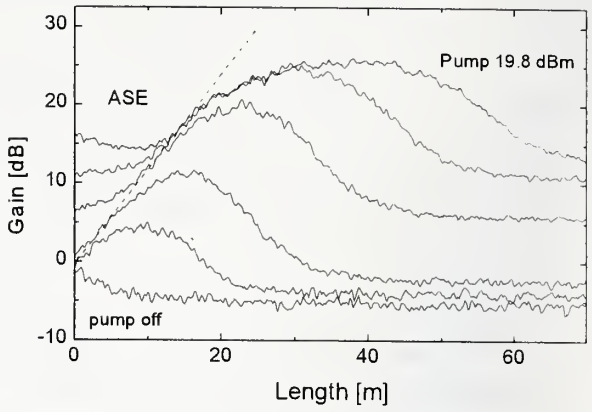

Figure 2 - Small signal gain curves of a 120 ppm Erbium doped fiber for co-propagating pump and signal. Intermediated curves were taken each 3 dB pump level.

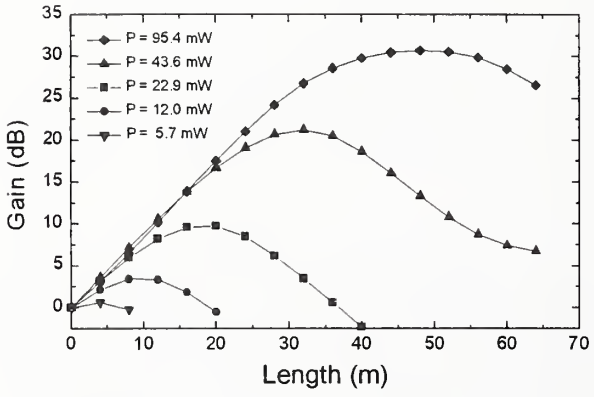

Figure 3 - Simulated distributed gain.

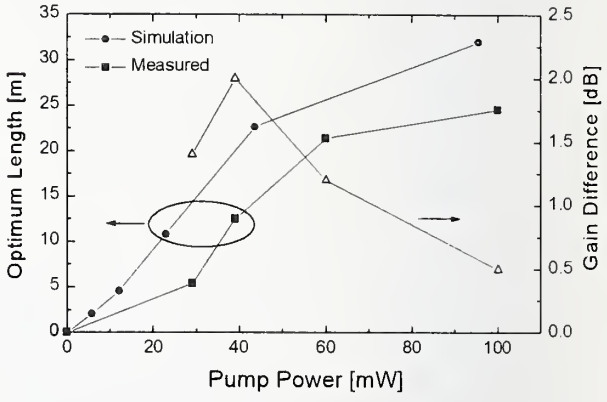

Figure 4 - Optimum length as fuction of pump power and gain difference between calculated and measured length.

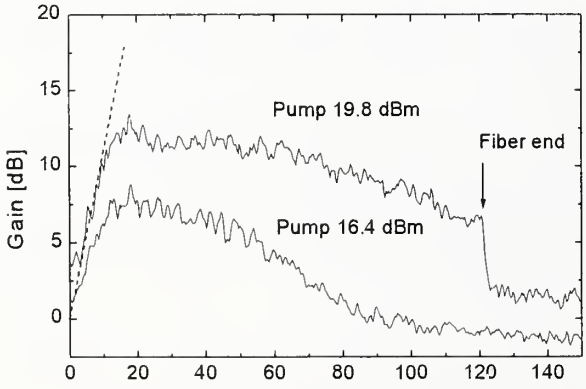

Figure 5 - Large signal gain curves of a 120 m long 120 ppm Erbium doped fiber.

POLARISATION OFDR FOR MEASUREMENTS OF BIREFRINGENCE AND POLARISATION MODE COUPLING LENGTHS IN OPTICAL FIBRES

B. Huttner, J. Reecht and N. Gisin (1)
R. Passy and J.P. von der Weid (2)

(1) Group of Applied Physics
University of Geneva
20 Rue de L'Ecóle de Medecine,
CH1211, Geneva 4, Switzerland

(2) Center for Telecommunication Studies
Pontificia Universidade Catolica do Rio de Janeiro
Rua Marques de Sao Vincente 225, Rio de Janeiro, 22453-900 Brazil

Abstract: Measurements of the intrinsic birefringence of optical fibres is performed at 1550 nm using the Optical Frequency Domain Reflectometry technique. Polarisation mode coupling length is obtained from local birefringence and polarisation mode dispersion measurements.

Introduction

Polarisation Mode Dispersion (PMD) is a statistical quantity describing the effects of the distributed birefringence in the distortion of a light signal along an optical fibre. In the theoretical modeling of this phenomenon the fibre can be described as a concatenation of pieces of homogeneous fibres with a mean modal birefringence B (B is generally expressed in ps/km) [1]. Their mean length is known as the coupling length h. For fibres which are long compared to h, the PMD of the fibre is equal to $B\sqrt{hl}$, so that the knowledge of this parameter h is very important in the transmission properties of single mode fibres.

Optical Frequency Domain Reflectometry is well known as a tool for optical fibres and devices characterization [2]. In this technique, the frequency of the laser source is linearly swept as a function of time, and the reflected field under investigation interferes coherently with a fixed reflection, known as the local oscillator (LO) field. Due to the linear frequency sweep of the source, for each reflection in the fibre there is a corresponding beat frequency, so that the intensity of the reflected field from each point can thus be obtained as the Fourier transform of the interference signal. Since the state of polarisation (SOP) of the reflected field with respect to the LO affects the intensity of the interference signal, OFDR is naturally a polarisation sensitive reflectometer. In this sense, the OFDR is a useful complement to the Polarisation OTDR (POTDR) [3], and enables to measure short-scale effects, albeit at a much shorter distance than the POTDR [4]. In this work, we use the OFDR technique to analyze polarisation effects in the Rayleigh backscattering signal in order to get information on the local birefringence along the fibre.

For one homogeneous trunk of fibre with modal birefringence B, the theoretical model [5,6] predicts that the Rayleigh backscattering signal detected by the OFDR oscillates with two characteristic periods, L_h and $L_h/2$, where $L_h = \lambda/cB$ is the polarisation mode beat length[1]. Intuitively, $L_h/2$ appears because the signal travels forth and back, so that the effective length of fibre is double. L_h appears when the polarisation of the LO or the polarisation at the input is parallel to the birefringence axis. The relative intensity of these two components therefore depends on the polarisation. For a real fibre, modeled as a concatenation of homogeneous trunks, this intensity changes during the propagation, due to the random mode couplings. The determination of

[1] Note that this is valid only when the birefringence Δn is independent of the frequency, which is a very good approximation for optical fibres.

these two periods enables to obtain L_h, and through it the local birefringence. The combination of this measurement and of the PMD enables to determine the polarisation mode coupling length of the fibre.

Experimental procedure

The description of our OFDR has been given in previous works [2]. A standard single mode fibre, with a rather high value of the PMD, was used to demonstrate the polarisation mode coupling length determination. The PMD was measured by the interferometric method [1], to give $1.9\,\mathrm{ps}/\sqrt{\mathrm{km}}$. A 5-m long piece of this fibre was kept loose on the optical table, to avoid any bending effect. The far end reflection of the measured fibre was eliminated in order to reduce the noise floor due to the phase noise of the laser. The fading noise of the Rayleigh backscattering intensity was eliminated by averaging the FFT spectra while slowly sweeping the laser central wavelength [2]. The full wavelength range, (< 1 nm) was small enough to average out the random fluctuations of the Rayleigh backscattering intensity without disturbing the polarisation state of the reflected field.

Results and discussion

The result of the OFDR scan is presented in Fig. 1 where the oscillations induced by the local birefringence can be clearly seen. A Fourier Transform of this curve is shown in the inset, and gives the frequency of these oscillations, about $3.3\,\mathrm{m}^{-1}$. A small second peak, at $6.6\,\mathrm{m}^{-1}$, is an indication that the main peak corresponds to the beat length L_h, while the second peak corresponds to $L_h/2$. The fact that both peaks appear in the Fig. 1 helps identifying the correct beat length to be $L_h = 30\,\mathrm{cm}$. This would correspond to a PMD of $17\,\mathrm{ps}$ for a 1 km-long optical fibre with no mode coupling, a value much higher than the one measured experimentally. This confirms that this fibre has some mode coupling. The equation linking the PMD, the intrinsic birefringence and the coupling length is derived in [1]. For the case of a coupling length h which is small with respect to the fibre length l we get:

$$\mathrm{PMD} = \frac{\lambda}{cL_h}\sqrt{lh}\,. \qquad (1)$$

From Eq. (1), we derive the value of the coupling length: $h \approx 12\,\mathrm{m}$. We emphasize that a measurement of the PMD alone cannot give the value of this parameter. For example, a low value of the PMD may be due either to a low intrinsic birefringence, or to a small coupling length. Our measurement thus enables a more complete characterization of the optical fibre.

The same setup can be used for the determination of induced birefringence. For example, we have also performed experiments with optical fibres wrapped around spools of various sizes. The typical variation of L_h as R^2, where R is the radius of the spools was observed [7]. It may be also possible to use the OFDR to measure the twist-induced birefringence, as was done in [8].

Conclusion

We have used the OFDR to analyze polarisation effects in optical fibres. Measurement of the intrinsic birefringence, together with a measurement of the global PMD of the fibre enabled us to estimate the coupling length of the fibre. This work is an example of the use of the OFDR as a complement to the POTDR, which gives information on polarisation effects in optical fibres on a much larger scale (resolution of several meters, range of several kilometers). The OFDR is well adapted to measurements with range below one hundred meters, and resolution of a few centimeters.

Acknowledgements

This work was supported by Swiss CTI Project 3160.1, by the European ACTS under the BLISS AC065 project, and by CpqD Telebras under the contract JPqD 779/97. We acknowledge stimulating discussion with our COST 241 partners.

References

[1] N. Gisin, J.P. Von der Weid and J.P. Pellaux, "Polarisation mode dispersion of short and long single-mode fibres", J. Lightwave Technol., 1991, vol. 9, pp. 821-827.

[2] J.P. von der Weid, R. Passy, G. Mussi and N. Gisin, "On the characterization of optical fibre network components with optical frequency domain reflectometer", J. Lightwave Technol. 1997, vol. 15, pp. 1131-1141.

[3] A.J. Rogers, "Polarisation-optical time domain reflectometry: a technique for the measurement of field distributions", Appl. Opt. 20, pp. 1060-1074 (1981).

[4] A. Tardy, M. Jurczyszyn, F. Bruyere, M. Hertz and J.L. Lang, "Fibre PMD analysis for optical-fibre cable using polarisation OTDR", in Optical Fibre Communication Conference, 1995 OSA Technical Digest Series (Optical Society of America, Washington DC, 1995) pp. 236-239.

[5] E. Brinkmeyer, "Forward-backward transmission in birefringent single-mode fibres: interpretation of polarisation-sensitive measurements", Opt. Letts 6, pp. 575-577 (1981).

[6] E. Chausse, N. Gisin, Ch. Zimmer and B. Perny, "Polarisation mode dispersion analyses with polarisation OTDRs", in European Fibre Optic Communications and Networks 1995 (The European Institute for Communications and Networks, 1995) pp.185-189 (Note that in Eq. (2) in this work, a term: $\cos(\omega B z)(\vec{p}\cdot\vec{e}_z)$ is missing in the squared expression).

[7] R. Ulrich, S.C. Rashleigh and W. Eickhoff, "Bending-induced birefringence in single-mode fibres", Opt. Letts. 5, pp. 273-275 (1980).

[8] R.E. Schuh, J.G. Ellison, A.S. Siddiqui and D.H.O. Bebbington, "Polarisation OTDR measurements and theoretical analysis on fibres with twist and their implications for estimation of PMD", Elec. Letts. 32, pp. 387-388 (1996).

Figures

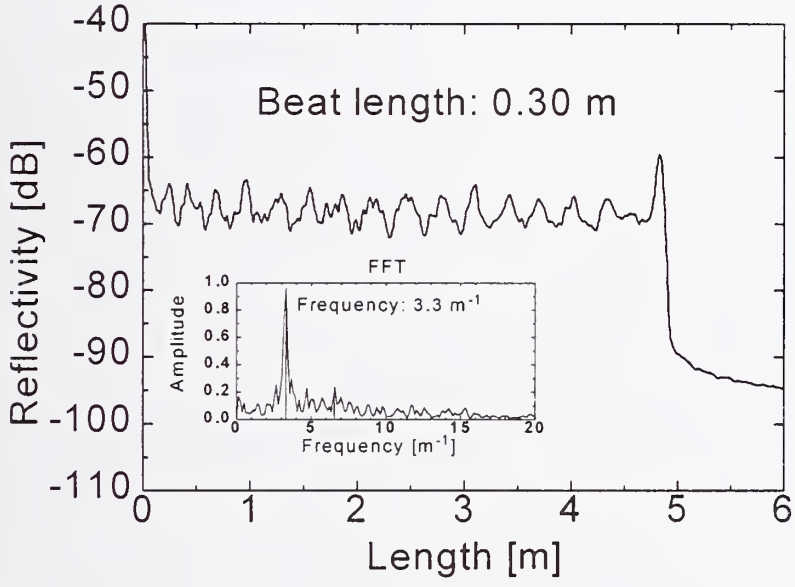

Figure 1

POFDR measurement of a single mode fibre. The oscillations in the Rayleigh backscattering are due to the intrinsic birefringence of the fibre. The main peak in the Fourier transform corresponds to a periodicity of 3.3 m^{-1}, whereas the double frequency is barely visible at 6.6 m^{-1}. The polarisation beat length is $L_b = 30\,cm$, while the second peak corresponds to $L_b/2$.

BEAT-LENGTH MEASUREMENT IN HIGHLY MODE-COUPLED SINGLE-MODE FIBERS BY MEANS OF FOURIER TRANSFORM OF BACKSCATTERED SIGNAL

Fabrizio Corsi, Andrea Galtarossa, Luca Palmieri
DEI Università di Padova, Via Gradenigo 6/A,
35131 Padova ITALY

Abstract *We present a new method able to determine the mean value of beat length in highly polarization-coupled, randomly perturbed, single-mode fibers. Our method is based on the analysis of the power spectrum of the backscattered signal. Numerical results fit very well with theoretical predictions .*

Introduction Nowadays, backscattering technique is the most diffused method for optical fiber characterization regarding losses in optical link up to one hundred of kilometers in length. Its success is due to its simplicity, high dynamic range and, mainly, because it is a one-end measure. Moreover, it has been also shown that polarization sensitive backscattering technique [1][2] could be a suitable tool to perform beat length measurement for fiber in so called short-length regime, i.e. when the correlation length L_C is large compared to the fiber length L ($L/L_C \to 0$) [3][4][5].
Recently, we presented an original theory to show the capability of backscattering technique to perform complete polarization mode dispersion characterization of fiber also in long-length regime ($L/L_C \to \infty$) considering spatial evolution of Stokes parameters of the backscattered signal as a function of scattering point through the fiber [6]. We have shown also that our method permits to measure the mean beat length L_B and the polarization mode coupling using a polarization sensitive backscattering technique, simply considering the ratio between the number of extrema (N_E) compared to the number of fixed-level crossing points (N_ν) [7], ν being a fixed value of the normalized backscattered signal ($0 \le \nu \le 1$). We used a linearly polarized input field, and we placed a linear polarizer in front of the photodiode in detection; polarizer axis was perfectly aligned with respect the state of polarization on the input signal. We found that for fiber in low-polarization coupling regime it results $L_B = 4\, L/N_E$, while for fiber in high-polarization coupling regime it results $L_B = 4\, L\, \nu^{1/2}/N_\nu$.
The aim of this work is to present a new method based on analysis of the Fourier transform of the backscattered signal that permits to calculate the mean value of L_B. In particular we find that the mean value of the beat length is strictly related to inverse of the standard deviation (STD) of the power spectrum.

Theoretical background The 3 components of the normalized Stokes vector $\overline{S}(z)$, representing the evolution of the state of polarization of a monochromatic field propagating through a loss-less, randomly perturbed, single-mode fiber can be related to the input one $\overline{S}_o$, by means of $\overline{S}(z) = \mathbf{R}\,\overline{S}_o$, z being the position along the fiber, while $\mathbf{R}=\mathbf{R}(z)$ is the Muller matrix of the fiber.

In a similar way, we may introduce $\overline{S}_B(z)$ that is the Stokes vector of the backscattered field. If we use a quasi-monochromatic pulse, the backscattered signal may be written as follows [7]:

$$\overline{S}_B(z) = \mathbf{M}\mathbf{R}^T\mathbf{M}\mathbf{R}\,\overline{S}_o \tag{1}$$

where, ^{T} is the transpose and $\mathbf{M}$=*diag(1,1,-1)* a diagonal matrix. From now on, subscripts *F* and *B* refer, respectively, to forward and forward-backward propagation.

Let us place a polarizer having Stokes vector $\overline{p}$ in front of the photodiode. The normalized power of the signal passed through the polarizer is given by [7]:

$$\widetilde{T}(z) = \frac{1}{2}[1 + \overline{S}_B(z)\cdot\overline{p}]. \tag{2}$$

Because of randomness, $\mathbf{R}$ and, consequently, $\widetilde{T}(z)$ are stochastic process. We show hereafter that, under suitable hypothesis, it is possible to retrieve information on the mean beat length considering the standard deviation (STD) of Fourier transform of the backscattered signal.

It can be shown that $\mathbf{R}(z)$ can be considered *asymptotically stationary* as z increases so that the probability density function of $\widetilde{T}$ at a distance z converges to a z-independent function [8]. Because statistical description of $\widetilde{T}(z)$ depends on the mutual orientation of polarizer with respect to state of polarization of input signal, we will assume the input field to be linear polarized and the output polarizer to be perfectly aligned to the input state of polarization ($\overline{p} = \overline{S}_o$); consequently, it results $<\widetilde{T}(z)>= 2/3$ [7]. Let us consider a mean-shifted transmission $T(z) = \widetilde{T}(z) - 2/3$, that has a zero-mean value ($-2/3 \le T(z) \le 1/3$). The transmission $T(z)$ will be treated as an ergodic random process following the same procedures used in [9] to compare the differential group delay measured by means of interferometric method with respect to fixed polarizer method.

Our results will be valid for a fiber in *long-length regime* that means the length Δz of the fiber under test is much larger than any variations in $T(z)$. Let us introduce

$$H(z) = \int_{\Delta z} T(\eta)T(\eta + z)d\eta = \Delta z R_{TT}(z\ ) \tag{3}$$

where $R_{TT}(z)$ is the autocorrelation of $T(z)$ that coincides with the expected value of $T(\eta)T(\eta + z)$. Moreover, we define $h(\omega_z)$ the Fourier transform of $H(z)$; since $h(\omega_z)$ is an even function its variance σ_h^2 reads

$$\sigma_h^2 = \frac{\int h(\omega_z)\omega_z^2 d\omega_z}{\int h(\omega_z)d\omega_z} = -\frac{1}{4\pi^2}\frac{H''(0)}{H(0)} \tag{4}$$

where $H''(0)$ is the second derivative of $H(z)$ evaluated at $z = 0$. Please note that with respect to [9], there is a factor $1/4\pi^2$ because of a different definition of the Fourier transform.

In [8] we found that the state of polarization of forward signal may be completely defined by $\overline{S}_F = (cos\xi cos\psi, cos\xi sin\psi, sin\xi)$, where ξ and ψ are random variables, $\xi \in [-\pi/2, \pi/2]$ and $\psi \in [0, 2\pi]$, whose probability density functions (PDFs') read, respectively,

$$f_\xi(\gamma) = \frac{cos\gamma}{2} \qquad\qquad f_\psi(\alpha) = \frac{1}{2\pi}. \tag{5}$$

Moreover, T and T' may be written as follows:

$$T = \frac{1}{2}(1 + cos2\xi) \qquad T' = -(\bar{\beta}_L \cdot \hat{u})sin2\xi, \tag{6}$$

where $\bar{u} = (sin\psi, -cos\psi, 0)$, $\bar{\beta} = (\beta_1, \beta_2, \beta_3)$ is the local birefringence vector while $\bar{\beta}_L = (\beta_1, \beta_2, 0)$ is the vector that describes the linear component of the local birefringence.

In highly mode-coupling regime, the correlation length of the perturbation affecting the fiber is much smaller with respect to the beat length. Consequently, the state of polarization of the signal $\bar{S}_F(z_1)$ may be considered statistically independent of the value assumed by $\bar{\beta}_L(z)$, whenever $z \geq z_1$. Furthermore, the two components $\bar{\beta}_L(z)$, i.e. β_1 and β_2, are assumed to be Gaussian variables, statistically independent, with zero mean value, and with the same standard deviation σ_β. By means of relationships introduced in [9]

$$H(0) = \Delta z \langle T^2 \rangle \qquad H''(0) = -\Delta z \langle T'^2 \rangle \ , \tag{7}$$

we may obtain the following results:

$$H(0) = \Delta z \langle T^2 \rangle = E[\cos^4 \xi] = \Delta z \frac{4}{45} \tag{8}$$

$$H''(0) = -\Delta z \langle T'^2 \rangle = E[sin^2\psi]\ E[sin^2 2\xi]\ E[|\bar{\beta}_L|^2] = -\Delta z \frac{4}{15}\ E[|\bar{\beta}_L|^2],$$

and, consequently, $2\pi^2\sigma_h^2 = 3\sigma_\beta^2$. Let us define the mean value of the beat length, L_B, as follows: $L_B = 2\pi / E[|\bar{\beta}_L|]$. Because $|\bar{\beta}_L|$ depends on two statistically independent Gaussian variables, it is Rayleigh distributed. As a consequence, the mean value of the beat length reads:

$$L_B = \sqrt{\frac{12}{\pi}} \frac{1}{\sigma_h} \cong \frac{1.96}{\sigma_h} \tag{9}$$

Numerical results We tested numerically eq. (9), modeling the fiber by means of a cascade of randomly rotated waveplates [7] so to obtain a fiber of total length of 26,624 m. Additional parameters introduced were the sampling length L_S that defines the spatial resolution, i.e. the distance between two adjacent scattering points, and the rotation length L_R, i.e. the length of each waveplate. For all the examples reported in the following we tested numerically that $\bar{S}_F(z)$ covered uniformly the Poincaré sphere, to be sure that fibers were in long-length regime. Numerical results were averaged over an ensemble of 100 fibers and are summarized in TAB.I ($L_B > L_R$) and TAB.II ($L_R > L_B$). TAB.I and TAB.II show that expected values of beat length are very close to theoretical predictions when $L_S << min\{L_B, L_R\}$. It means that the spatial resolution has to be small enough compared to longitudinal fluctuations of the fiber. A reasonable accuracy may be

TAB. I

L_S (m)	13.0	6.5	3.25	1.625	0.8125	
L_B (m)	103.7	49.4	22.1	15.1	14.9	T.V.=15.0
L_B (m)	100.6	44.4	30.0	29.5	29.7	T.V.=30.0
L_B (m)	94.1	49.2	43.8	44.3	44.6	T.V.=45.0

(L_R=13m, L=26,624m; T.V. is the theoretical value of L_B)

TAB. II

L_S (m)	13.0	6.5	3.25	1.625	0.8125	
L_B (m)	101.8	50.5	24.4	11.0	8.1	T.V.=8.0
L_B (m)	101.6	48.7	22.1	16.1	16.0	T.V.=16.0
L_B (m)	98.0	44.2	32.9	31.8	31.8	T.V.=32.0

(L_R=52m, L=26,624m; T.V. *is the theoretical value of L_B)*

achieved when $L_S < min\{L_B, L_R\}/5$. Furthermore, even if our theory applies rigorously only to highly polarization-coupled fibers ($L_R << L_B$), numerical results seem to be close to theoretical ones for fibers in long-length regime, independently of the ratio L_R/L_C.

Conclusion We presented a new technique able to measure the mean value of the beat length of a single-mode randomly birefringent optical fiber by means of the power spectrum analysis of the backscattered signal. We used a linearly polarized input signal in transmission and a linear polarizer followed by a photodiode in detection. Polarization axis of the linear polarizer was perfectly aligned with the state of polarization of the input signal. We showed that the mean value of the beat length is strictly related to the standard deviation of the Fourier transform of the backscattered signal passed through the polarizer. In particular, the larger the STD of the backscattered signal, the smaller the mean value of the beat length. Numerical results fit very well theoretical predictions when spatial resolution of backscattered signal is small compared to spatial scale of fluctuations of fiber under test.

Acknowledgements We thank prof. C. G. Someda for fruitful suggestions. Our work was partially supported by an EEC/ ACTS/ ESTHER project. It is also part of cooperation agreement between CSELT and Consorzio Padova Ricerche.

References

1. Rogers A. J., *Applied Optics*, pp. 1060-1074, 1981.
2. Kim B. Y. and Choi S.S., *Optics Letters*, pp. 578-580, 1981.
3. Galtarossa A., Pistolato P., Schiano M., *Proc. EFOC&N.* pp. 190-192, 1995.
4. Ellison J. G. and Siddiqui A. S., *IEEE Ph. Tech. Letters*, pp.246-248, 1998.
5. Poole C. D., Nagel J., in *Optical Fiber Telecommunications III A*, I. P. Kaminow and T. L. Koch eds, Academic Press, 1997
6. Galtarossa A., Corsi F., Palmieri L., *Proc. OFC'98*, San Jose (CA), paper ThR4.
7. Galtarossa A., Corsi F., Palmieri L. , "Polarization mode dispersion characterization of single-mode optical fiber using backscattering technique", accepted for publication in *IEEE J. Light. Technology.*
8. Corsi F., Galtarossa A., Palmieri L., "Beat-length characterization based on backscattering analysis in highly polarization coupled single-mode fibers ", *to be published.*
9. Heffner B. L., *Optics Letters*, pp. 113-115, 1996.

Spun fibre parameter extraction using Polarimetric Optical Time Domain Reflectometry

J.G. Ellison and A.S. Siddiqui

Department of Electronic Systems Engineering, University of Essex, Colchester CO4 3SQ, UK

Abstract

The spatial frequencies present in a polarimetric optical time domain reflectometer trace of spun fibre are a strong function of external twist and initial spinning parameters. In this paper we show how analysis of the spatial frequencies in the POTDR trace in conjunction with the backscattered state of polarisation evolution can determine the spinning parameters of the spun fibre.

Introduction

The recent commercial availability of spun fibres has enabled a significant reduction in the Polarisation Mode Dispersion (PMD) of newly deployed systems. These spun fibres are produced by applying a sinusoidal torque to the fibre being drawn, alternatively in the clockwise and anti-clockwise direction. This has the effect of 'scrambling' the linear birefringence axes and hence reducing the effective linear birefringence. In [1] we presented a technique for estimating the residual linear birefringence within the spun fibre using Polarimetric Optical Time Domain Reflectometry (POTDR) [2], and hence provide an indication of how effective the chosen spinning parameters were for a particular fibre sample. In this paper we show how examining the twist dependency of the spatial frequencies and the state of polarisation (SOP) evolution in the POTDR trace allows information about the spinning parameters themselves to be extracted. This single-ended, non destructive technique may be of use to fibre manufacturers as a check to ensure that the spinning process is imparting the correct spin to the fibre itself.

Theory

The backscattered SOP evolution has been computed by modelling the fibre as a series of linear retarders whose angle of azimuth varies sinusoidally along the fibre in accordance with the spin period, Λ_γ, and the spin amplitude, A_γ. Each of the linear retarders has a linear birefringence determined by an initial, unspun linear birefrigence, β_L. The application of external twist, γ, has been included in the model by an additional azimuth rotation of the linear retarders following the twist, and a circular birefringence component related to the external twist by the stress-optic coefficient, g. The spatial frequencies present in the backscattered SOP evolution were obtained by performing a Fast Fourier Transform upon each of the Stokes parameters.

Fig. 1 shows the backscattered spatial frequencies as a function of externally applied twist for an initial linear birefringence, β_L, of 2.5 rad/m, a spin period, Λ_γ, of 2 metres, and a spin amplitude, A_γ, of 1 turn. The occurrence of a spatial frequency at 0.5 cycles/m for most values of twist is immediately obvious and corresponds to the spin period, Λ_γ. Extraction of the other two parameters, the spin amplitude and initial linear birefringence, is more difficult however. A large number of simulations were performed with various starting parameters to attempt to uncover a systematic trend. The height and position of the 'eye' patterns varies strongly with A_γ and Λ_γ, and less so with β_L, but other than the regular appearance of a constant spatial frequency at $1/\Lambda_\gamma$, a systematic pattern is difficult to see. Extraction of A_γ and β_L from the spatial frequency map of a real fibre must therefore be performed by best fit matching against the simulated spatial frequency map whose parameters are chosen by trial and error. This process may be hastened by a comparison between the measured and simulated SOP evolutions at key twist rates, namely at the maximum opening of an 'eye' and at the crossover points between 'eyes'. The size of the characteristic looped figure of eight pattern at the

'eye' crossover points is determined by the magnitude of A_γ and β_L and helps provide a starting value and constraint for the values used in the simulation.

Results

A spun dispersion shifted fibre was suspended in a 30m long catenary such that a known twist could be applied to the fibre. The POTDR [2] was used to measure the backscattered SOP evolution and spatial frequencies for a number of different twist rates. From the spatial frequency data, the spin period, Λ_γ, was identified as 1.65m, and an examination and comparison of the SOP evolution against trial simulation data provided a range of possible values for the spin amplitude and initial linear birefringence. The best match from a range of simulation runs was fine-tuned until the simulated spatial frequencies and SOP evolution closely matched the measured spatial frequency data and SOP evolution. Fig. 2 shows the final spatial frequency map for a linear birefringence, β_L, of 3 rad/m and spinning parameters $A_\gamma = 1.1$ turns and $\Lambda_\gamma = 1.7$m. The simulated and measured SOP evolution for a particular twist rate is given in figs. 3a and 3b and shows a reasonable agreement in the overall shape. Note that the SOP evolution becomes very convoluted and shows a strong sensitivity to the spinning parameters themselves. It is therefore unreasonable to expect an exact agreement between the SOP evolutions in theory and practice due to small irregularities in the spinning process.

As a check of the accuracy of the extracted spinning parameters, the differential group delay (DGD) versus twist characteristics were measured using the Jones Matrix Eigenanalysis technique and compared with the theoretical plot obtained by a numerical method [3] for the given spinning parameters (figs. 4a and 4b). As can be seen from the results, the measured and theoretical DGD plots match well, giving some confidence to the values of the spinning parameters extracted.

A sample of the same fibre produced without spin was also measured with the POTDR to confirm a value for the initial linear birefringence, β_L. This was found to be 1.7 rad/m, a value different from that obtained in the spun fibre. The discrepancy may be due to the mechanics of the spinning process itself which may increase the internal linear birefringence.

Conclusions

We present a technique for extracting the spinning parameters used in the manufacture of a spun fibre using POTDR. Although the technique is not perfect yet, with some refinement it should be of use to fibre manufacturers to help verify that the spinning process is imparting the correct spin to the fibre produced.

Acknowledgements

This work was carried out under EPSRC Research Grant number GR/K49454. The industrial partners are BT Laboratories, Martlesham Heath, Ipswich, UK and Alcatel Submarine Networks, Greenwich, London, UK.

References

[1] J. G. Ellison and A. S. Siddiqui, "Estimation of linear birefringence suppression in spun fibre using polarimetric optical time domain reflectometry," Conference on Lasers and Electro-Optics (CLEO '98), San Francisco, paper no. C Th 057, 1998.

[2] J. G. Ellison and A. S. Siddiqui, "A Fully Polarimetric Optical Time Domain Reflectometer," IEEE Photonics Technology Letters, vol. 10, no. 2, pp. 246-248, 1998.

[3] R. E. Schuh, X. Shan and A. S. Siddiqui, "Polarisation mode dispersion in spun fibres with different linear birefringence and spinning parameters," 4th Optical Fibre Measurement Conference (OFMC '97), NPL, Teddington, London, pp. 122-125, 1997.

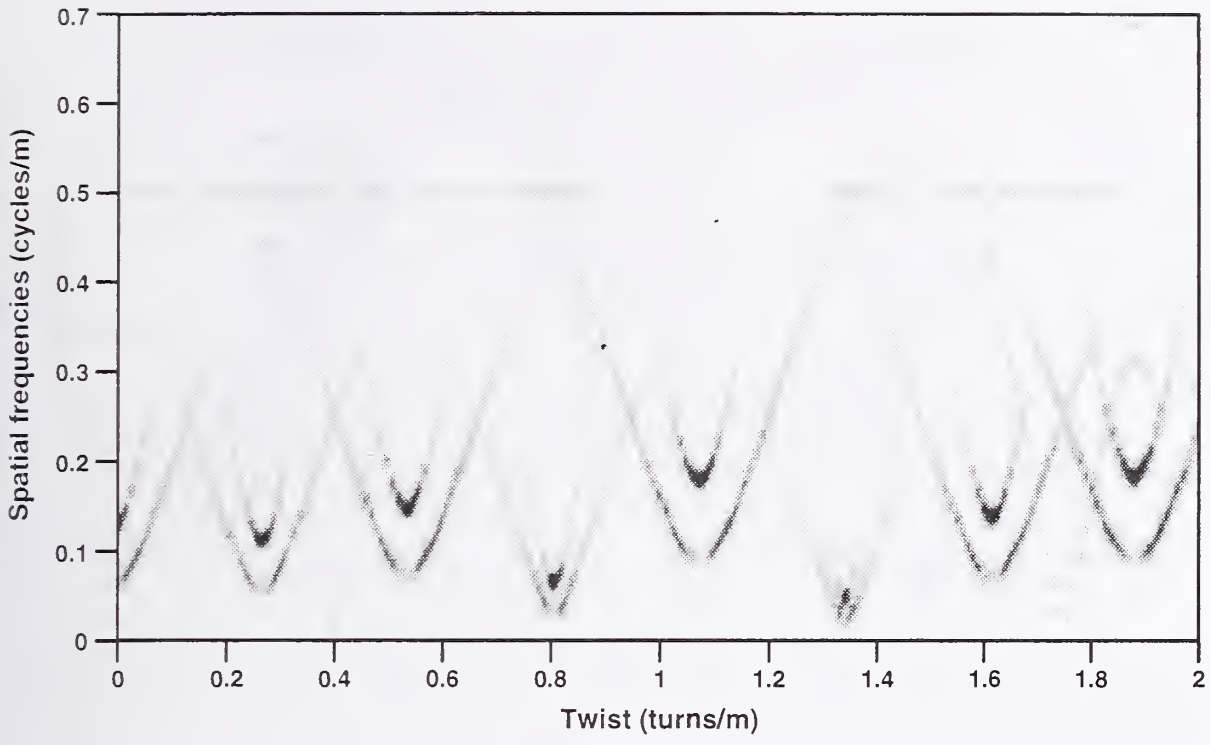

Fig. 1 Simulated spatial frequencies versus twist for β_L = 2.5 rad/m, Λ_γ = 2m and A_γ = 1 turn. Density of print represents the normalised amplitude at that frequency.

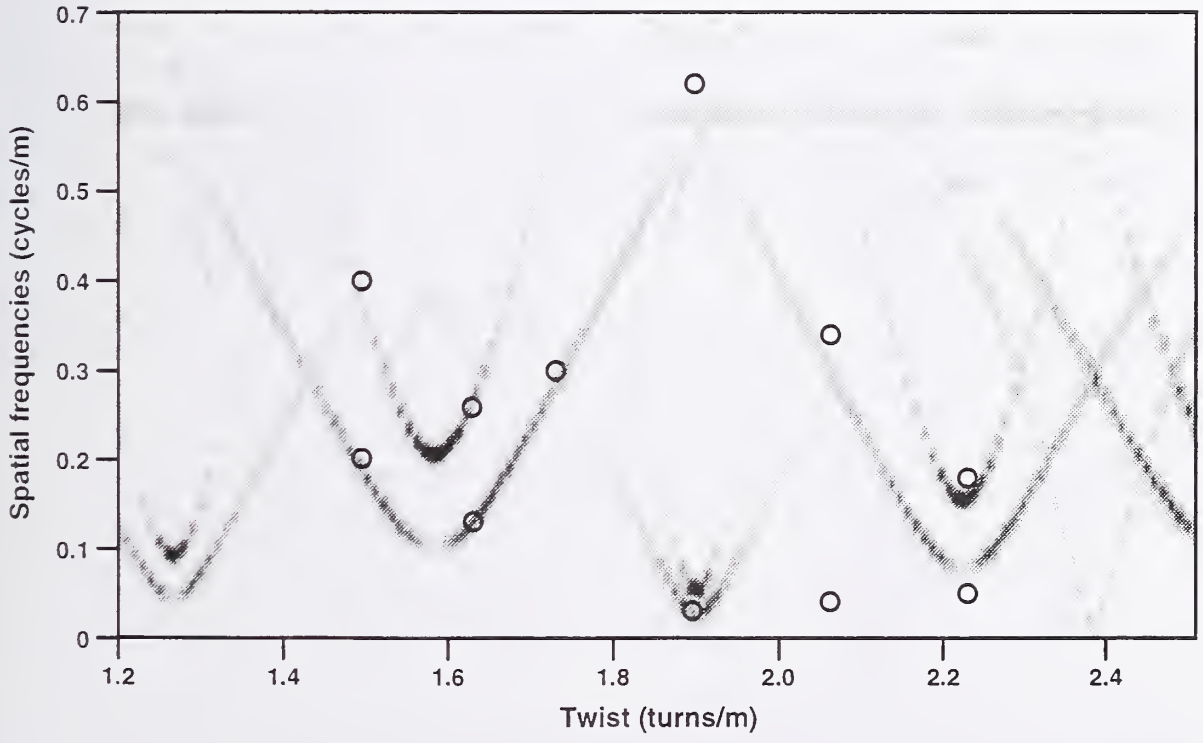

Fig. 2 Simulated and measured (O) spatial frequencies versus twist for β_L = 3 rad/m, Λ_γ = 1.7m and A_γ = 1.1 turns.

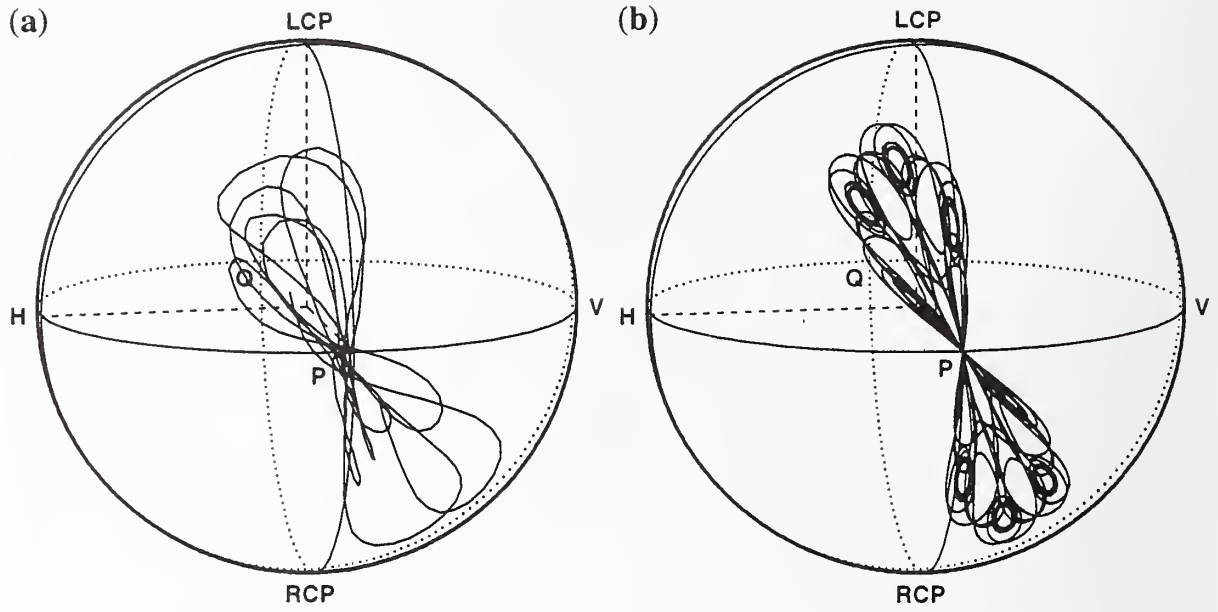

Fig. 3 Backscattered SOP evolution at a twist rate of 1.75 turns/m, (a) measured and (b) simulated with β_L = 3 rad/m, Λ_γ = 1.7m and A_γ = 1.1 turns.

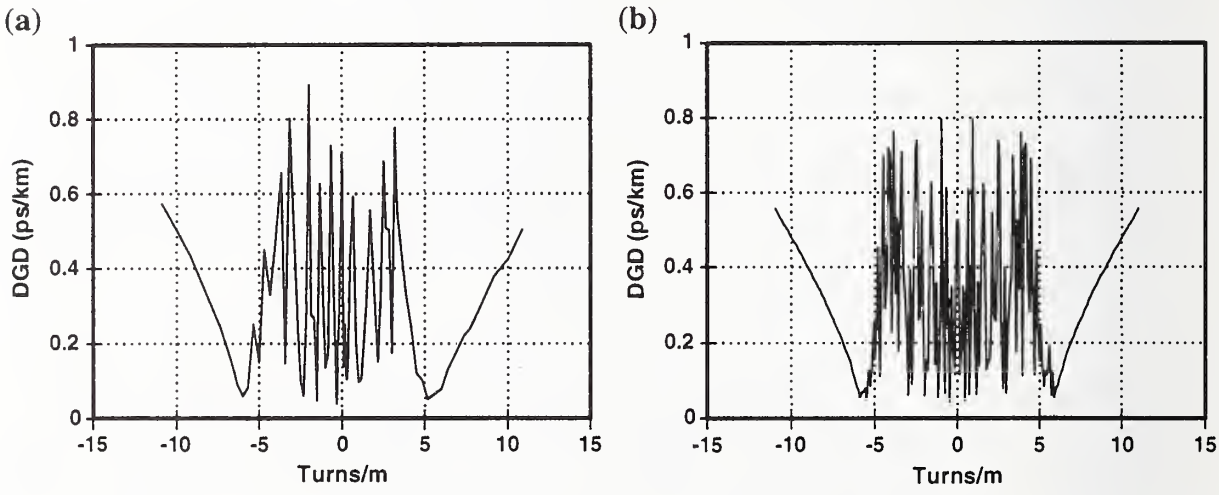

Fig. 4 DGD versus twist characteristics, (a) measured and (b) simulated with β_L = 3 rad/m, Λ_γ = 1.7m and A_γ = 1.1 turns.

Characterizing Multimode Fiber Bandwidth for Gigabit Ethernet Applications
(Invited)

Michael J. Hackert
Corning, Inc., SP-BN
Corning, NY 14831

Introduction

The demand for ever increasing volumes of data transmission is driving new development in the data communication marketplace. Sources, fiber, receivers, and connectors all are being re-engineered to provide low cost solutions to fill the needs of the market place. This paper describes the latest, on going technical developments regarding the application of multimode optical fiber for data communication.

The private premise or fiber to the desk (FTTD) market has two underlying needs: one is for low costs and the other is for industry accepted standards. New technologies such as vertical cavity surface emitting lasers (VCSELs) provide the promise of low costs (comparable to light emitting diodes – LEDs) combined with superior performance previously unobserved[1]. For example, VCSELs can easily operate at 2 Gigabit and produce milliwatts of power with threshold currents so low that they can be driven directly from logic gates without the need for drivers. These sources operate at short wavelengths around 850 nm. Standard single-mode fiber (SMF) is not designed to operate at this wavelength whereas multimode fiber (MMF) is ideally suited. In addition, low cost silicon detectors provide good responsivity at this wavelength as well as high speed. An additional benefit is that the VCSEL manufacturing process provides the promise of readily controlling their launch power distributions. The Gigabit Ethernet standard, which recently was approved under the direction of the IEEE 802.3z committee, is providing the standardization the marketplace wants. Thus, the stage is set for renewed interest in multimode fiber. The combination of low cost connectors, inexpensive sources and detectors, and multimode fiber provides a cost-effective solution for current data communication needs.

In order to apply multimode fiber to higher speed applications, numerous technical considerations, which had not been significant during the development of slower speed system standards such as Fiber Distributed Data Interface (FDDI)[2], required investigation and resolution. The Telecommunication Industry Association (TIA) responded to industry's need by providing a forum for various participants to come together to do the fiber and source development (TIA FO-2.2 Task Group on Modal Dependence of Bandwidth). The IEEE provided the forum to develop a gigabit system standard (IEEE 802.3z). The results reported herein come from work of each of those groups.

DMD and Bandwidth Fundamentals

Multimode fiber's information carrying capacity typically is rated in terms of a bandwidth length product (MHz-km) that can be used to determine how far a system can operate at what bit rate[3]. A simple intuitive model for the bandwidth characteristics considers the fiber to consist of a number of discrete delay lines, each of which corresponds to a particular mode[4,5,6]. A conceptual model is shown in Figure 1. In the figure, the low order modes (LOM) correspond to the modes or rays propagating down the center of the fiber; the high order modes (HOM) propagate near the core/clad interface; and the intermediate modes propagate in between. Although somewhat counter intuitive, the intermediate modes carry most of the power.

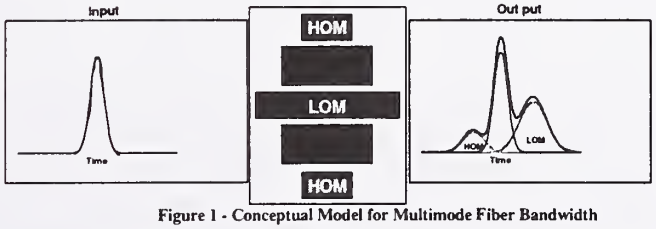

Figure 1 - Conceptual Model for Multimode Fiber Bandwidth

In an ideal fiber, all of the delays are tuned to be identical. Thus, when a temporally narrow pulse of light is launched into the fiber, its shape is maintained at the output. However, as the example in Figure 1 shows, the over exaggerated delay error causes the output pulse to be broadened. The high order mode

power arrives late relative to most of the power (in the intermediate modes), and the low order modes arrive early. Thus, the bandwidth is reduced and the information carrying capacity is limited.

This model then explains why bandwidth is launch dependent. The output pulse given in Figure 1 corresponds to an overfilled launch where all of the modes are excited with the maximum amount of power they can carry. This launch is defined by standards[7]; and a typical source that this might correspond to is an LED. If the launch power distribution is then reduced so that only the lower and intermediate modes are excited, the power in the late peak of the pulse disappears, the pulse width decreases, and the bandwidth goes up. The analogy can be extended equally as well where the launch is restricted to just the lowest order modes and the output pulse becomes very narrow. Thus, if all of the modes of a multimode fiber are not tuned perfectly, the bandwidth can change as the launch power distribution changes.

The tuning of these modes is quantified by the differential mode delay (DMD) measurement. The DMD is a process tuning tool which measures the delay of each of the modes. It has never been standardized because it is difficult to implement, costly to run, and not a functional input measure for system modeling. Bandwidth, on the other hand, is functional and is used in system modeling[3]. The DMD consists of recording the mean delay as a spot of light formed by a single-mode fiber is scanned across the input of the fiber. The typical technique for this measurement is a variation of the time domain bandwidth measurement[7] - a high speed pulse is used. The US National Institute of Standards and Technology (NIST) recently reported on improved resolution using a frequency domain technique that allows measurement of short lengths (approx. ten meters or ±0.3 ps/m)[8]. An example is given in Figure 2 where delay (given in psec/m or nsec/km) is plotted versus offset of the single-mode spot where positive delay corresponds to increased time.

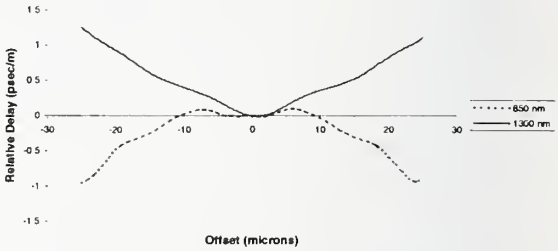

Figure 2 - Differential Mode Delay for TIA TG 2.2 Round Robin Cable (Fiber 7)

The DMD measurement effectively is a very precise measure of the graded index of a multimode fiber. Measures of the index such as the Refracted Near-field (RNF) measurement[7] fail to have sufficient resolution to see the delay errors that are significant for tuning a multimode fiber. Figure 3 shows an example of a perfect alpha profile and a perturbed profile which reduced the modeled bandwidth by approximately a factor of two. It is evident from the figure that the difference is barely perceptible. Typical RNF measurement equipment has insufficient resolution to measure such a small difference (just another challenge to tuning for increased bandwidth). Fortunately, a theoretical foundation to model bandwidth from DMD data was completed during early fiber development[4,5,6]. The models provide sufficient accuracy to estimate average performance when empirical adjustments are made. However, the precision is somewhat limited.

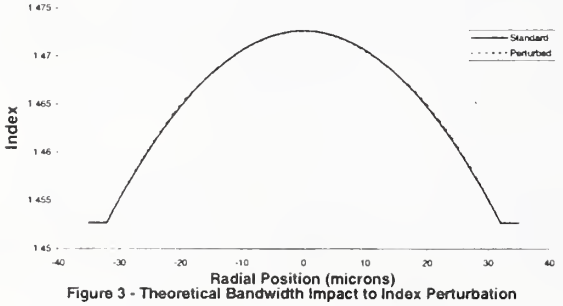

Figure 3 - Theoretical Bandwidth Impact to Index Perturbation

The maximum theoretical bandwidth of a given multimode fiber design is limited by the maximum number of modes. There are approximately 2.5 times as many modes in 62.5 µm fiber as there are in 50 µm fiber. This can be seen in Figure 4 where the maximum theoretical bandwidth is plotted versus wavelength. Consequently, higher bandwidths can be achieved with 50 µm fiber. This is traded

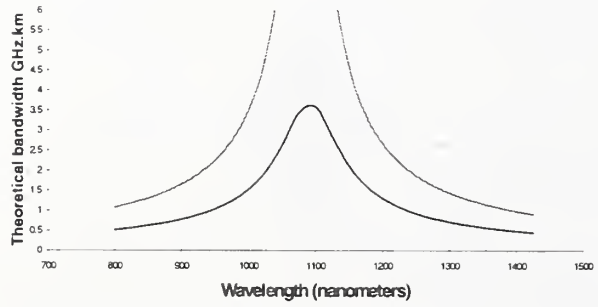

Figure 4 - Theoretical Bandwidth for Graded Index core Multimode Fibers

off against the greater light gathering ability of the larger core (62.5 µm versus 50 µm) and larger numerical aperture (NA) (0.275 versus 0.20, respectively). This makes 62.5 µm fiber ideally suited for LED based applications since LEDs typically have large NAs and spot sizes, and 50 µm fiber ideally suited for laser based applications.

The index of the glass varies as a function of wavelength. This gives rise to the relationship between bandwidth and wavelength shown in Figure 4. The fiber designer can move the wavelength of peak bandwidth through the tuning process. Key applications in the last ten years have focused attention to 1300 nm operation with a specification of 160 MHz-km at 850 nm and 500 MHz-km at 1300 nm on 62.5 µm fiber (FDDI grade). This has moved the wavelength of peak bandwidth for 62.5 µm fiber to 1300 nm. 50 µm fiber has sufficiently high bandwidth that by tuning the fiber for peak bandwidth approximately halfway between 850 and 1300 nm, 500 MHz-km can be achieved in both windows.

At the wavelength of peak bandwidth, the DMD profile for an ideal fiber is flat. However as we move off this peak wavelength, a systematic error in the DMD profile becomes evident. The DMD profile shifts upward or to later delays for shorter wavelengths and downward or earlier delays for longer wavelengths. The intuitive model given in Figure 1 corresponds to the latter, longer wavelength case. This wavelength relationship suggests that for restricted launches produced by lasers, the 850 nm bandwidth should increase relative to the overfilled launch for 62.5 µm fiber; and the bandwidth at both wavelengths for 50 µm fiber should increase. Exploitation of this opportunity has been a topic of standards development for the last couple of years and its investigation is ongoing.

Development of a New Multimode Standard

Besides the development of new, short wavelength source technology, the development of the Gigabit Ethernet Standard beginning around 1995 was another driving force. Its need was simple – go faster, farther, and cheaper than past standards to fill the current channel capacity constraints. Miscellaneous laboratory experiments showed that significantly higher bandwidths could be achieved when the reduced launches of the new system sources were used with standard multimode fiber. In January of 1996, interested companies formed the TIA FO-2.2 Task Group on Modal Dependence of Bandwidth. Its objective was to determine if a means of ensuring consistent improved performance could be developed through a combination of both control of the source to produce a consistent restricted launch condition and an additional fiber characterization which confirms a new minimum performance with this controlled launch.

Some of the initial results (circa 6/96) are given in Figure 5 and Table 1. A histogram is graphed for the increase in fiber bandwidth at 850 and 1300 nm (expressed as a ratio) between a highly restricted launch (namely that produced by SMF) and an overfilled launch. Data for 26 fibers are graphed and the mean and range are tabulated. The average bandwidth is approximately doubled. This held out the promise that a solution could be found.

Table 1

	850 nm	1300 nm
Mean	2.0x	2.8x
Range	1.1 to 10.8x	1.1 to 5.0x
Count	26	26

Note: 1300 nm values were limited by the maximum measurement ability of the measurement system.

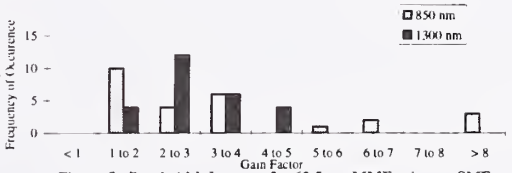

Figure 5 - Bandwidth Increase for 62.5 um MMF using an SMF Launch

The first key action of the Task Group was to implement an inter-laboratory measurement round robin. Its objective was to evaluate the inconsistencies in observations between laboratories by providing a consistent sample set to participants and a well defined set of launch conditions. A secondary objective of the round robin was to gain additional characterization information of fiber performance with actual system sources. Towards this end, a round robin cable was fabricated consisting of nine 62.5 µm fibers and six 50 µm fibers. The fibers were selected to incorporate the widest range of performance while attempting to select standard grade fiber. The bandwidth criteria attempted to include fibers with a wavelength of peak

bandwidth at 850 nm, 1300 nm, and in between 850 and 1300 nm. A 3 km length was fabricated and 300 meter sister pieces were shared with participants. All fibers were assumed to be identical.
A number of launch conditions were included in the round robin. They included:

1) the standard overfilled launch (OFL per FOTP 54[7]),
2) a number of conditions thought to reflect actual launch distributions by lasers (not to mention expected to be easily implemented and anticipated to be reasonably robust),
   a) a 50 μm spot created by overfilling a 50 mm fiber and
   b) a 30 μm spot generated by applying a five turn 5 mm diameter mandrel to an overfilling 50 μm fiber, and
3) actual direct connection measurements using transceivers
   a) VCSEL and compact disk (CD) lasers in the 850 nm window and
   b) Fabry Perot (FP) lasers designed to operate with SMF (and recommended for the Gigabit Ethernet standard for both fiber types).

Eight participants performed testing, and NIST supervised the round robin and analyzed the large amount of information which was collected.

The results of this analysis are given in Figures 6, 7, and 8. Figure 6 and 7 show the percent increase in 850 and 1300 nm bandwidth, respectively, for the various launches compared to overfilled. Figure 8 shows the normalized spread in the mean values reported by the participants for the various launches. Fibers number 1 through 9 are 62.5 μm fiber and 10 through 15 are 50 μm fiber.

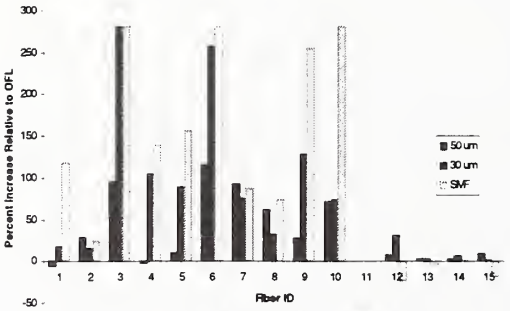

Figure 6a - TIA Round Robin 850 nm Bandwidth Increase for Fixed Launches

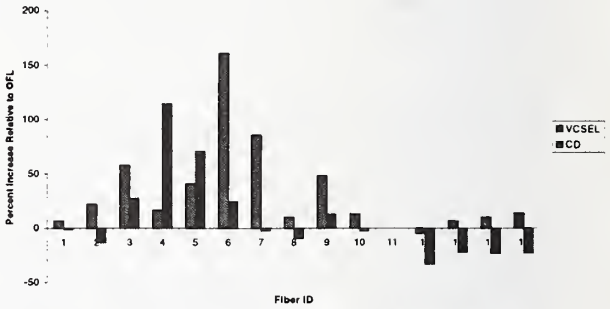

Figure 6b - TIA Round Robin Short Wavelength Bandwidth Increase for Direct Source Connection

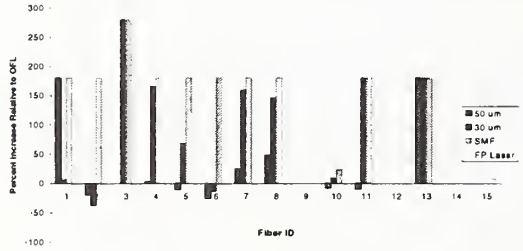

Figure 7 - TIA Round Robin 1300 nm Bandwidth Increase

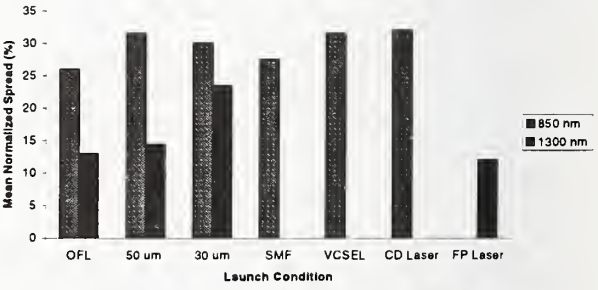

Figure 8 - TIA Round Robin Interlaboratory Bandwidth Launch Comparison

Although the data had a high level of variability, a couple of observations could be made. First, the best inter-laboratory agreement was achieved for the overfilled launch. It tended to be the most conservative measure of bandwidth for both the fixed launches and the direct connection measurements (excluding 1300 nm FP lasers). Also it agreed best with the original OFL factory measurements. These results effectively confirmed the results and conclusions drawn in the late 1970s when the OFL launch was selected for standardization. Second, a significant amount of the bandwidth results exceeded the bandwidth capability of the test apparatus. This was especially true at 1300 nm and for the restricted launches on 50 μm fiber. However, the direct connection of 1300 nm FP SMF lasers produced consistent bandwidth decreases relative to overfilled. Bandwidth collapse as great as 40-50 percent was observed. The Gigabit Ethernet

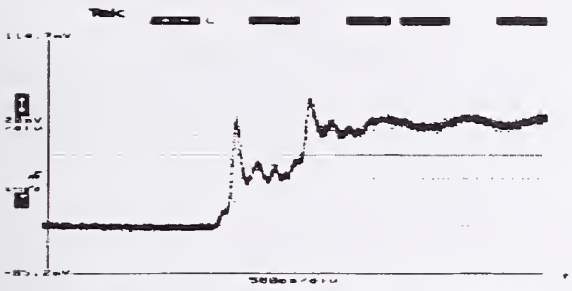

Figure 9 – Rising Edge of Digital Signal Showing Plateauing

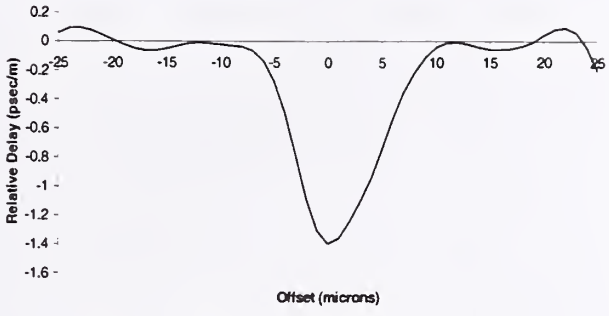

Figure 10 - DMD at 1300 nm for 62.5 um Fiber with Centerline Error

standards group's reaction was to establish link lengths (especially for 1300 nm and 62.5 μm fiber) based on significantly reduced fiber bandwidths.

Approximately a month or two after the release of these results, another issue arose. Laboratory results using 1300 nm FP SMF lasers and the recommended length of 62.5 μm fiber (standard grade similar to the installed base) did not achieve the required bit error rate for Gigabit Ethernet operation (8/1/97 Dave Hyer, DEC). The effect was consistent with different 1300 nm single-mode sources and fibers, and scaled with fiber length. An example of the rising edge of the digital signal exiting a link is given in Figure 9. The stair step formed on the rising edge is caused by two discrete delays occurring in the fiber. An example of the DMD of a fiber showing this effect is given in Figure 10. The DMD is flat over most of the radial extent of the fiber, but shows a large delay error for the lowest order modes on center, such as might be caused by a center line dip. The OFL bandwidth for this fiber is high since most of the power is carried in the intermediate modes which are well tuned. Thus, this fiber works as desired for overfilling sources such as LEDs (for which 62.5 μm fiber was designed) but runs into this issue when ultra restricted, single-mode launches such as those generated by the 1300 nm SMF FP laser are used. Since the original SMF launch results in 1996 did not show this collapse, the offset of 3 – 7 mm introduced by a MMF connector also is necessary. Such a connector typically is present on the jumper connecting the source to the cable plant.

Faced with an installed base of multimode fiber, whose bandwidth was unknown for such restricted launches, the Gigabit Ethernet standards group chose to control the launch distribution produced by the source. After evaluating various launch specifications and control mechanisms, it was agreed that sources must meet a coupled power ratio (CPR) requirement and that 1300 nm operation would require an offset launch patch cord[9].

CPR measurement is described in OFSTP 14[7] and consists of taking the ratio of the power coupled into SMF compared to MMF. The requirement ensures that a source launches a power distribution which is fairly overfilling. The offset patch cord achieves a significantly over filling power distribution by launching from a single-mode fiber into a multimode fiber through a controlled offset created by a special connector. The source must be designed to couple efficiently into the SMF launch fiber. By controlling the source launch conditions as well as adding a receiver bandwidth requirement and reallocating the jitter budget, agreement was achieved on the link lengths in the current standard and reproduced in Table 2.

Table 2 – Gigabit Ethernet Standard Link Length Specification

Bandwidth (850/1300 nm) (MHz-km)	62.5 μm		50 μm	
	160 / 500	200 / 500	400 / 400	500 / 500
850 nm	220 m	275 m	500 m	550 m
1300 nm	550 m	550 m	550 m	550 m

NOTE: 1300 nm operation requires offset patchcord.

Current Opportunities

Although the Gigabit Ethernet standard now is finalized, the possibility still exists for developing a methodology for achieving improved system performance over multimode fiber. The laboratory test results over the last few years holds the promise that a reliable solution can be found. Informal discussions have begun among members of the IEEE 802.3z regarding longer link lengths especially for short wavelength operation. Also, the TIA Task Group is still actively continuing its work.

There are three steps to a final solution. First, an effective means must be found to characterize the source power distribution. All experts involved in the decision to use CPR to control the source launch distribution were not satisfied with the ability of CPR to adequately specify a launch. It did at least ensure that an ultra restricted launch was avoided. The TIA Task Group is currently investigating Mode Power Distribution (MPD) measurement[7,10,11] as an alternative. Current consensus is that MPD provides a thorough characterization of a launch distribution. The second step consists of selecting a range of source launch distributions that will achieve improved performance with a range of allowable fiber profiles. It will require interaction between source and fiber manufacturers. DMD modeling of fiber bandwidth for various launch conditions can be used to determine the acceptable source and fiber characteristics that can consistently be supplied. The last step is to develop practical test methods to control the source launch distribution and characterize the fiber performance for the agreed upon restricted launch condition. Like DMD, MPD has practical limitations for use in specifications. Consequently, it is anticipated that an alternate can be found similar to CPR.

Acknowledgments

The author would like to express his appreciation to the individuals and organizations that are participating in the ongoing development work whose contributions are documented herein. The author would especially like to thank John Schlager and Doug Franzen of NIST for their contributions.

NIST, Lucent, Spectran, Corning, Siecor, Honeywell, HP, Cielo / VIXEL, IBM, DEC, Cabletron, Raytheon, and Unisys.

References

1) K. Giboney, L.B. Aronson, D.E. Lemof, "VCSELs, The Ideal Light Source for Data Nets," IEEE Spectrum, vol. 35 no. 2, February 1998, pp. 43-53.
2) ISO/IEC 9314-3, Information Processing Systems - Fiber Distributed Data Interface (FDDI) – part 3: Physical Layer Media Dependent (PMD).
3) Bandwidth model developed for IEEE P802.3z Specification for 802.3 Full Duplex Operation Supplement to Carrier Sense Multiple Access with Collision Detection (CSMA/CD) Access Method and Physical Layer Specification for 1000 Mb/s Operation.
4) Mammel & Cohen, 'Numerical Prediction of fiber transmission characteristics from arbitrary refractive-index profiles', Appl. Optics 21 (1982), pp 699-703.
5) Petermann, K., 'Simple Relationship between Differential Mode Delay in Optical Fibres and the deviation from optimum profile', Elec. Lett. 14 (1978), pp 793-4.
6) Olshansky, R., 'Pulse broadening caused by deviation from the optimal index profile', Applied Optics 15 (1976), pp 782.
7) TIA References: Fiber Optic Test Procedures (FOTPs) - TIA-455, Optical Fiber System Test Procedures (OFSTPs) - TIA-526, and Informative Test Methods (ITM) - TIA-TSB62.
8) S.E. Mechels, J.B. Schlager, D.L. Franzen. "High-Resolution Differential Mode Delay Measurement in Optical Fibers using a Frequency-Domain Phase-Shift Technique," Photonics Technology Letters, vol. 9, no. 6, June 1997, pp. 794-6.
9) L. Raddatz, I.H. White, D.G. Cunningham, M.C. Nowell, "An Experimental and Theoretical Study of the Offset Launch Technique for the Enhancement of the Bandwidth of Multimode Fiber Links," vol. 16, no. 3, March 1998, pp. 324-31.
10) S. Piazzola, G. DeMarchis, "Analytical Relations Between Modal Power Distribution and Near-Field Intensity in Graded-Index Fibres," Electronics Letter, 1979, no. 15, pp. 721-2.
11) M. Calzavara, P. DiVita, U. Rossi, "Mode Power Distribution Measurements in Optical Fibres," CSELT Rapporti Technici, vol. XI, no. 5, October, 1981, pp. 447-51.

Effect of Launch Conditions on Power Penalties in Gigabit Links Using 62.5μm Core Fibers Operating at Short Wavelength

Petar Pepeljugoski[a], John Abbott[b] and Jim Tatum[c]

[a]IBM TJ Watson Research Center, Yorktown Heights, NY 10598
[b]Corning Incorporated HPME-01-024, Corning NY 14831
[c]Honeywell Microswitch, 830 East Arapaho, Richardson, TX 75081

1. Introduction

An insatiable demand for information bandwidth has led to an explosion of fiber optic networks operating at and above 1Gb/s. There is current development effort by several standards bodies, including the IEEE 802.3z, ATM and Fibre Channel to develop communications standards for gigabit/sec speeds and beyond. For premises distances, the most cost effective optical networks use multimode fiber. The multimode fiber was designed and specified for light emitting diodes (LEDs). However, the LEDs can not achieve gigabit/sec speeds, thereby requiring the use of semiconductor laser diodes. Therefore, there is a need to recharacterize and respecify links for multimode fiber excited by laser diodes. In developing the communications standards, significant differences between the measured fiber bandwidth using historical overfilled launch conditions and those measured using laser launches have been found. In most cases, there was a significant increase in the fiber modal bandwidth using the laser launches; however, there were a few cases in which the bandwidth fell below its rated value. One of the essential requirements of the new communications standards was the ability to address the ubiquitous 62.5μm multi-mode fiber. The rated minimum bandwidth of Fiber Distributed Data Interface (FDDI) grade fiber is 160MHz·km at 850nm, and 500MHz·km at 1300nm. With 1300nm laser excitation, the effective bandwidth of the FDDI 62.5 μm fiber was below specification in nearly ten percent of the fiber population sampled. An offset launch technique has been described to eliminate the problem [1]. This has proven to be costly, and is not practical for the lower cost, higher volume 850nm solutions.

In this paper, we investigate the performance of the 62.5 μm core fiber under various launch conditions. In our study, both CD lasers and VCSELs were used, with variable spot sizes and numerical apertures, generating numerous launched power distributions into the optical fiber. Whereas previous analyses of fiber links have used only the fiber bandwidth as the predictor of link performance [1], we use the entire impulse response of the fiber to calculate both the inter-symbol interference (ISI) and the deterministic jitter (DJ) in the link. Our analysis yields more realistic results than those based on a simple Gaussian response of the fiber transfer function. We find that current IEEE 802.3z (Gigabit Ethernet) link lengths are quite conservative, and typical system performance will greatly exceed the specified 220m link length for FDDI fiber.

2. Method of measurements and analysis

The modal power distribution (MPD) in an optical fiber was measured using a technique similar to that described in reference [2]. In our case, a CCD camera was used to capture the laser's intensity profile with a resolution of 0.2 μm. Additionally, time averaging was employed to reduce the effect of speckle on the near field patterns. The lasers were driven under normal system parameters. The two dimensional data from the CCD camera was analyzed to obtain the intensity distribution, mode transfer function (MTF), MPD, and the 95% cumulative power distribution (CPD). Additionally, the coupled power ratio (CPR) was measured. Circular symmetry was assumed and Figure 1 is a plot of the mode power distribution as a function of mode group number for each laser.

Once the near field intensity profile in the fiber is known, the mode power distribution is estimated following the procedure of Calzavara et al. and Daido et al. [3,4]. This procedure uses the ratio of the derivative of the near field intensity to that of an overfilled launch. Even if the 2D data was azimuthally averaged, we still found it necessary to radially smooth the intensity data to get a workable mode power distribution. Other approaches to obtain the MPD include fitting the beam profile with a sum of Gaussian beams with different offsets and beam diameters (whose individual modal excitations can be calculated exactly) or fitting the beam profile to a sum of modal contributions.

Once the modal power distributions of the individual sources are known, they are used with mode delays to numerically model pulse propagation through the optical fiber. The mode delays for the model were determined from a set of 237 measured index profiles by a perturbation method [5]. Only profiles with overfilled bandwidth that was predicted to meet FDDI requirements (160/500 MHz·km) were used. The mode delays of the individual modes were assumed to be fully coupled and averaged together within each mode group. The transfer function of each optical fiber for each launch condition is then calculated, taking into account differential modal attenuation [6]. The output pulse from the optical fiber is represented as a weighted sum of Dirac delta impulses. The transfer function of the fiber is given by:. $H(if)=\Sigma C_k \exp(-i2\pi f\tau_k)$. The amount of power and the propagation delay time of the k^{th} mode is given by c_k and τ_k (ns/km) respectively. The 3dB fiber bandwidth is determined by the minimum frequency that satisfies the condition $|H(f)|/|H(0)|=0.5$. For the fiber lengths under consideration, we assume without loss of generality, the mode attenuation is uniform, and there is no mode coupling within the fiber.

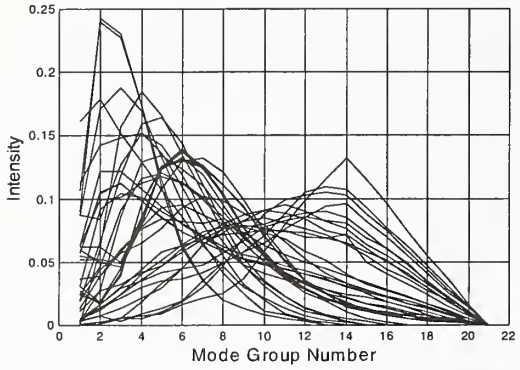

Figure 1. Mode power distribution for all devices used

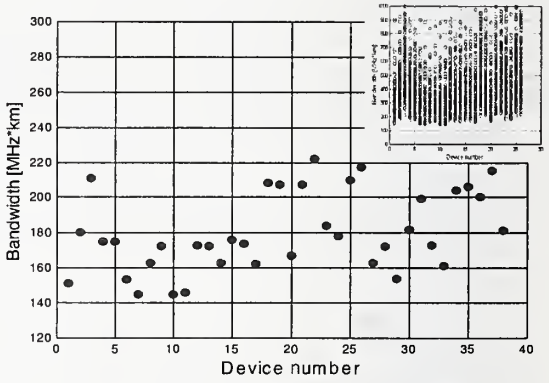

Figure 2. Minimum fiber bandwidth·distance product for each device. The inset shows bandwidths for all fibers and devices

3. Correlation of fiber bandwidth and beam profile parameters

The predicted bandwidths are given in Fig. 2. Of the 9006 simulations performed (237 fiber types and 38 sources) only 0.3% result in the fiber bandwidth falling below the 160MHz·km specification of FDDI. For 32 of the 38 sources the predicted bandwidth was above 160MHz·km for all fibers, and for 11 of the 38 sources the predicted bandwidth was above 200MHz·km for all fibers. We are interested in characterizing the robust sources which fall in this upper category.

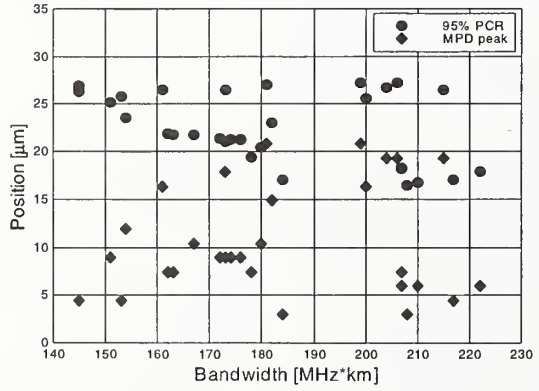

Figure 3. 95% CPD and peak of MPD as a function of minimum fiber bandwidth.

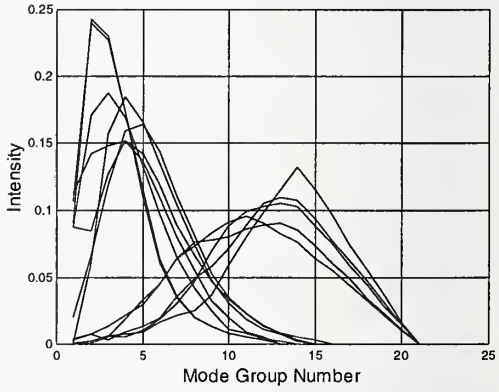

Figure 4. Mode power distribution for devices with bandwidth above 200 MHz km.

In an effort to relate the fiber bandwidth to easily measured parameters, we have examined the bandwidth as a function of 95% CPD, modal power distribution, full width half maximum (FWHM) and coupled power ratio. Figure 3 is a plot of the minimum modal bandwidth for our devices as a function of the 95% CPD and peak of the MPD. While each of the measures of fiber intensity distribution have merit, we find that no method is entirely predictive.

Our data set shows that the following sets of intensity distribution criteria are sufficient to achieve the minimum overfill bandwidth (160 MHz·km): a) 95% CPD less than 25μm and more than 10μm; b) the mode power distribution peaks between 10μm and 25μm; c) coupled power ratio greater than 9dB; d) FWHM between 10μm and 20μm. What we found upon further analysis was that the sources whose minimum predicted bandwidth was significantly above the 160MHz·km fell into two categories: either the modal power distribution was skewed toward the center with little power on the outside, or the power was skewed to the outside with little power in the center. Figure 4 shows the MPD for the sources with a minimum predicted bandwidth of more than 200 MHz·km.

4. Calculations of Deterministic Jitter and ISI Penalty

The link simulations were performed assuming the worst case parameters (as used in IEEE802.3z) for both the transmitter and the receiver. We used the Matlab™ based IBM OBST optical link simulator tool, which has built in models for each component in the link (laser, fiber and the receiver). Our simulations used a modification of a linear laser model which takes into account the duty cycle distortion at the laser output caused by laser turn-on delay. The receiver was modeled as an 800 MHz 4th order low pass Butterworth filter. The simulator was modified to take into account the fiber model described above. The accuracy of the simulator has been previously verified to match experimental results [7]. Our simulations used a transmitter with a rise time of 350ps, and deterministic jitter of 65 ps, sending a repeating k28.5 pattern. The numerical results of the simulator included the bandwidth of the optical fiber, the ISI penalty, and the deterministic jitter (DJ) seen by an analog receiver at the end of the fiber link. The DJ was calculated at the *maximum* horizontal eye closure measured at the zero point in an AC receiver. The simulations were done for link lengths of 220m and 300m.

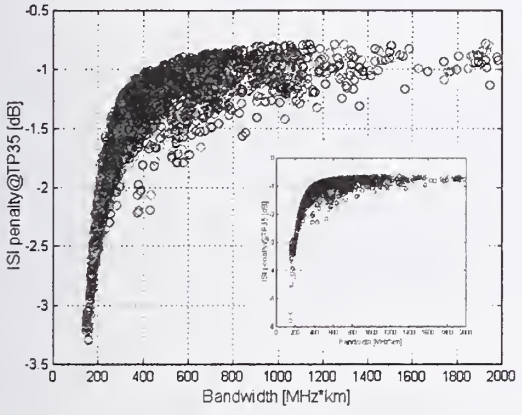

Figure 5. ISI penalty as a function of the bandwidth distance product. The fibers were 220m long. The inset shows the ISI penalty for 300m long fibers.

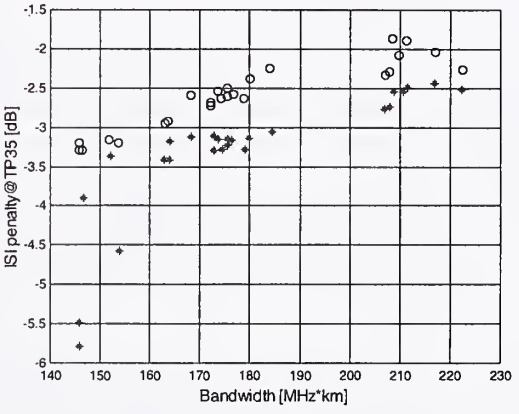

Figure 6. Comparison of the maximum penalties for fibers 220 m (circles) and 300 m long (asterisks). Only for bandwidths less than 160 MHz·km the penalty difference becomes significant.

Figure 5 is a plot of the ISI penalty as a function of the fiber bandwidth-distance product for a 220m optical link. There are three distinct regions of the curve. The first, for fiber bandwidths less than ~300MHz·km, indicates a unique correlation of the system ISI penalty to the fiber bandwidth. In this region, the system ISI penalty is dominated by the bandwidth of the optical fiber. In the second region, between ~300MHz·km and ~1200MHz·km, the system ISI penalty is determined by a complex interaction of the fiber transfer function, the laser transmitter and the receiver. The exact ISI penalty is extremely dependent on the details of the input optical pulse. As can be seen from figure 5, the ISI penalty can range as much as 2dB for a given fiber bandwidth. Clearly the system and fiber response do not have Gaussian shapes. The third region is above ~1200MHz·km where the variance in the ISI penalty decreases, and the ISI penalty begins to be dominated by the finite bandwidth of the laser transmitter and the receiver. Similar comments can be made about the inset to Figure 5, which is the ISI penalty as a function of fiber bandwidth-distance product for a 300m optical link. Figure 6 shows the maximum ISI penalties at 220m and 300m as a function of the bandwidth-distance product. For bandwidths greater than 160 MHz·km the difference between 220m links and 300m links is less than 0.7 dB, below 160 MHz·km the difference between link lengths becomes very significant. Figure 7 is a plot of the deterministic jitter in the link at the output of the analog section of the receiver as a function of the fiber bandwidth-distance product. Again, there appears to be three regions of interest, and similar discussion to

that for the ISI applies. The unique relationship between the fiber bandwidth and the deterministic jitter allows for operation of carefully controlled links with fibers having a bandwidth-distance product less than 200MHz·km. As the link length is increased to 300m, the deterministic jitter increases substantially for fiber bandwidths below 200MHz·km.

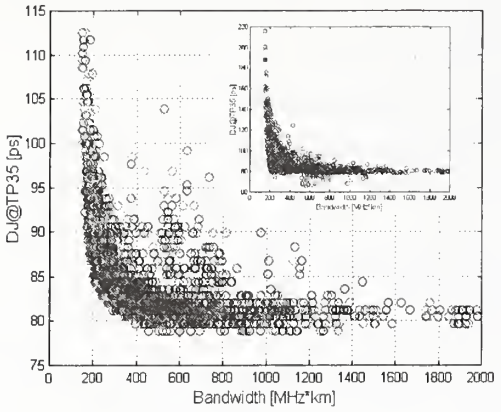

Figure 7. Deterministic jitter at the output of the analog section of the receiver, for 220m long fibers. The inset shows the jitter for 300m long fibers. Note that 40% increase in fiber lengths almost doubled the jitter.

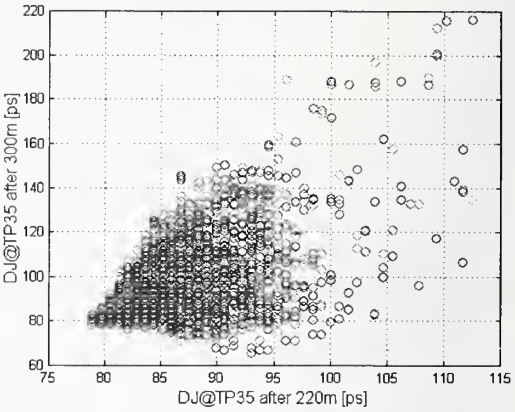

Figure 8. Comparison of deterministic jitter for 220m and 300m long link. This figure illustrates the complex dependence of the jitter in the link on the fiber length, bandwidth and DC unbalance.

Simple link models can often lead to wrong conclusions and conservative estimates. There is quite complex relationship between jitter and link distance, as illustrated in Figure 8. It appears that it is difficult to predict the jitter for longer links, based on measurement at shorter distances. While the DJ introduces a DC imbalance, after the signal travels through the fiber, the DJ effects are initially reduced due to ISI and the resulting trend to DC balance. As fiber lengths are further increased, the ISI begins to reintroduce DJ. We find the amount of jitter will depend on many factors, including the actual pulse shape of the signal and the impulse response of the fiber, not just the bandwidth.

5. Conclusions

In this paper, we investigated the effects of launch conditions on the fiber bandwidth and the link penalties. Our results show that several parameters may be necessary to fully predict the operation of a fiber optic link. Our results also show that while there is correlation between the bandwidth and the link ISI penalty, this correlation becomes rather weak for bandwidths exceeding 200 MHz·km. Our investigations show not only that the current Gigabit Ethernet lengths can be achieved, but they can be greatly exceeded. Therefore, robust, inexpensive short wavelength solutions, will continue to dominate the gigabit LAN market.

References

[1] Raddatz, L et al., "Influence of Restricted Mode Excitation on Bandwidth of Multimode Fiber Links", IEEE Photonics Technology Letters, vol. 10, no. 4, April 1998, pp. 537-539.

[2] Telecommunication Industry Association OFSTP-ITM-3

[3] Calzavara, M. *et al.*, "Mode power distribution measurements in optical fibers," CSELT Technical Report **IX** (5), pp. 447-451, (1981).

[4] Daido, Y, *et al.*, "Determination of modal power distribution in graded-index optical waveguides from near field patterns and its application to differential mode attenuation measurement," Applied Optics, **18**, pp. 2207-2213, (1979).

[5] Olshansky, R., "Pulse Broadening Caused by Deviations from the Optimal Index Profile", Applied Optics **15**(3) March 1976 pp.782-788.

[6] Marcuse, D., Principles of Optical Fiber Measurements. New York: Academic Press, 1981.

[7] Pepeljugoski, P., presentations to the IEEE802.3z MBI study group

Improved Performance in Short-Haul Multimode Fibre Systems by Using Low-Order Launch Conditions

Robert S. Billington[1], Jerry M. Benson[2], Timothy C. E. Jones[2] and John C. C. Nelson[1]

[1] *Institute of Integrated Information Systems, School of Electrical and Electronic Engineering, University of Leeds, Leeds, Yorkshire, LS2 9JT, UK.*

[2] *Centre for Quantum Metrology, National Physical Laboratory, Teddington, Middlesex, TW11 0LW, UK.*

Multimode fibre is increasingly being deployed in local area networks and as part of the control systems in vehicular environments. A significant constraint on the use of this technology in critical systems is the uncertainty in the optical power loss over highly-connected short lengths of fibre which may be subjected to severe bending. In this paper, a summary is presented of launch-dependent effects together with experimental bending loss and simulated splice loss results. These indicate that the use of restricted launch conditions leads to more predictable losses as well as higher bandwidth than if a simple overfilling launch is used.

1) INTRODUCTION

Equalisation of optical path lengths in multimode fibre, and consequently maximisation of the fibre bandwidth, can best be achieved by grading the refractive index of the core to give an almost parabolic index profile [1]. Within such graded-index fibres, modes may be broadly described as low-order or high-order, where low-order modes propagate close to the centre of the fibre core and high-order modes have a significant component near the core-cladding interface.

Experimental investigations have shown that by selectively exciting the low-order modes of a graded-index fibre, modal dispersion can be minimised. This has been performed by using a controlled launch system [2] , and launching from a single mode fibre either directly [3] or via bulk optics [4].

Rayleigh scattering from dopant atoms in the fibre core and imperfections at the core-cladding boundary and on-axis induce mode-dependent attenuation effects with the general tendency that high-order modes suffer greatest attenuation [5]. The measured attenuation of multimode fibre has been found experimentally to be dependent on the modal power distribution (MPD) [2]. Results for cabled fibre, connectors and power splitters have also shown that power loss from low-order modes is less than that from high-order modes [6,7].

In this paper, experimental results are presented which show that low-order modes are significantly more immune to losses due to macrobending and microbending than high-order modes. In addition, simulation results from a model of a laterally offset butt-coupled joint show that connector losses can be minimised by launching power only into low-order modes.

The combined effect of all these results is that by using a low-order launch, the bandwidth of a multimode system will be maximised and the total power loss will be far less dependent on fibre handling and connectorisation than if an overfilling launch is used. It should therefore be easier to calculate the power budget for a system with a smaller uncertainty than is possible for the case of unrestricted launches.

2) BENDING LOSS

The experimental system shown in figure 1 has been constructed at The National Physical Laboratory; it can be used to perform controlled launches into multimode fibre and scan the transmitted near-field leaving the far end for the purposes of modal analysis [8]. The controlled launch system was used to generate launches which

predominantly excited low-order modes. By placing the input end of the fibre in direct contact with the LED source, overfilling launches could also be performed.

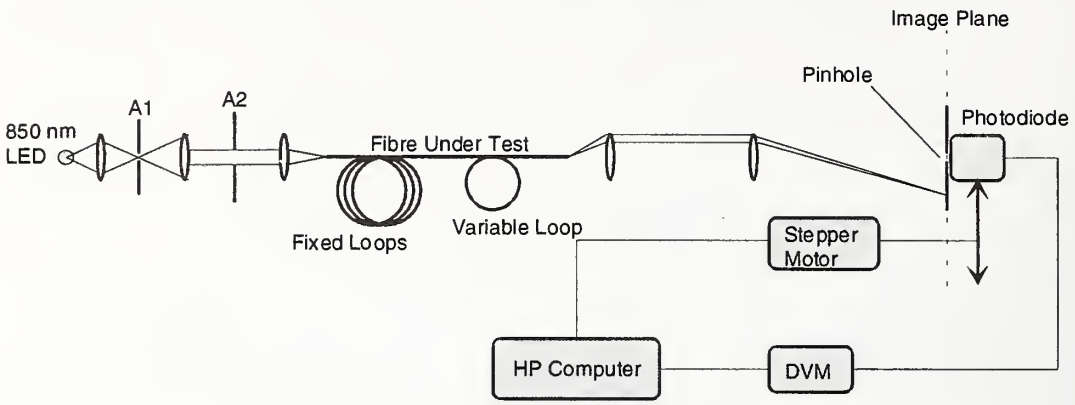

Figure 1. Controlled launch and near-field scanning systems.

2.1) Macrobending

A 5 m long sample of 62.5/125 μm graded-index fibre was mounted in the controlled launch system and arranged to include a variable-diameter loop. Transmitted near-field (TNF) scans were performed on the intensity profile at the output end of the fibre for a number of loop diameters. The experiment was also repeated using an overfilling launch to excite the fibre. The measured near-fields for a number of loop diameters with intensity in arbitrary intensity units (aiu) are shown in figure 2. The near-fields were then curve-fitted and converted into modal power distributions following [7]. Total guided powers in arbitrary power units (apu) leaving the fibre were then calculated from these MPDs and are shown in figure 3.

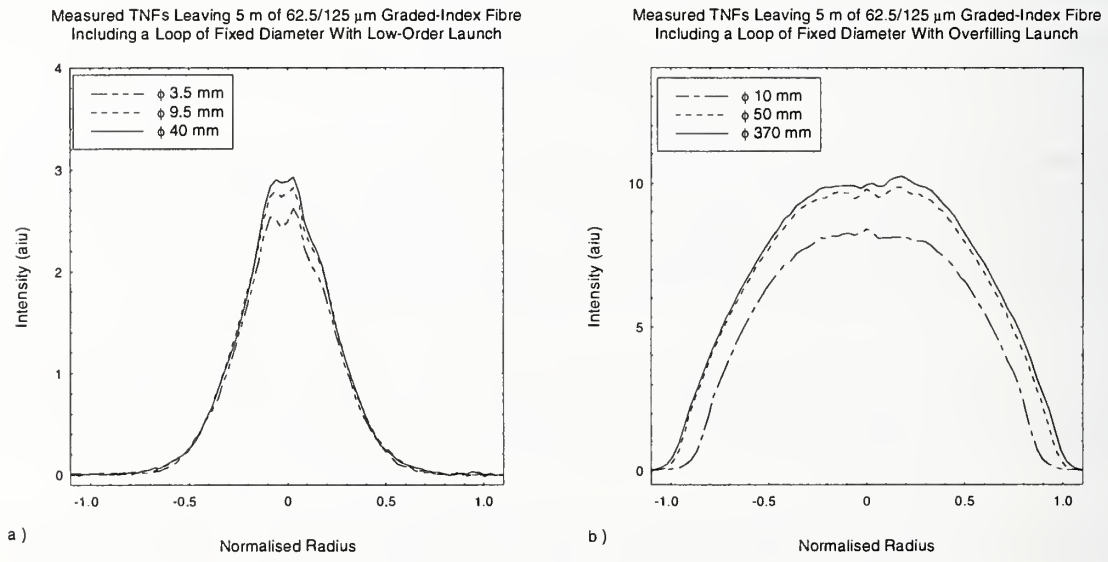

Figure 2. Transmitted near-field intensity distributions leaving 5 m of 62.5/125 μm graded-index fibre including a single loop for a) low-order and b) overfilling launch conditions.

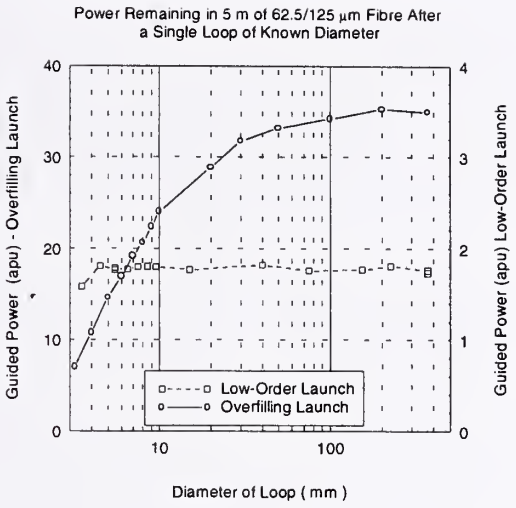

Figure 3. Calculated optical powers leaving the fibre sample for low-order and overfilling launch conditions with various loop diameters.

It can be seen from figures 2 and 3 that using overfilling launch conditions, whilst coupling more power into the fibre than a restricted launch, does lead to considerably greater sensitivity to bending. The actual power leaving the output end of the fibre with no bends of less than 370 mm diameter was estimated to be approximately 1.5 µW for the low-order launch and approximately 30 µW for the overfilled launch.

2.2) Microbending

The experimental system illustrated in figure 1 was also used to investigate the effects of microbending on the modal power distribution in a bare 2 m length of 62.5/125 µm graded index fibre. The microbending device consisted of two aluminium plates lined with copper gauze between which the fibre could be compressed by adding a weight to the upper plate. The weave of the copper gauze was such that the microbends had a period of between approximately 0.5 mm and 1.0 mm. Low-order and overfilling launches were again used to excite the fibre and near-field scans were performed with and without the microbending device in place. The measured near-fields with and without microbending are shown in figure 4.

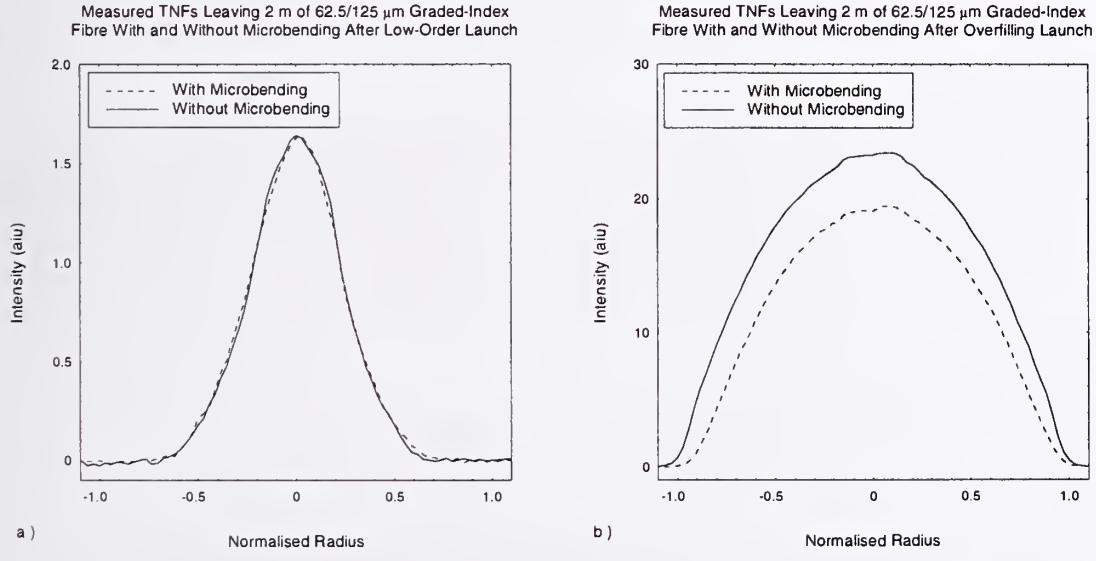

Figure 4. Transmitted near-field intensity distributions leaving a 2 m sample of 62.5/125 µm graded-index fibre with and without microbending for a) low-order and b) overfilling launch conditions.

The attenuation due to microbending was calculated to be -0.16 dB ±0.16 dB for the low-order launch and 1.52 dB ±0.20 dB for the overfilling launch. Microbending may be introduced into fibres by the cabling process and the severity of these imperfections may therefore vary from cable to cable. The restricted launch should avoid cable-dependent microbending loss by not exciting the high-order and leaky modes which are most easily coupled out of the fibre by waveguide perturbations.

3) SIMULATED CONNECTOR LOSS

Demountable connectors with slight lateral offsets were modelled by calculating the transfer of power between modes of two identical fibres with zero longitudinal and angular offsets. Three modal power distributions were passed to the connector model and were then compared with the predicted output modal power distributions to produce the excess loss values shown below in figure 5b. Transmitted near-fields corresponding to the three input modal power distributions are shown in figure 5a.

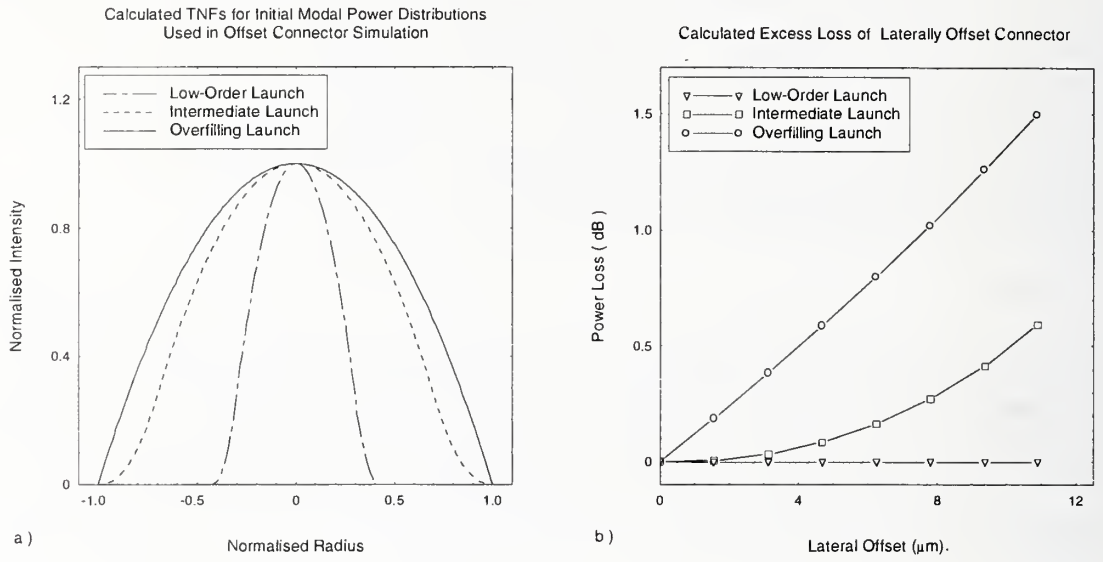

Figure 5. Simulated excess losses for three different initial power distributions entering a laterally offset connector. Losses due to reflection will be independent of the modal power distribution and have been omitted.

4) CONCLUSIONS

Experimental and simulation results have been presented which show that the use of a restricted launch into a multimode system will result in more predictable and less sensitive system attenuation than a simple overfilling launch. This, together with the improved bandwidth which can be achieved when restricting the launch conditions, make this launch attractive for planning short-haul systems where the path of the fibre may need to be flexible or where "worst case" losses need to be considered. Realising the restricted launch in a practical system could be done by using laser sources or pigtailing LED sources to small-core, low NA fibres which can then be connected to the multimode system.

5) ACKNOWLEDGEMENTS

This work was funded by EPSRC and The National Physical Laboratory.

6) REFERENCES

[1] Gloge, D. , Marcatili, E. A. J. , " Multimode Theory of Graded-Core Fibers", Bell System Technical Journal **52**, *pp* 1563 - 1578, (1973).

[2] Hackert, M. J. , " Explanation of Launch Condition Choice For GRIN Multimode Fiber Attenuation and Bandwidth Measurements" , Journal of Lightwave Technology **10**, No. 2, *pp* 125 - 129, (1992).

[3] Haas, Z. , " A Mode-Filtering Scheme for Improvement of the Bandwidth-Distance Product in Multimode Fiber Systems", Journal of Lightwave Technology **11**, No. 7, *pp* 1125 - 1130, (1993).

[4] Franzen, D. L. *et a.l* , " Differential Mode Delay Measurements in Multimode Fibers Using a Frequency Domain Technique with Variable Launch", 4th Optical Fibre Measurement Conference, Teddington, UK, *pp* 109 - 112, (1997).

[5] Olshansky, R. , Oaks, S. , " Differential Mode Attenuation Measurements in Graded-Index Fibers", Applied Optics **17**, No. 11, *pp* 1830 - 1835, (1978).

[6] Yang, S. *et a.l* , " Interlaboratory Comparison of Mode Transition Matrices", Applied Optics **32**, No. 30, *pp* 5997 - 6005, (1993).

[7] Yang, S. , *et al.* , " Transfer Function Analysis of Measured Transfer Matrices", Applied Optics **28**, No. 15, *pp* 3148 - 3157, (1989).

[8] Billington, R. S. *et al* , "Development of a Multimode Fibre Simulation Tool for Characterising Attenuation as a Function of Launch Conditions and Handling" , 4th Optical Fibre Measurement Conference, Teddington, UK, *pp* 113 - 116, (1997).

Differential Mode Delay Measurements On Multimode Fibers in the Time and Frequency Domains

J. B. Schlager and D. L. Franzen
National Institute of Standards and Technology, 325 Broadway, Boulder CO 80303

Introduction

Multimode fiber bandwidth is currently measured using an overfilled launch condition. Such a launch is achieved by uniformly exciting the core and launching with a numerical aperture (NA) that exceeds the NA of the fiber.[1] This launch provides a reproducible way to predict the bandwidth performance of LED-based fiber networks. New high-speed fiber networks, however, take advantage of the faster modulation capabilities of laser sources like vertical cavity surface emitting lasers (VCSELs) and Fabry-Perot lasers. These sources typically underfill the available mode volume of the fiber. In most cases these underfilled or restricted laser launches give bandwidth performances that meet or exceed the bandwidth performances predicted with overfilled launches. The specific behavior, however, depends on the differential mode delay (DMD) of the fiber's refractive index profile. We have developed a frequency-domain DMD measurement system with a temporal resolution of 0.2 ps. This represents a more than 50 times improvement over more conventional time-domain DMD measurement systems.[2] The new system allows accurate DMD measurements on shorter fiber samples, and the DMD results compare well with those obtained using the time-domain technique.

Frequency Domain Method

The frequency-domain technique employs an integrated optic intensity modulator that sinusoidally modulates light from an 850 nm or 1300 nm laser source at 1.9 GHz. Light exiting the single-mode fiber pigtail of the modulator is launched into the multimode fiber under test using a butt-coupled launch ($\lesssim 5$ μm separation). The RF phase of the detected light at the output of the multimode fiber is compared to a reference signal derived from the crystal oscillator driving the modulator. Any change in the delay of the propagation path results in a phase shift, which is detected by a vector voltmeter. The DMD profile of a fiber is acquired by scanning the single-mode fiber across the core in 1 μm steps and recording the change in RF phase. Good cleave quality for both the single-mode launch fiber and the multimode test fiber is important. Fiber end preparation is monitored using an interferometric microscope to check flatness and perpendicularity.

Comparison with Time Domain Method

To compare DMD measurements made using this technique with the conventional time-domain method, which measures time-of-flight differences for short optical pulses,[3] we obtained four different 600 m lengths of 62.5/125 μm, graded-index multimode fiber. Each 600 m sample was cut into three pieces— two 50 m pieces from each end and the remaining 500 m center piece. The 50 m lengths were measured using the frequency-domain system, and the central 500 m was measured with the time-domain system. By

measuring both ends separately, we were able to detect possible changes in DMD over the 600 m of fiber. Figures 1-4 show time-domain and frequency-domain DMD data collected for two fiber samples at the source wavelengths of 850 nm and 1300 nm. Part (a) of each figure shows the relative delay in pulse waveforms as obtained from a sampling oscilloscope. To obtain these traces, pulses of 150 ps duration at 850 nm and 60 ps at 1300 nm were launched into the test fiber using the same butt-coupled launch setup as the frequency-domain system. Large area detectors (200 μm diameter at 850 nm and 150 μm at 1300 nm) minimized mode filtering effects but also limited the temporal resolution of the time-domain system to an impulse response of 200 ps at 850 nm and 115 ps at 1300 nm. Part (b) of each figure shows the DMD data obtained from both the frequency- and time-domain systems. Good agreement exists for the four cases. Figure 4 shows that when pulse splitting is observed in the time domain, the mean delay of the waveform (as opposed to the delay of the waveform's peak) compares more favorably with the frequency-domain result.

DMD Length Dependence

Figure 5 illustrates the capability of the frequency-domain technique to capture changes in DMD over relatively short lengths of fiber. Three 50 m sections, separated by roughly 500 m, were sampled from a 2.2 km spool of commercial 62.5/125 μm fiber. The peak DMD excursion varies from a value of 1.1 ps/m in the first section to 3 ps/m in the third section at a separation of 1070 m. Such variations in DMD may be important when considering length scaling of bandwidth measurements made on long (~10 km) fiber samples that ultimately are cut into shorter lengths (~500 m) for application in local area networks.

Acknowledgements

This work was partially supported by the Office of Naval Research and the Space and Naval Warfare Systems Center.

References

1. "Mode scrambler requirements for overfilled launching conditions to multimode fibers," Telecommunications Industry Association Fiber Optic Test Procedure FOTP-54.
2. S. E. Mechels, J. B. Schlager, and D. L. Franzen, "High-Resolution Differential-Mode Delay Measurements in Optical Fibers Using a Frequency-Domain Phase-Shift Technique," *Photonics Technology Letters*, vol. 9, pp. 794-796, June 1997.
3. R. Olshansky and S. M. Oaks, "Differential mode delay measurement," in *Proc. 4th Eur. Conf. Optical Communication (ECOC)*, Genova, Italy, 1978, pp. 128-132.

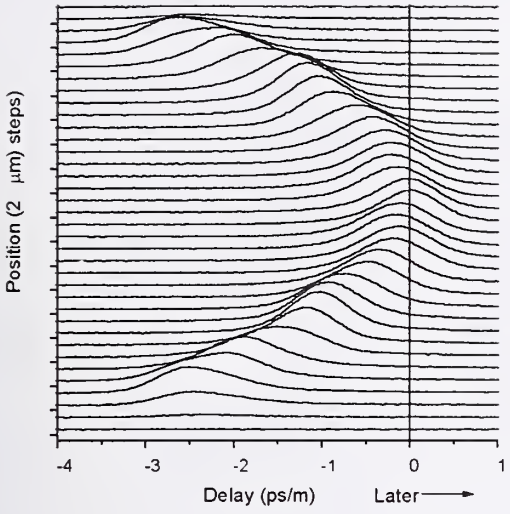

Fig. 1 (a) Relative pulse delay at 850 nm for 500 m 62.5/125 μm fiber 1.

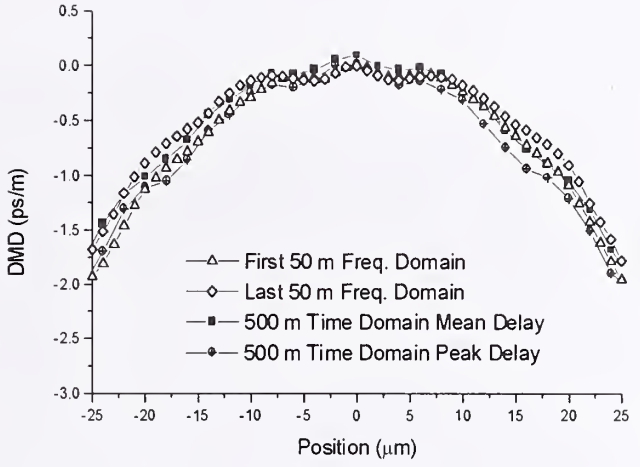

Fig. 1 (b) DMD at 850 nm from frequency- and time-domain techniques for fiber 1.

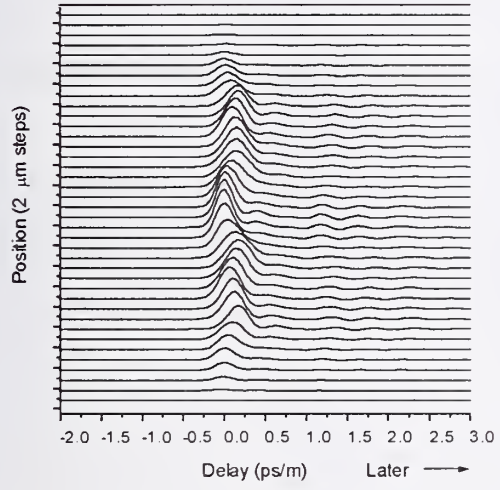

Fig. 2 (a) Relative pulse delay at 1300 nm for 500 m 62.5/125 μm fiber 1.

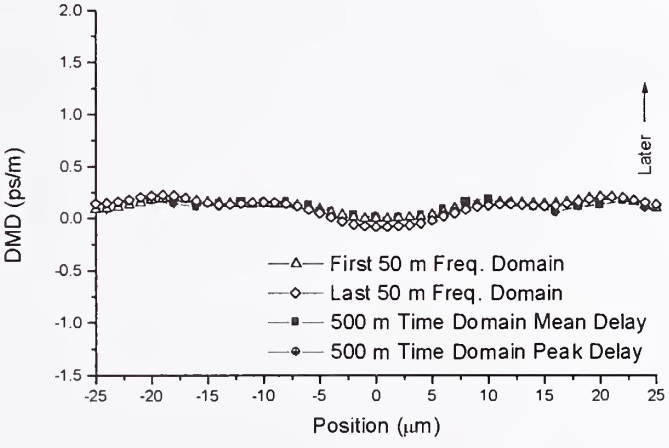

Fig. 2(b) DMD at 1300 nm from frequency- and time-domain techniques for fiber 1.

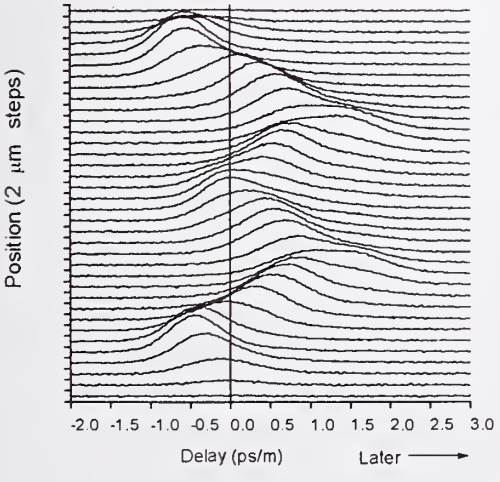

Fig. 3 (a) Relative pulse delay at 850 nm for 500 m 62.5/125 μm fiber 2.

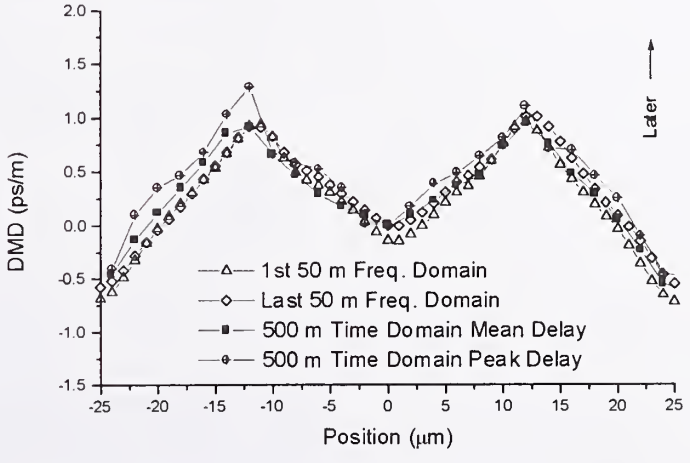

Fig. 3 (b) DMD at 850 nm from frequency- and time-domain techniques for fiber 2.

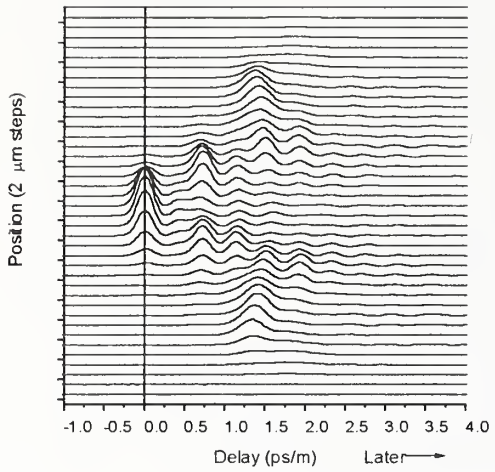

Fig. 4 (a) Relative pulse delay at 1300 nm for 500 m 62.5/125 μm fiber 2.

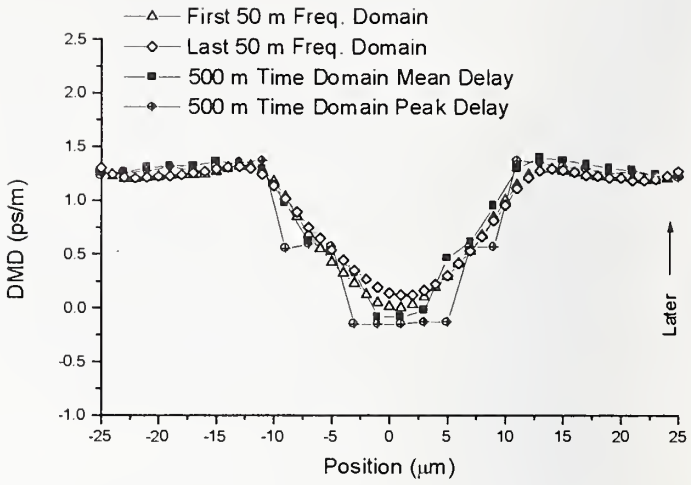

Fig. 4 (b) DMD at 1300 nm from frequency- and time-domain techniques for fiber 2.

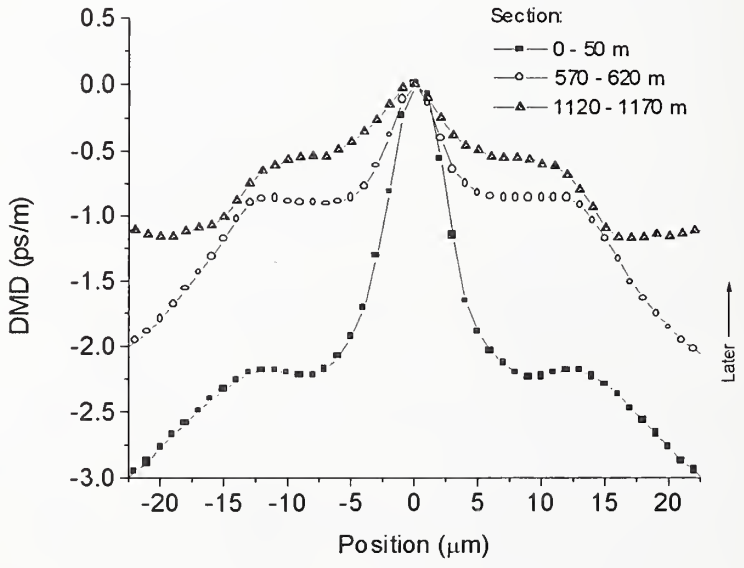

Fig. 5 DMD at 850 nm for three 50 m sections from a 1.17 km sample of 62.5/125 μm multimode fiber.

Ultra-high resolution two dimensional differential mode delay measurements of multimode fibers

Constantine T. Markos, Alfred D. Ducharme, and Gerry Wyntjes
Visidyne, Inc., 10 Corporate Place, South Bedford Street, Burlington, MA 01803

ABSTRACT

The study of Differential Mode Delay (DMD) in multimode graded-index fibers received much attention until approximately the mid-1980's[1,2]. The number of papers decreased thereafter most likely as a result of diminished use of multimode fibers in long-distance and high-bandwidth applications. The recent decision to use multimode fiber for short distance (< 550 m) Gigabit Ethernet has sparked new interest in the effects of DMD on the bandwidth of multimode fibers[3]. To date, only single axis scans of DMD for telecommunication fibers have been published[4]. In this paper we describe a two-dimensional DMD (2D-DMD) measurement for two standard telecommunication fibers, 50 um and 62.5 um diameters. These measurements were made using a proprietary Digital Phase Processor (DPP) which allowed us to achieve an ultra-high time delay resolution of 50 femto-seconds.

1. Experimental Setup

The DMD measurement technique is illustrated in Fig. 1. An intensity modulated 830 nm laser diode is coupled into a 5 um single-mode fiber (SMF) . The SMF is mounted on an XYZ translation stage. The multimode fiber (MMF) under test is mounted on a second stationary stage. A selective mode launch technique is used to excite discrete mode groups in the MMF by raster scanning the SMF over the face of the MMF[1].

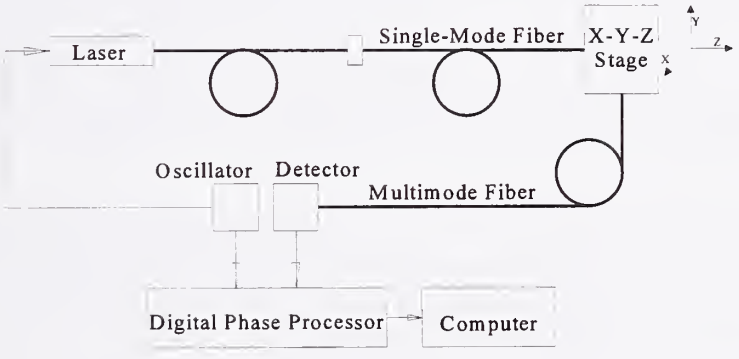

Figure 1. 2D-DMD measurement experimental set-up.

The other end of the MMF is directly coupled onto a photodiode detector which detects the modulated light after it has passed through the MMF. The reference modulation is compared with the detected modulation and the phase difference between these signals is calculated by the DPP. Although different mode groups in a graded-index fiber are designed to have the same mode delay small perturbations in the optimal index profile are manifested as DMD. These differences are measured and stored in a two-dimensional array in a personal computer.

2. Measurements

Figure 2a shows the results for the DMD measurement of a 50 um graded-index MMF fiber as a function of the position. This measurement shows a peak time delay of 18 ps/meter, however, the average delay near the fiber center is less than 9 ps/meter. In viewing the 2-D plot, the DMD has a structure showing that the construct of the fiber is asymmetric. The lowest time delay surrounds the center of the fiber. This suggests that there is a central dip in the index of refraction profile. Also, there are numerous contours which also suggests that there are ripples in the index profile.

The 62.5 um fiber, Fig. 3a, shows an extremely asymmetric shape in the DMD profile and has a peak time delay of 27 ps/meter. However, this plot shows that the lowest time delay is at the center and has an elliptical shape. Like the 50 um fiber, this plot suggests that there are ripples and large variations in the index profile. Figure 3b shows the effect of the elliptical shape in the X and Y direction.

3. Conclusion

We have demonstrated an ultra-high resolution DMD in two dimensions. The measurements show that there are large structures and asymmetries in the time delays. Suggesting that there are variations, ripples, and central dips in the index of refraction profile. These variations will widen the impulse response of the MMF which reduces the bandwidth. Two-dimensional DMD provides the important information needed by fiber manufacturers as feedback for quality control in manufacturing. This would be a valuable tool for fiber manufacturers since it provides the information needed to see all the variations in the index profile. One-dimensional scans provide only limited DMD information.

More measurements are needed to better understand the construct of multi-mode fibers. Due to lack of funding the XYZ stage used in the experiment was crude, which made raster scanning the MMF difficult. A computerized motor stage is being obtained to sample smaller spatial increments of the fiber face. A Mach-Zehnder amplitude modulator will also be used in future measurements to modulate the amplitude of a laser diode. Modulating the amplitude of the light external to the laser would eliminate small errors in the wavelength.

Visidyne, Inc. is currently working on a computer simulation of the DMD effect written in IDL (Interactive Data Language) image processing software. Visidyne, Inc. is in the process of commercializing this DMD measurement system, and has begun a marketing study to determine the feasibility and demand for a 2D-DMD test system.

4. References

(1) H. Kobrinski, and G. J. Herskowitz, "Characterization of optical fibers by a differential excitation technique," *Applied Optics*, Vol. 22, No. 23, Dec. 1983.

(2) D. Gloge, and E. A. J. Marcatili, "Multimode Theory of Graded-Core Fibers," *The Bell System Technical Journal*, Vol. 52, No. 9, Nov. 1973, p. 1563.

(3) Gigabit Ethernet accelerating the standard for speed, *White Paper*, Gigabit Ethernet Alliance, 1997.

(4) J. B. Schlager, S. E. Mechels, and D. . Franzen, "High resolution differential delay measurements and bandwidth of multimode fibers," *IEEE LEOS*, Vol. 2, Nov. 1997.

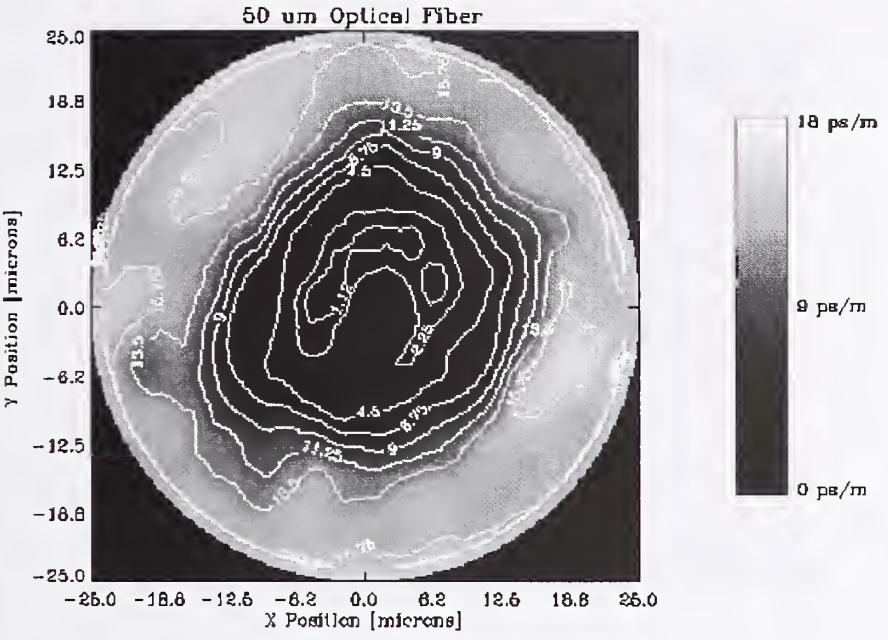

(a)

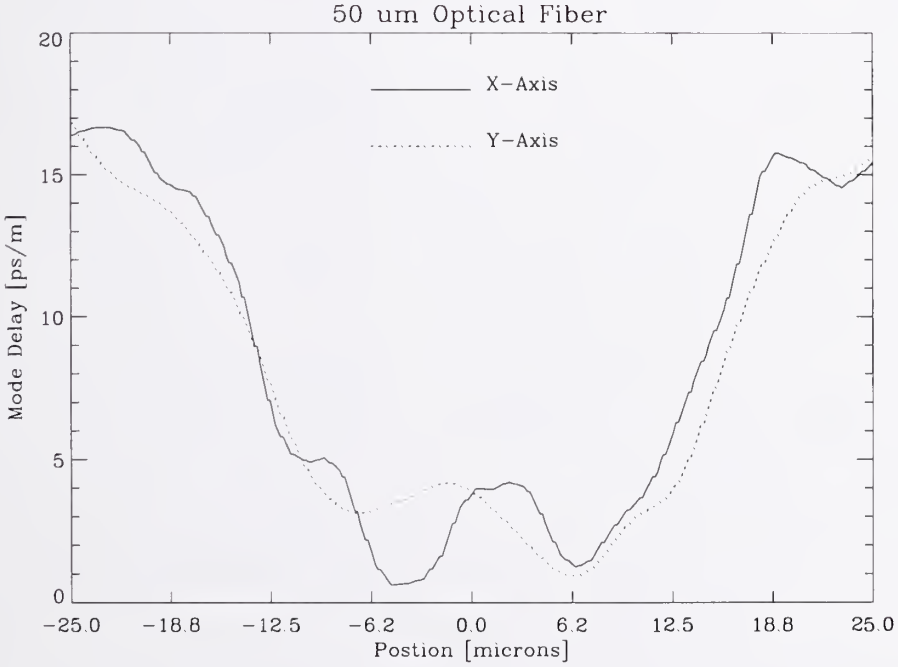

(b)

Figure 2. DMD measurements for the 50 um fiber in (a) 2-D and (b) 1-D.

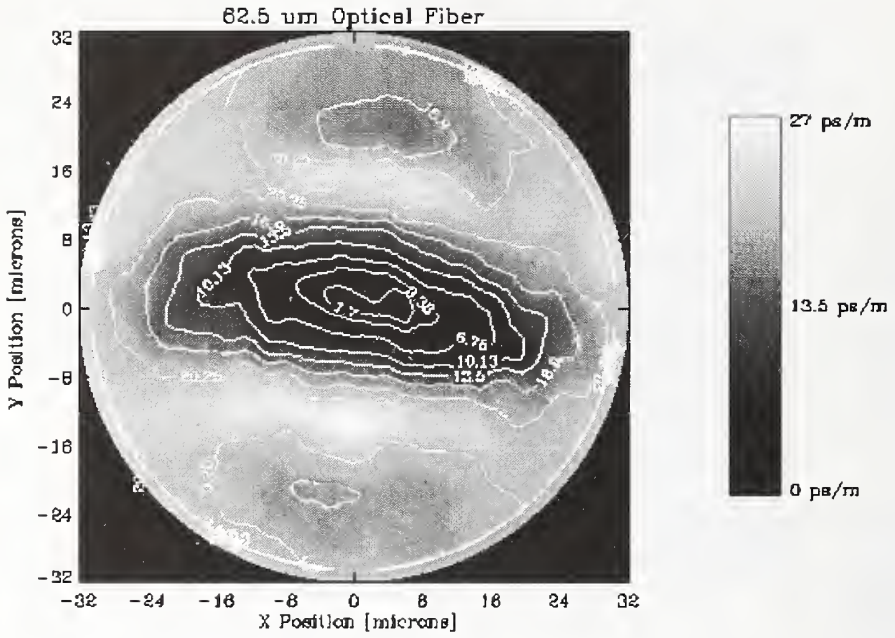

(a)

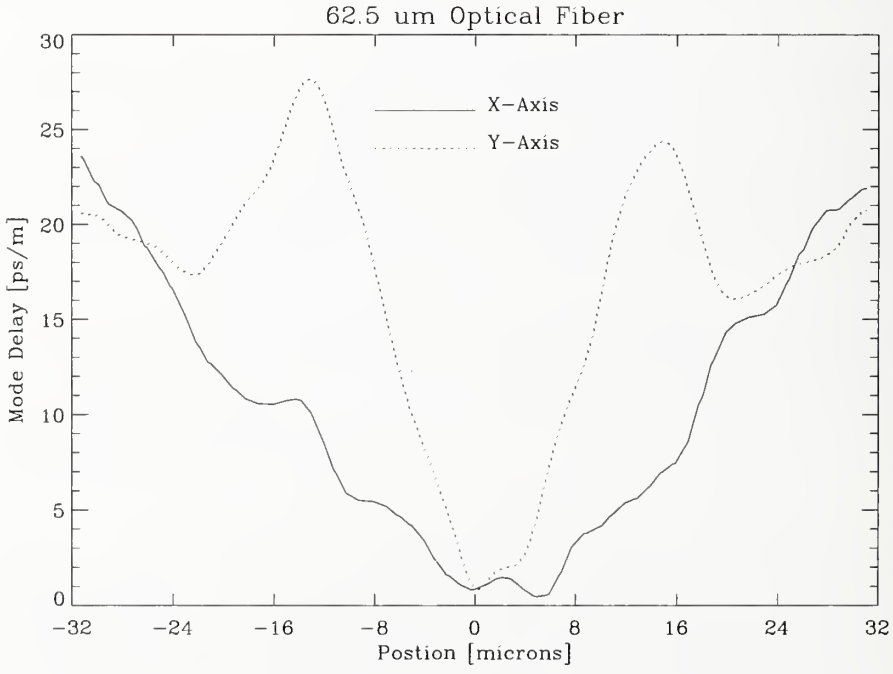

(b)

Figure 3. DMD measurements for the 62.5 um fiber in (a) 2-D and (b) 1-D.

Intermodal Dispersion and Mode Coupling in Perfluorinated Graded-Index Plastic Optical Fiber

Michael Dueser, W. R. White, and W. A. Reed
Bell Laboratories, Lucent Technologies
600 Mountain Ave.
Murray Hill NJ 07974

Tsuyosi Onishi
Asahi Glass Company
1150 Hazawa-cho, kanagawa-ku, Yokohama-shi Japan

In recent years, there has been great interest in use of plastic optical fiber (POF) for local area network (LAN) applications. Because polymer materials have much lower elastic moduli than silica, it is possible to produce plastic fibers with very large cores and still maintain acceptable mechanical properties. Thus, plastic fibers offer the potential for inexpensive and robust interconnection as well as simplified production of active system components. Additional impetus has been provided by dramatic reductions in absorption loss, made possible by the introduction[1] of amorphous perfluorinated polymers for POF applications. Also, graded-index multimode plastic fibers with non-ideal index profiles have shown[2,3] bandwidths higher than would be expected from standard calculations of intermodal dispersion. It has been suggested[3] that the last phenomenon derives from a high degree of mode coupling in plastic fiber, and there is convincing evidence that significant mode mixing occurs in step-index plastic fibers produced from standard protonated polymers, such as polymethyl methacrylate (PMMA). If this result holds true for POF in general, this will be another important benefit of plastic fiber for LAN applications. In this paper, we present differential mode delay (DMD) measurements which strongly suggest mode mixing occurs on very short length scales in perfluorinated plastic optical fiber. To our knowledge, this work represents the first DMD measurements performed on perfluorinated POF. Also, since we measure fiber with much lower loss than that obtained in conventional POF, we may examine intermodal dispersion at length scales longer than those previously accessible.

In a differential mode delay experiment[4], one excites a multimode fiber with a pulsed source having a spot size much smaller than the fiber diameter. By varying the position at which the input spot impinges on the endface of the fiber, one changes the relative excitation of different modes. In particular, moving the launch position away from the center of the fiber core redistributes power from low-order modes into higher-order modes. Thus, by measuring the time required for the input pulse to propagate through the fiber as a function of the launch position, one may probe intermodal dispersion in the fiber. Fig.1 describes an apparatus which we have constructed to perform DMD measurements of large core plastic fiber. An 820nm diode laser generates pulses of width 200ps with a repetition rate of 1MHz, output through a pigtailed 5μm diameter 0.12 N.A. singlemode fiber. We mount the singlemode output in an actuator which performs a two-dimensional scan over the surface of the multimode fiber of interest. At the output of the multimode fiber, we use a combination of a graded index rod lens and a plano-convex lens to focus the output pulse onto the 200 μm active area of a Hamamatsu C4258 detector. The output of this detector connects directly to the sampling head (model SD-22) of a Tektronix CSA 803 digital oscilloscope, which triggers from the pulsed source.

With this instrument, we have examined perfluorinated graded-index plastic optical fiber produced[5] by the Asahi Glass Company. This fiber had outer diameter 350 μm, with a core diameter of approximately 140 μm. The index profile is approximately parabolic, with a core refractive index of 1.355, and a cladding refractive index of 1.342. At 820 nm, this fiber has a loss of 60 dB/km. To prepare the fiber for measurement, we polish the fiber ends by dipping[6] in a perfluorinated solvent.

Figure 2 shows typical pulses measured with various launch positions after propagation through a 118m length of the POF. For a launch position at the center of the core, the output pulse shows only a slight

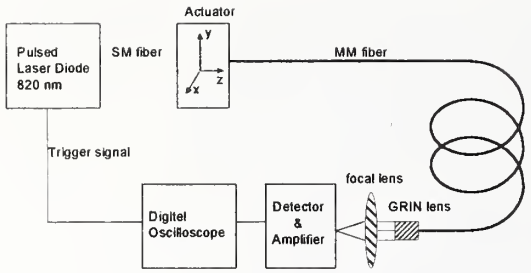

Figure 1 Schematic diagram of experimental apparatus

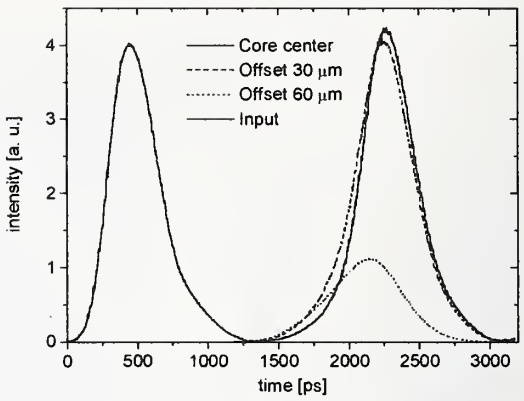

Figure 2 Typical output and input pulses

broadening compared to that measured for a very short (1 m) length. (Pulse heights have been scaled to compensate the ~7 dB loss occurring in the fiber.) As we move the input position away from the core center, the pulse is slightly broadened and attenuated, and the broadening and attenuation becomes more pronounced as the offset approaches the core radius. More importantly, the centroid time delay of the pulse decreases with offset, as a result of intermodal dispersion. In this particular fiber, the centroid delay decreases with increasing offset, indicating a larger propagation velocity for higher-order modes. Such a result is expected for fibers with an overcompensated index profile. To map the dependence of pulse delay and attenuation on launch position, we systematically scan the pulsed source over the face of the fiber in 15μm steps, and measure the integrated intensity and centroid time delay of the output pulse for each launch position. Since we expect cladding modes to be strongly attenuated by the coiling of the fiber during measurement, we minimize the influence of these modes by measuring only under launch conditions where the integrated intensity of the output pulse is at least 10% of that measured for a launch into the center of the fiber core. We have verified that this cutoff criterion results in a constant scan area for all fiber lengths measured, indicating that the measurements presented here are not significantly influenced by cladding modes launched at the input.

Fig.3 shows a typical result of pulse delay measurements in a scan over the fiber. In this plot, each contour represents a range of pulse delays of 40 ps, with the darkest contour representing the longest delay range. In this measurement, one may readily observe that the pulse delay has a slight azimuthal asymmetry with respect to the launch position. This pattern changes only slightly with fiber length, so presumably the observed asymmetry arises from a similar asymmetry in the index profile. Also, the position dependence of the pulse delay increases very rapidly near the periphery of the core. Since the source spot has finite size, this position dependence probably accounts for the broadening observed in pulses injected near the periphery.

While the characteristic pattern of delays shown in Fig. 3 does not change with fiber length, the magnitude of the variations naturally decreases with length. To make a simple metric of the magnitude of the variations, we have calculated the standard deviation of the delays measured at the 50 measurement points nearest to the core center, corresponding to a sampling area slightly smaller than that in Fig.3. As we show in Fig.4, this RMS delay variation, σ, depends on fiber length in a way that is reasonably well described by a power law, $\sigma \propto L^{0.57}$. From this result alone, we may infer clear evidence of coupling between modes, since uncoupled modes would show delay variations proportional to the first power of length, which is clearly inconsistent with our observations. Indeed, the observed length dependence is quite close to the dependence $\sigma \propto L^{0.5}$ expected from a diffusive theory[7] of mode coupling. It is worth noting that the length dependence observed here is identical to that seen[3] in pulse broadening measurements of step-index PMMA POF under overfilled launch conditions. Presumably, we would observe linear intermodal dispersion at lengths below the characteristic length for mode coupling, but this characteristic length appears to be well below the shortest length (20 m) measured in these experiments.

In plastic fibers of the type discussed here, many possible sources of mode coupling exist. As the fiber cools from the melt state during the draw process, thermally excited fluctuations of density and composition, as well as polymer orientation, become frozen into the fiber, resulting in very short length scale

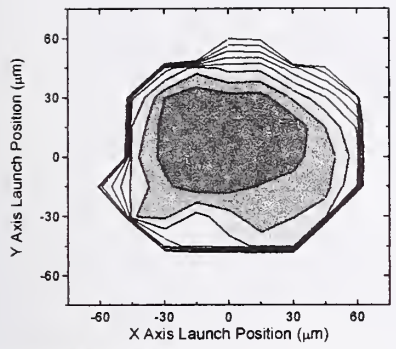

Figure 3 Variation of pulse delay with launch position. Darker contours represent longer delay, and the spacing between contour levels is 40 ps.

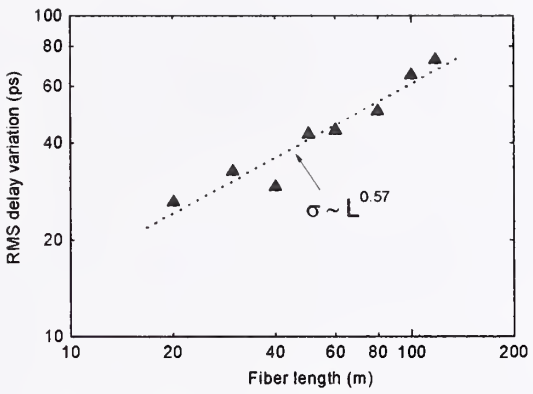

Figure 4 Dependence of delay variation on fiber length

inhomogeneities. Our measurements[8] of light scattering in bulk samples with composition similar to that of the core show that these intrinsic fluctuations produce a Rayleigh scattering intensity corresponding to a loss of ~10 dB/km. In addition to these fluctuations, one might expect extrinsic sources of scattering, such as voids, cracks, microbends, index profile variations, and diameter variations introduced during the draw process. Indeed, since the measured loss is roughly 60 dB/km, and we know that the absorption loss is negligible in these perfluorinated materials, we may be sure that extrinsic sources of scattering dominate the loss in this fiber. If mode coupling resulted primarily from the intrinsic scattering sources, then the characteristic length on which mode mixing occurred would be larger than that on which those fluctuations scattered light from the fiber, since Rayleigh scattering is isotropic and the low NA would allow only a small fraction of the scattered light to be recaptured in core modes. Thus, intrinsic fluctuations would produce mode mixing only after hundreds of meters, so we may conclude that extrinsic sources are primarily responsible for the mode mixing observed here. This result is expected, since extrinsic scattering sources may exist on larger length scales, resulting in strongly forward scattering, and more efficient mode mixing for a given rate of attenuation.

In conclusion, we have presented differential mode delay measurements of perfluorinated graded-index plastic optical fibers, and these measurements have shown for the first time that intermodal dispersion scales roughly as the square root of length in these fibers. This result strongly suggests that the characteristic length for mode coupling is less than 20 meters, so that mode coupling greatly improves the bandwidth of perfluorinated POF over lengths appropriate for LAN applications. Since precise control of the index profile is difficult in plastic fibers, this outcome also has positive implications for the prospect of large scale production of POF with high bandwidth. Finally, since extrinsic scattering sources appear to dominate the mode coupling, our measurements suggest the possibility of tailoring these extrinsic inhomogeneities to produce rapid mode coupling with minimal loss.

Acknowlegements

The authors acknowledge many useful discussions with L. L. Blyler, A. F. Garito, C. Koeppen, Y. Koike, X. Quan, and R. Shi.

References

[1] E. Nihei, T. Ishigure, N. Tanio, and Y. Koike, *IEICE Trans. Electron.*, v.E80-C, 117 (1997).
[2] T. Ishigure, A. Horibe, E. Nihei, and Y. Koike, *J. of Lightwave Tech.*, v.13, 1686 (1995).
[3] G. Jiang, R. F. Shi, and A. F. Garito, *IEEE Photonics Tech. Lett.*, v. 9, 1128 (1997).
[4] Dietrich Marcuse, "Principles of Optical Fiber Measurements", Academic Press, New York (1981).
[5] H. Murofushi, *Proc. Fifth Int. Conf. Plastic Optical Fibers and Applications*, p.17, (1996).
[6] Noriyuki Yoshihara, Proc. *Sixth Int Conf Plastic Optical Fibers and Applications*, p. 27, (1997).
[7] D. Gloge, *Bell Syst. Tech. J.*, v.51, 1767 (1972).
[8] W. R. White. and Pierre Wiltzius, to be published.

Measurement of Skew in GI MM optical ribbon fibers

Masateru Tadakuma Osamu Aso Shu Namiki

Optical transmission systems group wp-project team R&D division, Furukawa Electric Co., Ltd.
6, Yawatakaigan-dori, Ichihara, Chiba, 290-8555 Japan
phone:+81-436-42-1724 fax:+81-436-42-9340 e-mail:tadakuma@ch.furukawa.co.jp

Abstract

Since the skew tolerated in parallel interconnections is about one to several ps/m, it is necessary to measure the ribbon fibers skew with precision of the order of 0.1ps/m. We have realized two methods to measure skews of multimode (MM) ribbon fibers. One is pulse delay method, and the other is phase shift method. In the pulse delay method , an optical short pulse source which generates Gaussian pulses with 130ps pulse width was used and the difference of the delay time (skew) between a reference fiber and others in the ribbon fibers was measured. We could achieve the measurement standard deviation within 7ps for a 100m ribbon fiber (0.07ps/m). In the phase shift method, we measured skews using a network-analyzer and optimized the measurement conditions. It enabled us to measure skews with the standard deviation of 0.04ps/m.

1. Introduction

Recently, in the fields such as large capacity switching systems and massively parallel processors, highspeed synchronous parallel frame-to-frame and board-to-board data transmissions tend to limit the degree of freedom in designing the system structure. Optical interconnections using optical fiber arrays are expected to alleviate the system- to-system interconnection bottleneck. Components of optical parallel interconnections include transmitter and receiver modules which carry laser diode (LD) and photodiode (PD) arrays, respectively, and multichannel optical ribbon fibers which connect the transmitters to the receivers. Low cost fiber-optic links use multimode (MM) fibers with either a 50 or 62.5μm diameter graded index (GI) core, as this results in large optical alignment tolerances and more robust fiber splices and connector components. In this transmission system, the delay time difference (skew) of signals between optical fibers in ribbon fibers becomes an important factor. The ribbon fibers skew limits the longest transmittable length. Generally, the skew tolerated in parallel interconnections is about one to several ps/m. Therefore, it is necessary to measure the ribbon fibers skew with precision of the order of 0.1ps/m. In this report, we have developed the skew measurement methods of the multichannel multimode ribbon fibers.

2. Skew measurement method

Similar to chromatic dispersion measurement, skews can be measured by the the pulse delay method and phase shift method .

1) Pulse delay method

In the pulse delay method, the optical short pulse launched into the fiber under measurement and the delay time difference is determined from the propagation time of the pulse. An optical pulse from a laser diode (LD) modulated with a pulse generator is injected into the fiber. The light emitted from the fiber is observed by an optical sampling-oscilloscope. Skews are calculated by comparing between observed output pulse positions.

2) Phase shift method

In the phase shift method, sinusoidally modulated light is launched into the optical fiber, and the light emitted from the fiber is converted into an electrical signal by a photodetector. The phase angle difference of this output light to a reference signal is measured for each fiber and determines the ribbon fibers skew [1] [2].

3. Study of the pulse delay method

We have developed a measurement system based on the pulse delay method and reduced measurement deviations. The improved experimental setup is shown in Fig.1.An electrical signal generated by a pulse

generator is converted into an optical pulse via a LD and separated into two ports by a coupler. Pulses propagating along a reference fiber and another fiber under measurement are recoupled by the coupler at the output. Both ends of the test ribbon fibers are bared and cut square, and set on fiber-positioning holes of mechanically transferable (MT) ferrules. These MT ferrule-endfaces contact with MT ferrule endfaces of fanout devices which convert a twelve-fibers ribbon to twelve individual fibers. We measured the arrival time using the optical sampling oscilloscope. The delay time of the pulse propagating along the reference fiber is taken as the reference time, skew is decided as the difference between the reference time and the delay time of the fiber under measurement. For a multi-channel fiber ribbon, the reference fiber is fixed while the other fibers are set as the fiber under measurement in turn.

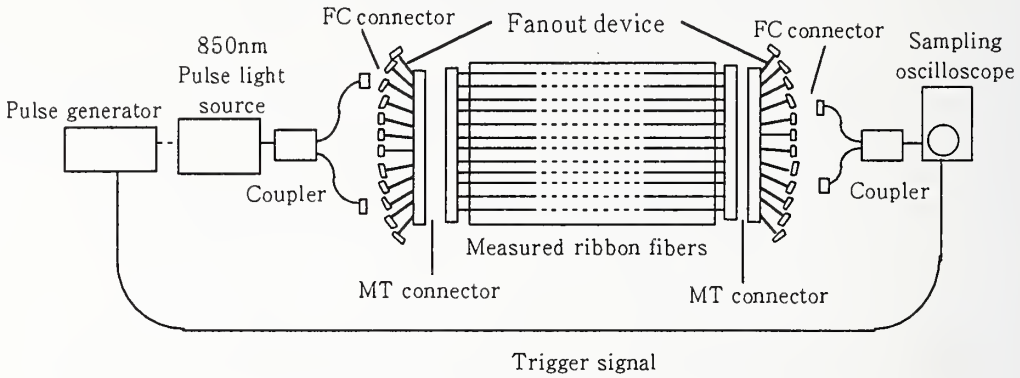

Fig.1 The improved measurement system

In the measurement system shown in Fig.1, pulses from two fibers happened to overlap each other at the optical sampling oscilloscope and it was difficult to distinguish one pulse from the other. Therefore we prepared different lengths in the output coupler's ports. In the pulse delay method, the optical pulse source condition is important. Factors necessary for the skew measurement can be listed as follows. 1.Stability of pulse profile 2.Narrow pulse width The reason of the first factor is because the delay time is decided by fitting observed pulse profile with the most appropriate function. By the second factor,it is expected to decrease observational error at pulses' position. To meet these factors, the vertical cavity surface emitting laser (VCSEL) was used and modulated with a 400ps width signal near lasing threshold. The short pulse forms a Gaussian profile with the wavelength of 850nm, the pulse width of 130ps and the repetition frequency of 100MHz. We fitted pulses with Gaussian function and decided the center position of the pulses on the time axis. The skew is determined thereby. Fig.2 shows the skew obtained from this method.

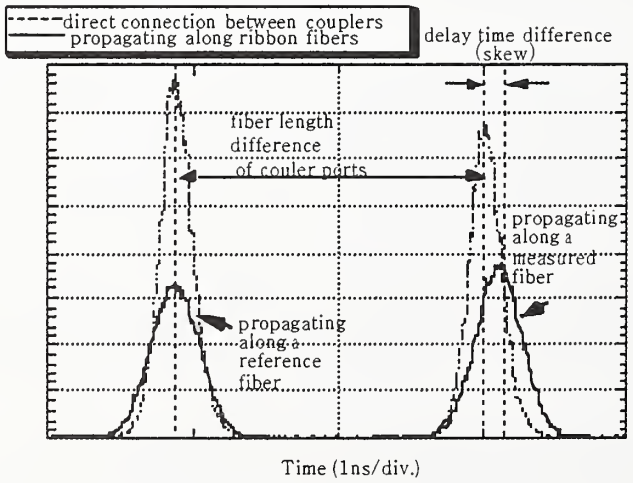

Fig.2 Skew measurement from observed pulse profile

4. Study of the phase shift method

In the phase shift method, to measure the signal phase emitted from the fiber, a network-analyzer is used.The phase value measured by the network-analyzer is the phase difference between the original signal generated from the analyzer and the signal through the fiber. For small measurement deviation ,we have selected a better light source out of two, as described below, and investigated the network-analyzer settings. The experimental setup is shown in Fig.3.

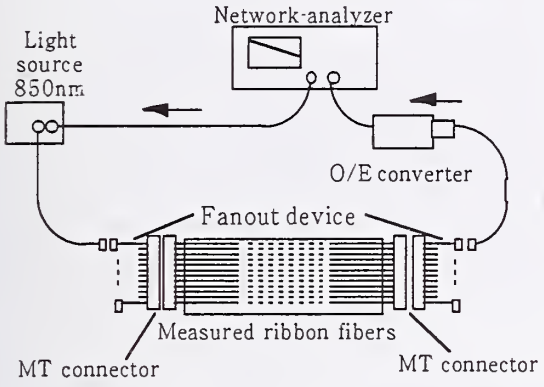

Fig.3 The phase shift measurement system

Table.1 Skew meansurement conditions

Frequency (Hz)	800M
Average times	10
Measurement time	12s/1fiber (2.5minutes/12ch-ribbon fibers)

In the setup shown in Fig.3, we removed the ribbon fibers and formed a short circuit by MT connectors of input and output sides. We then compared measurement deviations using a multimode LD with those and using a VCSEL. In the same condition, we calculated deviations of measured values for ten times. The measurement deviation with the VCSEL was about 1.6ps smaller than that with the multimode LD. Since many different wavelength axial-modes oscillate in a multimode LD, slightly different velocities of those axial-modes might increase measurement deviation. Furthermore, the measurement condition of the network-analyzer has been optimized. It is considered that factors which influence measurement accuracy of the network-analyzer are modulation frequency, sweep time (resolution bandwidth), and average times. Since delay time per phase angle is reduced by raising the modulation frequency, it becomes possible to measure with better resolution. But the frequency is limited by the modulation bands of the light source and the receiver. By extending the sweep time and increasing average times, it enables us to bring out a good performance of the analyzer, but measurement time becomes long. During long time measurement, the temperature changes of the test ribbon fibers occur and cause the deviation of measurement phase angles, true skew value is not well defined. In so doing, we have optimized and found the measurement conditions which bring the best performance out of this setup. The result is shown in Table.1.

5. Skew measurement deviations

12ch MT ferrules are used at both ends of the test ribbon fibers to connect with fanout devices in both the pulse delay method and the phase shift method. In Fig.3, to evaluate measurement deviations due to changes in alignment conditions of MT ferrules, we investigated skew value deviations for 10 reconnections while both ends of the test ribbon fibers were cut square and set on fiber-positioning holes of MT ferrules at each reconnection. To eliminate the effect of changes of fiber length by temperature deviation, the test ribbon fibers were placed into a thermal chamber to maintain constant temperature at 25℃. The phase shift method was used. The result is shown in Table.2.

Table.2 Skew value deviation of a sample fiber for 10 reconnections

	Fiber length=100m	
Fiber number in12ch-ribbon fibers	No.6	No.12
Standard deviation of measured value (ps)	1.224	1.799

It is considered that the measurement deviations due to reconnections are jointly caused by fluctuations of the light source and the network-analyzer, by the variation in bared and cut fibers lengths of both the test ribbon fibers ends, and by delay time difference between propagating modes along fibers. The maximum variation in

bared and cut fibers lengths of one end of the test ribbon fibers is about 50μm (the corresponding propagation time is about 0.25ps). At joints between ribbon fibers under measurement and fanout devices, fiber cores face each other. If the fanout fiber is joined to the fiber in the ribbon but with axial misalignment,the light will be coupled to different propagation modes, and different modes will propagate at slightly different velocities along the fiber, and measured skew values will vary.

6. Measurement results of 12-channel GI MM ribbon fibers skew

Skews of 12-channel ribbon fibers constituted of GI multimode fibers with core diameter 62.5μm were measured by both the pulse delay method and the phase shift method. For each fiber of the ribbon, we calculated the average of the delay time differences between the reference fiber and the fiber under measurement, for five times. The reference fiber is fiber No.1 in Fig.4. The measured ribbon fibers are 100m long. In the pulse delay method,the standard deviation of measured values for five times was 0.068ps/m, while in the phase shift method, the standard deviation was 0.042ps/m. The skew across the 12-channel ribbon fibers was 196.1ps/100m by the pulse delay method, 185.1ps/100m by the phase shift method.

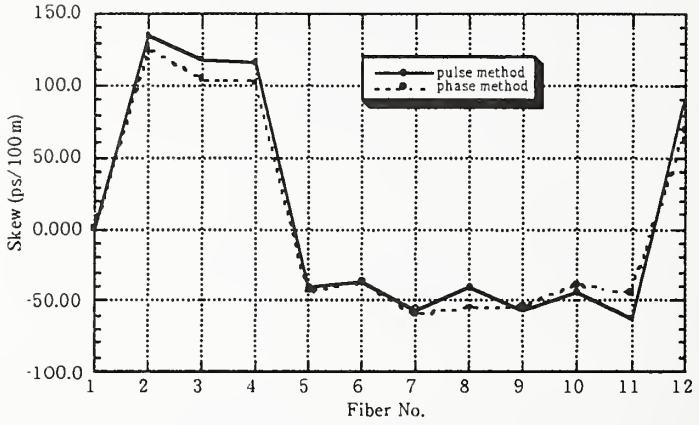

Fig.4 Skew of the 12-channel ribbon fibers

Table.3 Skew of measured 12ch ribbon fibers

Fiber core/outer diameter	Phase shift method (ps/m)		Pulse delay method (ps/m)	
	Skew	Standard deviation	Skew	Standard deviation
62.5/125μm	1.851	0.042	1.961	0.068

The difference of skew values between the two skew methods was 11ps. It is considered that the difference is caused by the launch and environmental conditions of the ribbon and fanout devices.

7. Conclusion

We have developed two methods to measure skews of GI multimode ribbon fibers. One method is the pulse delay method and the other is the phase shift method. In the pulse delay method, observed pulse profiles were fitted by a Gaussian function to decide accurate delay time. The standard deviation of the measurement was 6.8ps for 100m (0.068ps/m) .In the phase shift method, by the optimization of measurement conditions, it enabled us to measure with the standard deviation of 0.042ps/m. Both methods developed in this work have achieved sufficient measurement precision.

8. References

[1] R. Matsuoka et al., "Measuring method for Ribbon fiber Skew" Tech. Digest-Symposium on Optical Fibre Measurements 1992,ed. by G.W.Day and D.L.Franzen,pp.41-44 1992.

[2] A. J.Barlow et al, "Measurement of ultra-low skew in ribbon fibers" Tech. Digest-Optical Fibre Measurement Conference 1997

Gratings for WDM Systems – Review of Applications and Critical Measurements

Peter A. Krug, John Canning and Dmitrii Yu. Stepanov

Australian Photonics Cooperative Research Centre, OFTC
101 National Innovation Centre
Australian Technology Park
Eveleigh, NSW 1430
Australia

1. INTRODUCTION

Since their invention less than a decade ago, side-written optical fibre Bragg gratings (FBGs) [1] have progressed rapidly from laboratory curiosities to commercially important devices in optical communications and sensing. With the advent of wavelength division multiplexing (WDM) in optical communication networks, the role of FBGs has become crucial. The stringent demands on performance of FBGs in a variety of WDM applications has tested the ingenuity and skill of those who manufacture them, and have called for increasingly complex grating structures to be realised. Consequently, the development of techniques for the measurement of grating performance and structure has become a field of research and development in its own right.

In this paper, we review the important applications of fibre Bragg gratings, and their close relatives, the so-called "long period" cladding mode coupling gratings [2], and describe some of the techniques used to quantify their optical response and physical structure.

2. APPLICATIONS

2.1 Filtering

Because of the large wave vector mismatch between the incident and reflected waves, a simple Bragg grating is essentially a narrow band device. For highly reflecting gratings produced by periodic refractive index changes of order 10^{-3}, reflection bandwidths are of the order 1nm or less. Such spectral widths typically correspond to a single channel in a WDM communications system. To obtain a filter response covering more than a single channel, a number of modifications of the grating structure can be employed. These grating structures, several of which will be discussed below, include grating structures modified by sampling [3], chirping [4], concatenation, or overwriting of multiple gratings in a length of fibre. An alternative approach is to use a long period grating (LPG) which couples a core-guided mode to a co-propagating cladding mode [2]. Because the difference in wave vectors between the incident and resonantly coupled waves is much smaller than in a FBG, the resonant bandwidth is correspondingly larger. Typical resonant bandwidths of 5nm or more can easily be achieved [5]. Some examples of filtering applications in WDM systems are presented below.

Gain equalisation in nonlinear wavelength conversion. Morgan et al [6] have used a filter comprising 9 concatenated FBGs to equalise the wavelength converted signals generated by four wave mixing in a semiconductor optical amplifier. Without equalisation, the conversion efficiency of the converter varies by up to 13dB over the 10 wavelength channels, spaced 100GHz apart. With equalisation, the channel-to-channel variation in conversion efficiency was reduced to ±1.5dB.

Gain flattening in an erbium doped fibre amplifier. Wysocki et al [7] have shown that almost perfect flattening of the gain of an erbium doped fibre amplifier (EDFA) can be achieved by use of a filter comprising several LPGs whose strengths, centre wavelengths and spectral widths were optimised by computer modelling. The

resultant net gain was flat to within ±0.5dB over a wavelength range of 1528.1nm to 1568.1nm. A major advantage of LPGs over FBGs in this application is that while FBGs reflect the resonantly coupled light, LPGs couple the rejected light into the cladding of the fibre, where it can be easily dumped, for example by use of an absorbing coating on the fibre.

Tuneable equalisation of EDFA gain. Kim et al [8] have used acoustic standing waves in a length of fibre to produce tuneable LPGs. The periodic microbending losses induced in the fibre by the acoustic wave, rather than ultraviolet light induced index changes, are responsible for the coupling to cladding modes. By simultaneously exciting the fibre with several radio frequency sinusoidal acoustic signals, the researchers were able to demonstrate complex, tuneable filtering profiles. Such rapidly tuneable filters are likely to find immediate application in *actively* controlling the gain profile of EDFAs.

2.2 Multiplexing and Demultiplexing

Simple demultiplexing. Mizrahi et al [9] demonstrated 4 channel demultiplexing using pairs of non-spectrally overlapping gratings, arranged such that each grating pair transmitted one WDM channel (in the gap between the two reflection bands) and reflected all other WDM channels. A 1 x 4 fused fibre splitter with one such grating pair filter on each output arm was able to separate the channels, with a selectivity of better than 35dB.

Add-drop multiplexing. Giles and Mizrahi [10] demonstrated that a FBG placed between two 3-port optical circulators can be used to drop an optical signal whose wavelength is reflected by the grating, and insert a new signal at the same wavelength. Because the insertion loss of optical circulators is less than 1dB port-to-port, the total insertion loss for any of the three signal paths (through, add and drop) is less than 2dB.

Using an array of four concatenated FBGs, each controlled by a piezoelectric actuator, Quetel et al [11] demonstrated a programmable add/drop multiplexer. The selection of channels to be dropped was made by dc voltages applied to the piezoelectric actuators. Switching times of 30μs were achieved.

2.3 Dispersion Compensation

Since the first experimental demonstration of dispersion compensation using a chirped fibre Bragg grating in 1994 [12], the chirped FBG has shown itself to be a serious competitor with dispersion compensating fibre (DCF) for WDM transmission at 1.5μm in standard fibre. Its advantages over DCF include its negligible polarisation mode dispersion (PMD), low insertion loss, compactness and, potentially, lower cost. However, significant ingenuity has been necessary to fabricate chirped fibre Bragg gratings with bandwidths sufficiently large to cover four or more WDM channels. Ouellette et al [13] showed that a chirped FBG that is also periodically sampled can achieve dispersion compensation simultaneously at multiple signal wavelengths. Such gratings can be fabricated by sampling a chirped grating (for example by introducing spatially periodic phase steps [13], or equivalently, by overwriting chirped gratings centred at the signal wavelengths, in a single length of fibre. Chirped gratings able to compensate for 50km worth of group velocity dispersion in 8 channels have recently been reported [14]. Alternatively, continuously chirped gratings up to one metre and longer, with bandwidths covering a substantial fraction of the EDFA gain spectrum have been reported [15].

An alternative way to use fibre Bragg gratings for group velocity dispersion compensation is to use the dispersion of a grating in transmission, just outside its reflection band. Eggleton et al [16] have demonstrated use in transmission of a semi-apodised, unchirped FBG to compensate for dispersion of 72km of standard fibre at 1544nm.

Several techniques have been reported for writing chirped gratings for dispersion compensation, including translation of the fibre or the phase mask or rotation of interferometer mirrors during ultraviolet exposure; deformation of the fibre following grating inscription [4]; concatenation of short, uniform gratings centred at increasing or decreasing wavelength. All such gratings suffer from small imperfections which produce noise-like ripples in the group delay spectrum. Minimisation of these ripples has been a major focus of groups working on chirped gratings. The measurement of group delay, therefore, has been of particular importance. This is discussed in section 3.2.

2.4 Optical Sources

FBGs have been used in many ways as resonator elements for fibre and semiconductor lasers, and to stabilise the wavelengths of various lasers. An extensive review of applications of fibre gratings in fibre lasers and amplifiers was recently published by Archambault and Grubb [17]. A few examples are presented below.

Wavelength stabilisation of semiconductor lasers. Morton et al [18] used a chirped FBG in a lensed fibre pigtail as a wavelength selective resonator element in a modelocked hybrid semiconductor laser. The laser was only stable when the chirp direction was such that the grating period increased with increasing distance from the laser chip.

Multi-wavelength fibre lasers. Chow et al [19] used both a chirped FBG pair [20] and a sampled FBG to produce simultaneous lasing on several lines in an erbium doped fibre ring laser. They obtained simultaneous emission on eight lines when the erbium doped fibre was cooled to 77K, to suppress the Doppler broadening of the emitting transition.

Step-tuneable fibre laser. Ibsen et al [21] used a pair of sampled FBGs as resonator elements in a linear cavity erbium doped fibre laser. The sampling periods of the two FBGs were different, and selected such that only one resonant peak of each grating was coincident with a resonant peak of the other grating at any time. Small strain applied to one of the gratings changed the wavelength of the coincident resonance so as to cause the output of the laser to jump successively to different peaks in the grating response spectra. The laser tuned in approximately 2nm steps over a wavelength range 1532 to 1549nm with a strain of only 0.14% applied to one of the gratings.

Multi-order fibre Raman laser. Grubb et al [22] used nested pairs of FBGs, each pair resonant with one order of Raman emission from an optically pumped germanosilicate fibre. 1.7W of output at 1480nm, being the fifth order of Raman emission of the 1175nm wavelength pump, was emitted with a slope conversion efficiency of 46%. A similar device, configured as an amplifier at 1310nm, has produced a gain of 40dB and an output power of +24dBm [23].

3. GRATING MEASUREMENTS

The optical response of a grating can, in principle, be obtained from perfect knowledge of its structure. Conversely, full information about a grating's structure can be calculated by appropriate inverse scattering calculations based on its reflection, transmission, loss and phase spectra [24]. Below, we present recent techniques for characterisation of grating structures and optical responses of gratings.

3.1 Reflection and Transmission Spectra

Power reflection and transmission spectra are most rapidly measured using a broadband source, such as a superluminescent light emitting diode or a superfluorescent doped fibre, together with an optical spectrum analyser (OSA). The minimum resolvable spectral feature is $\geq$ 0.07nm for most commercial OSAs, although instruments incorporating Fabry-Perot étalons, capable of resolving 0.001nm are now becoming available. However, measurements at such high resolutions are very slow, because of broadband source intensity limitations. For faster measurements at picometre resolutions, the universally accepted spectrometer comprises a step-tuneable external cavity semiconductor laser and an optical power meter. The trade-off between the two schemes involves speed and resolution. While broadband sources and OSAs can capture a spectrum in one or a few seconds, the tuneable laser and power meter can take minutes to tens of minutes or more, depending on the required resolution and spectral range. An additional limitation, especially with the scanning source method, is the relative lack of absolute wavelength calibration. Use of an optical wavemeter can greatly improve wavelength calibration (and prevent inaccuracies due to source mode hopping), at the expense of significant cost and increased measurement duration.

Some spectral features, such as the narrow transmission band in a $\pi/4$ phase shifted grating [25] can be 1pm wide or less. Stepanov et al [26] have demonstrated an ultrahigh resolution variant of the tuneable wavelength scanning method to measure grating spectra. They report using RF modulation of an optical source to produce a

tuneable sideband, which is used as the probe. The researchers achieved a measurement resolution of 100kHz (approximately 10^{-6}nm), which is limited by the laser linewidth. The time required for a measurement is of the order of one millisecond.

Measurement of grating sidebands and other weak features is limited by the dynamic range of the measurement technique. The finite selectivity of an OSA and the presence of broadband amplified spontaneous emission in narrowband tuneable sources limit detectability of such weak features to about –30dB. Use of a narrowband tuneable filter can allow measurement to about –60dB.

3.2 Group Velocity Dispersion

The most commonly employed technique to measure the group velocity dispersion is based on a technique of Ryu et al [27]. The output of a narrowband, tuneable optical source is externally RF modulated to produce sidebands. The modulated signal in reflected from (or transmitted through) the FBG, and the phase difference between sidebands is measured by a vector voltmeter or network analyser. The phase difference is a measure of the average dispersion of the grating over a range given by the modulation frequency. Tuning the wavelength of the source enables the dispersion to be measured as a function of wavelength. Dispersion measurement resolution better than 5ps/nm, which is essential for resolving the group delay ripples which plague chirped FBG dispersion compensators, is easily achieved by this method.

Ouellette and Stepanov [28] reported a novel measurement technique based on measuring the reflected light in two orthogonal polarisation modes. Use of a broadband source and optical spectrum analyser enables the measurement of the group velocity delay spectrum in a very short time, using only a very simple optical setup.

3.3 Spatial Profile

Although measurement of the transmission, reflection, loss and delay spectra can, in principle, enable one to calculate the spatial structure of a grating, any noise or inaccuracy in the measured spectra will lead to ambiguities in solutions of the inverse scattering calculation. The problem is compounded in the case of complex grating designs. Therefore, it is necessary to obtain direct measurements of grating structure. A number of techniques have been reported.

Index modulation depth. Krug et al [29] focussed a visible HeNe laser beam, angled at the first order Bragg diffraction angle, onto the core of a fibre containing a grating. The fibre grating diffracted a fraction of the incident beam, with a diffraction efficiency proportional to the square of the index modulation depth Δn. By scanning the probing beam along the grating in the axial (z) direction, and recording the intensity of the diffracted light beam as a function of z, they obtained a direct measure of the index profile, $\Delta n(z)$. Ouellette et al [30] used this method to characterise both a fibre grating, and the phase mask which had been used to fabricate it.

Side scatter measurement of grating resonant structure. Canning et al [31] have developed a powerful FBG characterisation method based on spatially resolved measurement of light incoherently scattered within the grating, and emitted from the side of the fibre. The origin of the side-emitted light is Rayleigh scattering, from defects generated in the core during the ultraviolet inscription of the grating. Because the intensity of the scattered light at axial position z is proportional to the light intensity inside the core at z, a spatially resolved measurement of the scattered light clearly shows the structure of the resonant light field in the grating. The beauty of the method is that it can be performed over a range of wavelengths. A three dimensional plot of scattered intensity as a function of spatial position and wavelength shows such grating features as chirp [32], phase discontinuity and apodisation [33].

3.4 Polarisation Properties

The photoinduced index change used to produce a fibre grating is generally anisotropic. This has a significant impact on the properties of the grating, and can affect the performance of devices which employ the gratings. Examples include polarimetric fibre sensors and FBG dispersion compensators [4, 12-16], where the phase of the reflected light is of critical importance. Measurements of UV induced birefringence using transmission

ellipsometry have been reported [34, 35]. These papers identified polarisation of the UV light and geometrical asymmetry of the writing process as the origins of the anisotropy. Stepanov et al [36] have developed a simple and inexpensive reflection ellipsometry technique to characterise the polarisation properties of FBGs. Reflection ellipsometry is a technique based on measurements of the states of polarisation of the incident and reflected waves. The essential optical components for the measurement are a polarising beamsplitter and a quarter wave plate. As mentioned in section 3.2, Ouellette and Stepanov [28] used essentially the same measurement setup to show that the retardance spectrum of a chirped FBG can be translated into a group velocity delay spectrum.

4. CONCLUSIONS

Fibre gratings have found many applications in WDM telecommunication systems. It is likely that commercial WDM systems will employ fibre gratings, in filtering, in dispersion compensation, in sources and amplifiers and for multiplexing and demultiplexing. Accurate, fast and convenient measurements of the optical response and structure of fibre gratings have been seen to be crucial in designing gratings to suit particular applications, and in evaluating the performance of the fabricated gratings. Several such techniques have been presented.

REFERENCES

[1] G. Meltz, W.W. Morey and W.H. Glenn, *Formation of Bragg Gratings in Optical Fibers by Transverse Holographic Method*, Optics Lett., **14**, 823-5 (1989)

[2] A.M. Vengsarkar, P.J. Lemaire, J.B. Judkins, V. Bhatia, T. Erdogan and J.E. Sipe, *Long-Period Fiber Gratings as Band-Rejection Filters*, J. Lightwave Tech., **14**, 58-65 (1996)

[3] B.J. Eggleton, P.A. Krug, L. Poladian and F. Ouellette, *Long Periodic Superstructure Gratings in Optical Fibres*, Electron. Lett., **30**, 1620-2 (1994)

[4] P.A. Krug, T. Stephens, G. Yoffe, F. Ouellette, P. Hill and G. Dhosi, *Dispersion Compensation Over 270km at 10Gbit/s Using an Offset-Core Chirped Fibre Bragg Grating*, Electron. Lett., **31**, 1091-2 (1995)

[5] D. B. Stegall and T. Erdogan, *Long-Period Fiber Grating Devices Based on Leaky Cladding Mode Coupling*, Bragg Gratings, Photosensitivity, and Poling in Glass Fibers and Waveguides: Applications and Fundamentals, OFC 1997 Technical Digest Series, vol. 17, paper BSuB2, pp. 16-8 (1997)

[6] T.J. Morgan, R.S. Tucker and G. Yoffe, *Passive optical Equalization of Wavelength Converters Based on Four-Wave Mixing in Semiconductor Optical Amplifiers*, Photonics Tech. Lett, **10**, 522-4 (1998)

[7] P.F. Wysocki, J. Judkins, R. Espindola, M. Andrejco, A. Vengsarkar and K. Walker, *Erbium-Doped Fiber Amplifier Flattened Beyond 40nm Using Long-Period Grating*, OFC'97 Proceedings, postdeadline paper PD2 (1997)

[8] H.S. Kim, S.H. Yun, I.K. Kwang and B.Y. Kim, *All-Fiber Acousto-Optic Tuneable Notch Filter with Electronically Controllable Spectral Profile*, Optics Lett, **22**, 1476-8 (1997)

[9] V. Mizrahi, T. Erdogan, D.J. DiGiovanni, P.J. Lemaire, W.M. MacDonald, S.G. Kosinski, S. Cabot and J.E. Sipe, *Four Channel Fiber Grating Demultiplexer*, Electron. Lett., **30**, 780-1 (1994)

[10] C.R. Giles and V. Mizrahi, *Low-Loss Add/Drop Multiplexers for WDM Lightwave Networks*, Proc. 1OOC'95, paper ThC2 (1995)

[11] L. Quetel, L. Rivoallan, E. Delvaque, H. Poignant, M. Monerie and T. Georges, *Programmable Fiber Grating Based Wavelength Demultiplexer*, OFC'96 Proceedings, paper WF6 (1996)

[12] B.J. Eggleton, P.A. Krug, L. Poladian, K.A. Ahmed and H.-F. Liu, *Experimental Demonstration of Compression of Dispersed Optical Pulses by Reflection from Self-Chirped Optical Fibre Bragg Gratings*, Optics Lett., **19**, 877-9, (1994)

[13] F. Ouellette, P.A. Krug, T. Stephens, G. Dhosi and B. Eggleton, *Broadband and WDM Dispersion Compensation Using Chirped Sampled Fibre Bragg Gratings*, Electron. Lett., **31** (11), 899-901 (1995)

[14] T. Stephens, J. Arkwright, K. Hinton, D.Y. Stepanov, P.A. Krug, B. Smith, G. Dhosi, G. Yoffe and F. Ouellette, *Fiber Gratings for Dispersion Compensation*, Invited paper at OFC'98, paper TuM1, p. 71 (1998)

[15] R. Kashyap, A. Ellis, D. Malyon, H.-G. Froehlich, A. Swanton and D.J. Armes, *Eight Wavelength x 10Gb/s Simultaneous Dispersion Compensation Over 100km Single-Mode Fiber Using a Single 10 Nanometer*

Bandwidth, 1.3 Meter Long, super-Step-Chirped Fiber Bragg Grating With a Continuous Delay of 13.5 Nanoseconds, Proceedings of ECOC'96, paper ThB.3.2 (1996)

[16] B. Eggleton, T. Stephens, P.A. Krug, G. Dhosi Z. Brodzeli and F. Ouellette, *Dispersion Compensation Using a Fibre Grating in Transmission*, Electron. Lett., **32**, 1610-1 (1996)

[17] J.-L. Archambault and S.G. Grubb, *Fiber Gratings in Lasers and Amplifiers*, J. Lightwave Tech., **15**, 1378-90 (1997)

[18] P.A. Morton, V. Mizrahi, P.A. Andrekson, T. Tanbun-Ek, R.A. Logan, P. Lemaire, D.L. Coblentz, A.M. Sergent, K.W. Wecht and P.F. Sciortino Jr., *Mode-locked Hybrid Soliton Pulse Source with Extremely Wide Operating Frequency Range*, Photonics Tech. Lett., **5**, 28-31 (1993)

[19] J. Chow, G. Town, B. Eggleton, M. Ibsen, K. Sugden and I. Bennion, *Multiwavelength Generation in an Erbium-Doped Fiber Laser Using In-Fiber Comb Filters*, Photonics Tech. Lett., **8**, 60-2 (1996)

[20] G.E. Town, K. Sugden, J. Williams, I. Bennion and S.B. Poole, *Wide Band Fabry-Perot-Like Filters in Optical Fibers*, Photonics Tech. Lett., **7**, 78-80 (1995)

[21] M. Ibsen, B.J. Eggleton, M.G. Sceats and F. Ouellette, *Broadly Tuneable DBR Fibre Laser Using Sampled Fibre Bragg Gratings*, Electron. Lett., **31**, 37-8 (1995)

[22] S.G. Grubb et al, *High-power 1.48μm Cascaded Raman Laser in Germanosilicate Fibers*, Proceedings of Optical Fiber Amplifiers and Their Applications'95, paper SaA4 (1995)

[23] S.G. Grubb, T. Erdogan, V. Mizrahi, T. Strasser, W.Y. Cheung, W.A. Reed, P.J. Lemaire, A.E. Miller, S.G. Kosinski, G. Nykolak and P.C. Becker, *1.3μm Cascaded Raman Amplifier in germanosilicate Fibers,* Proceedings of Optical Fiber Amplifiers and Their Applications'94, paper PD3 (1994)

[24] L. Poladian, *Group Velocity Reconstruction for Fibre Bragg Gratings in Reflection and Transmission*, Optics Lett., **22**, 1571-3 (1997)

[25] J. Canning and M.G. Sceats, *π-Phase-Shifted Periodic Distributed Structures in Optical Fibres by UV Post-Processing*, Electron. Lett., **30**, 1344-5 (1994)

[26] D. Yu. Stepanov, J. Canning and Z. Brodzeli, *Real-Time Characterisation of Fibre Grating Fabry-Perots and Phase-Shifted Gratings with 100kHz Resolution*, submitted to Symposium on Optical Fiber Measurements (1998)

[27] S. Ryu, Y. Horiuchi and K. Mochizuki, *Novel Chromatic Dispersion Measurement Method Over Continuous Gigahertz Tuning Range*, J. Lightwave Technol., **7**, 1177-80 (89)

[28] F. Ouellette and D. Yu. Stepanov, *A New Technique for Measuring the Group Delay of Chirped Fiber Bragg Gratings*, OFC'97 Tech. Digest, paper WJ1, pp. 153-154 (1997)

[29] P.A. Krug, R. Stolte and R. Ulrich, *Measurement of Index Modulation Along an Optical Fiber Bragg Grating*, Optics Lett., **20**, 1767-9 (1995)

[30] F. Ouellette, P.A. Krug and R. Pasman, *Characterisation of Long Phase Masks for Writing Fibre Bragg Gratings*, Optical Fibre Tech., **2**, 281-284 (1996)

[31] J. Canning, M. Janos and M.G. Sceats, *Rayleigh Longitudinal Profiling of Optical Resonances Within Waveguide Grating Structures Using Sidescattered Light*, Optics Lett., **21**, 609-11 (1996)

[32] J. Canning, M. Janos, D. Yu. Stepanov and M.G. Sceats, *Direct Measurement of Grating Chirp Using Resonant Side Scatter Spectra*, Electron. Lett., **32**, 1608-10 (1996)

[33] J. Canning, D.C. Psaila, M.G. Sceats and M. Janos, *Fibre Grating Characterisation Using Side-Scatter Techniques*, Proc. Symposium on Optical Fiber Measurements'97, pp. 6-9 (1997)

[34] T. Erdogan and V. Mizrahi, *Characterization of UV-Induced Birefringence in Photosensitive Ge-Doped Silica Optical Fibers*, J. Optics Soc. Am. B, **11**, 2100-5 (1994)

[35] A.M. Vengsarkar, Q. Zhong, D. Inniss, W.A. Reed, P.J. Lemaire and S.G. Kosinski, *Birefringence Reduction in Side-Written Photoinduced Fiber Devices by a Dual-Exposure Method*, Optics Lett., **19**, 1260-2 (1994)

[36] D. Y. Stepanov, I.M. Bassett, T. Ryan and F. Ouellette, *Ellipsometry of Fibre Bragg Gratings*, Proc. Australian Conf. on Optical Fibre Technology, pp. 164-7 (1995)

Real-time characterisation of fibre grating Fabry-Perots and phase-shifted gratings with 100 kHz resolution

D. Yu. Stepanov, J. Canning, and Z. Brodzeli

Australian Photonics Cooperative Research Centre
Optical Fibre Technology Centre, The University of Sydney

Abstract

We demonstrate a real-time measurement technique capable of sub-MHz resolution for characterization of fibre Bragg gratings in transmission.

1. Introduction

Phase-shifted fibre Bragg gratings (FBG) [1] and distributed Bragg reflector (DBR) Fabry-Perot (FP) interferometers [2] have applications in dense wavelength-division multiplexing (WDM) systems, distributed-feedback (DFB) fibre lasers, and photonic signal processing. A π-phaseshift introduced in the physical centre of a uniform fibre Bragg grating results in a transmission notch in the middle of the grating bandgap. Depending on the grating strength or the interferometer finesse, the bandwidth of the notches may be very narrow, often well below the 1 pm (~125 MHz at 1550 nm) resolution of semiconductor tunable laser sources commonly used for spectral characterization of fibre Bragg gratings. Slow environmental perturbations may affect the results of the conventional measurements when the laser source is scanned across the wavelength range of interest. When setting each wavelength, the laser experiences relaxation oscillations and it takes hundreds of milliseconds to stabilize the lasing frequency. Further, longer delays are necessary if absolute wavelength measurements, obtained by continuous referencing to a slow scanning Michelson interferometric wavemetre, are desired.

In this paper, we demonstrate a simple technique for real-time measurements of spectral features of fibre Bragg gratings on a sub-MHz scale.

2. Measurement technique

The schematic of the experimental setup is shown in Figure 1 and consists of a tunable laser source (TLS), a network analyzer (NA), an amplitude electro-optic modulator (EOM), a photodetector (PD), an oscilloscope and a grating device under test. The NA serves as a source of radio-frequency (RF) signal, with the frequency swept across the band of interest. The RF signal drives the EOM and the frequency separation between the optical carrier and the modulation sidebands is swept over time. By blocking the carrier and one of the sidebands, the remaining sideband acts as a high-resolution light source which is swept across the RF band.

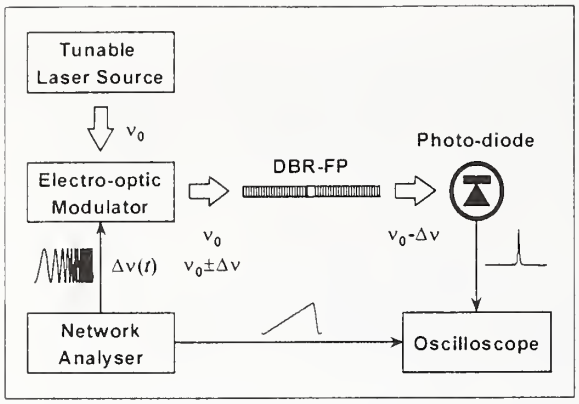

Figure 1. Schematic of the high-resolution measurement setup.

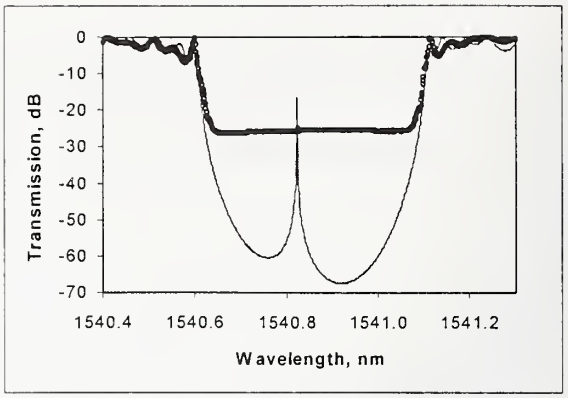

Figure 2. Grating transmission spectrum measured (open circles) using conventional technique and simulated (solid line) using the parameters shown in the text.

3. Experimental results and discussion

In this work, we characterized high-finesse DBR-FP interferometers and phase-shifted FBGs. An optical spectrum of a DBR-FP measured in transmission using a conventional setup which consists of a TLS with 0.001 nm resolution and a PD is shown in Figure 2 with open circles. The transmission notch in the bandgap is hardly resolvable using this setup. We also calculated the grating transmission using the following parameters: κ =8.9 cm^{-1}, L =11.17 mm, λ_B =1540.867 nm, Q =-0.065 nm/cm^2, where κ is the grating strength, L is the total length of the DBR-FP consisting of two gratings 5.85 mm and 3.95 mm long and a 1.2 mm gap between them, λ_B is the Bragg wavelength of the grating, Q is the quadratic chirp. Some deviation of the measured spectrum from the calculated one can be explained both by the deviation of the real DBR-FP from our model and by systematic experimental errors introduced into the measurement setup by the TLS. The laser was found to produce mode hops within 80 pm range when step-tuned either because of the TLS software faults or because of the feedback from the fibre grating. The -25 dB noise floor is determined by the spontaneous emission outside the lasing wavelength. The spontaneous emission noise also contributes to the measurement results at the edges of the grating bandgap causing the 'rounding' effect.

In the high-resolution measurements, the TLS wavelength was tuned close to the transmission notch. The grating reflectors used in the interferometer were sufficiently broad so that on one side of the carrier frequency one sideband is reflected whilst on the other side the other sideband is swept across the transmission notch as the modulation frequency is scanned.

The transmitted signal is plotted against the sweep time (versus modulation frequency as the modulation frequency was swept) on the oscilloscope screen. The whole RF span required to cover the transmission notch could be processed within tens of milliseconds. The frequency resolution was limited by the accuracy of the RF applied to the modulator, the TLS linewidth (~100 kHz) and the response time of the photodiode. In this experiment, the TLS linewidth is the major limiting factor. The high-resolution spectrum of the DBR-FP is shown in Figure 3. The horizontal scale defines the frequency downshift, $\Delta\nu$, of the red sideband from the carrier frequency which was set to $\nu_0 \approx$194.446 THz (1541.777 nm). Hence, the absolute frequency of a spectral feature can be determined as $\nu = \nu_0 - \Delta\nu$. This could be important for characterization of an environmentally

stable packaged device in an application where an accurate measurement of the absolute frequency is required, such as referencing of the optical frequency scale for WDM communications [3]. The device was not packaged. Moreover, there was a different tension applied to the device for the conventional and high-resolution measurements explaining the mismatch of the wavelength scale in Figure 2 with ν_0.

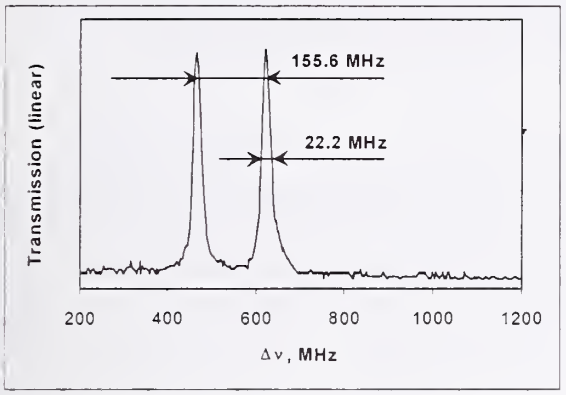

Figure 3. Polarization splitting of the transmission passband observed using setup shown in Figure 1.

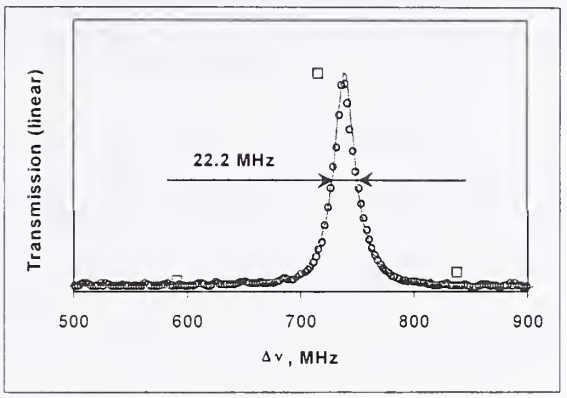

Figure 4. Transmission passband measured (open circles) for a single polarization using a linear polarizer and calculated with 1.25 MHz (solid line) and 125 MHz (open squares) step using calculation parameters shown in the text.

Polarization splitting of 155.6 MHz is apparent from the high-resolution spectrum shown in Figure 3. The laser source used in the experiment had a single linear polarization output which evolved by the time it reached the structure, allowing both polarization states of the device to be observed. Birefringence of the fibre sample calculated from the polarization splitting is about 10^{-6} which is the same order of value as measured in [4] for the fibre without a grating and fabricated using the same recipe.

The optical spectrum shown in Figure 4 with open circles was obtained by filtering the output using a linear polarizer aligned parallel to one of the DBR-FP birefringent axes. The bandwidth of the transmission notch was found from the high-resolution spectra to be 22.2 MHz implying very high finesse of the DBR-FP. A frequency mismatch of about 100 MHz between the subsequent measurements of the transmission passband represented in Figures 3 and 4 probably arose from environmental perturbations during the insertion of the polarizer into the setup since the grating was not properly packaged.

The optical spectrum calculated using the same parameters that we used to fit the transmission spectrum in Figure 2 is represented in Figure 4 with a solid line. It shows excellent agreement with the experimentally measured spectrum. For comparison, the transmission passband calculated with the minimum resolvable step of the TLS of 0.001 nm is shown in Figure 4 with open squares. Clearly, the conventional technique fails to resolve the passband as it is represented by only one data point in the plot.

In the experiment, a modulation sideband of the modulated optical carrier was used and its transmission through grating devices was measured while sweeping the modulation frequency. Another approach, similar to that described in [5], involves measuring the beat frequency between the carrier and the modulation sideband. A single sideband (SSB) modulation technique should be

employed in this case.

The technique in its current implementation does not allow the measurement of absolute values of transmission through the notch. This requires a calibration to the signal passed outside the bandgap. Since outside the bandgap the sideband used in the measurements could not be separated from the carrier and the other sideband, such a calibration has not been performed. The aim of the measurements was to spectrally resolve the passband and measure its bandwidth.

4. Conclusion

In conclusion, we have demonstrated a simple and accurate real-time high-resolution technique for measuring spectral features in fibre Bragg grating transmission spectra. The resolution was limited to the 100 kHz linewidth of the semiconductor laser source used in the measurement setup. The technique can be used both for precise characterization of fine structure observed in low resolution optical spectra of fibre grating devices, and in sensor applications where environmental variables are measured versus a change in grating spectral features.

5. Acknowledgements

The authors would like to acknowledge G. Yoffe and B. Smith from the Australian Photonics CRC for fabrication of the grating structures.

6. References

[1] J. Canning and M. G. Sceats, "π-phase-shifted periodic distributed structures in germanosilicate fibre by uv post-processing", *Electron. Lett.*, **30**(16), 1344–1345, (1994).

[2] W. W. Morey, T. J. Bailey, W. H. Glenn, and G. Meltz, "Fiber Fabry-Perót interferometer using side exposed fiber Bragg gratings", in *Tech. Digest of Conf. on Opt. Fiber Commun. (OFC'92)*, 1992, paper WA2.

[3] C. Gamache, M. Têtu, C. Latrasse, N. Cyr, M. A. Duguay, B Villeneuve, "An optical frequency scale in exact multiple of 100 GHz for standardization of multifrequency communications", *IEEE Photon. Technol. Lett.*, **8**(2), 290–292 (1996).

[4] F. Ouellette and D. Yu. Stepanov, "A new technique for measuring the group delay of chirped fibre Bragg gratings", in *Tech. Digest of Conf. on Opt. Fiber Commun. (OFC'97)*, Dallas, Texas, February 16–21, 1997, paper WJ1.

[5] J. E. Romn, M. Y. Frankel, and R. D. Esman, "High resolution technique for characterizing chirped fiber gratings", in *Tech. Digest of Conf. on Opt. Fiber Commun. (OFC'98)*, San Jose, California, February 22–27, 1998, paper TuA5.

OTDR-like dispersion-map measurements

Jürgen Gripp and Linn F. Mollenauer

Bell Labs, Lucent Technologies, Holmdel, New Jersey 07733

We have developed an instrument for fast, convenient and accurate measurement of the dispersion map $D(z)$ of optical fibers. Access to only one end of the fiber is required, making this technique perfectly suited for diagnosis of installed as well as spooled fibers. While low-loss fibers up to 45 km can be measured directly, we have also demonstrated a extended range of 75 km in low-loss fiber, and 22.5 km in high-loss, dispersion-compensating fiber by using Raman gain.

Since dispersion management has become the key in the design of ultra high capacity fiber optic transmission systems, there is a great need for fast, precise and convenient measurement of dispersion maps $D(z)$. Various techniques, based on modulational instability[1], or the phase-matching of four-wave-mixing products[2,3] have been proposed and tested. However, all these approaches suffer from certain common drawbacks, viz., they measure the wavelength of zero dispersion λ_0 instead of $D(z)$, they require time consuming data collection over a wide wavelength range, and the resulting amplitude profile does not necessarily allow an unambiguous reconstruction of spatial information. Our instrument, on the other hand, overcomes all of these disadvantages by using an optical-time-domain-reflectometry (OTDR-like) technique previously invented by one of us[4] and subsequently adopted by several other groups[5,6]. A measurement typically takes no more than a few seconds, and the data is unambiguously and almost instantaneously analyzed. We have successfully measured samples of every important fiber type, including various dispersion-shifted fibers with $0 < |D| < 11$ ps/nm/km, standard fiber with $D \approx 17$ ps/nm/km, and dispersion-compensating fiber with $D \approx -100$ ps/nm/km.

At the basis of our method are the four-wave mixing processes

$$\omega_S = 2\omega_1 - \omega_2 \,, \tag{1a}$$

$$\omega_A = 2\omega_2 - \omega_1 \,, \tag{1b}$$

(see Fig.1). Two photons at ω_1 (or ω_2) combine to create one photon at ω_2 (or ω_1) and one Stokes (or anti-Stokes)-photon. The four frequencies are equally spaced by $\delta\omega$ to satisfy energy conservation. For non-zero dispersion these two processes are subject to wave-vector mismatches that are directly proportional to $D(\omega_1)$ and $D(\omega_2)$. For example process (1a) leads to

$$\delta k(\omega_1) = k_2 + k_S - 2k_1 = -2\pi c D(\omega_1) \left(\frac{\delta\omega}{\omega}\right)^2 = -2\pi c D(\lambda_1) \left(\frac{\delta\lambda}{\lambda}\right)^2 \,. \tag{2}$$

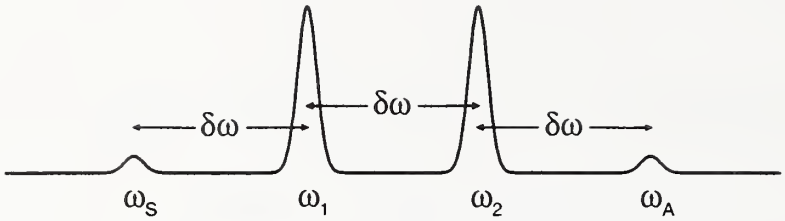

Fig. 1. Four-wave mixing spectrum.

(For process (1b), replace the subscript 1 with 2 and the subscript A with S.) It is important to notice that this result is independent of third order dispersion[4]. Our instrument initiates measurement of this wave-vector mismatch by launching two strong submicrosecond pulses at λ_1 and λ_2 simultaneously into the fiber (see Fig. 2). While the pulses travel down the fiber, the four-wave mixing fields they create (at λ_S and λ_A) oscillate in intensity with a spatial frequency that is directly proportional to the wave-vector mismatch. For the Stokes field, for example, the spatial frequency F_S is given by

$$F_S = \frac{|\delta k(\lambda_1)|}{2\pi} = cD(\lambda_1)\left(\frac{\delta\lambda}{\lambda}\right)^2 . \tag{3}$$

The instrument measures the spatial oscillation, either at the Stokes or the anti-Stokes frequency, as temporal oscillations in the received, Rayleigh-backscattered light. The backscattered light at either λ_S or λ_A passes a narrow filter, is detected, and the resultant electrical signal of frequency $f(t) = \frac{c}{2n}F_S(z)$ is digitized. The signal is then converted into the dispersion map $D(z)$ through an efficient, FFT-based algorithm (described below).

To achieve the highest possible accuracy and spatial resolution, several properties of the launched pulses have to be carefully controlled: First, the power levels have to be kept below the level for stimulated Raman scattering, and, if $\lambda_0 < \lambda_{1,2}$, below that for modulational instability. Second, the linewidths have to be large enough to avoid stimulated Brillouin scattering.

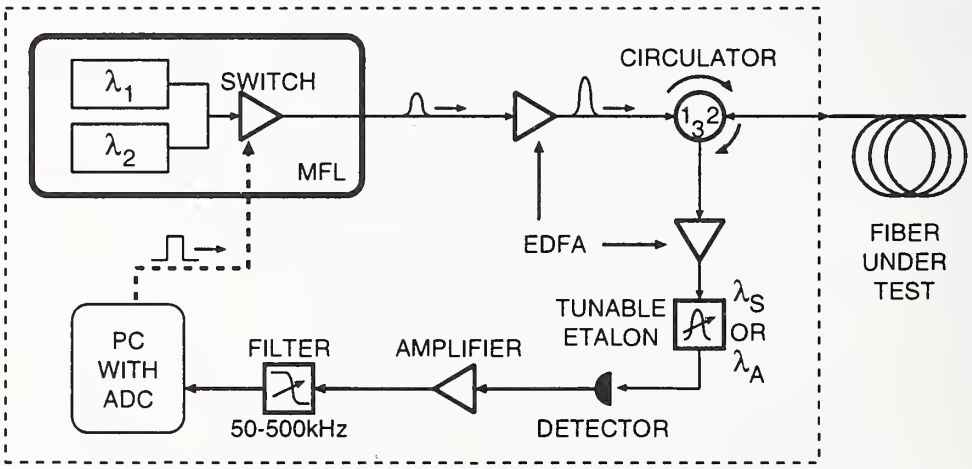

Fig. 2. Schematic of the instrument. A multi-frequency laser (MFL)[7] generates a few milliwatts CW at λ_1 and λ_2 and shapes 0.8 μs pulses through use of an extra-cavity semiconductor optical amplifier switch. The pulses are then amplified up to 1W and sent into the fiber under test. A circulator directs the Rayleigh-backscattered light into another amplifier, through a narrow filter (at either λ_S or λ_A) and into a detector.

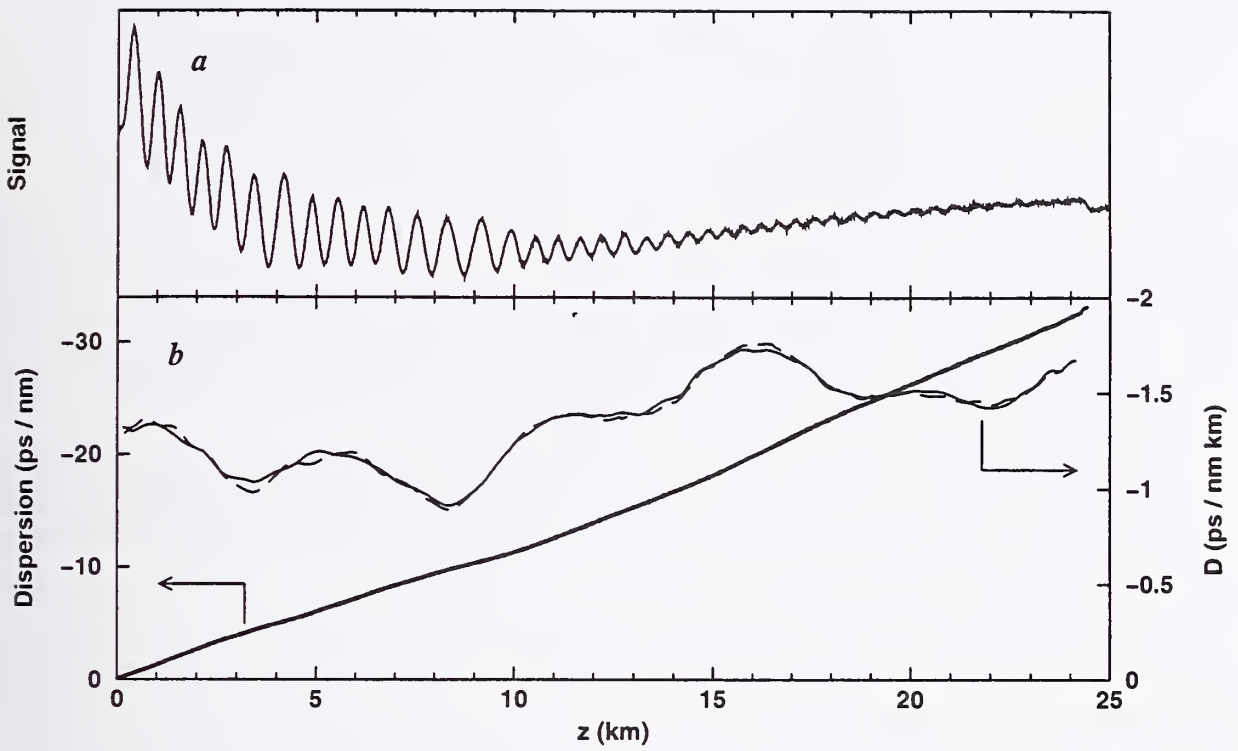

Fig. 3. *a*: Signal of a 25 km span of dispersion shifted fiber. *b*: Solid thick curve: Dispersion at $\lambda = 1552$ nm. Solid thin curve: D measured from left to right. Dashed thin curve: D measured from right to left.

Finally, $\delta\lambda$ must be choosen according to the approximate value of D, to yield the best compromise between spatial resolution, which increases with increasing $\delta\lambda$, and signal strength, which decreases with increasing $\delta\lambda$. Also, of course, $\delta\lambda$ must be stable and precisely defined, since the measured dispersion is inversely proportional to $\delta\lambda^2$ (see Eq. (3)). Table 1 shows values typically used by the instrument.

Figure 3*a* shows a typical signal returned from a 25 km span of dispersion shifted fiber, taken at 1555 nm with $\delta\lambda = 3.6$ nm. To compute the curves of implied dispersion (Fig. 3*b*), the instrument takes a FFT of the signal, eliminates the negative part of the resulting symmetric spectrum, and then performs an inverse FFT; this effectively converts the linear, real-valued oscillation of Fig. 3*a* into a circular oscillation in the complex plane. The curvature of the circular oscillation is directly proportional to $D(z)$ and the dispersion is obtained by taking its integral. It should be noted that the algorithm is fast and accurate, requiring less than one second on a 133 MHz Pentium processor.

Fiber Type	$\lvert\bar{D}(1550\text{nm})\rvert$ (ps/nm/km)	$\delta\lambda$ (nm)	spatial resolution (m)
dispersion compensating	80 to 100	0.6	220 to 280
standard	≈17	1.2	≈330
dispersion shifted	1 to 10	1.8 to 3.6	250 to 600

Table 1. Parameters used for different fiber types.

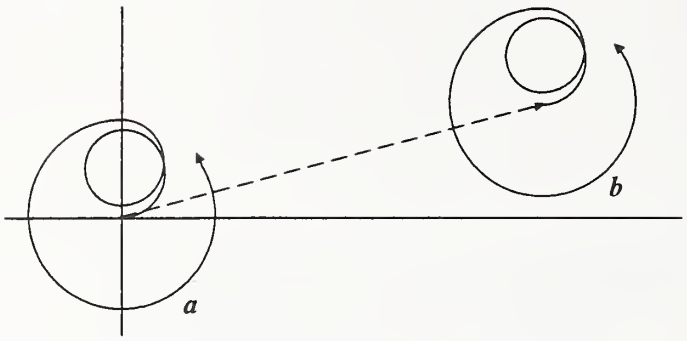

Fig. 4. Possible evolution of the Stokes vector. *a*: without coherent field. *b*: with coherent field (dashed arrow). Case *a* leads to no measurable power change on the last turn, in case *b* the oscillations can be detected all the way through.

To illustrate the precision of the instrument, we plot D for two measurements, taken from either end of the span. The measurements have a spatial resolution of 500 m and a relative uncertainty in D of less than 2%.

We have recently made two other significant improvements. The first consists of adding a small coherent "seed" field at the signal frequency $\lambda_S(\lambda_A)$. We generate this seed by sending the two probe fields at λ_1 and λ_2 through a semiconductor optical amplifier. The four-wave mixing fields it produces are small compared to the probe fields, but are considerably larger than the four-wave mixing fields generated in the fiber itself. The resulting displacement of the net signal field away from the origin (see Fig. 4) has two benefits: First, the seed enhances the intensity of the measured signal, since the net signal now represents the beat between the (large) seed and the (smaller) fiber signal. Second, a potential problem depicted in Fig. 4 is avoided, i.e., that a sudden change in the dispersion could cause the Stokes field to rotate around the origin, leading to a much decreased intensity oscillation. That is, with the coherent seed field present, the oscillation of the field vector always translates into an intensity oscillation.

The second improvement extends the range of the instrument with the help of Raman gain. The signal decay rate is four times higher than the absorption rate of the fiber under test[4]. Given the current sensitivity of the instrument, this limits the range of regular measurements to under 50km, even for fibers with lowest loss coefficients. However, we can maintain a measurable signal power over significantly longer distances by sending a few hundred milliwatts of 1450 nm Raman pump light into the fiber both from the near end and the far end (see Fig. 5). Note that even

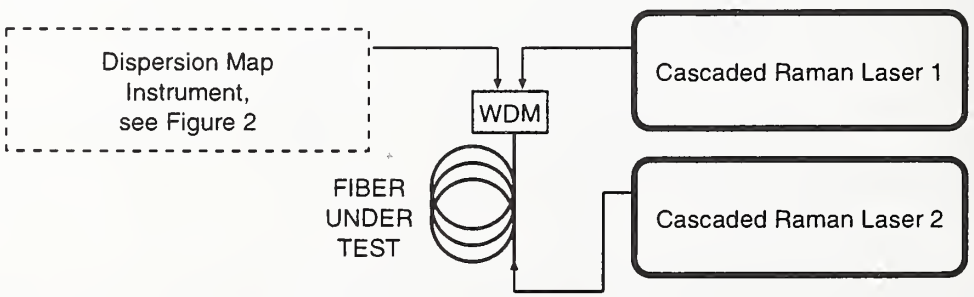

Fig. 5. To extend the range of the instrument, two cascaded Raman lasers provide Raman gain from both ends of the fiber.

in this case, the instrument itself requires access from only one end of the fiber, since the pump lasers do not require any synchronization with the measurement. Thus, even with Raman gain, the OTDR-like technique maintains its unique and very important ability to measure the dispersion maps of installed fibers in the field.

Figure 6 shows a measurement of 75 km of an experimental dispersion shifted fiber (DSF) with a loss coefficient of 0.21 dB/km. First we performed the measurement on the entire span, pumping from both ends, and then on sub-spans of 25 km length each, without pump. Note that without pumping, a measurement of the entire 75 km would not be possible, since in that case the signal power would decrease by an untenable 63 dB over the length of the span. From the nearly perfect fit of the two resultant sets of curves, we infer that the measurement uncertainty is small, i.e., the accumulated dispersion deviates by less than ± 0.1 ps/nm over the first 25 km, by less than ± 0.2 over the next 25 km, and by less than ± 0.3 km over the last 25 km. This means that the accumulated dispersion has an exceedingly small relative uncertainty of $\pm 0.3\%$ over these distances. Finally, note that the dispersion parameter D varies from about -2 to -0.5 ps/nm/km. This variation shows how important it is for the construction of dispersion managed systems to be able to measure the actual dispersion maps of the fibers.

Figure 7 shows a measurement of 22.5 km of dispersion compensating fiber (DCF) with a loss coefficient of 0.51 dB/km, pumped only from the far end. We measured the fiber from both ends and obtained equally small uncertainties as in the case of the dispersion shifted fiber. The measurements of these two fiber types with very different dispersion values demonstrate the flexibility of the

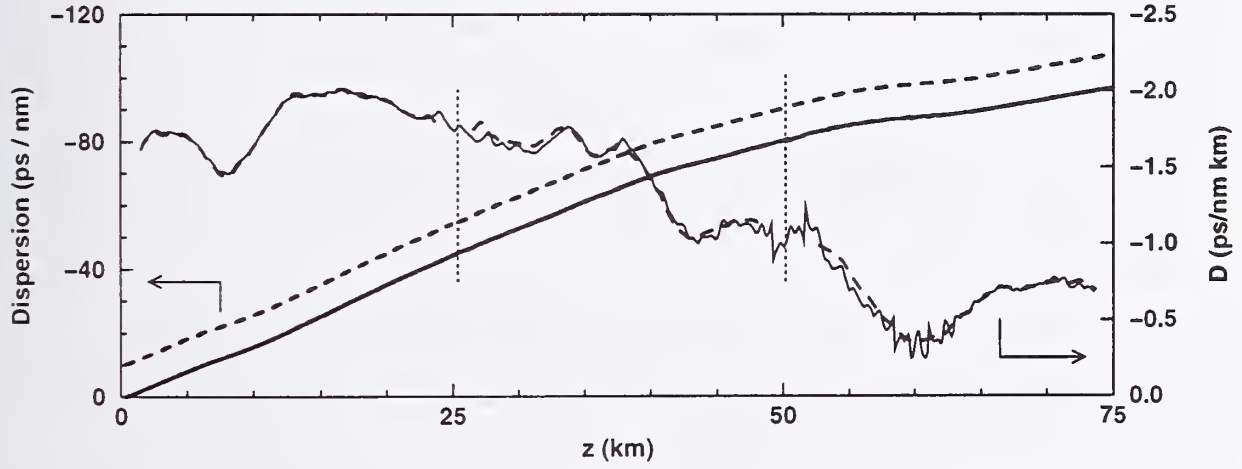

Fig. 6. Dispersion shifted fiber, measured with pump light from both ends. $\delta\lambda = 2.4$ nm. Solid thick curve: Dispersion at $\lambda = 1552$ nm obtained from one measurement of the entire span. Dashed thick curve: Dispersion obtained from three separate measurements of 25 km each. We shifted the dashed curve up by 10 ps/nm for better visibility of the two virtually identical curves. Solid thin curve: D from the measurement of the entire span. Dashed thin curve: D from the three separate measurements. The two vertical dotted lines indicate the points where the fiber was cut.

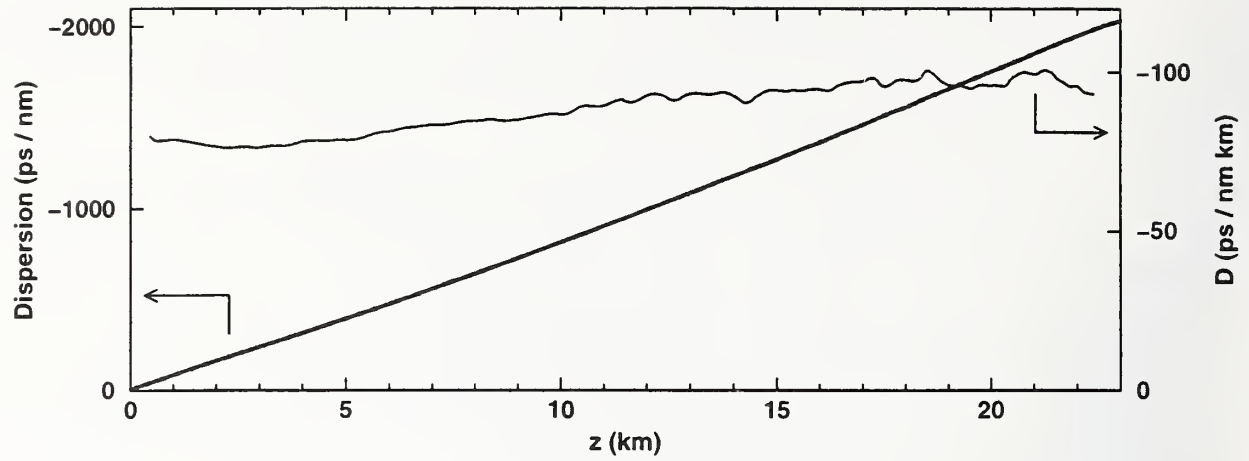

Fig. 7. Dispersion compensating fiber (DCF), measured with counterpropagating pump light. $\delta\lambda = 0.6$ nm. *b*: Thick curve: Dispersion at $\lambda = 1554$ nm. Thin curve: Dispersion parameter D.

OTDR-like dispersion measurement technique. In the near future, this instrument is most likely going to become an indispensable tool both for the design of dispersion managed fiber transmission systems and for the measurement of installed fibers.

We are very grateful to Christopher Doerr, Charles Joyner, and Larry Stulz for supplying us with multi-frequency lasers and to Olivier Ondet for helpful discussions.

References

1. S. Nishi and M. Saruwatari, Electron. Lett. **32**, 579 (1996).

2. R. M. Jopson *et al.*, Electron. Lett. **31**, 2115 (1995).

3. I. Brener, P. P. Mitra, and D. J. Thompson, in *Optical Fiber Communication Conference*, Vol. 2 of *OSA Technical Digest Series* (Optical Society of America, Washington, D. C., 1998), pp. 344–345.

4. L. F. Mollenauer, P. V. Mamyshev, and M. J. Neubelt, Opt. Lett. **21**, 1724 (1996).

5. N. G. R. Broderick, D. J. Richardson, and L. Dong, IEEE Photon. Technol. Lett. **9**, 1511 (1997).

6. M. Artiglia *et al.*, in *Optical Fiber Communication Conference*, Vol. 2 of *OSA Technical Digest Series* (Optical Society of America, Washington, D. C., 1998), pp. 179–180.

7. C. R. Doerr, C. H. Joyner, L. W. Stulz, and J. C. Centanni, IEEE Photon. Technol. Lett. **9**, 1430 (1997).

MEASUREMENT OF THE SPATIAL DISTRIBUTION OF THE ZERO-DISPERSION WAVELENGTH IN DS FIBERS BY BIDIRECTIONAL LINEAR REFLECTOMETRY

A. Rossaro M. Schiano, M. Dainese, F. Lovisolo**

CSELT, via Reiss Romoli 274, 10148 Torino (Italy)

***Politecnico di Torino, C.so Duca degli Abruzzi 24, 10129 Torino (Italy)**

Abstract

A linear bidirectional OTDR technique for the measurement of the spatial distribution of the zero dispersion wavelength has been applied to dispersion shifted terrestrial plants. In this paper results are presented and compared with other measurement methods demonstrating the good accuracy and reliability of the reflectometric technique.

1. Introduction

Measurements of Chromatic Dispersion (CD) uniformity are assuming high importance not only in the field of fiber optic production quality assurance, but also in the design of high capacity Wavelength Division Multiplexed (WDM) telecommunication systems. In fact, in amplified WDM transmission systems, where many high power channels are transmitted on a relatively narrow spectral range, impairments may be caused by Four-Wave Mixing (FWM) when the link CD is very low, i.e. in systems operating on Dispersion Shifted (DS) fibers [1]. While new plants can be designed with a careful choice of CD for each cable section, or even with dispersion-managing techniques, problems could originate in the upgrade of existing DS plants.

In this case, since FWM efficiency depends dramatically on the CD spatial distribution, it would be useful to measure such distribution by means of a simple, field usable technique. A large amount of experimental work has been carried out on this topic and many laboratory results have been reported in literature [2, 3, 4]. Also in the standardization bodies there is a strong interest on chromatic dispersion uniformity. Some contributions have already been presented, showing that a high uniformity of the Zero Dispersion Wavelength (ZDW or λ_0) is required for Non-Zero Dispersion (NZD) fibers and vice-versa a high non-uniformity is desirable for DS fibers [5].

This paper reports the results of ZDW measurements performed on a DS fiber installed plant by means of the bidirectional reflectometry technique in linear regime. This technique has been chosen for the simplicity of the measurement set-up in comparison with non-linear reflectometry, and has been especially tailored for measurements on DS fibers. The bidirectional linear reflectometry has been demonstrated enough accurate to perform a complete spatial characterization of a fiber in terms of Mode Field Diameter (MFD), CD and ZDW.

Results indicate that, at least in the considered plant, the concatenation of different fibers leads to large fluctuations of ZDW along the fiber length.

2. Bi-directional OTDR technique

In the following the method for measuring ZDW distribution based on bi-directional OTDR technique is summarized, with particular emphasis on its application to DS fibers.

It is well known that a bi-directional OTDR technique [6] allows to measure the spatial distribution of waveguide parameters [7]: in particular Mode Field Diameter (MFD) can be precisely measured in function of distance, provided that a reference fiber with a known MFD is available. Starting from the expression of the backscattered optical power: $P(z) = P_0 \alpha_S(z) S(z) \cdot 10^{-\frac{2}{10}\int_0^z \alpha(x)dx}$, it is straightforward to calculate the half-sum of the bidirectional OTDR traces:

$$I(z) = \frac{10Log_{10}P_1(z) + 10Log_{10}P_2(L-z)}{2} = 10Log_{10}\left[\alpha_S(z)S(z)\right] + \Lambda,$$

where α_S is the backscattering coefficient, *S(z)* is the recapture factor, and Λ is a constant. For step index fibers *S(z)* can be expressed in function of MFD *d(z)* (Petermann II definition):

$$S(z) = \frac{6}{\left(\frac{d(z)}{a}\right)^2 V^2} \frac{n_1^2 - n_2^2}{n_1^2}.$$

If a reference fiber is inserted before the fiber under test with a known MFD at location z_0, and neglecting longitudinal variations of α_S, MFD in function of distance can be easily calculated:

$$I'(z) = I(z) - I(z_0) = 20Log_{10}\frac{d(z_0)}{d(z)} \quad \Rightarrow \quad d(z,\lambda) = d(z_0,\lambda)10^{-\frac{I'(z,\lambda)}{20}}$$

Although previous relations hold strictly for step index fibers, their validity extends to DS fibers with negligible errors [8].
Examining now CD, it can be considered as the sum of different contributions:

$$D_{tot} = D_m + D_w + D_p$$

where: $D_m = -\frac{\lambda}{c}\frac{d^2n}{d\lambda^2}$ is the *material dispersion*, $D_w(z,\lambda) = \frac{2\cdot\lambda}{\pi^2 c n_1 \cdot d^2(z)}\left[1 - \frac{\lambda}{2\cdot d(z)}\cdot\frac{\partial d}{\partial\lambda}\right]$ is the *waveguide dispersion* and the D_p is the profile dispersion whose contribution has been considered negligible (in a first approximation).
It can be noted that waveguide contribution to chromatic dispersion can be easily expressed in terms of a wavelength derivative of MFD. From this point the analysis of Step Index (SI) and DS fibers will be performed separately. For SI fibers an analytical expression of the wavelength dependence of MFD can be derived, while for DS fibers, since the application of approximation methods, such as Equivalent Step Index (ESI), does not produce good results, the following numerical approach has been used. MFD behavior in function of wavelength, at a given position *z*, was considered linear between measured values at 1310 and 1550 nm and the corresponding wavelength derivative was used for the calculation of the local waveguide dispersion. This technique named Local Linear Interpolation, leads to accurate results as is shown in the next paragraph.
Material contribution to chromatic dispersion is calculated by means of the well-known Sellmeier equation. Finally, assuming a linear dependence of total chromatic dispersion from wavelength, it is easy to calculate the spatial distribution of λ_0 from the measured spatial distribution of CD evaluated at two or more wavelengths.

3. Measurement results

In this paragraph two examples of the evaluation of MFD and zero dispersion wavelength are reported. In the first case measurements have been performed in the laboratory on a concatenation of DS fibers bobbins (2 fibers 1 km long, and 1 fiber 10 km long), accurately chosen for their good longitudinal uniformity. In the second case, measurements have been performed on a plant, 46 km long, installed in urban ducts. Some important features of the DS fiber plant and of the measurement method as well are highlighted.
First of all, it can be noted that the reflectometric trace noise has a negligible influence on the measurement accuracy. Uncertainties in the order of 0.1 μm and 0.5 nm for Mode Field Diameter (Fig. 1,

3) and Zero Dispersion Wavelength (Fig. 2, 4) respectively can be achieved with commercial OTDR even on relatively long links.

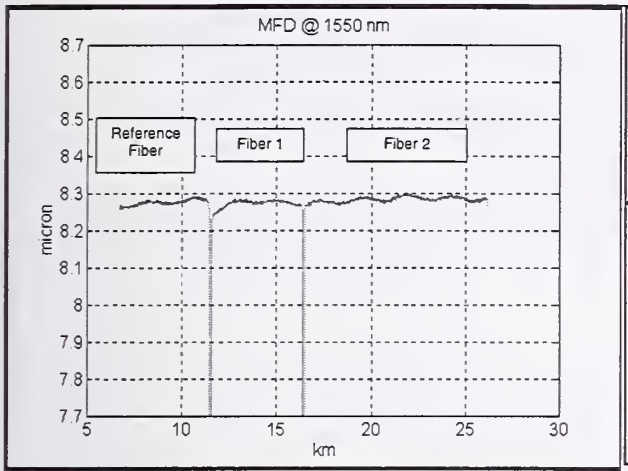

Fig. 1 - Measurement of mode field diameter uniformity on DS fibers

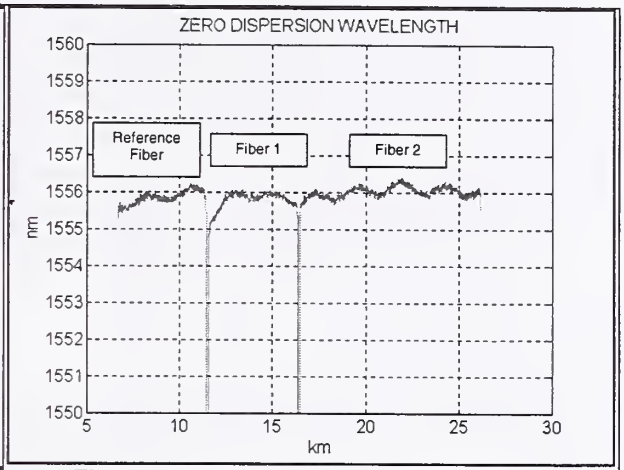

Fig. 2 – Measurement of zero dispersion wavelength uniformity on DS fibers

Moreover, slight periodic oscillations of both MFD and ZDW are evident in fig. 1 and fig. 2, and may be attributed to the drawing process.
Obtained results of MFD and ZDW are in very good agreement with the measurements performed, with other test methods, by the manufacturer, as reported in the following table:

	MFD by manufacturer (VAFF technique)	MFD by OTDR (bidirectional mesurements)	ZDW (λ_0) by manufacturer (PHASE SHIFT technique)	ZDW (λ_0) by OTDR (bidirectional mesurements)
Reference Fiber	8.3	8.28	1556	1555.8
Fiber 1	8.4	8.27	1556	1555.8
Fiber 2	8.4	8.28	1556	1556.0

In the second case, the bidirectional OTDR technique has been used on an installed plant to check if a WDM transmission system could be used.

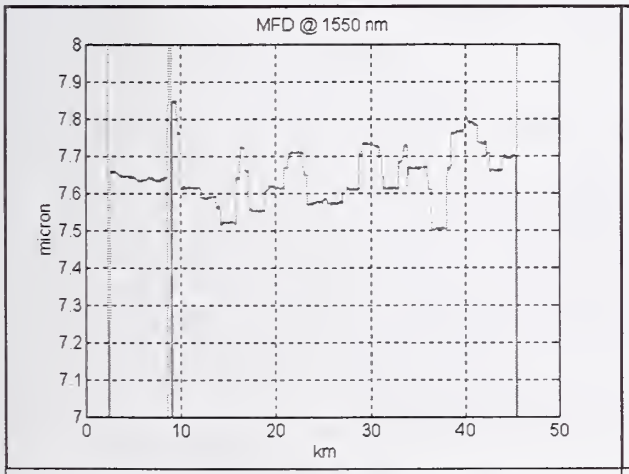

Fig. 3 - Distribution of mode field diameter @1550 nm on an installed DS fiber cable

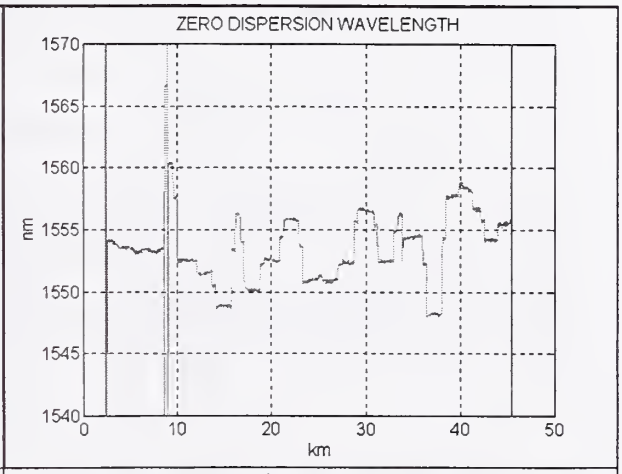

Fig. 4 - Distribution of zero dispersion wavelength on an installed DS fiber cable

Also in this case this technique seems to give very good results since the average ZDW evaluated by bidirectional OTDR (1553.6 nm) is very close to the value measured by a Phase Shift instrument (1553.9 nm).
It is straightforward to observe that the considered plant presents quite large longitudinal fluctuations both in MFD and ZDW. This is due to the concatenation of relatively short sections of cable with different dispersion characteristics.
Transmission experiments carried out on this plant have demonstrated that this configuration of dispersion distribution allows the transmission of 8X2.5 Gbit/s WDM signals without significant impairment even if one of the wavelengths is close to the average ZDW of the fiber.
Finally it is worthwhile to underline that by this simple bidirectional OTDR technique it is possible to characterize fibers not only in terms of attenuation and length, but also in terms of attenuation uniformity, mode field diameter and chromatic dispersion uniformity, giving a great support to fibers testing, expecially in the field.

4. Conclusions

The present contribution shows that OTDR technique based on bi-directional measurements at different wavelengths can be successfully used to measure local zero dispersion wavelength in DS optical links. Using this simple technique it is therefore possible a preliminary check on the CD distribution of a plant in order to assure the immunity of WDM systems from FWM impairment. Results indicate that, provided that a careful characterization of the reference fiber is performed, measurement accuracy and resolution are so high to allow the detection of fiber imperfection due to drawing process and CD longitudinal variations on several tens of kilometers of fiber.
Further developments of the technique are under study, concerning the accuracy and the measurement of small CD components such as the *profile dispersion*.

Acknowledgements

Authors express their gratitude to Dr. D. Cuomo, FOS SpA, for helpful discussions on OTDR tecnique.

References

[1] K. Inoue, *Four-wave mixing in an optical fiber in the zero dispersion wavelength region*, Journal of Lightwave Technology, Vol. 10, No. 11, 1992, pp. 1553-1561.

[2] M. Ohashi, M. Tateda, *Novel Technique for measuring longitudinal chromatic dispersion distribution in singlemode fibers*, Electronics Letters, Vol. 29, N. 15, 1993, pp. 426-428.

[3] K. Nakajima, M. Ohashi and Y. Miyajima, *Evaluation of chromatic dispersion distribution in a single-mode fiber*, OFMC '97, pp. 235-240.

[4] M. Artiglia et al., *Measurement of the dispersion map of installed G.653 fiber links using four wave mixing*, OFC'98, pp. 179-180.

[5] M. Ohashi, H. Okamura, *Comments on chromatic dispersion uniformity*, 1997 ITU-T Geneva '97 D.67 (WP4/15)

[6] M. Artiglia, A. Chiantore et al., *OTDR Trace Analysis for Fiber Characteristics Evaluation: a 'bi-directional' approach*, SOFM '94 Proceedings, pp.61-64

[7] P. Di Vita and U. Rossi, *Backscattering measurements in optical fibers: separation of power decay from imperfection contribution*, Electronics Letters, Vol. 15, N. 15, 1979, pp.467-469

[8] M. Ohashi, K. Nakajima, *Comments on an alternative test method for mode field diameter*, 1998 ITU-T Geneva '98 D.157 (WP4/15)

A NEW TECHNIQUE FOR ZERO-DISPERSION WAVELENGTH MAPPING IN SINGLE MODE FIBER WITH HIGH SPATIAL RESOLUTION

I. Brener (1), D.D. Lee (1), P.P. Mitra (1), D. Philen (2), D.J. Thomson (1)

(1) Bell Laboratories, Lucent Technologies, 600 Mountain Avenue, Murray Hill NJ 07974 (igal@lucent.com)
(2) Lucent Technologies, 2000 Northeast Expy, Norcross, GA 30071-2992

We present a new noninvasive and simple technique for measuring the spatial variation of the zero-dispersion wavelength (λ_0) in single-mode fibers. When applying this technique to dispersion shifted fibers we can resolve fluctuations in λ_0 of less than 0.05nm with a potential spatial resolution of better than 100m.

Introduction

Several non-destructive techniques have been developed lately in order to measure the chromatic dispersion (D) and the zero dispersion wavelength (λ_0) variations along the length of the fiber [1-5]. Most of the reported techniques rely on the use of four-wave mixing (FWM) as a probe for fluctuations in D and λ_0. We present a new and simple technique for measuring $\lambda_0(z)$, i.e. the variation of λ_0 along the fiber length, with great accuracy (<100m).

Theory

Assuming that the phase mismatch between all involved fields is position dependent, the FWM intensity after propagation in a fiber of length L is given by [6-7]:

$$I_{FWM}(q) \propto \left| \int_0^L dz e^{i\phi(z)} e^{-iqz-\alpha z} \right|^2, \quad q = \kappa\lambda, \quad \kappa = 2\pi c \left(\frac{\Delta\lambda}{\lambda}\right)^2 \frac{dD}{d\lambda}$$

$$\phi(z) = \kappa \int_0^z \lambda_0(y)dy \qquad (1)$$

λ_1 and λ_2 are the pump and probe wavelengths respectively, $\Delta\lambda=\lambda_1-\lambda_2$. In our terminology we call pump the laser wavelength closer to the FWM peak, so Eq. (1) is valid for the FWM field that satisfies $\omega_{FWM}=2\omega_1-\omega_2$. If we keep $\Delta\lambda$ fixed then κ becomes a constant of the experiment; q has dimensions of a wavevector. Thus the FWM efficiency as a function of λ measured at a constant detuning is governed by the Fourier transform of a phase-only function $e^{i\phi(z)}$ weighed by the absorption $e^{-\alpha z}$.

The goal is to obtain the profile $\lambda_0(z)$ from the measured quantity $I_{FWM}(\lambda)$ or, given $I(q)$, find $\phi(z)$. This is a nonlinear inversion problem and is closely analogous to inverting a Fourier transform. In fact, if the phase of the output electric field could be measured in addition to the intensity, then the inversion problem would be a straightforward inverse Fourier transform. In general, the loss of phase information would mean one could no longer invert the Fourier transform. However, in the special case we are dealing with here (namely the magnitude of the function is known both in real and Fourier space), the problem is known to have a unique inverse as long as $\phi(z)$ is analytic and $\alpha>0$ [8].

The existence of a unique inverse to the above problem does not in general guarantee that we will be able to perform the inversion in practice, because of measuremental uncertainties which lead to imperfect knowledge of $I(q)$, as well as possible difficulties in the inversion procedure. Also, in the above procedure, polarization effects have been neglected, which may in general be important. We find, in practice, that the inversion is possible, both in numerical simulations as well as in real fiber measurements in which the actual zero dispersion profile is determined by direct means. In general, the inversion procedure we use is to parametrize the function $\phi(z)$ in terms of a limited number of parameters, and then to find the values of the parameters that minimize the mean square error between the observations and the spectrum that would be generated by the parametrized $\phi(z)$. Several parametrizations are possible; for example, we have used both piecewise linear and an expansion of the phase in terms of a basis set, such as Chebychev functions.

In any parametrization, there is the important question of resolution. However, insight may be obtained from the corresponding linear inverse problem. In this case, the resolution would be given by $\Delta x=2\pi/\kappa(\lambda_{max}-\lambda_{min})$, where $(\lambda_{max}-\lambda_{min})$, represents the range over which we can acquire meaningful data. As an example, for a typical *25km* fiber spool and using $\Delta\lambda$=8nm, $(\lambda_{max}-\lambda_{min})\approx$20nm, so $\Delta x\approx$80m. In shorter spools, measuring with $\Delta\lambda = 6nm$ we obtain $(\lambda_{max}-\lambda_{min})\approx$40nm so $\Delta x\approx$50m. Longer integration time allows increasing $(\lambda_{max}-\lambda_{min})$ therefore mapping $\lambda_0(z)$ with a potential spatial resolution of less than 50*m* is feasible.

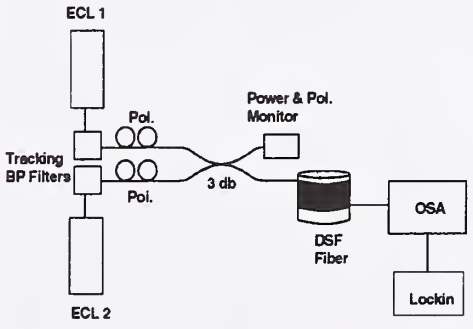

Figure 1: Experimental Setup

Experimental setup used to measure the fluctuation in λ_0. The two lasers are scanned at a constant detuning and the FWM peaks are recorded with either an optical spectrum analyzer (OSA) or a lockin amplifier

Experiment and results

The experimental setup used in this work is shown in Fig. 1. Two external cavity tunable lasers (ECL) are combined with collinear polarizations and launched into the fiber under test. We also use tracking bandpass filters at the output of each laser in order to suppress any spurious ASE background and improve the dynamic range of the measurement. The power of the tunable lasers is kept at a few dbm and thus nonlinearities are not important. The two tunable lasers are scanned together at a constant detuning $\Delta\lambda$ and the FWM peaks are analyzed in an optical spectrum analyzer or using lockin detection. This technique can be applied to any wavelength range covered by λ_0 provided that tunable lasers can be tuned through the wavelength region of interest. Conventional single mode fiber with λ_0~1.3 μm and new dispersion shifted fibers with λ_0>1.6 μm and λ_0<1.5 μm can be readily analyzed with our technique.

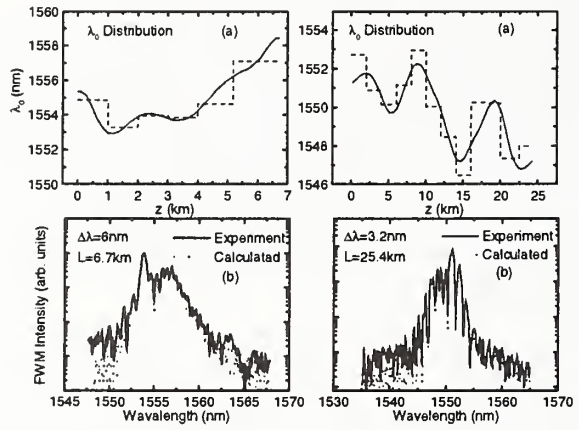

Figure 2: Example

(a) The calculated $\lambda_0(z)$ distribution for 2 fiber spools of 6.7 and 25.4 km; (b) the experimental FWM tuning curves and the calculated curves using the $\lambda_0(z)$ of Figs. 2(a).

In order to illustrate the capabilities of this technique we apply our procedure to two dispersion shifted fiber spools of 6.7 and 25km with average λ_0 of 1555 and 1550 nm, respectively. The step curves in Figs. 2(a) correspond to a destructive measurement of λ_0 for both spools performed using conventional techniques. The calculated $\lambda_0(z)$ profile using an improved basis of orthogonalized sines and cosines is shown by the continuous curve in Figs. 2(a). The inferred profile matches the observed spread in λ_0 extremely well. Furthermore, the experimental spread in λ_0 is consistent with the width of the FWM tuning curve, as shown in Figs. 2(a). The solid line in Figs. 2(b) show the experimental FWM tuning curves and the dashed curve shows the calculated FWM tuning curve using the inferred profile of $\lambda_0(z)$ for both fibers. There is a very good agreement for almost 3 orders of magnitude.

A limitation to this and all previous techniques based on FWM arises from polarization mode dispersion (PMD) and/or birefringence. This has been largely overlooked and deserves some discussion. When accounting for the electric field polarizations, the FWM efficiency in the present configuration is proportional to $\left|\vec{E_1}\cdot\vec{E_2}\right|^2$ [9]. If one assumes a constant birefringence Δn, this inner product will oscillate along the fiber length with a period of: $L_{coh}=\frac{1}{2}\frac{\lambda^2}{\Delta\lambda\cdot\Delta n}$. For example, if $\Delta n=10^{-8}$ and $\Delta\lambda$=10nm, then $L_{coh}\approx$12km. In reality, there will not be a simple expression for this "polarization coherence length" as Δn is stochastic. Nevertheless, from this estimate we can expect that the relative polarization between $\vec{E_1}$ and $\vec{E_2}$ will not be maintained over long fiber spans if $\Delta\lambda$ is finite. This will superimpose an unknown spatial oscillation in the FWM efficiency, which in turn will complicate the inversion process (although it will still be solvable). In order to illustrate this point, we measured FWM tuning curves for several 25km fiber spools with average PMD in the range of 0.03-0.2 $ps/km^{1/2}$, and for parallel and perpendicular polarizations. We find that in the spools with the highest PMD and for $\Delta\lambda\approx$8nm the FWM curves for both polarizations coincide, which means that the relative polarizations are completely lost after a certain length (probably much shorter than 25km). Consequently, the ultimate resolution that can be achieved by this (and similar) techniques will be determined by the largest $\Delta\lambda$ allowed by the PMD of the fiber under study. This holds as long as the inversion is carried out in the way presented in this paper. One may devise different inversion algorithms that could accommodate an additional spatial modulation in the FWM efficiency introduced by PMD. Finally, we note that the procedure presented in this paper can be generalized in order to map the variations of chromatic dispersion as a function of position.

In conclusion, we presented a new technique for mapping the spatial variations in the zero dispersion wavelength along the fiber length. The technique is easy to implement, avoids fiber nonlinearities through the use of low power CW lasers, and has the potential to map spatial fluctuations with an accuracy of better than 100m. The ultimate resolution is only limited by the polarization mode dispersion of the fiber.

references

/1/ M. Ohashi and M. Tateda, Electron. Lett. **29**, 426 (1993).

/2/ Y. Suetsugu, T. Kato, T. Okuno, and M. Nishimura, IEEE Phot. Tech. Lett. **7**, 1459 (1995).

/3/ S. Nishi and M. Saruwatari, Electron. Lett. **32**, 579 (1996).

/4/ M. Eiselt, R.M. Jopson, and R.H. Stolen, J. Lightwave Technol. **15**, 135 (1997).

/5/ L.F. Mollenauer, P.V. Mamyshev, and M.J. Neubelt, Opt. Lett. **21**, 1724 (1996).

/6/ K. Hill, D.C. Johnson, B.S. Kawasaki, and R.I. MacDonald, J. Appl. Phys. **49**, 5098 (1978).

/7/ K. Inoue, J, J. Lightwave Technol. **10**, 1553 (1992).

/8/ A.M.J. Huiser, P. van Toorn and H.A. Ferwerda, Optik **47**, 1 (1977).

/9/ K. Inoue, IEEE J. of Quantum Electr. **28**, 883 (1992).

ANALYSIS OF SECOND ORDER CHROMATIC DISPERSION VARIATION IN OPTICAL FIBER UNDER LARGE STRETCHING

SIMOHAMED L.M., AUGUSTE J.L., RIOUBLANC J., BLONDY J.M., REYNAUD F.

Groupe photonique, IRCOM (UMR 6615)
123, avenue A.Thomas, 87060 LIMOGES cedex -FRANCE-

Abstract:
Stretched fiber suffers opto-geometrical parameters modifications leading to group velocity dispersion evolution. By means of an interferometric device, the second order chromatic dispersion is characterized versus fiber stretching. The purpose of this paper is to fit the experimental results with a model taking into account photo-elastic tensor and wave guide geometry modifications.

Introduction:
In the frame of a large stroke optical fiber delay line implementation using silica fiber ability to induce large and variable group delay when they are stretched [1,2], we intent to express theoretically the second order chromatic dispersion evolution versus fiber stretching. The experimental characterization is achieved by using a fiber Mach-Zehnder interferometer. A spectral analysis of the interferometric mixing allows spectral phase determination and the second order chromatic dispersion is deduced from the phase curvature [3].
Two experimental configurations are performed. The first one consists in the accurate measurement of the second order chromatic dispersion evolution versus stretching. The aim of the second is to calibrate the variable additional chromatic dispersion induced by the stretching by means of a comparative study using a set of unstretched fiber samples. In the two configurations the experimental data are plotted versus the generated group delay.
In this first approach, a theoretical analysis of the experimental results is performed using a standard silica fiber model. Group velocity dispersion is deduced from computations taking into account the silica photo-elastic tensor, and the constant propagation variation resulting from the opto-geometrical deformations.

Experimental considerations:
The experimental set up is shown on figure 1. The Mach-Zehnder interferometer is implemented with a York HB 600 polarization-maintaining fiber in order to avoid polarization cross coupling. A high pressure Xenon lamp is used as source and the study is performed over a [650-850 nm] spectral range for which silica chromatic dispersion effects are important.

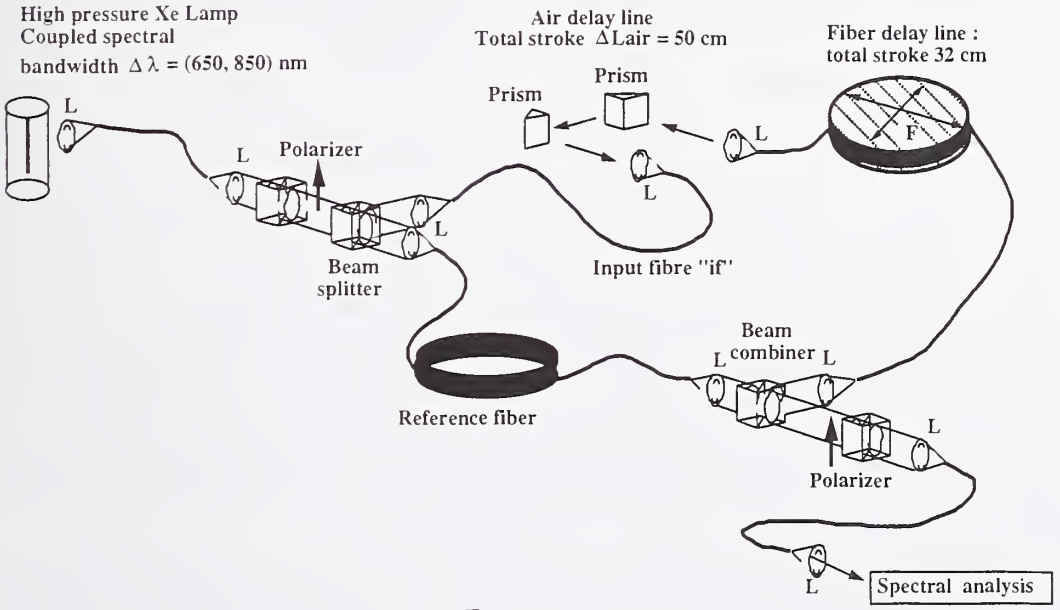

Fig. 1: Experimental setup.

The field amplitude division at the input of the interferometer and the flux recombination at the output are performed by two beam-splitters. The light source is linearly polarized and injected by means of microscope objectives into the two interferometric arm inputs, the optical fields being aligned with the fast axes of the fibers. The optical fiber delay line consists of fifteen-meter length of polarization maintaining fiber wound and glued on a rubber rim. A hydraulic pump drives the rubber rim radial expansion so that the fiber is uniformly stretched.
An air delay line consisting of a variable air path by motion of a motorized translation is integrated in one of the interferometric arm in order to adjust the zero group delay. The interferometric mixing available at the output of the interferometer is spectrally analyzed by means of a prism spectroscope with a linear CCD detector.
The phase shift $\Phi(\nu)$ between the two interferometric arm can be expressed as:

$$\Phi(\nu) = \Phi_f(\nu) + \Phi_0(\nu) \qquad (1)$$

where $\Phi_f(\nu)$ is the phase shift introduced by the propagation in the fibers and $\Phi_0(\nu)$ results from the air path propagation.
The fiber contribution $\Phi_f(\nu)$ may be represented as a first approximation by the sum of a linear term and a quadratic one where as $\Phi_0(\nu)$ consist in a linear term. For a zero group delay obtained experimentally by adjusting the air delay line the second order phase shift is only remaining and can be expressed by:

$$\Phi(\nu) = \left[\frac{\delta^2 \beta_1}{\delta \nu^2} \cdot L_1 - \frac{\delta^2 \beta_2}{\delta \nu^2} \cdot L_2 \right] \cdot \frac{(\nu - \nu_0)^2}{2} \qquad (2)$$

where β_i .(i=1 or 2) is the propagation constant, and L_1, L_2 are the fiber length in the two interferometric arms. This quadratic term results from the group velocity dispersion and is fully sufficient to fit accurately the experimental analysis [4].
In order to characterize and scale the chromatic dispersion variation versus fiber stretching two experimental configurations are compared (figure 2).

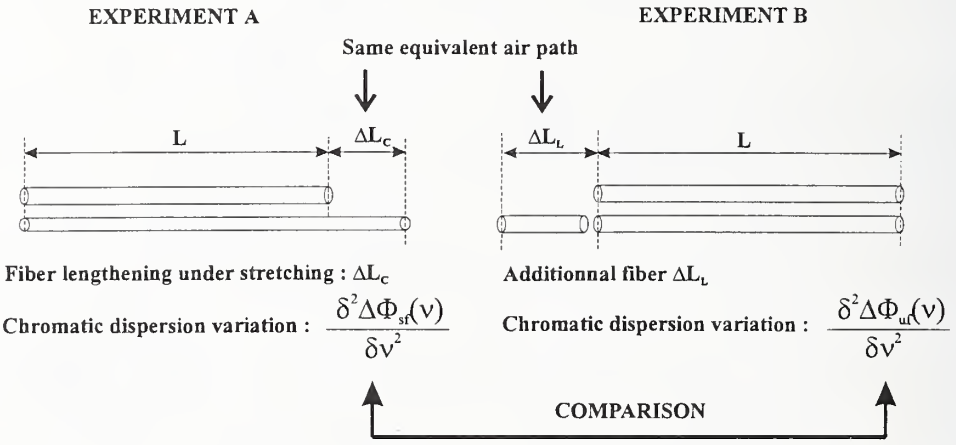

Fig. 2: Comparative study between the chromatic dispersion of a stretched fiber and an unstretched one.

* In the first case, (denoted experiment A, figure 2, left side), the phase variation $\Delta\Phi_{sf}$ results from fiber stretching: The pressure, applied on the optical delay, is increased by step of 0.5 bar over a 0 bar-6 bar span. At each step, the zero group delay is adjusted. The resulting channeled spectrum is displayed on the linear CCD detector and the parabolic phase shift is determined as a function of the frequency.
* In the second case (experiment B, figure 2, right side), the phase shift $\Delta\Phi_{uf}$ varies versus the fiber length: The fiber length of the interferometric arm including the free beam air delay line is modified by replacing the input fiber labeled "if" (figure 1). For each replacement, the zero group delay is adjusted and the associated phase shift determined.
Figure 3 reports the two second order chromatic dispersions variation of the two configurations versus the generated air path. The two curves exhibit a linear behavior of the second order chromatic dispersion coefficient. The slope is a=1.03 rad.ps^{2}m^{-1} for experiment A, and a=1,3 rad.ps^{2}m^{-1} for experiment B. Thus, for a given air delay, the additional chromatic dispersion of the stretched fiber remains smaller than the one of an unstretched fiber.

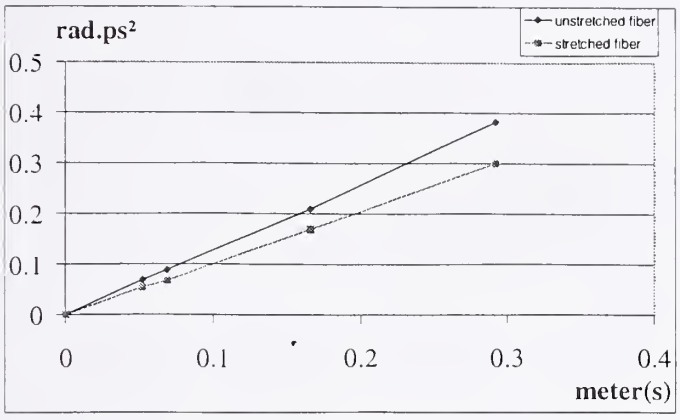

Fig. 3 : Evolution of the second order phase term versus the generated air path.

Theoretical model [5,6,7]

Assumptions : The optical fiber used in the experiment is a polarization maintaining fiber glued on a variable diameter drum. Only one axis of the fiber is used so we consider an equivalent step index fiber which refractive index is deduced from the real index profile of the polarization maintaining fiber. In order to simplify the model, we assume that the drum diameter is enough important to ensure that the experimental configuration is equivalent to a wave guide axial elongation.

An optical fiber under strain suffers opto-geometrical parameters modifications. The deformation vector ε can be written by the following expression :

$$\varepsilon = \begin{vmatrix} -\nu_p \varepsilon_z \\ -\nu_p \varepsilon_z \\ \varepsilon_z \end{vmatrix} \qquad (3)$$

where ν_p is the Poisson coefficient of the silica (ν_p=0.17), and ε_z the axial elongation.

This vector shows clearly that the volume is not preserved, the Poisson coefficient ν_p <1. Then, when the fiber is under stress, the core and cladding radius decrease and the index repartition is modified. The waveguide propagation characteristics determination makes necessary to derive the material refractive index modification from geometrical deformation. The photoelastic effect describes the relation between the mechanical strain and the resulting refractive index change in the material. We can define the strain-optic tensor by :

$$P_{i,j} = \begin{vmatrix} P_{11} & P_{12} & P_{12} \\ P_{12} & P_{11} & P_{12} \\ P_{12} & P_{12} & P_{11} \end{vmatrix} \qquad (4)$$

and the resulting refractive index change Δn_i : $\Delta n_i = \sum_j P_{ij}\varepsilon_j$ with i = r, θ, z (5)

In order to compute the effective index of the stretched waveguide the following parameters are taken into account:

-Modification of core diameter.

-Modification of the core and cladding refractive indexes.

In a second phase, this effective index evolution can be fitted by a second order polynomial approximation, allowing us to express the propagation constant and its successive derivatives. In this approximation the variation of Pij tensor versus frequency are neglected.

In the case of experiment A we express the second order phase term in the stretched fiber by:

$$\frac{\partial^2 \Delta\Phi_{sf}}{\partial \nu^2} = \frac{\partial^2 \beta_C}{\partial \nu^2}(L + \Delta L_C) - \frac{\partial^2 \beta_L}{\partial \nu^2} L \qquad (6)$$

where ΔL_C is the axial elongation, L the length of the fiber under testing, β_L and β_C are the propagation constants in the unstressed and stressed fiber and $\Delta\Phi_{sf}$ the second order phase term variation in the stressed fiber.

In the second part of calculation, the phase variation results from fiber lengthening and the second order term variation can be expressed by :

$$\frac{\partial^2 \Delta\Phi_{uf}}{\partial \nu^2} = \frac{\partial^2 \beta_L}{\partial \nu^2} \Delta L_L \qquad (7)$$

where ΔL_L is the fiber length added in order to have the same group delay than in the first part of calculation. Eq.6 and Eq.7 are plotted in the following figure in order to compare the difference of the second order phase term in a stretched fiber and an unstretched one (fig. 4).

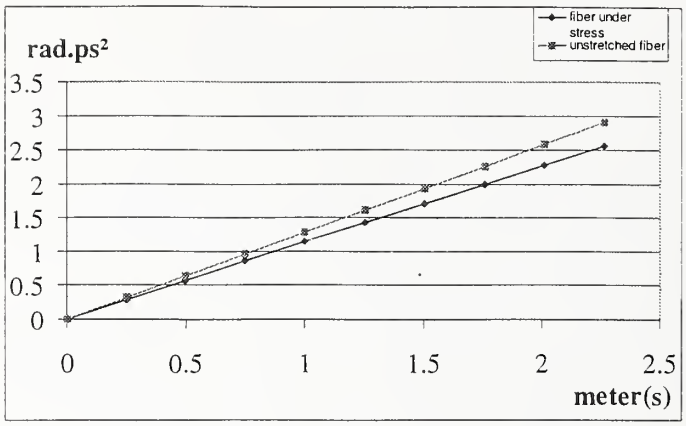

Fig. 4: Evolution of the second order phase term for several equivalent generated air delay.

We obtain a slope of 1.29 rad ps^2 m^{-1} for the unstretched fiber and 1.13 rad ps^2 m^{-1} for the fiber under strain. We can note that the difference is only 10% between the theoretical and experimental values for the stretched fiber, leading to a discrepancy of 30% for the difference between the theoretical evaluation and the experimental measurement of the second order phase term in a stretched or unstretched fiber. The assumptions introduced in the theoretical development allow a good approximation.

Discussion and Conclusion

The developed model allows simple calculations which gives results in good agreement with the experiment.
The 30 % slope difference between experimental and theoretical stretched fiber can be explain by the relative approximations : The experiment has to be implemented using a polarization maintaining fiber in order to avoid cross coupling perturbations. As long as only one principal axis of this fiber is fed, our model simulates an index step fiber that fit the experimental refractive index.
Assuming the photo-elastic coefficient to be achromatic, this result can be extrapolated to different spectral domain. The emerging data on dispersion effects allows to design optical fiber delay lines in the frame of correlation or synchronization of optical fields.

BIBLIOGRAPHY

[1] SIMOHAMED L.M., DELAGE L., REYNAUD F. : "An optical fibre delay line with a 318 mm stroke", *Pure and Applied optics*, 1996, **5**, p.1005.
[2] SIMOHAMED L.M., REYNAUD F. "A two meter stroke optical fibre delay line ", *Pure and Applied optics*, 1997, **6**, p.37.
[3] SHANG H. T. "Chromatic dispersion measurement by white-light interferometry on metre-length single-mode optical fibers", *Electron. Letter*, 1981, **17,** 17, p.603.
[4] REYNAUD F., ALLEMAN J.J., CONNES P. "Interferometric control of fiber lengths for a coherent telescope array", *Applied Optics*, 1992, **31**, 19, p.3736.
[5] LAGAKOS N., BUCARO J.A., LARZYNSKI J. : "Temperature-induced optical phase shifts in fibers", *Applied Optics*, 1981, **20**, 13, p.2305.
[6] BERTHOLDS A., DÄNDLIKER R. : "Deformation of single-mode optical fibers under static longitudinal stress", *Journal of Lightwave Tech.*, 1987, **5**, 7, p.895.
[7] RIOUBLANC J. : "Etude d'un système de stabilisation passive de la dérive en température de la longueur d'onde d'accord des réseaux de Bragg", **Ph D thesis**, Université de LIMOGES, 1997.

Fiber Dispersion Measurements using a Supercontinuum Fiber Laser

F. Koch, S.V. Chernikov, and J. R . Taylor

Femtosecond Optics Group, Physics Department, Imperial College, Prince Consort Road, London SW7 2BZ , UK

Broadband sources operating in the spectral range of 1 to 1.8 μm are of significant interest for the purpose of characterisation of single mode optical fibers and fiber based components. Standard measurements in single mode optical fibers like losses, chromatic dispersion, polarisation mode dispersion are commonly performed with tuneable lasers or superfluorescent sources in one of the two spectral regions around 1300 nm and 1550 nm. Recently, we have demonstrated a supercontinuum fiber laser based on a self-Q-switched Ytterbium fiber laser [1]. The laser generates a continuos super-continuum spectrum from 0.8 to 2 μm with an extremely high spectral brightness ~ 0.2 mW/nm within the range of 1.1-1.75 μm which is for comparison at least four orders of magnitude brighter than a single mode fiber coupled conventional "white-light" source operating in this spectral range. A typical spectrum of the source is illustrated in Figure 1. The laser operates in a self-Q-switch mode generating pulsed with a duration of a couple of nanoseconds at 10-20 kHz repetition rate. Here we report on applications of the source for measurement of dispersion characteristics of various types of single mode fibers.

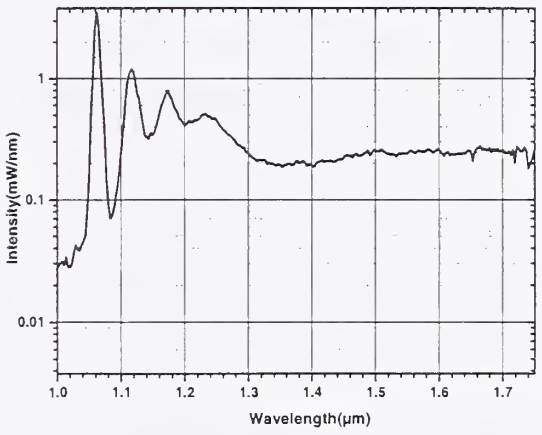

Figure 1 Spectrum of supercontiuum laser source

Two different techniques were used to measure the dispersion: interferometric measurement and time of flight measurement [2]. The interferometric measurements were undertaken using a fiber Mach-Zehnder interferometer comprising two 3dB-couplers with an air gap in the reference arm and test fiber typically ~60cm long in the other arm. All measurements were undertaken in spectral domain using a conventional spectrum analyser. Representative interferometric measurement patterns are shown in Figure 2. The positions of the minima , maxima and centre of the interferometric pattern were used to determine the dispersion of the fiber. The dispersion characteristics of the fiber can then be calculated either based on a single short measurements or by scanning the length of the reference arm.

By scanning the length of the reference arm of the interferometer, the centre wavelength where two arms of the interferometer optically are equal moves as shown in the Figure 2. The group delay as a function of the wavelength follows directly from this measurements, and the chromatic dispersion can be found by differentiating the curve. This technique could be used for measurement of dispersion of all types of fiber. In particular, we studied the dispersion properties of various dispersion compensating fibers(DCF) in the range of 1.1 to 1.7 μm. Some results are shown in Figure 3.

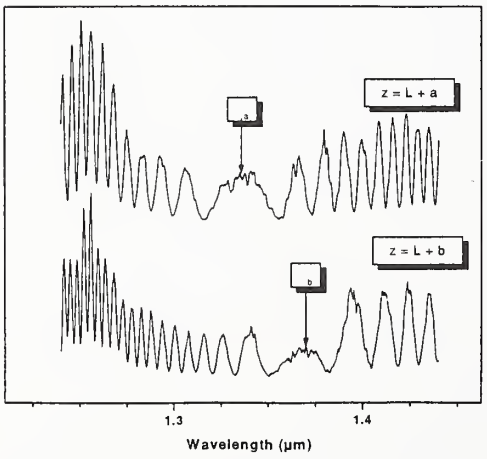

Figure 2 Representative interference patterns

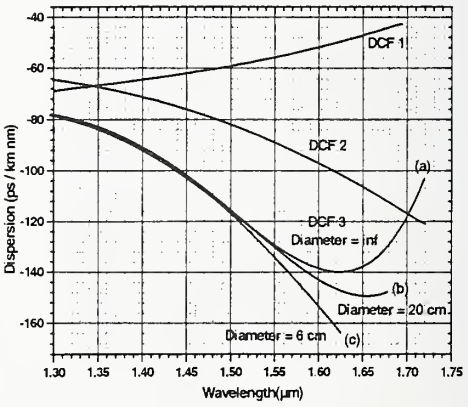

Figure 3 Measured chromatic dispersion of three different dispersion compensating fibers

The dispersion curve depends strongly on the design of the dispersion compensating fibre. The other important feature of DCF is that the dispersion can strongly be affected by fiber bending. The effect was investigated using the above measurement technique. Curves (a), (b) and (c) in Figure 3 show the dispersion curves of the same fiber placed in a coil for a number of bending diameters. The bending effects the value of the dispersion, slope and also the shape of the curve. The results are well explained by theoretical modelling and are of importance not only for application but also for design optimisation of dispersion compensating fibers.

The information about the fiber dispersion can also be obtained from a single shot measurement of interferometric pattern similar to those shown in Figure 2. By measuring the period of oscillations in the pattern, it is possible to determine the dispersion, dispersion slope, zero dispersion wavelength and even dispersion curve in the entire spectral range. For these "single shot" type measurements, the stability of the interferometer is extremely important in order to obtain accurate results.

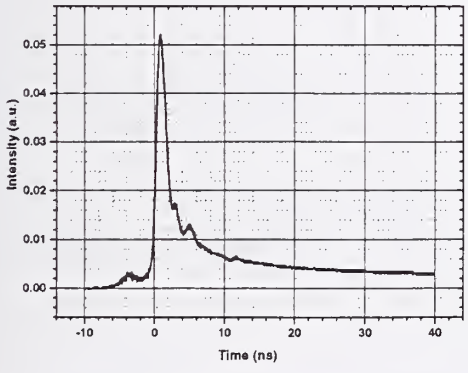

Figure 4 Pulse in time domain at 1550nm

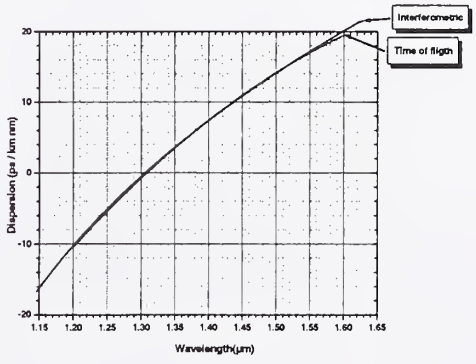

Figure 5 Dispersion measured by different techniques

The interferometric technique is suitable for measurements in short pieces of fiber typically from tens of centimetres up to a few meters. For evaluation of long fibers (from hundreds of meters to tens or even hundreds of kilometres), the time-of-flight type of measurements can be implemented using this supercontinuum source. For the measurements, the spectrum of the source was first sliced using a simple diffraction-

grating-based monochromator with fiber input and output. The monochromator was adjusted to ~ 2-3 nm bandwidth, and could be tuned within the entire spectrum of the source. A typical shape of the filtered pulse is shown in figure 4. The rise time of the pulse was less than 0.5 nsec limited by the resolution of the detection set-up included a fast detector and digital oscilloscope. This resolution was however sufficient to measure reliably the dispersion of dispersion compensating or dispersion shifted fibers with the minimum lengths of 200 m and 3 km respectively. As an illustration, figure 5 shows the dispersion curves measured by the interferometric and time-of-flight techniques in a short and long pieces of the standard telecommunication fiber. The results show the reliability of the measurements even in the vicinity of zero dispersion.

In conclusions, we have demonstrated the application of the supercontinuum fiber laser for measurements of dispersion in various singe mode fibers. The source which is currently available as a compact diode pumped package, looks very promising for applications in various fiber characterisation apparatuses.

References:

[1] S.V. Chernikov, Y. Zhu, J. R. Taylor, V.P. Gapontsev: "Supercontinuum self-Q-switched ytterbium fiber laser", Optics Letters, Vol. 22, No. 5, March 1, 1997, p. 298-300

[2] Leonard G. Cohen: "Comparison of single-mode fiber dispersion measurement techniques", Journal of Lightwave Technology, Vol. LT-3, No. 5, October 1985, p. 958-966

PLANAR COMPONENTS FOR DENSE-WDM

J.Amin, R.O.Maschmeyer, A.Beguin, C.Lerminiaux*, D.Trouchet*, N.Boos* and C.Nicolas**

Corning Inc.
Corning, NY 14831
Tel: (607) 974 3042 Fax: (607) 974 3518 Email: aminj@corning.com

(*) Corning S.A
7bis, Avenue de Valvins, 77210 Avon, France

The seemingly limitless demand for bandwidth created by the phenomenal growth of industry sectors such as Internet and high-speed data has spurred service providers to push for new ways to expand their fibre-optic cable capacity. Affordable bandwidth in network backbones is becoming a scarce commodity, with many fibre networks in the US operating close to their maximum overall capacity. In order to keep up with this ever-rising demand for capacity, carriers are installing wavelength-division mutliplexed (WDM) networks, where multiple channels located on separate wavelengths are simultaneously transmitted down an optical fibre. System houses are currently offering 8 and 16 wavelength solutions to the capacity dilemma, each wavelength separated by 100GHz and delivering 2.5 Gbs^{-1} of bandwidth, for an aggregate of upto 40 Gbs^{-1}, and systems capable of carrying OC-192 line rates ($10Gbs^{-1}$) have also been installed. With no sign of abatement in user demand for bandwidth, there is already talk in the industry of installing 40- and 80-channel systems by mid-1999. In addition, creating reliable network infrastructures for WDM has led to a surge in R&D on optical add-drop multiplexers and optical cross-connect systems, which will enable all-optical networks to perform at a higher level than electronic networks.

The adoption of these dense-WDM (DWDM) functions in network architectures requires, in addition to highly advanced gain-flattened amplifiers, the availability of key optical components such as multiplexers and demultiplexers, dispersion compensators, switches, and tunable filters. Planar waveguide devices have recently started playing a role in WDM, in particular for passive optical components required in multi-wavelength systems, where the planar configuration offers the advantage of compactness through manipulation of all wavelengths on a single chip. The most attractive of such passive planar devices is the phased array demultiplexer, which is currently finding commercial application in 8- and 16-channel networks. In addition, laboratory demonstrations of 40-channel devices have also been made. Other commercially available planar WDM devices include switches and switch arrays, generally composed of Mach-Zehnder elements or digital Y-branches. Lattice filters for gain-flattening in amplifiers and also for providing tunable dispersion compensation have also been explored in various research laboratories. In this presentation, the state-of-the-art of planar components and their applications for DWDM will be discussed, highlighting key measurement issues in the characterisation of these devices.

2.5 Gb/s PRBS Extinction Ratio "Eye Diagram" Measurements of Biased and Bias Free™ Lithium Niobate OC-48 Modulators

by: David Williams, Adnan Akhtar, Dan Attanasio, David R. Maack
and Greg McBrien
of
Uniphase Telecommunication Products
Electro-Optic Products Division
1289 Blue Hills Avenue
Bloomfield, CT 06002

INTRODUCTION

The rapid entry of narrow band WDM technology into today's telecommunication systems has introduced a number of new components into the hardware infrastructure raising issues of which measurements, measurement procedures and pass/fail criteria to use in reliability and qualification testing. With many of these components, industry standard measurement techniques have not yet been established. One of these, lithium niobate OC-48 modulators, fall into this category of new components without a history of measurement pedigree. Fortunately, standard 2.5 Gb/s Pseudo Random Binary Sequence (PRBS) Extinction Ratio "Eye Diagram" Measurements with the proper modified procedures and setup can accurately predict how well this component will operate in a system.

Lithium niobate modulators are complex components that combine optical, electrical and RF functions. Each of these functions have a number of intrinsic measurable properties which when combined, fully characterize the modulator's overall performance. Unfortunately, many of these are strongly correlated such that a simple criteria for each separate parameter is inadequate to properly define system acceptability. The eye diagram, on the other hand, measures the extrinsic performance of the modulator as the system would see it by completely integrating the intrinsic properties.

MODULATOR TYPES

Complicating eye diagram measurement procedures for lithium niobate modulators is that there are two different types of modulators -- bias ready and Bias Free™. The main differences are quadrature bias methods and internal polarization properties. In order for the modulator to properly operate in the system, it must be held at quadrature. In the Bias Free™ type, the modulator is set to quadrature through internal manufacturing techniques. With the bias ready type, the modulator is set to quadrature by application of an external DC bias voltage that is determined through a complex control loop. The Bias Free™ type is highly polarized, only allowing the TE state of polarization to propagate while the bias ready type passes both states, TE and TM, with the TE state being dominant.

THE EYE DIAGRAM MEASUREMENT

The eye diagram measurement is performed from the perspective of a digital transmission system with emphasis on system performance rather than single component performance. The key system performance parameters derived from the eye diagram are extinction ratio, rise and fall times, Q, jitter, and crossing percentage. From a pass/fail criteria perspective, extinction ratio is the most important of these system performance parameters. The higher the extinction ratio the more margin the system has to overcome added noise in the communication link.

Extinction ratio is the ratio (in dB) of the average optical energy in a logic one level Er(1) to the average optical energy in a logic zero level Er(0). The average optical energy is measured by first defining a masked off area centered on each logic level of the eye diagram. The masked off area is dimensioned to conform to the SONET eye diagram mask for OC-48. Using the vertical histogram mode measurement features of the signal analyzer, the average value of each logic level is determined within the masked off area.

The measurement equipment's dark state is a critical parameter that will degrade the extinction ratio measurement if not accounted for. This dark state is an electrical offset generated by the detector and signal analyzer with the laser source off. In order to correct for this electrical offset , an average baseline correction (C_{base}) value is determined using the mask and vertical histogram method. The average baseline correction is subtracted from each logic level's average value before extinction ratio is calculated.

$$\text{Extinction Ratio} = 10 \log_{10} [(Er(1) - C_{base}) / (Er(0) - C_{base})] \text{ dB}$$

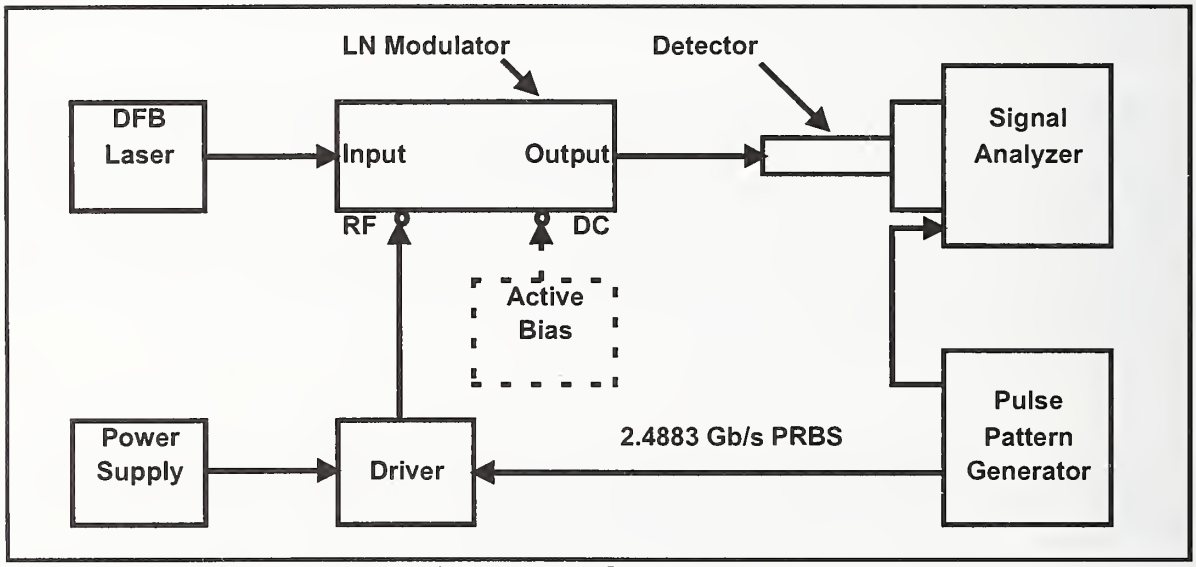

Figure 1 Block Diagram of Eye Diagram Test Setup

EYE DIAGRAM TEST SETUP

The digital transmission system consists of a CW DFB laser, lithium niobate (LN) modulator, modulator driver, detector and communications signal analyzer (see fig. 1). To test system performance, a transmitted data stream consisting of a pseudo random binary sequence of 2^{23}-1 bit length is used. Each component of the digital transmission system has some contribution to the accuracy and repeatability of the eye diagram measurement.

The DFB laser is pigtailed with PM fiber with the laser's TE mode coupled to the fiber's slow axis. It is important that the output polarization extinction ratio be high enough to minimize optical propagation in the TM mode. A poor polarization extinction ratio will appear as attenuation in the highly polarized Bias Free™ modulator. This attenuation will effect the overall sizing of the displayed eye diagram, but have no effect on the extinction ratio measurement as long as there's sufficient power at the detector. For the bias ready device which supports the TM mode, a poor output polarization extinction ratio will degrade the extinction ratio measurement by increasing the average power in the zero logic level.

The modulator's optical output is a single mode (SM) fiber which is terminated in the detector. The critical issue with the detector is not to exceed the maximum peak input power of the detector. Eye diagram waveforms can be distorted by an oversaturated detector. A constant value of optical power should be used with one note that optical power of a modulator biased at quadrature is 3dB down from the peak optical power during modulation. Also the detector's 3dB bandwidth should be three times the bit rate that is to be measured.

The modulator driver' s RF output is connected to the modulator's RF port. The modulator has to be driven precisely from the "Off" state to the "On" state in order to get the best eye diagram performance. The drive voltage required is determined by the modulator switching voltage, $V\pi$. If the drive voltage is too high or too low the eye diagram logic levels will be corrupted as shown in the underdriven case in figure 2. The thickening of both logic levels is primarily due to the underlying electrical reflections generated by non-ideal modulator S11 and modulator driver S22. When the drive is set to the optimum point most of this waveform structure is eliminated due to the "filtering" function of the sinusoidal electro-optic transfer unique to the lithium niobate modulator.

For the bias ready modulator, the phase setting is critical when performing the eye diagram measurement. An improper phase setting during the eye diagram measurement will degrade the measured extinction ratio. An example of a degraded eye due to the phase set significantly above quadrature is shown in figure 3.

CONCLUSION

The evolution of the measurement techniques and experiences presented in this paper, provide a foundation for accurate and repeatable eye diagram measurements of lithium niobate modulators. It is important to remember that the eye diagram measurement is a system measurement with all components contributing to the final measurement. With attention paid to the measurement techniques and subtleties, one can achieve the best eye diagram performance using a lithium niobate modulator (see figure 4).

REFERENCES

1. K. Smith and G. Hetu, "Discussion of Extinction Ratio Measurement," Tektronix, Inc., (1991)
2. Bellcore , "Synchronous Optical Network (SONET) Transport Systems: Common Generic Criteria", GR-253-CORE, Issue 2, (1995)
3. M. Hart, C. Duff, S. Hinch, " Firmware Measurement Algorithms for the HP83480 Digital Communications Analyzer", Hewlett Packard Journal (1996)

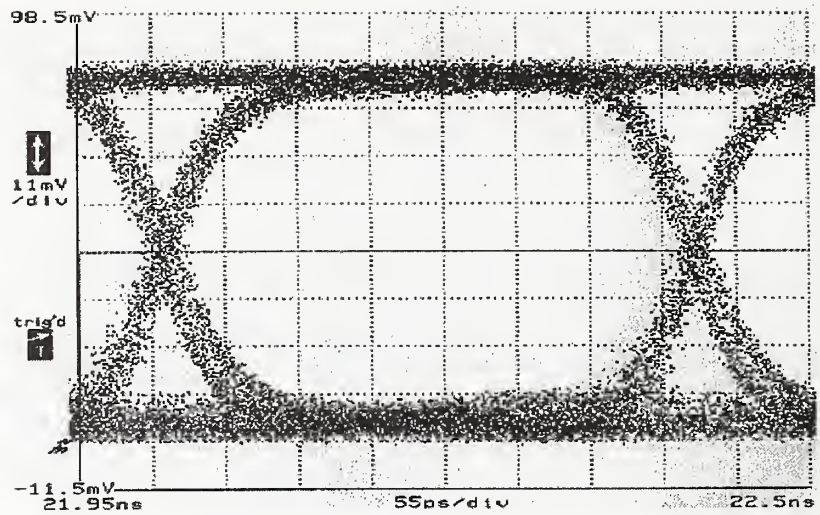

Figure 2 - Underdriven LN Modulator

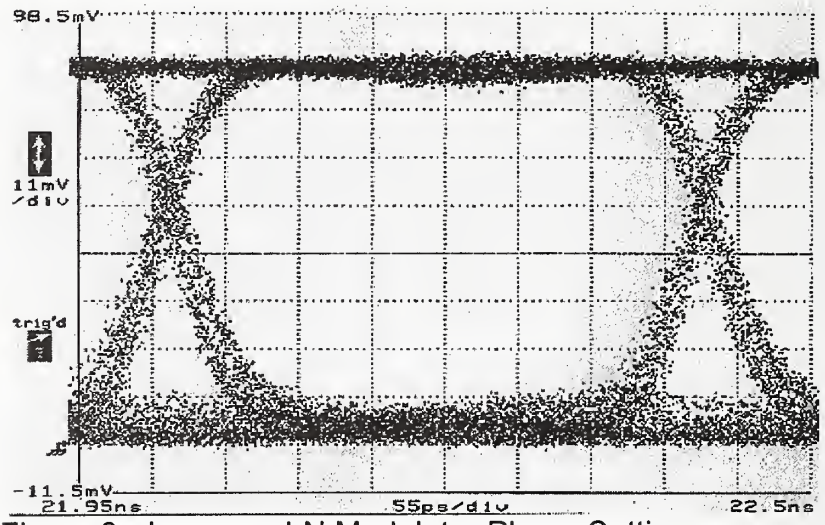

Figure 3 - Improper LN Modulator Phase Setting

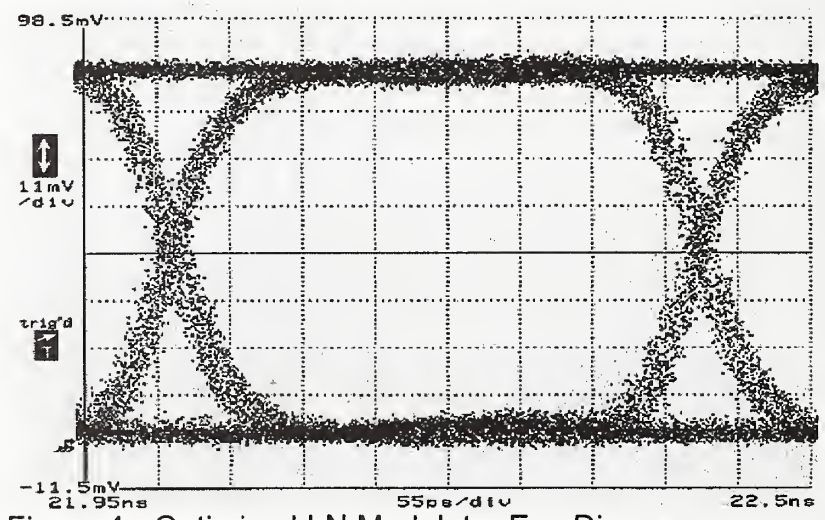

Figure 4 - Optimized LN Modulator Eye Diagram

Dependence of the composition of $InAs_{1-x}Sb_x$ on the mole fraction of In in the melt using LPE.

Vishal Chatrath, S.J.Chua and G.Karunasiri

Center for Optoelectronics, National University of Singapore, 10 Kent Ridge Crescent, Singapore 119260

Dr.Y.Mao

Applied Physics Division, School of Physics & Materials, Lancaster University, Lancaster LA 4YB

Abstract: The liquid phase epitaxial technique was used to grow InAsSb on the Gasb substrate using Sb as a solvent. This study departs from the traditional approach where the mole fraction of the group III component (In) was kept constant while varying the ratio between the group V components (As, Sb) to change the value of "x" in $InAs_{1-x}Sb_x$. In our study we were able to achieve a variation in "x" by keeping the ratio of group V components (As and Sb) constant, while varying the In mole fraction in the melt. With this approach a wider range of temperature can be used for the growth, and layers with both positive and negative lattice mismatch can be obtained without any indication of substrate erosion. To the best of the author's knowledge this is the first study of this kind.

1. INTRODUCTION

There has been a growing interest in the III-V ternary alloy $InAs_{1-x}Sb_x$ as a material for the fabrication of as a material for the fabrication of infrared light emitting diodes and detectors for use in spectroscopic analysis, optical fibre communication and defense applications. The $InAs_{1-x}Sb_x$ is regarded as a promising material because of its room temperature energy gap covering 3-5 μm range of the spectrum when grown on near lattice matching InAs or GaSb substrates.

In this work we investigate the effect of the variation of the mole fraction in the melt of a group III component (In) on the composition of the group V components (As, Sb) in the epitaxial layer. Previous work in the growth of this material was confined to varying one of the group V elements (As, Sb) in order to change the composition of the epitaxial layer. Hence, to the best of the author's knowledge this is the first attempt to understand and explain the influence that the group III component can have on the composition of the ternary.

2. EXPERIMENTAL PROCEDURES

High quality lattice-matched epitaxial layers of n-$InAs_{1-x}Sb_x$ (where x is in the vicinity of 0.09) were grown by LPE on Te doped GaSb substrates (EPD<5000) supplied by ATRAMET Inc. The horizontal sliding boat technique was used and growth from Sb solution was employed to avoid substrate erosion. Growth was carried out at three different temperatures of 565°C, 567°C and 570°C using different mole-fractions in the melt.

Smooth mirror-like epitaxial layers of $InAs_{1-x}Sb_x$ of controllable uniform thickness were obtained under close lattice matching conditions by using 2-7 °C melt super-cooling. The thickness of the epitaxial layer used in the study were typically 4-6 μm and cleaved stained samples showed no evidence of any substrate erosion. After the epitaxial growth the samples were analyzed under the Philips DCD3 double crystal X-ray diffractometer (DCDX). From the peaks obtained, the lattice mismatch between the substrate and the epitaxial layer can be calculated from which we could deduce the composition of the epitaxial layer.

3. RESULTS AND DISCUSSION

The width of a Bragg reflection inevitably indicates the crystal quality of the grown layer. The full-width-at-half-maximum (FWHM) of a perfect reflection is calculated as around 10" by B. E. Warren since a perfect GaAs (004) reflection is about 8~9". This is used as the criterion when evaluating the crystal quality.

Figure 1(a) is the DCXD curve for the epilayer grown. Four peaks were observed, two each for the substrate and the epitaxial layer. The reason

for the two peaks is the incompatibility of the GaAs reference crystal in the DCXD with the material under analysis. The two peaks to the left correspond to the substrate and the magnitude of the split (~30 arc sec.) is typical. The two peaks to the right correspond to the epilayer. If the epilayer peaks are to the right of the substrate peaks then it corresponds to a positive lattice mismatch and vice versa. If the lattice matching is too close then the peaks tend to overlap.

Under these conditions curve fitting is used to see the various components as shown in Figure 1(b). From the figure the percentage lattice mismatch can be calculated. Further, applying Vegard's Law, the composition of the epilayer can be obtained and the results are plotted in Figure 2.

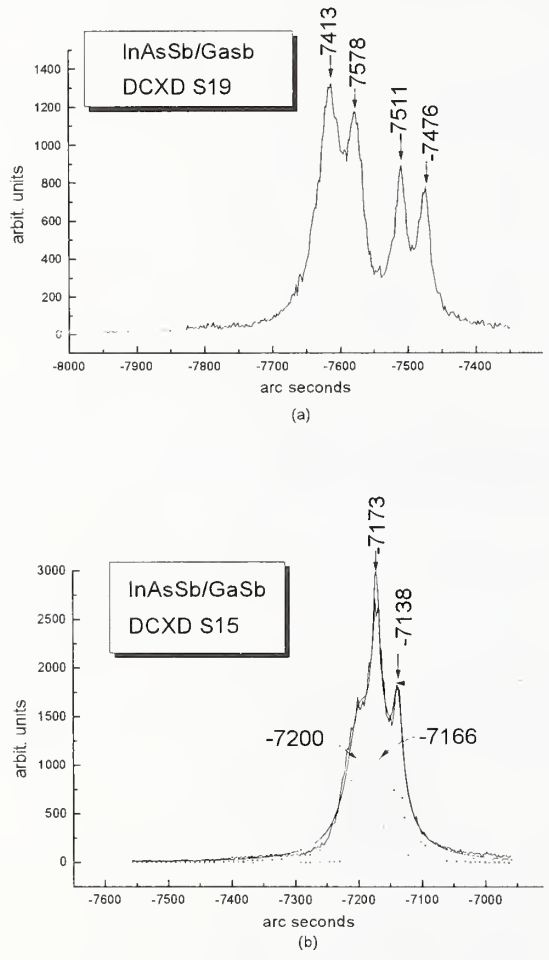

Fig.1(a) Typical DCXD curves. (a) shows a epitaxial layer of a larger lattice constant than the suhstrate. (b) shows a closely lattice matched structure. Here the curve has been resolved to show the individual peaks.

A curve of the Sb composition in the solid versus the mole fraction of In in the melt is given in Figure 2(b). The result suggests that with the increase in the In mole fraction in the melt the Sb composition in the melt, increases, thus edging out As. This effect can be understood by close reference to the thermodynamics involved in the LPE growth. Fig 3 illustrates the density variation in LPE solution. This would mean that the denser components in the melt tend to remain towards the bottom of the well, edging out the less dense ones

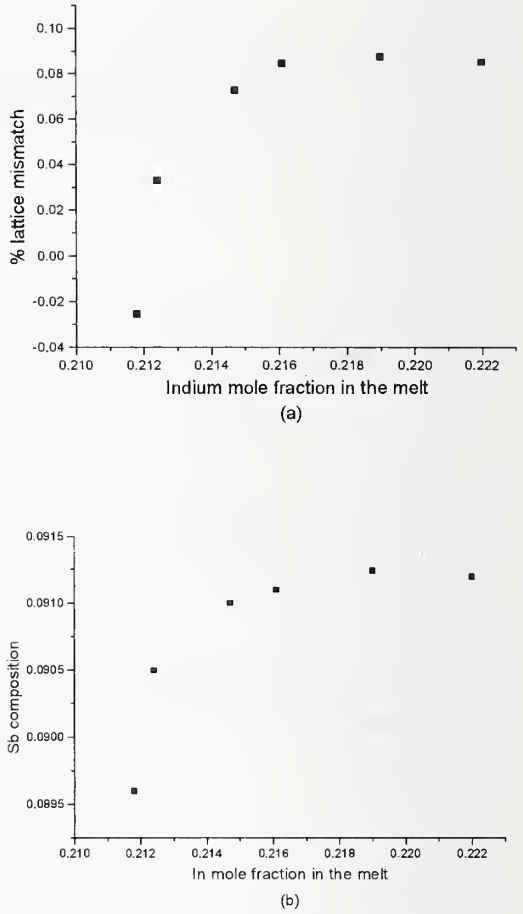

Fig 2 (a) Variation of Sb composition in the epitaxial layer $InAs_{1-x}Sb_x$ with change in the mole fraction in melt. (b) Variation of lattice mismatch with increasing In mole fraction in the melt.

The relative densities of the of the components are as follows:

Arsenic (As):	5.72 gm/cm^3
Antimony (Sb):	6.618 gm/cm^3
Indium (In):	7.31 gm/cm^3

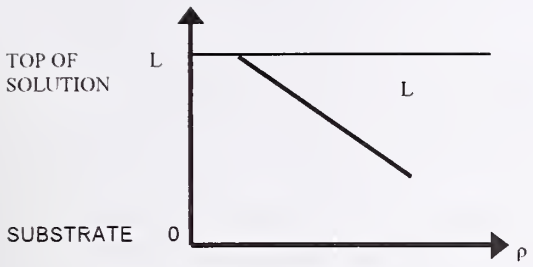

Fig. 3 Density variation in LPE solution.

As more In is added, it sinks to the bottom thus edging out the other two components namely As and Sb. But this effect is more pronounced for As than Sb because of Sb being denser than As. Thus in the region of the melt close to the substrate, the fraction of Sb with respect to As increases. This means there is more Sb available to occupy the group III sites, thus increasing the composition of Sb in epitaxial layer. Since the lattice constant of the epitaxial layer is a function of the composition, we can also see a variation in the lattice parameters. This is shown Figure 4. But increasing the In mole fraction beyond a certain level a which the lattice mismatch tends to remains constant. This effect can be attributed to the fact that LPE growth being an equilibrium process, the substrate crystal does not tolerate the epilayer to grow beyond a certain level of lattice mismatch. Doing growths at different temperatures further strengthened the validity of this theory. When the growth was carried out at a higher temperature of 570°C the same trend was seen with the increasing In mole fraction (Fig4).

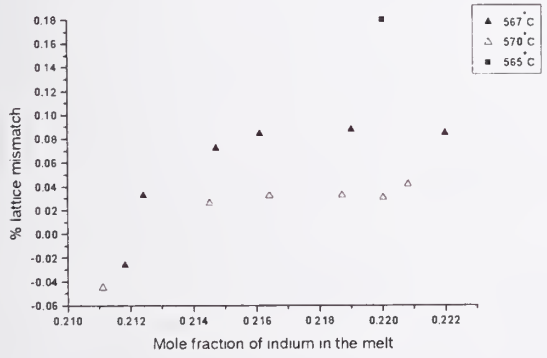

Fig.4 Variation in the lattice mismatch of InAsSb with respect to the GaSb substrate under different temperature conditions.

The interesting thing to note is that when the growth temperature was decreased the incorporation of Sb in the layer increased resulting in the decrease in the composition of As. This is in support of the above-proposed theory and can be explained as follows. With the increase in temperature the convection currents played a stronger part which reduced the tendency of the In (the heaviest component) to displace As (the lightest component) from the lower reaches of the melt solution. That means that more As was able to come in contact with the group V sites more readily and thus its composition in the epitaxial layer was increased.

Growth at 565°C also supported this hypothesis. Here the convection effect was lowered due to the lowering of the temperature which increased the chance of In displacing As from the vicinity of the substrate, resulting in an increase of Sb composition in the epitaxial layer. Unfortunately the growth window at 565°C is very narrow making it difficult to do a growth with a different mole fraction.

4. CONCLUSION

A new model for the LPE growth has been demonstrated. The effect of the density of the components incorporating the melt has been shown to be quite significant. This heralds a new area on which further study can be carried out.

References:
1. Y. Mao and A. Krier, J.Crystal Growth, 133(1993) 108-116.
2. Y. Mao and A. Krier, J.Phys. Chem. Solids Vol. 56 No. 5, pp. 759-766, 1995.
3. T.C. Hasenberg et al, Electron. Lett. 31(4), 275 [16 Feb 1995].
4. H.K. Choi and G.W. Turner, Appl. Phys. Lett. 67(3), 332 [17 July 1995].
5. H. Lee, et al. Appl. Phys. Lett. 66(5), 1942 [10April 1995]

Active Mode-Hop Suppression in External Cavity Lasers

Shigenori Mattori, Takanori Saitoh, Shigeru Kinugawa, and Koichiro Miyagi
Research Laboratory, ANRITSU CORPORATION

Abstract We have demonstrated active mode-hop suppression in external cavity semiconductor lasers including a wavelength-selecting diffraction grating, based on closed-loop control to nullify the difference between the oscillation wavelength and selected wavelength due to the change in diffraction angle. Our approach can be adopted for most Littman-type external cavity lasers with simple attachments; it will be useful for continuous wavelength sweeping and for long-term wavelength stabilization, such as pump sources of atomic frequency standards.

1. Introduction

Recently, optical frequency measurement and control are becoming very important in optical communications, especially for WDM and coherent systems. Also, these techniques are needed in spectroscopy and laser cooling. External cavity semiconductor lasers (ECLs)[1] are used widely for such applications because of the wide tuning range and narrow spectrum line width, as well as the simple structure. However, mode-hopping sometimes occurs in ECLs, which limits the applications.

Many improvements have been made from the aspects of mechanics and system tuning. However, such approaches have never been completely successful because suppression of mode-hopping (MHS) requires severe conditions. To solve these difficulties, we investigated active MHS based on closed-loop control.

2. Cause of Mode-Hopping and Conventional MHS

ECLs usually consist of an optical resonator including a laser diode (LD) with an anti-reflection film on the end facet, and a diffraction grating. The oscillation wavelength is determined by two factors: the resonance modes of the cavity, and the band selected by the diffraction grating. We call the center wavelength of the selected band "selected wavelength," and the wavelength difference between the oscillation wavelength and the selected wavelength "detuning." Mode-hopping occurs if the detuning becomes much larger than half of the mode spacing. Therefore, MHS requires control of these two factors.

Conventional MHS techniques are classified into two types: (1) suitable and accurate mechanical design, and (2) simultaneous precise control of the above two factors. In normal Littman-type ECLs[2], setting a suitable mirror rotation pivot cancels detuning at any rotation angle[3]. In other words, this approach reduces the two factors to one by mechanical linkage. However, this approach has severe demands for implementation, initial adjustment, and maintenance, because the pivot position is critical, typically within 50 μm for a continuous wavelength sweep of 10-nm span in the 1.5-μm region. To use approach (2), the relationship between the wavelength and the two factors must be determined and saved at initial tuning. Nevertheless, the data saved in

any initial table will eventually become partly unusable due to long-term drift.

From the control viewpoint, conventional MHS techniques are based on open-loop control. In other words, all behavior is based on the initial conditions, so the performance is generally sensitive to incomplete initial adjustment, environmental change, and any kind of drift.

3. Principle of Active MHS

To solve this difficulty, we propose active MHS based on closed-loop control to nullify the detuning. The most important item in achieving this goal is detuning detection.

Figure 1 shows the (exaggerated) change in the diffraction angle caused by detuning on a Littrow-type ECL, where λ is oscillation wavelength, and λ_g (fixed in figure) is the selected wavelength. When there is no detuning ($\lambda = \lambda_g$), the diffracted beam returns exactly on the optical axis of the incident beam (Fig. 1 (b)). Assuming that the axis of the incident beam is geometrically non-variant for wavelength change, at detuning, the diffracted beam tilts from the axis as shown in Figs. 1 (a) and 1 (c).

The change in the diffraction angle is observed as beam displacement using a beam sampler and a screen (or CCD array, etc.) in the far field as shown in Fig. 2 (a). The displacement is almost proportional to the detuning because the change of the diffraction angle corresponding to the detuning is usually smaller than 0.01°. To achieve simple detection, we imagined two photo-detection areas and their input powers S_1, S_2, as shown in Fig. 2 (b). We defined the normalized power difference of both sides (NPD) as $(S_2\text{-}S_1)/(S_1+S_2)$. For a Gaussian beam, figure 2 (c) shows the NPD versus detuning normalized by the resolution bandwidth of the grating. The upper abscissa shows the displacement normalized by the beam diameter in the far field. On the other hand, for actual Littman-type ECLs, the ratio of the resolution bandwidth to the free spectral range (FSR) of the cavity is less than 20; mode-hopping occurs if the detuning becomes larger than half of FSR, namely, larger than 0.025 of the resolution bandwidth. From Fig. 2 (c), a detuning of 0.025 of the resolution bandwidth gives an NPD of about 0.05, or 5% of the full scale, which is easy to detect. Consequently, a small change in detuning that never causes mode-hopping can be detected by measuring NPD in most Littman-type ECLs.

4. Experimental Setup

Figure 3 shows a diagram of the experimental setup. The ECL includes an additional beam sampler and PZT actuator. For detection, the beam sampler leads the beam outside the cavity, and has a reflectivity of 20%. The PZT actuator can translate the mirror in the 6-μm range, independently of the rotation.

The FSR of the ECL is 2 GHz (16 pm) at 1520 nm. The estimated resolution bandwidth is about 20 GHz (160 pm). The micrometer driven by a stepping motor rotates the mirror and changes the wavelength; the ratio of the wavelength change to the micrometer displacement is approximately -3 pm/0.25 μm. To achieve frequent mode-hopping, the rotation pivot is not at the best position for continuous wavelength sweeping.

The detector consists of a lens and a CCD camera, because the displacement can be monitored

directly. (Use of a bisection-photodiode would simplify the actual detector.) The lens focuses the reduced far field pattern on the focal plane and the CCD camera detects the beam spot image. A computer converts the image data into the NPD. In addition, the control system can adjust the length of the PZT actuator to nullify the NPD. Feedback control matches the oscillation wavelength with the selected wavelength by changing the cavity length.

5. Experimental Results

First, we observed the relationship between the NPD and wavelength. Figure 4 shows the NPD (dots) and wavelength (line) in the acquisition order as wavelength was decreased and then increased over an 0.8-nm span. The NPD jumps at several points (triangles), also the wavelength hops over about 16 pm at the same points. We confirmed similar results at other measurements including about 50 mode-hops at each wavelength change of 0.16 nm on average. These results show that detuning can be estimated by observing the NPD. The averages of the NPD (dashed lines) are clearly different depending on the direction of the wavelength change. We think this is due to cross saturation between resonance modes[4]. However, the hysteresis is favorable because it expands the tolerable detuning range without mode-hopping.

Next, we demonstrated active MHS. Figure 5 (a) shows the wavelength (diagonal curve) and its increments for each step (dots) measured under active MHS control. The wavelength increments of about 3pm are determined by the micrometer displacement step (-0.25 μm), except at the beginning of the rotation shown on the right. The figure clearly shows that there is no mode-hopping over the 1.2-nm span. The span, which is restricted by the movable range of the PZT actuator, is 7.5 times the average span without control (0.16 nm). In contrast, Fig. 5 (b) shows the wavelength and its increments measured without active MHS control; several dots near 16 pm indicate the occurrence of mode-hopping.

6. Conclusion

We propose an active MHS control technique for ECLs based on closed-loop control to nullify detuning due to the change in diffraction angle. We demonstrated detection of the angle change and MHS in a Littman-type ECL with simple attachments. Our approach can be adopted for most Littman-type ECLs; it will be useful for continuous wavelength sweeping and for long-term wavelength stabilization, such as pump sources of atomic frequency standards.

References

[1] For example, M. W. Fleming and A. Mooradian, *IEEE J. Quantum Electron.*, vol. **QE-17**, No. 1, 44-59, 1981

[2] K. C. Harvey and C. J. Myatt, Optics Lett., vol. **16**, No. 12, 910-913, 1991

[3] H. Lefevre *et al.* (Photonetics S.A.), US Patent No. 5594, 1995

[4] M. Yamada, *IEEE J. Quantum Electron.*, vol. **QE-19**, No. 9, 1365-1380, 1983

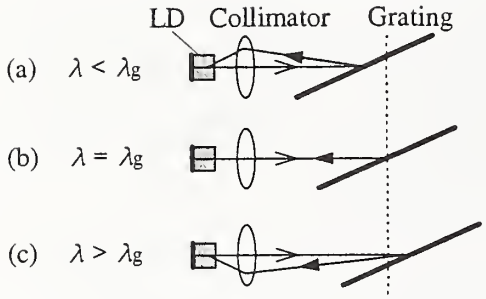

Fig. 1 Illustration of diffraction angle in ECL due to detuning

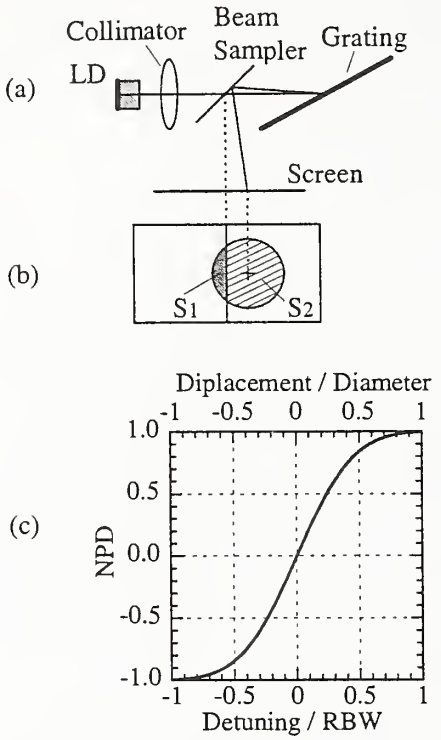

Fig. 2 (a) Illustration of beam displacement, (b) detection powers in two areas, (c) calculation of NPD versus normalized detuning (RBW; resolution bandwidth of the grating)

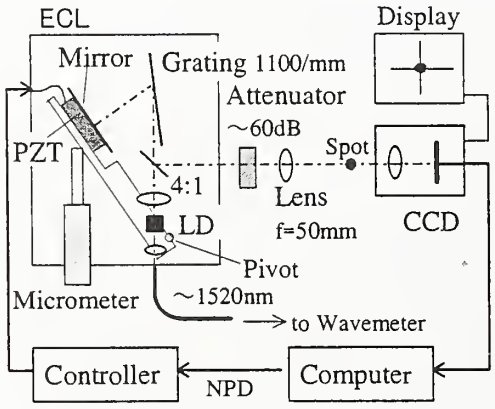

Fig. 3 Experimental setup

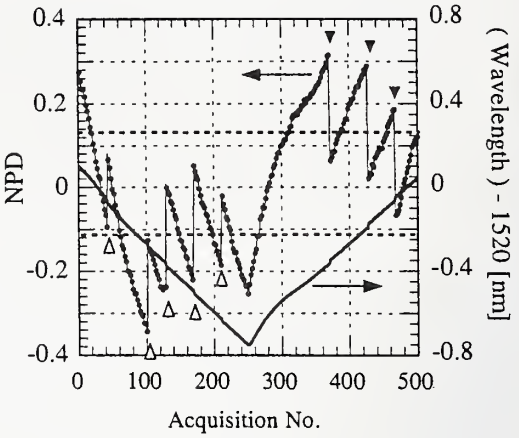

Fig. 4 Measured NPD and wavelength in order of acquisition.

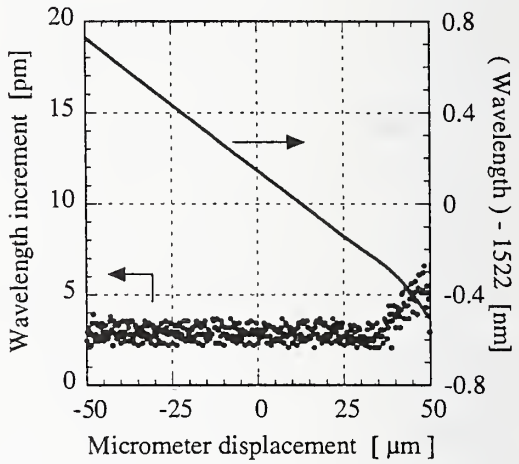

(a) with control

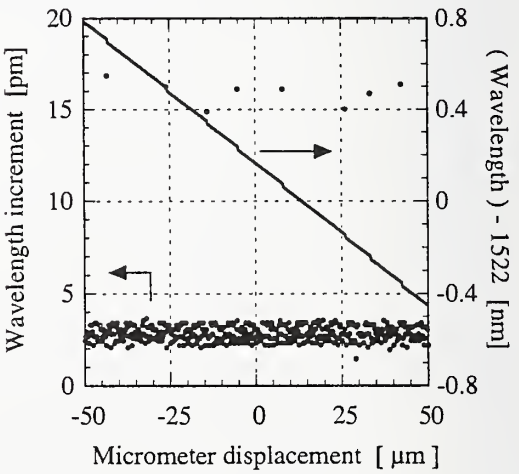

(b) without control

Fig. 5 Wavelength increment for each step of micrometer displacement (dots)

AUTHOR INDEX

NIST Technical Publications

Periodical

Journal of Research of the National Institute of Standards and Technology—Reports NIST research and development in those disciplines of the physical and engineering sciences in which the Institute is active. These include physics, chemistry, engineering, mathematics, and computer sciences. Papers cover a broad range of subjects, with major emphasis on measurement methodology and the basic technology underlying standardization. Also included from time to time are survey articles on topics closely related to the Institute's technical and scientific programs. Issued six times a year.

Nonperiodicals

Monographs—Major contributions to the technical literature on various subjects related to the Institute's scientific and technical activities.

Handbooks—Recommended codes of engineering and industrial practice (including safety codes) developed in cooperation with interested industries, professional organizations, and regulatory bodies.

Special Publications—Include proceedings of conferences sponsored by NIST, NIST annual reports, and other special publications appropriate to this grouping such as wall charts, pocket cards, and bibliographies.

Applied Mathematics Series—Mathematical tables, manuals, and studies of special interest to physicists, engineers, chemists, biologists, mathematicians, computer programmers, and others engaged in scientific and technical work.

National Standard Reference Data Series—Provides quantitative data on the physical and chemical properties of materials, compiled from the world's literature and critically evaluated. Developed under a worldwide program coordinated by NIST under the authority of the National Standard Data Act (Public Law 90-396). NOTE: The Journal of Physical and Chemical Reference Data (JPCRD) is published bi-monthly for NIST by the American Chemical Society (ACS) and the American Institute of Physics (AIP). Subscriptions, reprints, and supplements are available from ACS, 1155 Sixteenth St., NW, Washington, DC 20056.

Building Science Series—Disseminates technical information developed at the Institute on building materials, components, systems, and whole structures. The series presents research results, test methods, and performance criteria related to the structural and environmental functions and the durability and safety characteristics of building elements and systems.

Technical Notes—Studies or reports which are complete in themselves but restrictive in their treatment of a subject. Analogous to monographs but not so comprehensive in scope or definitive in treatment of the subject area. Often serve as a vehicle for final reports of work performed at NIST under the sponsorship of other government agencies.

Voluntary Product Standards—Developed under procedures published by the Department of Commerce in Part 10, Title 15, of the Code of Federal Regulations. The standards establish nationally recognized requirements for products, and provide all concerned interests with a basis for common understanding of the characteristics of the products. NIST administers this program in support of the efforts of private-sector standardizing organizations.

Consumer Information Series—Practical information, based on NIST research and experience, covering areas of interest to the consumer. Easily understandable language and illustrations provide useful background knowledge for shopping in today's technological marketplace.
Order the **above** *NIST publications from: Superintendent of Documents, Government Printing Office, Washington, DC 20402.*
Order the **following** *NIST publications—FIPS and NISTIRs—from the National Technical Information Service, Springfield, VA 22161.*

Federal Information Processing Standards Publications (FIPS PUB)—Publications in this series collectively constitute the Federal Information Processing Standards Register. The Register serves as the official source of information in the Federal Government regarding standards issued by NIST pursuant to the Federal Property and Administrative Services Act of 1949 as amended, Public Law 89-306 (79 Stat. 1127), and as implemented by Executive Order 11717 (38 FR 12315, dated May 11, 1973) and Part 6 of Title 15 CFR (Code of Federal Regulations).

NIST Interagency Reports (NISTIR)—A special series of interim or final reports on work performed by NIST for outside sponsors (both government and non-government). In general, initial distribution is handled by the sponsor; public distribution is by the National Technical Information Service, Springfield, VA 22161, in paper copy or microfiche form.

U.S. Department of Commerce
National Institute of Standards and Technology
325 Broadway
Boulder, Colorado 80303-3328